— Project Review —

Consortium Project on
Seismic Inverse Methods for Complex Structures

Vail, Colorado, May 11-14, 2009

2008-09 CWP Students and Research Leaders:

Jyoti Behura	Luming Liang	Steve Smith
Norm Bleistein	Yongxia Liu	Roel Snieder
Filippo Broggini	Yong Ma	John Stockwell
Yuanzhong Fan	John Mathewson	Mamoru Takanashi
Farnoush Forghani-Arani	Derek Parks	Ilya Tsvankin
Rodrigo Felício Fuck	Francesco Perrone	Xiaoxiang Wang
Dave Hale	Xia (Rosie) Qin	Ran Xuan
Myoung Jae Kwon	Paul Sava	Jia Yan
Ken Larner	Bharath Shekar	Tongning (Tony) Yang

Visiting Scholars:

Seiichiro Kuroda, Sr. Researcher, Natl. Agricultural and Food Research Org., Japan
Evert Slob, Assoc. Professor, TU Delft, The Netherlands
Chenghong Zhu, Sr. Researcher, Sinopec, China

Visiting Students:

Clement Fleury Jürg Hunziker Hossein Mehdi-Zadeh
Mattia Miorali Ali Moradi Tehrani

CWP Staff:

Pam Beckman, Program Assistant
Barbara McLenon, Publications Specialist

Center for Wave Phenomena
Colorado School of Mines, Golden, Colorado 80401
email: cwpcsm@dix.mines.edu http://www.cwp.mines.edu

Contents

Acknowledgments

This project review book is prepared for the sponsors of the Consortium Project at the Center for Wave Phenomena. The Consortium Project provides substantial funding for the overall research and educational program at the Center. The Center has also received funds from the following agencies:

- Abu Dhabi National Oil Company
- U.S. Department of Energy
- ExxonMobil Upstream Research Company
- Landmark / Halliburton
- National Science Foundation
- Petroleum Research Fund of the American Chemical Society
- Research Partnership to Secure Energy for America
- Shell Gamechanger Program
- StatoilHydro

We are extremely grateful for the support of these agencies during the past year and for that of the Consortium sponsors who are listed here.

Aramco Service Company
BHP Billiton Petroleum
BP America Inc.
Bureau of Geophysical Prospecting
CGGVeritas Services (U.S.) Inc.
Chevron Energy Technology Co.
China Petroleum & Chemical Corp.
ConocoPhillips
Devon Energy Corporation
EnCana Corporation
ENI-AGIP E & P Division
ExxonMobil Upstream Research Co.
Hess Corporation
ION Geophysical Corp.
Japan Oil, Gas, and Metals Nat'l Corp.
Landmark / Halliburton
Petrobras America Corp.
PGS Inc.
Shell International E & P
StatoilHydro
Talisman Energy Inc.
TGS-Nopec Geophysical Co.
Total E & P Services
WesternGeco L.L.C.
Woodside Energy Ltd.

CWP Policy on Proprietary Printed Material

New printed material that is produced at the Center for Wave Phenomena under Consortium support is presented to Sponsors before it is released to the general public. We delay general publication by at least 60 days so that Sponsors may benefit directly from their support of the Center for Wave Phenomena.

During this delay, Sponsors may make whatever use of the material inside their organization that they deem proper. However, we expect that all Sponsors will respect the rights of other Sponsors, and of CWP, by not publishing these results externally and independently, in advance of this 60-day delay (even with attribution to CWP). Please refer to your Consortium Membership Agreement under the paragraph entitled "Sponsor Confidentiality Obligation."

Those reports in this book that were produced primarily under consortium support and have not been previously distributed or submitted for publication, will be available for general distribution by October 1, 2008.

If you have independently generated results that duplicate or overlap these, and plan to submit them for publication under your own name before this date, please notify us immediately, so that misunderstandings do not arise.

Welcome From the Director

The Center for Wave Phenomena celebrates its 25th Anniversary this year. This milestone marks the continued innovation and education of a center originally founded by Norm Bleistein, Jack Cohen, Frank Hagin, and John DeSanto. It is a privilege in my new role as director of CWP to give leadership to our center. I am thankful for my predecessors, including recent past directors Ken Larner and Ilya Tsvankin, for giving shape to such a vibrant center focused on discovery and learning. Over the summer we held a retreat with the faculty and staff of CWP to rethink and articulate our goals and values. Central in the outcome of the retreat was that we aim at not only producing world-class research, but also at creating a nurturing environment for students; a research and learning environment that helps students realize their potential and that fosters a balanced growth in intellectual and human skills needed for effective and compassionate leadership. The students, staff, and faculty at CWP constitute a wonderful composite of people. What a joy it is to work with this group!

With great pleasure, we welcome representatives of our sponsor companies to the 25th Annual Project Review Meeting, and look forward to the opportunity to exchange ideas and thoughts about this past year's projects and about plans for the future. Dialogue with sponsor representatives helps us to focus on the scientific problems that are important to your organizations. We look forward to using the Project Review Meeting as a platform for such discussions.

This edition of the report on the Consortium Project at the Center for Wave Phenomena summarizes much of the research conducted within CWP since the 2008 Project Review Meeting. Note that the papers in this report and those presented orally during the meeting, May 11–14, 2009, only partially overlap.

Roel Snieder, Director
Center for Wave Phenomena
May 2009

Papers in this Report

The papers in this volume are grouped into the following categories: interferometry, electromagnetic fields, time-lapse, anisotropy, imaging, and image processing & interpretation. These categories show both similarities to and differences from those of the past few years, indicative of both the continuity and expanding breadth of our research program.

Interferometry

The section on **interferometry** opens with an overview paper of *Snieder, Miyazawa, Slob, Vasconcelos, and Wapenaar* who compare approaches to interferometry based on correlation,

stress-related prestack traveltime shifts for a compacting reservoir embedded in a medium with different elastic properties. They show that, although the excess stress field is sensitive to the contrast in the rigidity modulus across the reservoir boundaries, the influence of background heterogeneity is mostly confined to the reservoir and its immediate vicinity. As is the case for a homogeneous background medium, the offset dependence of traveltime shifts for realistic layered models is mostly controlled by stress-induced anisotropic velocity perturbations. *Fuck and Tsvankin* employ the theory of nonlinear elasticity based on third-order elastic tensors to study stress-induced anisotropy observed, for example, near compacting hydrocarbon reservoirs and salt bodies. They present an intuitive and algebraically simple formalism designed to predict the anisotropic symmetry of a stressed medium from the symmetry of the third-order elastic tensor and properties of the applied stress/strain.

Anisotropy

Four papers comprise the section on **anisotropy**. *Behura and Tsvankin* study the influence of the angle between the real and imaginary parts of the wave vector ("inhomogeneity angle") on attenuation and velocity in arbitrarily anisotropic media using the first-order perturbation theory verified by exact numerical modeling. They show that the group attenuation coefficient measured from seismic data is insensitive to the inhomogeneity angle and can be used to estimate the intrinsic quality factor and the relevant attenuation-anisotropy parameters. *Söllner, Tsvankin, and da Silva* present a time-migration methodology for multi-azimuth P-wave data from azimuthally anisotropic, weakly heterogeneous media. They derive the azimuthally varying diffraction time function and define the "migration-velocity ellipse," which solves the mismatch problem that occurs in conventional processing of multi-azimuth surveys. The algorithm is successfully tested on synthetic data generated for a horizontally layered azimuthally anisotropic medium and an isotropic model with a dipping interface in the overburden. *Wang and Tsvankin* combine 2D P-wave stacking-velocity tomography with borehole data to estimate the interval parameters of tilted transversely isotropic (TTI) media and build an initial anisotropic model for migration velocity analysis. They show that if the symmetry axis is nearly orthogonal to the medium interfaces, the algorithm can resolve the interval symmetry-direction velocity V_{P0} and the anisotropy parameter δ, while the parameter ϵ cannot be constrained without using nonhyperbolic moveout. *Yan and Sava* describe a procedure for elastic wave-mode separation in anisotropic TTI media based on polarization vectors evaluated at every location in space. This technique is implemented in the space-domain using finite-difference operators that represent the polarization vectors as functions of elastic parameters and tilt. The main application of this procedure is in multi-component elastic reverse-time migration.

Imaging

Research on **imaging** is reported in four contributions. *Yang and Sava* explore the kinematic attributes of extended space-time imaging conditions developed for wave-equation migration.

Overview of Developments in CWP

CWP Faculty and Staff

There has been no change in the CWP faculty group since the 2008 Project Review Meeting. The full-time CWP academic faculty includes Dave Hale, Paul Sava, Roel Snieder (director), and Ilya Tsvankin. In accordance with the rotation plan approved by the CWP faculty in 2004, Roel Snieder assumed the position of CWP director in June 2008. Ken Larner and Norm Bleistein remain part of the team in their "retirement," and are actively involved in many aspects of our research and education program. In December, 2008, Michelle Szobody changed positions and now is office manager of the Department of Geophysics at the Colorado School of Mines. She is succeeded in CWP by Pam Beckman who is the new program assistant. Pam manages the CWP office in a professional and cheerful way. Publication specialist Barbara McLenon provides essential assistance in preparing our publications. John Stockwell not only manages the computer systems of CWP, but his insight and expertise in the mathematical aspects of geophysics are also invaluable. John is the manager of Seismic Unix and is instrumental in maintaining and promoting this software for seismic data processing.

Students, Post-Doctoral Fellows, and Long-Term Visitors

During the 2008-2009 academic year, 14 graduate students were doing research in CWP. Five new CWP students (Filippo Broggini, Luming Liang, Francesco Perrone, Bharath Shekar, and Mamoru Takanashi) started their graduate studies in the Fall of 2008. During 2008, three students completed their degree work: John Mathewson, MSc.; Gabriela Melo, MSc.; and Rodrigo Fuck, PhD. Eduardo Filpo Ferreira da Silva joined CWP as a post-doctoral fellow starting in March, 2007 for an 18-month period. Eduardo is a geophysicist with Petrobras, Brazil. Evert Slob has joined CWP as visiting professor for the period January-July, 2009, while on leave from Delft University of Technology. We have been pleased to welcome for several months, three of Evert's students from Delft: Jurg Hunziker, Mattia Miorali, and Ali Tehrani. Also joining Evert has been postdoctoral fellow Seiichiro Kuroda. Chenghong Zhu, from Sinopec, is visiting CWP from March through September, 2009, with the goal of establishing a collaboration between Sinopec and CWP. Walter Söllner of PGS (Oslo, Norway) spent six months of 2008 with CWP as a visiting scholar working on joint research projects.

Center Support

Currently the Consortium is supported by 25 companies including our newest sponsor, Marathon Oil Corporation. We thank the representatives of our sponsors for their continued support. A full list of sponsor companies over the term of the past year appears on the acknowledgment page at the beginning of this volume.

We have received approximately $840K of additional support since June, 2008, from the U.S. Department of Energy, National Science Foundation, Petroleum Research Fund of the American

the Consortium.

Educating our Students

The Department of Geophysics and other departments at the Colorado School of Mines offer numerous graduate courses from which CWP benefits. In addition to these courses, we have taken the following initiatives to educate CWP students.

English writing & speaking

For many students, especially international students, writing scientific papers is an onerous activity. Over the past several semesters, Diane Witters, a writing consultant whose expertise is English as a second language, has worked with CWP students to improve their writing skills, through one-on-one tutoring sessions and writing workshops. Diane closely coordinates her efforts with CWP faculty. In addition to helping students advance their writing skills, she has assisted foreign students to transition from the work-culture in their home country to the professional style common in the United States.

Mathematics

In order to ensure that CWP students master the mathematics needed for wave propagation and imaging, John Stockwell teaches a math clinic, which is a graduate course covering the mathematics needed for much of the research within CWP. The course is attended by a record number of students from CWP as well as from other research groups in the geophysics department. The feedback from students has been extremely positive.

The Art of Science

Roel Snieder offers the course "The Art of Science," which is aimed at helping graduate students develop effective research habits.

Short Courses and Workshops

The CWP faculty has been active in sharing their professional expertise by offering short courses to groups in academia and industry. Please contact CWP if you are interested in hosting one of these short courses.

- Ilya Tsvankin, with his long-time collaborator Vladimir Grechka of Shell, continued to offer the short course *Seismic anisotropy: Basic theory and applications in exploration and reservoir characterization* as part of the SEG Continuing Education Program. The course provides the necessary background information about anisotropic wave propagation and discusses modeling, inversion, and processing of seismic reflection and VSP data in the presence of anisotropy. The main emphasis of the course is on practical parameter-estimation methods for transversely isotropic and orthorhombic subsurface models.

Rock Abuse, led by Mike Batzle; and the Gravity/Magnetics Project, led by Yaoguo Li.

In addition, the CWP faculty have engaged in collaborative efforts with researchers elsewhere. Ilya Tsvankin is spending the Spring 2009 semester on sabbatical leave. He is working on a new book and plans an extended trip to Europe where he will do joint research with Sergei Shapiro at the Free University of Berlin and other colleagues from academia. He will also teach the anisotropy course in several European locations, give a seminar at the PGS office in Oslo, and present a paper at the EAGE Conference in Amsterdam. Other collaborations of the CWP faculty include:

- Norm Bleistein
  - Sam Gray and Yu Zhang (CGGVeritas)
  - Guanquan Zhang (Chinese Academy of Sciences)
- Dave Hale
  - Sverre Brandsberg-Dahl (PGS)
  - Richard Clarke (BP)
  - Marco Maučec and Bob Howard (Landmark)
  - Dave Nichols and John Mathewson (WesternGeco)
  - Joe Stefani (Chevron)
- Paul Sava
  - Clara Andreoletti and Nicola Bienati (ENI)
  - Sergey Fomel (UT Austin)
  - Paul Fowler (WesternGeco)
  - Ivan Vasconcelos (ION Geophysical)
  - Scott Morton (Hess)
  - Michael Payne, Jie Zhang, Anupama Venkataraman, Rongrong Lu, Alex Martinez (ExxonMobil)
  - Ioan Vlad (StatoilHydro)
  - Stewart Wright (Dawson Geophysical)
  - Yu Zhang and Sam Gray (CGGVeritas)
  - Malcolm McNeil (Woodside Energy)
  - Peter Traynin and Lorie Bear (ExxonMobil)
  - Eduardo Filpo Ferreira da Silva (Petrobras)
- Roel Snieder
  - Andrew Curtis and David Halliday (Edinburgh University)
  - Malcolm Sambridge (Australian National University)
  - Johannes Singer and Jon Sheiman (Shell International E&P)
  - Ivan Vasconcelos and Huub Douma (ION Geophysical)
  - Kees Wapenaar and Evert Slob (Delft Institute of Technology)
  - Kasper van Wijk (Boise State University)

- Served as Chair of the Board of Directors of the SEG Advanced Modeling Project (SEAM).
- Served on the Organizing Committee of the 13th International Workshop on Seismic Anisotropy (13IWSA), Winter Park, Colorado, August, 2008.
- Invited speaker for the Geophysical Society of Houston/SEG 2009 Spring Symposium honoring Frank Levin.

- Paul Sava

  - Presented a paper at the EAGE Annual Meeting in Rome (June 2008).
  - Served on the Technical Program Committee for the Annual SEG Meeting, Las Vegas.
  - Presented a paper at the SEG Annual Meeting, Las Vegas (November 2008), and co-authored two other presented papers.
  - Co-author of paper presented at the 13IWSA, Winter Park, CO (August 2008).
  - Traveled to Houston to collaborate with colleagues from ExxonMobil.
  - Traveled to Milan, Italy, to collaborate with colleagues from ENI.
  - Presented the two-day course Wavefield Seismic Imaging (WSI) in Houston, Paris, London, Singapore, Kuala Lumpur, Perth, Calgary, and Perth (again).
  - Served on the EAGE research committee.
  - Co-organized the Madagascar School held in Golden, Colorado (May, 2008).

- Roel Snieder

  - Served on the selection panel of the Spinoza Award of the Netherlands Organisation for Scientific Research. He made two trips to the Netherlands for meetings of the panel.
  - Served on the Earth Science Council of the US Department of Energy (DOE). He presented the lecture "Education for the Global Energy Challenge" at DOE
  - Organized, with co-conveners Kasper van Wijk, Alex Calvert, Matt Haney, and Albena Mateeva, the session "Innovations in Geophysics: A Tribute to Rodney Calvert" at the 2008 SEG Annual Meeting in Las Vegas.
  - Served on the SEG committee Geoscientsts Without Borders and organized the session "Increasing the societal impact of geophysics" at the 2008 Fall meeting of the American Geophysical Union.
  - Presented five papers at the 2008 Fall meeting of the American Geophysical Union.
  - Presented his outreach lecture "The Global Energy Challenge" more than 50 times at universities, community colleges, high school and elementary schools, service clubs, and churches. More information can be found at `http://www.mines.edu/~rsnieder/Global_Energy.html`.
  - Visited the University of Edinburgh to give a seminar on coda wave interferometry and present his course "The Art of Science" in a condensed form.

- Alexandre Araman, from Total S.A. in Pau (France) came to CSM in January 2008 to collaborate with CWP and RCP (the Reservoir Characterization Project) on research projects. Alexandre also took courses in the Professional M.S. Program and recently transferred to the thesis-based M.S. Program in geophysics.
- Clement Fleury, an MSc student from The City of Paris Industrial Physics and Chemistry Higher Educational Institution (ESPCI) is doing research with Roel Snieder (March–September 2009).

We also had a number of short-term visitors:

- Brad Artman, Spectraseis
- Craig Beasley, WesternGeco
- Jack Bouska, BP
- Sverre Brandsberg-Dahl (PGS)
- Richard Clarke (BP)
- Peter Duncan, Micro Seismic Inc.
- Richard Lindsay, Nobel Energy
- Marco Maučec and Bob Howard (Landmark)
- Rustom Mody, Baker Hughes
- Peter Molnar, University of Colorado
- Louise Pellerin, Green Engineering
- Kaoru Sawazaki, Tohoku University
- Niven Shumaker, Nobel Energy
- Don Vasco, Lawrence Berkeley National Lab
- Paul Williamson, Total
- Dan Wisecup, Wisecup Geophysical Consulting
- Frank Wuttke, Bauhaus University

Papers at SEG

CWP students and faculty presented a total of fifteen oral presentations, poster papers, and workshop contributions at the SEG Annual Meeting in Las Vegas. A number of these presentations resulted from collaborations with sponsor companies and academic groups. In addition, CWP faculty and students contributed seven presentations at the 2008 EAGE meeting in Rome.

[3] Mehta, K., Sheiman, J.L., Snieder, R., & Calvert, R. 2008b. Strengthening the virtual-source method for time-lapse monitoring. *Geophysics*, **73**, S73–S80.

[4] Miyazawa, M., Venkataraman, A., Snieder, R., & Payne, M.A. 2008a. Analysis of microearthquake data at Cold Lake and its applications to reservoir monitoring. *Geophysics*, **73**, O15–O21.

[5] Miyazawa, M., Snieder, R., & Venkataraman, A. 2008b. Application of seismic interferometry to extract P and S wave propagation and observation of shear wave splitting from noise data at Cold Lake, Canada. *Geophysics*, **73**, D35–D40.

[6] Payne, M., & Larner, K. 2008. Tips for making effective presentations. *The Leading Edge*, **27**, 423–428.

[7] Rosales, D., Fomel, S., Biondi, B., & Sava, P. 2008. Wave-equation angle-domain common-image gathers for converted waves. *Geophysics*, **73**(1), S17–S26.

[8] Sava, P., & Hill, S. 2009. Overview and classification of wave-equation depth imaging methods. *The Leading Edge*, **28**, 170–183.

[9] Sava, P., & Poliannikov, O. 2008. Interferometric imaging condition for wave-equation migration. *Geophysics*, **73**(2), S47–S61.

[10] Sava, P., & Vlad, I. 2008. Wave-equation migration velocity analysis tutorial. *Geophysics, in press.*

[11] Snieder, R., & Benson, S. 2008a. Education for the global energy challenge. *Physics Today*, **61**(7), 48–49.

[12] Snieder, R., & Benson, S. 2008b. Help make a difference with education and outreach for the global energy challenge! *The Leading Edge*, **27**, 1364–1370.

[13] Snieder, R., van Wijk, K., Haney, M., & Calvert, R. 2008. The cancellation of spurious arrivals in Green's function extraction and the generalized optical theorem. *Phys. Rev. E*, **78**, 036606.

[14] Tsvankin, I. 2008. Properties of evanescent waves in anisotorpic media. *Journal of Seismic Exploration*, **17**,, 237–251.

[15] Vasconcelos, I., & Snieder, R. 2008a. Interferometry by deconvolution, Part 1 Theory for acoustic waves and numerical examples. *Geophysics*, **73**, S115–S128.

[16] Vasconcelos, I., & Snieder, R. 2008b. Interferometry by deconvolution: Part 2 Theory for elastic waves and application to drill-bit seismic imaging. *Geophysics*, **73**, S129–S141.

base is the active membership in the "seisunix" listserver group (750 to 800 members), and general interest via downloads of more than 10 per day, though these may be more reflecting of internet bots, rather than real users. Release 42 of SU was issued on April 20, 2008, and contained many updates and new software. For details, please download the release notes from `http://www.cwp.mines.edu/cwpcodes`.

The open-source Mines Java Toolkit is available online from Dave Hale's home page at `http://www.mines.edu/~dhale/jtk/`. This software is the foundation for most of Dave's teaching and research, and is also being used by commercial software companies. Anyone with a web browser can view and download the always up-to-date source code repository.

Paul Sava and his students continue to work with and develop software for Madagascar, an open-source software package for geophysical data processing and reproducible numerical experiments. Its mission is to provide a convenient and powerful environment and a technology transfer tool for researchers working with digital image and data processing. The technology developed using the Madagascar project management system is transferred in the form of recorded processing histories, which become "computational recipes" to be verified, exchanged, and modified by users of the system. This open-source package is available from `http://rsf.sourceforge.net/`.

Annual Project Review Meeting

This year's Annual Project Review Meeting will be held on May 11-15, 2009, in Vail, Colorado. A tradition of recent years is that, prior to the meeting, we hold a short course for sponsors on a topic of particular interest within CWP. This year, in the afternoon of May 11, Bill Symes of Rice University will give a short course entitled "Velocity Analysis and Waveform Inversion." During the following three days, CWP students and faculty will present more than 20 research papers. In addition, the program will include two guest speakers: John Etgen from BP and Bill Dragoset from Western Geophysical. Thank you for joining us!

A comparison of strategies for seismic interferometry

R. Snieder[1], M. Miyazawa[1,2], E. Slob[3], I. Vasconcelos[1,4] and K. Wapenaar[3]

[1] *Center for Wave Phenomena, Colorado School of Mines, Golden CO 80401 email rsnieder@mines.edu*
[2] *Now at Disaster Prevention Research Institute, Kyoto University, Uji, Kyoto 611-0011, Japan*
[3] *Dept. of Geotechnology, Delft University of Technology, 2600 GA Delft, The Netherlands*
[4] *Now at ION Geophysical, GXT Imaging Solutions, Egham, Surrey, U.K.*

ABSTRACT

The extraction of the response from field fluctuations excited by random sources has received considerable attention in a variety of different fields. We present three methods for the extraction of the systems response that are based on cross-correlation, deconvolution, and the solution of an integral equation, respectively. For systems that are invariant for time-reversal the correlation method requires random sources on a bounding surface only, but when time-reversal invariance is broken, for example by attenuation, a volume distribution of sources is needed. For this reason the correlation method is not useful for diffusive or strongly attenuating systems. We provide examples of the three methods and compare their merits and drawbacks. We show that the extracted fields may satisfy different boundary conditions than does the physical field. This can be used, for example, to suppress surface-related multiples in exploration seismology, to study the coupling of buildings to the subsurface, and to remove the airwave in controlled source electromagnetics (CSEM).

Key words: interferometry, correlation, deconvolution, CSEM

1 INTRODUCTION

The extraction of information from random field fluctuations is a rapidly growing field in physics, acoustics, engineering, and geophysics. The widespread application of this idea has led to a variety of different names used for the method that include Green's function extraction, daylight imaging, the virtual source method, and seismic interferometry. In the exploration seismology community, the name seismic interferometry is now mostly used (Curtis *et al.*, 2006).

The theory for the extraction of the Green's function from field fluctuations has been known in the physics community under the name *fluctuation-dissipation theorem* (Callen & Welton, 1951; Weber, 1956; Kubo, 1966; Rytov *et al.*, 1989; Le Bellac *et al.*, 2004). This theorem states that for a Hamiltonian system in thermodynamic equilibrium the correlation of field fluctuations are related to the impulse response of the system. The name is poorly chosen, because there is, strictly speaking no dissipation in Hamiltonian systems. Tatarskii (Tatarskii, 1987) solved this problem by dividing a system that conserves energy into a part one is interested in, and a part that is irrelevant. The energy flow from the first part to the latter part then effectively acts as dissipation. We show that dissipation plays an interesting role in Green's function extraction.

As with so many developments in geophysics, Aki (Aki, 1957) pioneered in 1957 the use of microseismic noise to extract the properties of the near surface. Lobkis and Weaver (Lobkis & Weaver, 2001) gave the field new momentum with their derivation of Green's function extraction based on normal modes. They made two contributions. First, they showed that the Green's function can be extracted assuming that each mode is excited with the same energy, in other words: thermodynamic equilibrium is not essential. This is important, because the field fluctuations in a macroscopic body, such as the Earth, generally are not in thermodynamic equilibrium. Their second contribution is that they showed how useful the Green's function extraction can be in practical applications.

A flurry of applications appeared in different fields that include ultrasound (Weaver & Lobkis, 2001;

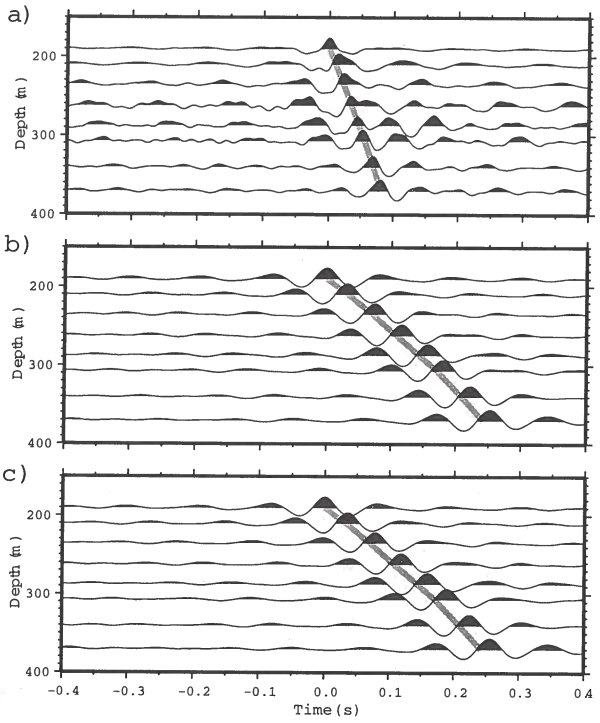

Figure 3. Cross-correlation between the waveforms at the top sensor and those at other sensors for different components: (a) vertical, (b) east-west, and (c) north-south. Grey lines indicate the travel time for P-waves (panel a) and S-waves (panels b and c). The P and S-wave velocities are known at Cold Lake.

averaged the cross correlations measured over a period of one month. The result, after bandpass-filtering between 10 and 55 Hz, is shown in figure 3 for the three components of the recorded motion. A downward propagating wave is clearly visible in the cross-correlation of the vertical components (panel a), and its arrival time agrees well with the travel time of a downward propagating P-wave. The cross correlation of the signals recorded at the vertical component thus clearly extracts downward propagating P-waves that are hidden in the noise of figure 2. The cross correlations of the east-west and north-south components (panels b and c, respectively) show waves that propagate downward with the shear velocity. The cross correlations of the horizontal components successfully extract downward propagating S-waves. By rotating the horizontal components, Miyazawa et al. (Miyazawa *et al.*, 2008) were able to measure shear wave splitting based on correlating the noise measurements.

There is a plethora of derivations of the Green's function extraction from cross-correlation starting from the derivation of the fluctuation-dissipation theorem for Hamiltonian systems in thermal equilibrium (Callen & Welton, 1951; Weber, 1956). Derivations based on normal modes are particularly elegant (Tatarskii, 1987; Lobkis & Weaver, 2001). Only closed system have, in general, normal modes. Alternative derivations, also valid for open systems of acoustic waves, have been developed using time-reversal invariance (Derode *et al.*, 2003b; Derode *et al.*, 2003a; Bakulin & Calvert, 2004), representation theorems (Wapenaar *et al.*, 2005; Wapenaar & Fokkema, 2006), and the summation of random incident plane waves (Weaver & Lobkis, 2005). The derivation based on representation theorems has been extended to elastic waves (Wapenaar, 2004).

For the Fourier convention $f(t) = \int F(\omega)\exp(-i\omega t)d\omega$, with ω is the angular frequency, the extraction of the frequency domain Green's function for acoustic waves is formulated mathematically as (Snieder *et al.*, 2007b)

$$G(\mathbf{r}_A,\mathbf{r}_B) - G^*(\mathbf{r}_A,\mathbf{r}_B) = 2i\omega \oint_{\partial V} \frac{1}{\rho(\mathbf{r})c(\mathbf{r})} G(\mathbf{r}_A,\mathbf{r})G^*(\mathbf{r}_B,\mathbf{r})dS\,. \quad (1)$$

In this expression $G(\mathbf{r}_A,\mathbf{r}_B)$ is the Green's function that accounts for wave propagation from $\mathbf{r}_B$ to $\mathbf{r}_A$, ρ the mass density, c the wave velocity, and the asterisk denotes complex conjugation. The integration is over a closed surface ∂V that encloses receivers at $\mathbf{r}_B$ and $\mathbf{r}_A$. Since a radiation boundary condition is used in this derivation (Wapenaar *et al.*, 2005), the closed surface must be sufficiently far from the receivers. Expression (1) and all other expressions in this work are valid in the frequency domain. For brevity the frequency-dependence is omitted throughout this work.

We first establish the connection with random pressure sources q at the boundary ∂V that excite field fluctuations. Suppose that these sources are spatially uncorrelated and satisfy

$$\langle q(\mathbf{r}_1)q^*(\mathbf{r}_2)\rangle = \frac{|S(\omega)|^2}{\rho(\mathbf{r}_1)c(\mathbf{r}_1)}\delta(\mathbf{r}_1-\mathbf{r}_2)\,, \quad (2)$$

where $|S(\omega)|^2$ is the power spectrum of the noise and $\langle\cdots\rangle$ denotes an ensemble average. In practice this ensemble average is replaced by a time average (Larose *et al.*, 2006a). The integral in expression (1) can be written as $\oint\oint (\rho(\mathbf{r}_1)c(\mathbf{r}_1))^{-1} G(\mathbf{r}_A,\mathbf{r}_1)\delta(\mathbf{r}_1-\mathbf{r}_2)G^*(\mathbf{r}_B,\mathbf{r}_2)dS_1dS_2$, together with equation (2) this gives

$$G(\mathbf{r}_A,\mathbf{r}_B) - G^*(\mathbf{r}_A,\mathbf{r}_B) = \frac{2i\omega}{|S(\omega)|^2}\langle p(\mathbf{r}_A)p^*(\mathbf{r}_B)\rangle\,, \quad (3)$$

where $p(\mathbf{r}_0) = \oint G(\mathbf{r}_0,\mathbf{r})q(\mathbf{r})dS$ are the field fluctuations excited by the random sources on the bounding surface. When sources are present only on part of the bounding surface, the correlation may lead unphysical arrivals (Snieder *et al.*, 2006b; Snieder *et al.*, 2008; Mehta *et al.*, 2008a).

Since complex conjugation in the frequency domain corresponds to time-reversal in the time domain,

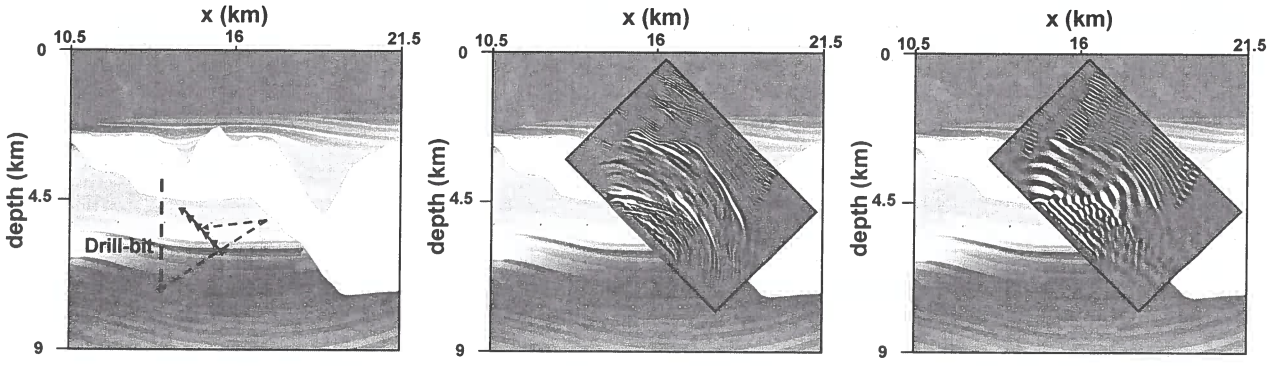

Figure 4. Left panel: the sigsbee model with a salt body shown in white. The hypothetical location of a drill bit and receivers (triangles) in a borhole are shown. Middle panel: the image obtained from deconvolution interferometry. Right panel: the image obtained from correlation interferometry.

The numerator in the last term of equation (5) describes the correlation of the Green's function that is similar to the integrand of expression (1). This suggest that deconvolution and correlation give virtually the same results. This would indeed be the case when the power spectrum $|G(\mathbf{r}_B, \mathbf{r})|^2$ in the denominator would be a smooth function of frequency. But this is not necessarily the case, especially for the important application where the Green's function consists of the superposition of interfering waves. The resulting notches in the power spectrum may make the power spectrum of the Green's function rapidly fluctuating with frequency. In this case one cannot expect that the deconvolution resembles the correlation.

The property that the deconvolution does not depend on the source spectrum is desirable, but this property comes at a price. Consider the special case where the points $\mathbf{r}_A$ and $\mathbf{r}_B$ coincide. In that case the deconvolution in equation (5) reduces to $V_{AA}(\omega) = 1$, which, in the time domain, corresponds to

$$V_{AA}(t) = \delta(t) \; . \tag{6}$$

This means that the field obtained by deconvolution vanishes for nonzero time when the receivers coincide. Physically this means that the deconvolved fields satisfy a *clamped boundary condition* (Vasconcelos & Snieder, 2008a) at one of the receivers. This tells us that deconvolution does not give the true Green's function, unless that Green's function also happens to satisfy a clamped boundary condition at that receiver. In that case, the field fluctuations would vanish as well at that receiver, and there would be nothing to record.

It is, however, not needed to deal with the clamped boundary condition when a perturbation approach is used. Suppose that the medium can be divided in a reference medium with field p_0 and Green's function G_0, and a perturbation with associated perturbations p_S and G_S in the field and Green's function, respectively. The reference medium could be smoothly varying medium, and the perturbation could be the rough medium fluctuations that generate reflected waves, but alternatively the reference medium could account for the subsurface before a time-lapse perturbation, and the perturbation could be the time-lapse change. The latter approach is natural in monitoring applications (Snieder *et al.*, 2007a).

Suppose one can separate for each source at location $\mathbf{r}$ the field into the field perturbation and the unperturbed field, and that one deconvolves those fields:

$$V'_{AB} = \frac{p_S(\mathbf{r}_A)}{p_0(\mathbf{r}_B)} = \frac{G_S(\mathbf{r}_A, \mathbf{r})}{G_0(\mathbf{r}_B, \mathbf{r})} = \frac{G_S(\mathbf{r}_A, \mathbf{r}) G_0^*(\mathbf{r}_B, \mathbf{r})}{|G_0(\mathbf{r}_B, \mathbf{r})|^2} \; . \tag{7}$$

Integration over all sources gives

$$\int_{\partial V} V'_{AB} dS = \int_{\partial V} \frac{G_S(\mathbf{r}_A, \mathbf{r}) G_0^*(\mathbf{r}_B, \mathbf{r})}{|G_0(\mathbf{r}_B, \mathbf{r})|^2} dS \; . \tag{8}$$

When the reference medium is smooth, G_0 does not consist of many interfering waves and usually is a smooth function of frequency. The numerator in expression gives the correlation between wavefield perturbations at $\mathbf{r}_A$ and unperturbed waves at $\mathbf{r}_B$. When the source is at such a location that it launches direct waves to $\mathbf{r}_B$ that are then reflected by the medium perturbation to propagate to $\mathbf{r}_A$, one retrieves the perturbed waves that propagate from $\mathbf{r}_B$ to $\mathbf{r}_A$ (Vasconcelos & Snieder, 2008a). In practice one sums over a range or sources near the stationary phase region for these arrivals. In practice one does not know the precise location and extent of the stationary phase regions, and one employs sources over a larger region that can be assumed to include the stationary phase zones.

In this approach one needs to separate the unperturbed field from the field perturbations. For waves this can sometimes be done using a time gate that separates the direct waves from reflected waves. This does, however, not work when the excitation has a long duration in the time domain. In that case the direction of wave propagation may be used to carry out this separation.

not give the response to a unit source at $\mathbf{r}'$, but instead relates the upgoing field at $\mathbf{r}$ generated by a unit downgoing field at $\mathbf{r}'$. This operator can be used, though, for imaging the region under the acquisition surface.

In figure 5 the upgoing and downgoing fields are indicated by straight lines, but that does not imply that the fields propagate in a homogeneous medium. In fact, the fields propagate through the real subsurface, which can be arbitrarily heterogeneous. Figure 5 depicts a point source at location $\mathbf{r}_S$, but in reality the source may have a finite extent. We simply use the coordinate $\mathbf{r}_S$ to label different sources. The source signal need not be known in the following. In the frequency domain the upgoing field is formed by the superposition of the downgoing field at all locations multiplied with the reflectivity operator

$$U(\mathbf{r},\mathbf{r}_S) = \int R(\mathbf{r},\mathbf{r}')D(\mathbf{r}',\mathbf{r}_S)dS' \,, \qquad (9)$$

where the integration $\int \cdots dS'$ is over the locations $\mathbf{r}'$ in the acquisition surface.

When the upgoing and downgoing fields are known, equation (9) is an integral equation for the reflectivity $R(\mathbf{r},\mathbf{r}')$. For a single source the solution of this equation is ill-posed. Physically this can be understood as follows. Suppose one has just one source at location $\mathbf{r}_S$, then it makes sense that one can not retrieve the reflectivity operator $R(\mathbf{r},\mathbf{r}')$ for all locations $\mathbf{r}$ and $\mathbf{r}'$, especially when the source is not at a favorable location as it is in figure 5. When there are, however, many sources at different locations $\mathbf{r}_S$, can use the combined set of equations (9) for all sources to solve for the reflectivity operator. The number of sources that are needed in practice for a stable reconstruction of the reflectivity operator depends on the frequency of the involved fields, the complexity of those fields, and on the location of those sources.

The connection with the deconvolution method of the previous section follows by assuming that downgoing fields are only present at one fixed location $\mathbf{r}'$ and that that downgoing fiels correspond to the unperturbed field while the upgoing field is the field perturbation. In that case $U(\mathbf{r},\mathbf{r}_S) = R(\mathbf{r},\mathbf{r}')D(\mathbf{r}',\mathbf{r}_S)$, and the reflectivity follows by deconvolving upgoing and downgoing fields: $R(\mathbf{r},\mathbf{r}') = U(\mathbf{r},\mathbf{r}_S)/D(\mathbf{r}',\mathbf{r}_S)$. The deconvolution method of the previous section can thus be seen as an approximation to the multidimensional deconvolution method.

A major advantage of the multidimensional deconvolution approach is that the retrieved reflectivity depends neither on the medium parameters above the acquisition surface, nor on the possible presence of a free-surface above the acquisition surface. The multidimensional deconvolution method is akin to *Noah's deconvolution* proposed by Riley and Claerbout (Riley & Claerbout, 1976), in which the ocean with a free surface is replaced by an unbounded water layer above the acquisition surface. Because of this replacement the retrieved

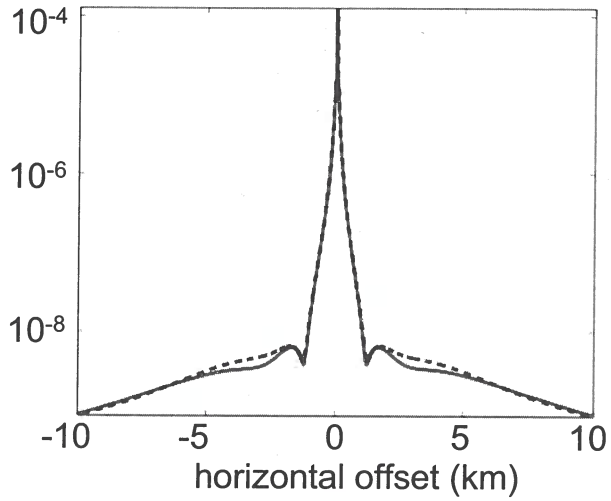

Figure 6. Electric field for the model without reservoir (dashed curve) and the model with a reservoir (solid curve).

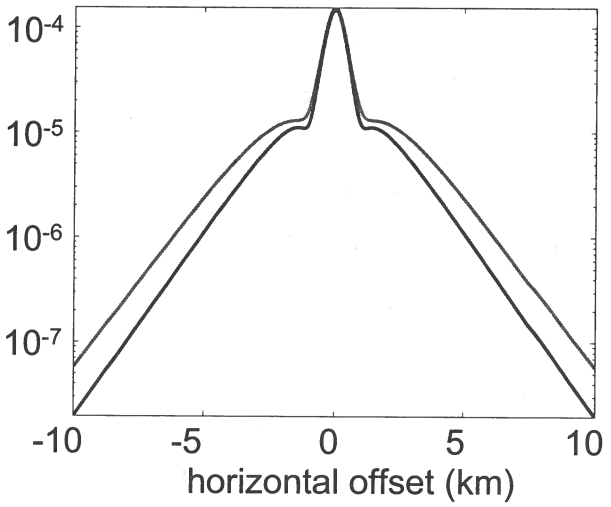

Figure 7. Electric field for the model without reservoir (bottom curve) and the model with a reservoir (top curve).

estimate of the reflectivity is not influenced by the reflections off the free surface above the acquisition plane.

Note that the multidimensional deconvolution method can be applied to any kind of field. We show an example of electromagnetic fields that propagate in the Earth's subsurface. Because of the electrical conductivity and employed frequency (0.25 Hz), such fields are of a diffusive nature, except in the air where the field propagates as wave. This application is of particular interest because in marine applications the propagation of electromagnetic fields through a shallow water layer and the

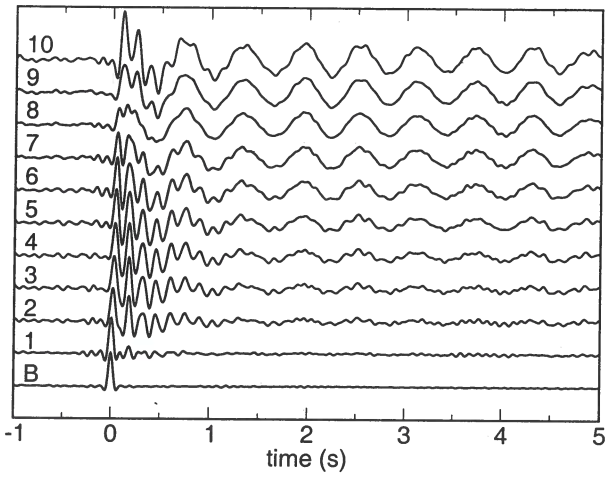

Figure 9. Waveforms of figure 8 after deconvolution with the motion in the basement.

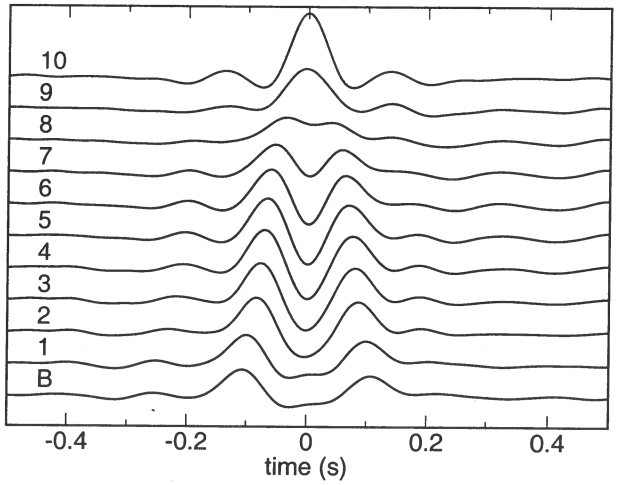

Figure 10. Waveforms of figure 8 after deconvolution with the motion at the top floor.

Claerbout, 1976; Kennett, 1979; Verschuur *et al.*, 1992; van Borselen *et al.*, 1996; Weglein *et al.*, 1998)

We illustrate the freedom to change the boundary conditions in seismic interferometry with the response of the Millikan library at Caltech extracted from recorded vibrations of the building after an earthquake (Snieder & Şafak, 2006). This building is shown in the left panel of figure 8 and the location of accelerometers in the basement and the 10 floors is marked with solid circles. The north-south component of the acceleration after the Yorba Lina earthquake is shown in the right panel. The motion increases with height in the building because of the increased sway of the building with height.

The response extracted by deconvolving the motion at every floor with the motion in the basement is shown in figure 9. As discussed in section 3 the extracted response now satisfies a clamped boundary condition in the basement, and indeed, in figure 9 the motion in the basement is a bandpass-filtered delta function in the basement. For nonzero times, the extracted motion in the basement vanishes. This is, of course, not the case for the real building. In fact, one can see in the bottom trace of the original data in figure 8 that the building is being shaken at its base throughout the arrival of the body wave coda and the surface waves that excite the building. In contrast, the extracted response in figure 9 is for a fictitious building whose base is excited by a bandpass filtered delta pulse and then remains fixed. Such a fictitious building has reflection coefficient $R = -1$ at the base, which precludes the transmission of energy from the subsurface into the building!

As another example we present in figure 10 the motion of the Millikan library after deconvolution with the motion at the top floor. Now the motion at the top floor is collapsed into a bandpass-filtered delta function. Note that this response is a-causal, but it still is a valid wave state of the building that consists of one upgoing wave that is reflected by the top of the building into a downgoing wave. Note that this downgoing wave is not reflected at the base of the building, this wave state thus corresponds to a fictitious building that has reflection coefficient $R = 0$ at its base. Physically, the reflection coefficient vanishes for this wave state because now the the deconvolved motion at the top floor is a bandpass-filtered delta function, hence the deconvolved motion at the top vanishes for nonzero time. Because of the absence of significant internal reflections in the building, see figure 10, any wave reflected upward at the base of the building would cause a nonzero displacement at the top for $t > 0$. Since the deconvolution precludes such motion, the base of the building must be reflection-less for this wave state. This would not be the case if the building would generate significant internal reflections.

The examples of figures 9 and 10 show that from the same data one can retrieve wave-states that satisfy different boundary conditions. The real building has neither reflection coefficient $R = -1$ nor $R = 0$. In the first case, energy would not be able to be transmitted into the building, while the latter case precludes the resonance that is clearly visible in figure 8 because all wave energy is radiated downward at the base. Examples of wave-states of the building that have reflection coefficient $R = 0$, but that are either purely causal or a-causal can be found in ref. (Snieder *et al.*, 2006a). Note that the extracted response in the figures 9 and 10 is solely based on processing of the recorded motion in figure 8. It does not involve numerical modeling of the building and the mechanical properties of the building need not be known.

In marine seismology the idea to change the boundary condition is of particular importance because reflec-

Correlation	Deconvolution	Multidimensional deconvolution
+ exact	+ valid for dissipative systems	+ valid for dissipative systems
+ stable	+ noise spectrum not needed	+ noise spectrum not needed
+ works for two receivers	+ works for two receivers	+ overburden is removed
	+ enhances temporal resolution	+ enhances temporal resolution
- volume sources for dissipative systems	- may be unstable	- needs up/down separation
- needs power spectrum	- correct to first order only	- equation may be ill-posed
		- needs complete coverage

Table 1. The advantages (+) and disadvantages (-) of the correlation method, the deconvolution method, and the multidimensional deconvolution method.

obtained reasonable models for the attenuation in California (Prieto *et al.*, 2009). As shown in equation (3) one must know the power spectrum of the excitation in order to extract the Green's function. For some applications this is not a problem, but in some application this is a restriction that cannot be ignored. As shown by Mehta et al. (Mehta *et al.*, 2008b), small variations in the characteristics of an airgun source lead in marine seismic applications based on the correlation method to spurious events when those variations are not properly accounted for.

The deconvolution approach holds for systems that are not invariant for time reversal as well. Equation (7) gives the perturbed Green's function for the two employed receivers. Note that this expression is solely based on the decomposition of the field in a reference field and a perturbation, but it makes no assumption about the underlying field equation. In the deconvolution approach the spectrum of the excitation need not be known because it does not influence the spectral ratio taken in the deconvolution. This is important in situations where the excitation is unknown, as is the case, for example in drill-bit seismics (Poletto & Miranda, 2004) when the vibrations of the drill-stem have not been recorded. As with the correlation approach one needs just two receivers, unless one employs array techniques such as frequency-wavenumber filtering to separate the unperturbed waves from the perturbed waves (Vasconcelos *et al.*, 2008b). The deconvolution corrects for variations in the spectral amplitude of the source, and therefore gives an extracted response with a larger bandwidth than cross-correlation does. This corresponds, in the time domain, to a response with a greater temporal resolution. This difference can clearly be seen by comparing the middle and right panels of figure 4. Deconvolution corresponds, in the frequency domain, to a spectral ratio. This ratio is unstable near notches in the spectrum. Many methods exists to stabilize the deconvolution (Webster, 1978); we used the water-level method in our applications. A drawback of the deconvolution is that it does not necessarily produce the Green's function. The extracted response at the reference receiver is a band-limited delta function, the response thus satisfies a clamped boundary condition at that point. In seismic exploration this may introduce spurious reflections, but these spurious reflections leave only a weak imprint on seismic images constructed from multi-offset data (Vasconcelos & Snieder, 2008a). On the other hand, in the examples of the analysis of the motion of the Millikan library the clamped boundary condition could be used the extract the building response under boundary conditions other than those of the physical building. This can be used to unravel the contributions of the mechanical properties of the building from the soil-structure interaction.

The multidimensional deconvolution approach is valid for systems that are invariant for time reversal as well as for those that are not invariant for time-reversal. The spectrum of the excitation needs not be known. In fact, in contrast to the correlation approach, the power spectrum of the excitation may vary between different noise sources, and as with the deconvolution method, this technique leads to a response with a larger temporal resolution than is produced by the cross-correlation. The imprint of the overburden is completely removed from the estimated reflectivity. This is of particular importance in applications where reflections from the free surface or an electromagnetic airwave contaminate measured fields. The method relies on up/down decomposition. This processing step may necessitate the use of arrays or the measurement of additional fields such as pressure and displacement in marine seismology or the measurement of electric and magnetic fields in electromagnetic applications, as well as on estimates of the near-surface impedance. The simultaneous solution of integral equation (9) for a number of sources may be unstable. As with the deconvolution such instability may be suppressed to a certain degree by regularization, or it may require increasing the number of sources used. In order to solve the integral equation one must have an array of sensors that adequately cover the acquisition surface. This restriction is particularly important when fields are measured along a line in the acquisition only.

This overview shows that one has considerable freedom in the choice of the method for extracting the system response from field fluctuations. The overview of merits and drawbacks of table 1 may aid the reader in choosing the optimal method for a particular

Seismol. Soc. Am., **91**, 347–364.

Malcolm, A., Scales, J., & van Tiggelen, B.A. 2004. Extracting the Green's function from diffuse, equipartitioned waves. *Phys. Rev. E*, **70**, 015601.

Mehta, K., Snieder, R., & Graizer, V. 2007a. Downhole receiver function: a case study. *Bull. Seismol. Soc. Am.*, **97**, 1396–1403.

Mehta, K., Bakulin, A., Sheiman, J., Calvert, R., & Snieder, R. 2007b. Improving the virtual source method by wavefield separation. *Geophysics*, **72**, V79–V86.

Mehta, K., Snieder, R., Calvert, R., & Sheiman, J. 2008a. Acquisition geometry requirements for generating virtual-source data. *The Leading Edge*, **27**, 620–629.

Mehta, K., Sheiman, J.L., Snieder, R., & Calvert, R. 2008b. Strengthening the virtual-source method for time-lapse monitoring. *Geophysics*, **73**, S73–S80.

Miyazawa, M., Snieder, R., & Venkataraman, A. 2008. Application of seismic interferometry to extract P and S wave propagation and observation of shear wave splitting from noise data at Cold Lake, Canada. *Geophysics*, **73**, D35–D40.

Moldoveanu, N., Combee, L., Egan, M., Hamson, G., Sydora, L., & Abriel, W. 2007. Over/under towed-streamer acquisition: A method to extend seismic bandwidth to both higher and lower frequencies. *The Leading Edge*, **26**, 41–58.

Morse, P.M., & Ingard, K.U. 1968. *Theorerical Acoustics*. New York: McGraw-Hill.

P., Gerstoft, Fehler, M.C., & Sabra, K.G. 2006. When Katrina hit California. *Geophys. Res. Lett.*, **33**, L17308.

Paul, A., Campillo, M., Margerin, L., Larose, E., & Derode, A. 2005. Empirical synthesis of time-asymmetrical Green functions from the correlation of coda waves. *J. Geophys. Res.*, **110**, B08302, doi:10.1029/2004JB003521.

Pharez, S., Hendrick, N., & Tenghemn, R. 2008. First look at seismic data from a towed dual-sensor streamer. *The Leading Edge*, **27**, 904–913.

Poletto, F., & Miranda, F. 2004. Seismic while drilling, fundamentals fo drill-bit seismic for exploration. *In:* K., Helbig, & Treitel, S. (eds), *Handbook of Geophysical Exploration*. Amsterdam: Elsevier.

Poletto, F., Malusa, M., Miranda, F., & Tinivella, U. 2004. Seismic-while-drilling by using dual sensors in drill strings. **69**, 1261–1271.

Prieto, G., Lawrence, J.F., & Beroza, G.C. 2009. Anelastic Earth Structure from the Coherency of the Ambient Seismic Field. *submitted to J. Geophys. Res.*

Rector, J.W., & Marion, B.P. 1991. The use of drill-bit energy as a downhole seismic source. *Geophysics*, **56**, 628–634.

Rickett, J.E., & Claerbout, J.F. 1999. Acoustic daylight imaging via spectral factorization; helioseismology and reservoir monitoring. *The Leading Edge*, **18**, 957–960.

Rickett, J.E., & Claerbout, J.F. 2000. Calculation of the sun's acoustic impulse response by multidimensional spectral factorization. *Solar Physics*, **192**, 203–210.

Riley, D.C., & Claerbout, J.F. 1976. 2-D multiple reflections. *Geophysics*, **41**, 592–620.

Ritzwoller, M.H. 2009. Ambient noise seismic imaging. *In: McGraw Hill Yearbook of Science and Technology 2009*. New York: McGraw-Hill.

Robinson, E.A. 1999. Seismic inversion and deconvolution. *In:* Helbig, K., & Treitel, S. (eds), *Handbook of Geophysical Exploration, 4B*. Amsterdam: Pergamon.

Roux, P., & Fink, M. 2003. Green's function estimation using secondary sources in a shallow water environment. *J. Acoust. Soc. Am.*, **113**, 1406–1416.

Roux, P., Kuperman, W.A., & Group, NPAL. 2004. Extracting coherent wave fronts from acoustic ambient noise in the ocean. *J. Acoust. Soc. Am.*, **116**, 1995–2003.

Roux, P., Sabra, K.G., Gerstoft, P., & Kuperman, W.A. 2005. P-waves from cross correlation of seismic noise. *Geophys. Res. Lett.*, **32**, L19303, doi: 10.1029/2005GL023803.

Rytov, S.M., Kravtsov, Yu.A., & Tatarskii, V.I. 1989. *Principles of statistical radiophysics. Vol. 3, elements of random fields*. Berlin: Springer.

Sabra, K.G., Gerstoft, P., Roux, P., Kuperman, W.A., & Fehler, M.C. 2005a. Surface wave tomography from microseisms in Southern California. *Geophys. Res. Lett.*, **32**, L14311, doi:10.1029/2005GL023155.

Sabra, K.G., Roux, P., Thode, A.M., D'Spain, G.L., & Hodgkiss, W.S. 2005b. Using ocean ambient noise for array self-localization and self-synchronization. *IEEE J. of Oceanic Eng.*, **30**, 338–347.

Sabra, K.G., Roux, P., Gerstoft, P., Kuperman, W.A., & Fehler, M.C. 2006. Extracting coherent coda arrivals from cross-correlations of long period seismic waves during the Mount St. Helens 2004 eruption. *J. Geophys. Res.*, **33**, L06313, doi:1029.2005GL025563.

Sabra, K.G., Conti, S., Roux, P., & Kuperman, W.A. 2007. Passive in-vivo Elastography from Skeletal Muscle Noise. *Appl. Phys. Lett.*, **90**, 194101.

Sabra, K.G., Srivastava, A., di Scalea, F.L., Bartoli, I., Rizzo, P., & Conti, S. 2008. Structural health monitoring by extraction of coherent guided waves from diffuse fields. *J. Acoust. Soc. Am.*, **123**.

Sawazaki, K., Sato, H., Nakahara, H., & Nishimura, T. 2009. Time-Lapse Changes of Seismic Velocity in the Shallow Ground Caused by Strong Ground Motion Shock of the 2000 Western-Tottori Earthquake, Japan, as Revealed from Coda Deconvolution Analysis. *Bull. Seismol. Soc. Am.*, **99**, 352–366.

Schuster, G.T., Yu, J., Sheng, J., & Rickett, J. 2004. Interferometric/daylight seismic imaging. *Geophys. J. Int.*, **157**, 838–852.

Sens-Schönfelder, C., & Wegler, U. 2006. Passive image interferometry and seasonal variations at Merapi volcano, Indonesia. *Geophys. Res. Lett.*, **33**, L21302, doi:10.1029/2006GL027797.

Shapiro, N.M., & Campillo, M. 2004. Emergence of broadband Rayleigh waves from correlations of the ambient seismic noise. *Geophys. Res. Lett.*, **31**, L07614, doi10.1029/2004GL019491.

Shapiro, N.M., Campillo, M., Stehly, L., & Ritzwoller, M.H. 2005. High-resolution surface-wave tomography from ambient seismic noise. *Science*, **307**, 1615–1618.

Slob, E., Draganov, D., & Wapenaar, K. 2007. Interferometric electromagnetic Green's functions representations using propagation invariants. *Geoph. J. Int.*, **169**, 60–80.

Snieder, R. 2004. Extracting the Green's function from the correlation of coda waves: A derivation based on stationary phase. *Phys. Rev. E*, **69**, 046610.

Snieder, R. 2006. Retrieving the Green's function of the diffusion equation from the response to a random forcing. *Phys. Rev. E*, **74**, 046620.

Lagrangian Green's function extraction, with applications to potential fields, diffusion, and acoustic waves

Roel Snieder[1], Evert Slob[1,2], and Kees Wapenaar[2]

[1] *Center for Wave Phenomena, Colorado School of Mines, Golden CO 80401, email rsnieder@mines.edu*

[2] *Dept. of Geotechnology, Delft University of Technology, P.O. Box 5048, 2600 GA Delft, The Netherlands*

ABSTRACT

The extraction of the Green's function from field fluctuations has led to formulations where for a particular application one retrieves either the real part of the Green's function $G + G^*$ or the imaginary part $G - G^*$. We explore the connection between these different formulations for Green's function extraction for general linear scalar systems and derive equations for the extraction for both the real or imaginary part of the Green's function. We show that for systems that are invariant under time reversal, one can either extract $G - G^*$ when the field is excited by sources on the boundary, or $G + G^*$ when sources are present throughout the volume. The freedom to extract either of these functions is important in situations where the imaginary part of the Green's function vanishes. This is the case, for example in static problems where the Green's function is real. We derive the Green's function extraction for potential field problems and for direct current problems in conducting media. For diffusive fields, the new formalism provides the ability to extract the Green's function either from injection sources or from current sources. We show for acoustic waves that $G - G^*$ can be obtained for systems that satisfy a radiation boundary condition, and that $G + G^*$ can be extracted for systems that satisfy homogeneous boundary conditions. The Green's function extraction formulated here corresponds, for acoustic waves, to a Lagrangian formulation rather than the Hamiltonian (energy) principles were used previously.

1 INTRODUCTION

The Green's function extraction from field fluctuations is an area that has recently gone through a spectacular growth (Wapenaar *et al.*, 2008). The technique is ultimately based on the fluctuation dissipation theorem (Callen & Welton, 1951; Weber, 1956; Tatarskii, 1987) formulated decades ago, but applications flourished when ultrasound measurements showed that this technique could be used in practice (Lobkis & Weaver, 2001; Weaver & Lobkis, 2001; Weaver & Lobkis, 2003; Malcolm *et al.*, 2004). The technique found many applications that include ocean acoustics (Roux & Fink, 2003; Roux *et al.*, 2004; Sabra *et al.*, 2005b), crustal seismology (Campillo & Paul, 2003; Sabra *et al.*, 2005a; Roux *et al.*, 2005), exploration seismology (Bakulin & Calvert, 2006; Mehta *et al.*, 2007; Hornby & Yu, 2007; Miyazawa *et al.*, 2008; Schuster, 2009), structural engineering (Snieder & Şafak, 2006; Snieder *et al.*, 2006; Kohler *et al.*, 2007; Sabra *et al.*, 2008; Todorovska, 2009), and medical diagnostics (Sabra *et al.*, 2007). There are several derivations for the theory of Green's function extraction that hold for a large class of linear scalar and vector systems (Wapenaar *et al.*, 2006; Snieder *et al.*, 2007; Weaver, 2008).

Derivations for Green's function extraction yield the sum or the difference of the causal Green's function and it's time-reversed counterpart. In the frequency domain, this corresponds to retrieving $G + G^*$ or $G - G^*$, where the superscript asterisk denotes the complex conjugate. (A notable exception is a derivation (Vasconcelos & Snieder, 2009) for the extraction of field *perturbations* for acoustic waves, that lead to expressions for the perturbed Green's function G_S rather than $G_S \pm G_S^*$.) In practice, it is not a problem that one extracts the superposition $G \pm G^*$; because of the causal properties of the Green's function one can reconstruct the time-reversed Green's function from the causal Green's func-

$$G^*(\mathbf{r}_A,\mathbf{r}_B) = \sum_n (-i\omega)^n \int_V a_n(\mathbf{r}) G(\mathbf{r},\mathbf{r}_A) G^*(\mathbf{r},\mathbf{r}_B) dV - \int_V G^*(\mathbf{r},\mathbf{r}_B) H(\mathbf{r}) G(\mathbf{r},\mathbf{r}_A) dV \ . \tag{4}$$

Interchanging the indices A and B, taking the complex conjugate, and using reciprocity ($G(\mathbf{r}_A,\mathbf{r}_B) = G(\mathbf{r}_B,\mathbf{r}_A)$) gives

$$G(\mathbf{r}_A,\mathbf{r}_B) = \sum_n (+i\omega)^n \int_V a_n^*(\mathbf{r}) G(\mathbf{r},\mathbf{r}_A) G^*(\mathbf{r},\mathbf{r}_B) dV - \int_V G(\mathbf{r},\mathbf{r}_A) H^*(\mathbf{r}) G^*(\mathbf{r},\mathbf{r}_B) dV \ . \tag{5}$$

Expressions (4) and (5) hold for the Green's function and its complex conjugate separately. For time-dependent problems, these functions are nonzero either for positive or negative time, and have for this reason been called *one-sided Green's functions* (Vasconcelos & Snieder, 2009).

Equations (4) and (5), in their current form, are not directly applicable to the extraction of the Green's function from field fluctuations. In order to extract the Green's function from field fluctuations, one needs to multiply the right hand side of these expressions with uncorrelated noise and rewrite the Green's function multiplied by the noise as the field fluctuations, e.g. (Wapenaar *et al.*, 2005; Snieder *et al.*, 2007). The volume integral $\int GHG^* dV$ is, in general, not symmetric in G and G^* because of the action of the differential operator H. In order to use expressions (4) and (5) for Green's function extraction, one must first rewrite the volume integral in such a way that it is symmetric in G and G^*.

To illustrate this last point we consider the important case

$$H(\mathbf{r}) f(\mathbf{r}) = \nabla \cdot (D(\mathbf{r}) \cdot \nabla f(\mathbf{r})) \ . \tag{6}$$

For the diffusion equation D is the diffusion parameter, for acoustic waves $D(\mathbf{r}) = 1/\rho(\mathbf{r})$, with ρ the mass-density, and for Schrödinger's equation $D = -\hbar^2/2m$. For the operator in expression (6) the application of Gauss' law gives

$$\int_V G^*(\mathbf{r},\mathbf{r}_B) H(\mathbf{r}) G(\mathbf{r},\mathbf{r}_A) dV = \oint_{\partial V} D(\mathbf{r}) G^*(\mathbf{r},\mathbf{r}_B) \frac{\partial G(\mathbf{r},\mathbf{r}_A)}{\partial n} dS - \int_V D(\mathbf{r}) \nabla G^*(\mathbf{r},\mathbf{r}_B) \cdot \nabla G(\mathbf{r},\mathbf{r}_A) dV \ , \tag{7}$$

where $\partial/\partial n$ denotes the derivative normal to the boundary ∂V. The surface integral vanishes when either the field or its normal derivative vanishes on ∂V, in which case

$$\int_V G^*(\mathbf{r},\mathbf{r}_B) H(\mathbf{r}) G(\mathbf{r},\mathbf{r}_A) dV = - \int_V D(\mathbf{r}) \nabla G^*(\mathbf{r},\mathbf{r}_B) \cdot \nabla G(\mathbf{r},\mathbf{r}_A) dV \tag{8}$$

In the left hand side the operator H acts only on $G(\mathbf{r},\mathbf{r}_A)$, hence $G^*(\mathbf{r},\mathbf{r}_B)$ and $G(\mathbf{r},\mathbf{r}_A)$ enter the left hand side in different ways. Expressions for Green's function extraction are based on the correlation of fluctuations $u(\mathbf{r}_A) = \int G(\mathbf{r},\mathbf{r}_A) q(\mathbf{r}) dV$ and $u(\mathbf{r}_B) = \int G(\mathbf{r},\mathbf{r}_B) q(\mathbf{r}) dV$, or on similar expressions containing the gradient of G (see section 4). For this reason, $G(\mathbf{r},\mathbf{r}_A)$ and $G^*(\mathbf{r},\mathbf{r}_B)$ must enter the resulting integral in the same way, and hence the used expression must be symmetric in $G(\mathbf{r},\mathbf{r}_A)$ and $G^*(\mathbf{r},\mathbf{r}_B)$. This is not the case with the left hand side of expression (8), but the right hand side *does* have the required symmetry in $G(\mathbf{r},\mathbf{r}_A)$ and $G^*(\mathbf{r},\mathbf{r}_B)$. In sections 4-6 we apply this property to a number of examples.

We next analyze the linear combination $G \pm G^*$. Subtracting expression (4) from (5) gives

$$\begin{aligned} G(\mathbf{r}_A,\mathbf{r}_B) - G^*(\mathbf{r}_A,\mathbf{r}_B) = \ & -2 \textstyle\sum_{n\ odd} (-i\omega)^n \int Re(a_n(\mathbf{r})) G(\mathbf{r},\mathbf{r}_A) G^*(\mathbf{r},\mathbf{r}_B) dV \\ & -2i \textstyle\sum_{n\ even} (-i\omega)^n \int Im(a_n(\mathbf{r})) G(\mathbf{r},\mathbf{r}_A) G^*(\mathbf{r},\mathbf{r}_B) dV \\ & + \int \left(G^*(\mathbf{r},\mathbf{r}_B) H(\mathbf{r}) G(\mathbf{r},\mathbf{r}_A) - G(\mathbf{r},\mathbf{r}_A) H^*(\mathbf{r}) G^*(\mathbf{r},\mathbf{r}_B) \right) dV \ , \end{aligned} \tag{9}$$

where Re and Im denote the real and imaginary parts, respectively. Adding expressions (4) and (5) gives

$$\begin{aligned} G(\mathbf{r}_A,\mathbf{r}_B) + G^*(\mathbf{r}_A,\mathbf{r}_B) = \ & 2i \textstyle\sum_{n\ odd} (-i\omega)^n \int Im(a_n(\mathbf{r})) G(\mathbf{r},\mathbf{r}_A) G^*(\mathbf{r},\mathbf{r}_B) dV \\ & +2 \textstyle\sum_{n\ even} (-i\omega)^n \int Re(a_n(\mathbf{r})) G(\mathbf{r},\mathbf{r}_A) G^*(\mathbf{r},\mathbf{r}_B) dV \\ & - \int \left(G^*(\mathbf{r},\mathbf{r}_B) H(\mathbf{r}) G(\mathbf{r},\mathbf{r}_A) + G(\mathbf{r},\mathbf{r}_A) H^*(\mathbf{r}) G^*(\mathbf{r},\mathbf{r}_B) \right) dV \ , \end{aligned} \tag{10}$$

Equation (9) and its application to the diffusion equation, acoustic waves, and quantum mechanics, was discussed earlier (Snieder *et al.*, 2007). In the following we discuss the connection between expressions (9) and (10) and the application to Green's function extraction from field fluctuations.

In the notation of expression (2), all $a_n = 0$, while H is given by expression (6) with D replaced by ε. We make this replacement throughout this section. If instead of the electrostatic problem we consider direct currents in a conducting medium, then the charge density $q(\mathbf{r})$ is replaced by a volume density of charge injection or extraction rate $-\dot{q}(\mathbf{r})$ (the minus sign comes from the historical convention that the loss of charge from the source region constitutes a positive electric current), and the electric permittivity $\varepsilon(\mathbf{r})$ is replaced by the conductivity $\sigma(\mathbf{r})$. This leaves equation (18) intact with different symbols (Stratton, 1941). This results in a formulation for direct current methods in conducting media.

First note that the Green's function solution to expression (18) is real, hence $G - G^* = 0$ and therefore one cannot retrieve G from the difference $G - G^*$. Using expression (10) together with equation (17) does lead to the following nontrivial relation for $G + G^*$:

$$\begin{aligned} G(\mathbf{r}_A,\mathbf{r}_B) + G^*(\mathbf{r}_A,\mathbf{r}_B) \quad &= -\oint_{\partial V} \varepsilon(\mathbf{r}) \left(G(\mathbf{r},\mathbf{r}_A) \frac{G^*(\mathbf{r},\mathbf{r}_B)}{\partial n} + \frac{G(\mathbf{r},\mathbf{r}_A)}{\partial n} G^*(\mathbf{r},\mathbf{r}_B) \right) dS \\ &\quad +2 \int_V \varepsilon(\mathbf{r}) \left(\nabla G(\mathbf{r},\mathbf{r}_A) \cdot \nabla G^*(\mathbf{r},\mathbf{r}_B) \right) dV \, . \end{aligned} \tag{19}$$

We now assume that either the potential G or the electrical field $\mathbf{E} = -\nabla G$ vanishes at ∂V, or that the boundary is at infinity. In those cases the surface integral vanishes and

$$G(\mathbf{r}_A,\mathbf{r}_B) + G^*(\mathbf{r}_A,\mathbf{r}_B) = 2 \int_V \varepsilon(\mathbf{r}) \left(\nabla G(\mathbf{r},\mathbf{r}_A) \cdot \nabla G^*(\mathbf{r},\mathbf{r}_B) \right) dV \, . \tag{20}$$

In appendix A we verify expression (20) explicitly for the special case of a homogeneous medium.

In order to establish the connection of this equation with the Green's function extraction from field fluctuations we will use the field generated by an electric dipole distribution $\mathbf{p}(\mathbf{r})$ (Griffiths, 1999)

$$u(\mathbf{r}_0) = \int_V \left(\nabla G(\mathbf{r}_0,\mathbf{r}) \right) \cdot \mathbf{p}(\mathbf{r}) dV \, . \tag{21}$$

We next consider random dipole sources that are spatially and directionally uncorrelated and satisfy

$$\langle p_i(\mathbf{r}_1) p_j(\mathbf{r}_2) \rangle = |S|^2 \varepsilon(\mathbf{r}_1) \delta(\mathbf{r}_1 - \mathbf{r}_2) \delta_{ij} \, , \tag{22}$$

where $|S|^2$ measures the strength of the dipole sources. For the moment we consider an ensemble of identical electrostatic systems, each with their own excitation by dipoles, and $\langle \cdots \rangle$ denotes the ensemble average. Multiplying expression (20) with $|S|^2$, using the fact that for this problem G is real, and using the summation convention, gives

$$\begin{aligned} G(\mathbf{r}_A,\mathbf{r}_B)|S|^2 \quad &= 2|S|^2 \int_V \varepsilon(\mathbf{r}) \partial_i G(\mathbf{r},\mathbf{r}_A) \partial_i G^*(\mathbf{r},\mathbf{r}_B) dV \\ &= 2 \int_V \int_V \varepsilon(\mathbf{r}_1) \delta(\mathbf{r}_1 - \mathbf{r}_2) \delta_{ij} \partial_i G(\mathbf{r}_1,\mathbf{r}_A) \partial_j G^*(\mathbf{r}_2,\mathbf{r}_B) dV_1 dV_2 \\ &= 2 \langle \int_V \partial_i G(\mathbf{r}_1,\mathbf{r}_A) p_i(\mathbf{r}_1) dV_1 \int_V \partial_j G^*(\mathbf{r}_2,\mathbf{r}_A) p_j(\mathbf{r}_2) dV_2 \rangle \\ &= 2 \langle u(\mathbf{r}_A) u^*(\mathbf{r}_B) \rangle \, , \end{aligned} \tag{23}$$

where the identity $\int f_i(\mathbf{r}) g_i(\mathbf{r}) dV = \int \int f_i(\mathbf{r}_1) \delta(\mathbf{r}_1 - \mathbf{r}_2) \delta_{ij} g_j(\mathbf{r}_2) dV_1 dV_2$ has been used in the second identity, expression (22) in the third equality, and expression (21) in the last identity.

This means that the electrostatic Green's function $G(\mathbf{r}_A,\mathbf{r}_B)$ follows from the ensemble average of the correlation of field fluctuations recorded at $\mathbf{r}_A$ and $\mathbf{r}_B$ that are excited by uncorrelated dipole sources. In reality one may not have an ensemble of identical electrostatic systems, but one may have a system where random sources fluctuate with time. When the characteristic time of the temporal variations in these dipole sources is large compared to the time it takes for light to propagate through the system, the response of the system is quasi-static. In that case the ensemble average can be replaced by a temporal average over the field fluctuations. In fact, the approach to replace an ensemble average by an average over time is common in seismology where averaging over multiple non-overlapping time windows is used to extract the dynamic Green's function (Larose *et al.*, 2006; Shapiro *et al.*, 2005; Sabra *et al.*, 2005a). By applying the same principle to quasi-static field fluctuations one can extract the electrostatic Green's function from temporal field fluctuations.

Charges are not created or destroyed in macroscopic amounts in a source-free region. This means that only dipoles or higher order multi-poles can excite field fluctuations. For the expected small moment fluctuations, where the local charge separation is orders of magnitude smaller than that of the measurement scale, the contribution of the dipole moments dominates the potential field, and, the electric potential is given by equation (21). The occurrence of dipole moments in a material can have four basic causes: electronic, ionic, dipolar and space charge polarization (Khesin *et al.*, 1996).

$$G(\mathbf{r}_A,\mathbf{r}_B) - G^*(\mathbf{r}_A,\mathbf{r}_B) = 2i\omega \oint_{\partial V} \frac{1}{\rho c} G(\mathbf{r},\mathbf{r}_A) G^*(\mathbf{r},\mathbf{r}_B) dS \,. \tag{33}$$

This well-known equation (Derode *et al.*, 2003; Wapenaar & Fokkema, 2006; Snieder *et al.*, 2007) states that the Green's function can be extracted from field fluctuations excited by sources on a closed surface surrounding $\mathbf{r}_A$ and $\mathbf{r}_B$.

When f and g satisfy the radiation boundary condition (32), $f\partial g^*/\partial n + g^*\partial f/\partial n = 0$. This term also vanishes when either the field or its normal derivative vanishes at the boundary ($p = 0$ or $\partial p/\partial n = 0$ at ∂V). We show in appendix B that for homogeneous boundary conditions the Green's function is real, hence $G - G^* = 0$, and only $G + G^*$ can provide a nontrivial expression for Green's function extraction.

Using the radiation boundary condition or homogeneous boundary condition in expressions (10) and (17) gives the following for the sum $G + G^*$

$$G(\mathbf{r}_A,\mathbf{r}_B) + G^*(\mathbf{r}_A,\mathbf{r}_B) = 2\int_V \frac{1}{\rho}\left((\nabla G(\mathbf{r},\mathbf{r}_A)\cdot\nabla G^*(\mathbf{r},\mathbf{r}_B)) - \frac{\omega^2}{c^2} G(\mathbf{r},\mathbf{r}_A) G^*(\mathbf{r},\mathbf{r}_B)\right) dV \,. \tag{34}$$

The last term on the right hand side comes from the contribution of a_2 to expression (10). This term has the same dependence on the Green's function as does the surface integral in expression (33), but now appears in a volume integral.

When the field satisfies the radiation boundary condition (32), the difference $G - G^*$ can be extracted by cross-correlating the pressure field excited by uncorrelated sources with power spectrum $|S(\omega)|^2$ at the bounding surface ∂V which leads to an expression identical to equation (27) but now for acoustic waves (Snieder *et al.*, 2009a). The situation is more complicated for the case of equation (34) for the sum $G + G^*$, which is applicable under radiation boundary conditions or under homogeneous boundary conditions.

For a general excitation $q(\mathbf{r})$ the pressure is given by $p(\mathbf{r}_0) = \int G(\mathbf{r}_0,\mathbf{r}) q(\mathbf{r}) dV$. Using the decomposition (31) in injection sources and body forces, the pressure can be written as

$$p(\mathbf{r}_0) = -i\omega \int G(\mathbf{r}_0,\mathbf{r}) \frac{Q(\mathbf{r})}{\kappa(\mathbf{r})} dV - \int G(\mathbf{r}_0,\mathbf{r}) \nabla\cdot\left(\frac{\mathbf{f}(\mathbf{r})}{\rho(\mathbf{r})}\right) dV \,. \tag{35}$$

Using Gauss's law, the last integral can be written as $\oint_{\partial V} G(\mathbf{r}_0,\mathbf{r})\mathbf{f}(\mathbf{r})/\rho(\mathbf{r})\cdot d\mathbf{S} - \int (\nabla G(\mathbf{r}_0,\mathbf{r}))\cdot(\mathbf{f}(\mathbf{r})/\rho(\mathbf{r}))\, dV$. When the body force vanishes on the boundary ∂V, the first term in this expression vanishes, and the pressure is given by

$$p(\mathbf{r}_0) = -i\omega \int G(\mathbf{r}_0,\mathbf{r}) \frac{Q(\mathbf{r})}{\kappa(\mathbf{r})} dV + \int (\nabla G(\mathbf{r}_0,\mathbf{r}))\cdot\left(\frac{\mathbf{f}(\mathbf{r})}{\rho(\mathbf{r})}\right) dV \,. \tag{36}$$

Consider first an experiment where only random injection sources excite field fluctuations and that these injection sources are spatially uncorrelated and satisfy

$$\langle Q(\mathbf{r}_1) Q^*(\mathbf{r}_2)\rangle = \kappa(\mathbf{r}_1)|S(\omega)|^2 \delta(\mathbf{r}_1 - \mathbf{r}_2) \,. \tag{37}$$

We assume there are no body forces acting ($\mathbf{f} = 0$), and denote the associated pressure response by p^Q. This response is given by the first term in the right hand side of equation (36), and the cross-correlation of the pressure fluctuations satisfies

$$\begin{aligned}
\langle p^Q(\mathbf{r}_A) p^{Q*}(\mathbf{r}_B)\rangle &= \omega^2 \langle \int G(\mathbf{r}_A,\mathbf{r}_1)\frac{Q(\mathbf{r}_1)}{\kappa(\mathbf{r}_1)} dV_1 \int G^*(\mathbf{r}_B,\mathbf{r}_2)\frac{Q(\mathbf{r}_2)}{\kappa(\mathbf{r}_2)} dV_2\rangle \\
&= \omega^2 \int\int \frac{G(\mathbf{r}_A,\mathbf{r}_1) G^*(\mathbf{r}_B,\mathbf{r}_2)}{\kappa(\mathbf{r}_1)\kappa(\mathbf{r}_2)} \langle Q(\mathbf{r}_1) Q^*(\mathbf{r}_2)\rangle dV_1 dV_2 \\
&= |S(\omega)|^2 \int \frac{\omega^2}{\rho c^2} G(\mathbf{r}_A,\mathbf{r}) G^*(\mathbf{r}_B,\mathbf{r}) dV \,,
\end{aligned} \tag{38}$$

where expression (37) and the relation $\kappa = \rho c^2$ have been used in the last identity. Consider next another experiment where the field fluctuations are excited by uncorrelated body forces that satisfy

$$\langle f_i(\mathbf{r}_1) f_j^*(\mathbf{r}_2)\rangle = \rho(\mathbf{r}_1)|S(\omega)|^2 \delta(\mathbf{r}_1 - \mathbf{r}_2)\delta_{ij} \,, \tag{39}$$

and that there are no injection sources ($Q = 0$). The pressure field p^f for these sources is given by the last term of expression (36), and the correlation of the field fluctuations satisfies

We have shown that for acoustic waves that satisfy a radiation boundary condition at a closed surface, uncorrelated sources at that surface suffice for the extraction of $G - G^*$. When volume sources are present, one can obtain the Green's function from the sum $G + G^*$. A practical limitation of the latter approach is that in this case one needs to record the field fluctuations generated by injection sources and by body forces separately. The ability to extract $G - G^*$ and $G + G^*$ from field fluctuations gives the principle of Green's function extraction a new degree of freedom that has the potential to open up new opportunities for the extraction of the system response from field fluctuations.

ACKNOWLEDGMENTS.

We thank Norm Bleistein, Filippo Broggini, and Jia Yan for their critical and constructive comments.

REFERENCES

Bahat, D., Rabinovitch, A., & Frid, V. 2005. *Tensile Fracturing in Rocks.* Berlin: Springer-Verlag.

Bakulin, A., & Calvert, R. 2006. The virtual source method: Theory and case study. *Geophysics*, **71**, SI139–SI150.

Callen, H.B., & Welton, T.A. 1951. Irreversibility and generalized noise. *Phys. Rev.*, **83**, 34–40.

Campillo, M., & Paul, A. 2003. Long-range correlations in the diffuse seismic coda. *Science*, **299**, 547–549.

Derode, A., Larose, E., Tanter, M., de Rosny, J., Tourin, A., Campillo, M., & Fink, M. 2003. Recovering the Green's function from far-field correlations in an open scattering medium. *J. Acoust. Soc. Am.*, **113**, 2973–2976.

Fink, M. 1997. Time Reversed Acoustics. *Physics Today*, **50**, 34–40.

Griffiths, D.J. 1999. *Introduction to Electrodynamics.* 3 edn. Upper Saddle River, NJ: Prentice Hall.

Hornby, B.E., & Yu, J. 2007. Interferometric imaging of a salt flank using walkaway VSP data. *The Leading Edge*, **26**, 760–763.

Khesin, B., Alexeyev, V., & Eppelbaum, L. 1996. *Interpretation of geophysical fields in complicated environments.* London: Kluwer Academic Publishers.

Kohler, M.D., Heaton, T.H., & Bradford, S.C. 2007. Propagating waves in the steel, moment-frame Factor Building recorded during earthquakes. *Bull. Seismol. Soc Am.*, **97**, 1334–1345.

Larose, E., Margerin, L., Derode, A., van Tiggelen, B., Campillo, M., Shapiro, N., Paul, A., Stehly, L., & Tanter, M. 2006. Correlation of random wavefields: an interdisciplinary review. *Geophysics*, **71**, SI11–SI21.

Lobkis, O.I., & Weaver, R.L. 2001. On the emergence of the Green's function in the correlations of a diffuse field. *J. Acoust. Soc. Am.*, **110**, 3011–3017.

Malcolm, A., Scales, J., & van Tiggelen, B.A. 2004. Extracting the Green's function from diffuse, equipartitioned waves. *Phys. Rev. E*, **70**, 015601.

Mehta, K., Bakulin, A., Sheiman, J., Calvert, R., & Snieder, R. 2007. Improving the virtual source method by wavefield separation. *Geophysics*, **72**, V79–V86.

Miyazawa, M., Snieder, R., & Venkataraman, A. 2008. Application of seismic interferometry to extract P and S wave propagation and observation of shear wave splitting from noise data at Cold Lake, Canada. *Geophysics*, **73**, D35–D40.

Roux, P., & Fink, M. 2003. Green's function estimation using secondary sources in a shallow water environment. *J. Acoust. Soc. Am.*, **113**, 1406–1416.

Roux, P., Kuperman, W.A., & Group, NPAL. 2004. Extracting coherent wave fronts from acoustic ambient noise in the ocean. *J. Acoust. Soc. Am.*, **116**, 1995–2003.

Roux, P., Sabra, K.G., Gerstoft, P., & Kuperman, W.A. 2005. P-waves from cross correlation of seismic noise. *Geophys. Res. Lett.*, **32**, L19303, doi: 10.1029/2005GL023803.

Sabra, K.G., Gerstoft, P., Roux, P., Kuperman, W.A., & Fehler, M.C. 2005a. Surface wave tomography from microseisms in Southern California. *Geophys. Res. Lett.*, **32**, L14311, doi:10.1029/2005GL023155.

Sabra, K.G., Roux, P., Thode, A.M., D'Spain, G.L., & Hodgkiss, W.S. 2005b. Using ocean ambient noise for array self-localization and self-synchronization. *IEEE J. of Oceanic Eng.*, **30**, 338–347.

Sabra, K.G., Conti, S., Roux, P., & Kuperman, W.A. 2007. Passive in-vivo Elastography from Skeletal Muscle Noise. *Appl. Phys. Lett.*, **90**, 194101.

Sabra, K.G., Srivastava, A., di Scalea, F.L., Bartoli, I., Rizzo, P., & Conti, S. 2008. Structural health monitoring by extraction of coherent guided waves from diffuse fields. *J. Acoust. Soc. Am.*, **123**.

Schuster, G. 2009. *Seismic Interferometry.* Cambridge, UK: Cambridge Univ. Press.

Shapiro, N.M., Campillo, M., Stehly, L., & Ritzwoller, M.H. 2005. High-resolution surface-wave tomography from ambient seismic noise. *Science*, **307**, 1615–1618.

Slob, E., & Snieder, R. 2009. Retrieving the potential field response from cross-correlations. *CWP Annual Project Review Book.*

Snieder, R. 2004. *A Guided Tour of Mathematical Methods for the Physical Sciences.* 2nd edn. Cambridge, UK: Cambridge Univ. Press.

Snieder, R. 2006. Retrieving the Green's function of the diffusion equation from the response to a random forcing. *Phys. Rev. E*, **74**, 046620.

Snieder, R. 2007. Extracting the Green's function of attenuating heterogeneous acoustic media from uncorrelated waves. *J. Acoust. Soc. Am.*, **121**, 2637–2643.

Snieder, R., & Şafak, E. 2006. Extracting the building response using seismic interferometry; theory and application to the Millikan Library in Pasadena, California. *Bull. Seismol. Soc. Am.*, **96**, 586–598.

Snieder, R., Sheiman, J., & Calvert, R. 2006. Equivalence of the virtual source method and wavefield deconvolution in seismic interferometry. *Phys. Rev. E*, **73**, 066620.

Snieder, R., Wapenaar, K., & Wegler, U. 2007. Unified Green's function retrieval by cross-correlation; connection with energy principles. *Phys. Rev. E*, **75**, 036103.

In the absence of attenuation the modes are real. The orthogonality relation of the modes follow from a standard derivation consisting of multiplying this expression with a mode u_m, integrating over volume, interchanging n and m and subtracting, applying Gauss' theorem and using that on the boundary either $u = 0$ or $\partial u/\partial n = 0$. This gives the following orthogonality relation that also defines the normalization of the modes

$$\int \frac{1}{\kappa} u_n u_m dV = \delta_{nm} \; . \tag{B2}$$

Eliminating u_n/κ in expression (B2) using the second term of equation (B1) and applying Gauss' theorem gives the following alternative orthogonality relation

$$\int \frac{1}{\rho} (\nabla u_n \cdot \nabla u_m) dV = \omega_n^2 \delta_{nm} \; . \tag{B3}$$

The Green's function has the following normal mode expansion (Snieder, 2004)

$$G(\mathbf{r}_1, \mathbf{r}_2) = \sum_n \frac{u_n(\mathbf{r}_1) u_n(\mathbf{r}_2)}{\omega_n^2 - \omega^2} \; . \tag{B4}$$

Since the modes are real, G is a real function as well.

We next express the integrals in the right hand side of equation (34) in normal modes. Using the previous expression and the relation $\kappa = \rho c^2$ gives

$$\int_V \frac{\omega^2}{\rho c^2} G(\mathbf{r}, \mathbf{r}_A) G^*(\mathbf{r}, \mathbf{r}_B) dV = \sum_{n,m} \frac{\omega^2}{(\omega_n^2 - \omega^2)(\omega_m^2 - \omega^2)} \left(\int \frac{1}{\kappa(\mathbf{r})} u_n(\mathbf{r}) u_m(\mathbf{r}) dV \right) u_n(\mathbf{r}_A) u_m(\mathbf{r}_B) \; . \tag{B5}$$

The orthogonality relation (B2) reduces the double sum in the right hand side to a single sum:

$$\int_V \frac{\omega^2}{\rho c^2} G(\mathbf{r}, \mathbf{r}_A) G^*(\mathbf{r}, \mathbf{r}_B) dV = \omega^2 \sum_n \frac{u_n(\mathbf{r}_A) u_n(\mathbf{r}_B)}{(\omega_n^2 - \omega^2)^2} \; . \tag{B6}$$

This expression differs from the the normal mode expansion (B4) by the square of the frequency difference in the denominator.

The first term in the right hand side of expression (34) can also be expressed in the normal mode expansion (B4):

$$\int_V \frac{1}{\rho} (\nabla G(\mathbf{r}, \mathbf{r}_A)) \cdot (\nabla G^*(\mathbf{r}, \mathbf{r}_B)) dV = \sum_{n,m} \frac{\omega^2}{(\omega_n^2 - \omega^2)(\omega_m^2 - \omega^2)} \left(\int \frac{1}{\rho(\mathbf{r})} (\nabla u_n(\mathbf{r}) \cdot \nabla u_m(\mathbf{r})) \, dV \right) u_n(\mathbf{r}_A) u_m(\mathbf{r}_B) \; . \tag{B7}$$

With the orthogonality relation (B3) the double sum can be reduced to a single sum over modes

$$\int_V \frac{1}{\rho} (\nabla G(\mathbf{r}, \mathbf{r}_A)) \cdot (\nabla G^*(\mathbf{r}, \mathbf{r}_B)) \, dV = \sum_n \omega_n^2 \frac{u_n(\mathbf{r}_A) u_n(\mathbf{r}_B)}{(\omega_n^2 - \omega^2)^2} \; . \tag{B8}$$

The dominant contribution to the response comes from eigenfrequencies ω_n close to the frequency of excitation (ω). A comparison of expressions (B6) and (B8) shows that the two integrals in equation (34) are of the same order of magnitude.

Subtracting equations (B6) and (B8) gives

$$\int_V \frac{1}{\rho} \left((\nabla G(\mathbf{r}, \mathbf{r}_A) \cdot \nabla G^*(\mathbf{r}, \mathbf{r}_B)) - \frac{\omega^2}{c^2} G(\mathbf{r}, \mathbf{r}_A) G^*(\mathbf{r}, \mathbf{r}_B) \right) dV = \sum_n \frac{u_n(\mathbf{r}_A) u_n(\mathbf{r}_B)}{\omega_n^2 - \omega^2} \; . \tag{B9}$$

By virtue of the expansion (B4) this is equal to the Green's function $G(\mathbf{r}_A, \mathbf{r}_B)$. Since the Green's function is real, expression (B9) constitutes an alternative proof of equation (34). Note that in order to obtain this result it is essential to subtract expressions (B6) and (B8) because it is this subtraction that gives the contribution $(\omega_n^2 - \omega^2)$ needed to make the numerator in expressions (B6) and (B8) equal to that of the Green's function in equation (B4).

Retrieving the potential field response from cross-correlations

Evert Slob[1,2] & Roel Snieder[1]

[1] *Center for Wave Phenomena, Colorado School of Mines, Golden, CO 80401, USA*
[2] *On leave from Department of Geotechnology, Delft University of Technology, Delft, The Netherlands.*

ABSTRACT

We show that the two-point cross-correlation of potential-field recordings is equal to the Green's function between the two points. This holds under the condition that spatially and temporally uncorrelated noise sources exist throughout the volume. They should have a known amplitude spectrum and their correlated strengths should be equal to the real part of the dissipative medium property function. Natural fluctuations, such as thermal noise, may occur that satisfy the necessary conditions. When these fluctuations are random deviations from a state of thermal equilibrium the fluctuation-dissipation theorem determines these external sources. This allows for Green's function retrieval for all types of fields that satisfy a similar quasi-static field equation. Under equilibrium conditions, possible downhole reservoir applications include virtual source DC electric resistivity measurements, fluid flow measurements and local temperature estimations.

Key words: Green's function retrieval, potential fields, thermal fluctuations, down hole.

1 INTRODUCTION

The notion of interferometry to mean the extraction of transmission or reflection responses from passive recordings, and use of the newly constructed data for imaging the surroundings has been known for more than 20 years (Scherbaum, 1987; Buckingham *et al.*, 1992). During the past eight years many interferometric methods have been developed for random fields and for controlled-source data. Many of the underlying theories have in common that the medium is assumed to be lossless. The main reason for this underlying assumption is that the wave equation in lossless media is invariant for time-reversal. For an overview of the theory of seismic interferometry or Greens function retrieval and its applications to passive as well as controlled-source data, we refer to a reprint book of Wapenaar *et al.* (2008), which contains a large number of papers on this subject.

It has been shown (Snieder, 2006; Snieder, 2007; Weaver, 2008) that a volume distribution of uncorrelated noise sources, with source strengths proportional to the dissipation parameters of the medium, precisely compensates for the energy losses. This approach holds both for waves in dissipative media and for pure diffusion processes. Recently Wapenaar *et al.* (2006) and Snieder *et al.* (2007) showed that interferometry by cross-correlation, including its extensions for wave fields and diffusive fields in dissipative media, can be represented in a unified form. This naturally leads to the question of whether potential fields can also be retrieved by cross-correlation of noise measurements. Potential fields are the late-time limits of quasi-static fields. Low frequency induced polarization methods use quasi-static electric fields. In practice potential field values are obtained by integrating measured field values. This is done by sampling the field at a certain rate and averaging the results over a predetermined time window. This average value is then stored as the value corresponding to the potential field. Therefore all potential field measurements involve a frequency bandwidth within which the potential field is measured. That is why there can be measurable effects of temporal fluctuations in a potential field.

Physical mechanisms for the noise sources were not identified in the previous studies on field correlations in

continuous outward pointing unit normal vector $\boldsymbol{n}^T = \{n_1, n_2, n_3\}$, to give

$$\int_{\mathbb{D}} \hat{V}_A \hat{I}_B \mathrm{d}^3\boldsymbol{r} = \int_{\mathbb{D}} (\nabla \hat{V}_A) \cdot \hat{\boldsymbol{\sigma}} \cdot (\nabla \hat{V}_B) \mathrm{d}^3\boldsymbol{r} - \oint_{\partial\mathbb{D}} \hat{V}_A \boldsymbol{n} \cdot \hat{\boldsymbol{\sigma}} \cdot \nabla \hat{V}_B \mathrm{d}^2\boldsymbol{r}. \quad (12)$$

To arrive at equation (12), integration by parts and Gauss' divergence theorem has been used in the integral containing the divergence operator. The resulting boundary integral runs over the outer boundary, where continuity conditions or explicit conditions of the Dirichlet and/or Neumann types are assumed to apply. In the latter case the boundary integral vanishes. Similarly, equation (4) for state A can be multiplied with $\hat{V}_B$ and integrated over the domain $\mathbb{D}$, resulting in

$$\int_{\mathbb{D}} \hat{V}_B \hat{I}_A \mathrm{d}^3\boldsymbol{r} = \int_{\mathbb{D}} (\nabla \hat{V}_A) \cdot \hat{\boldsymbol{\sigma}} \cdot (\nabla \hat{V}_B) \mathrm{d}^3\boldsymbol{r} - \oint_{\partial\mathbb{D}} \hat{V}_B \boldsymbol{n} \cdot \hat{\boldsymbol{\sigma}} \cdot \nabla \hat{V}_A \mathrm{d}^2\boldsymbol{r}. \quad (13)$$

Notice that the volume integral in the right-hand side of equation (12) is equal to the volume integral in the right-hand side of equation (13).

We now use delta functions for the sources, $\hat{I}_{A,B} = \delta(\boldsymbol{r} - \boldsymbol{r}_{A,B})$, and the potentials become Green's functions as defined by $\hat{V}_{AB} = \hat{G}(\boldsymbol{r}, \boldsymbol{r}_{A,B})$. For these sources and fields equations (12) and (13) become

$$\hat{G}(\boldsymbol{r}_B, \boldsymbol{r}_A) = \int_{\mathbb{D}} (\nabla \hat{G}(\boldsymbol{r}, \boldsymbol{r}_A)) \cdot \hat{\boldsymbol{\sigma}} \cdot (\nabla \hat{G}(\boldsymbol{r}, \boldsymbol{r}_B)) \mathrm{d}^3\boldsymbol{r} - \oint_{\partial\mathbb{D}} \hat{G}(\boldsymbol{r}, \boldsymbol{r}_A) \boldsymbol{n} \cdot \hat{\boldsymbol{\sigma}} \cdot \nabla \hat{G}(\boldsymbol{r}, \boldsymbol{r}_B) \mathrm{d}^2\boldsymbol{r}, \quad (14)$$

$$\hat{G}(\boldsymbol{r}_A, \boldsymbol{r}_B) = \int_{\mathbb{D}} (\nabla \hat{G}(\boldsymbol{r}, \boldsymbol{r}_A)) \cdot \hat{\boldsymbol{\sigma}} \cdot (\nabla \hat{G}(\boldsymbol{r}, \boldsymbol{r}_B)) \mathrm{d}^3\boldsymbol{r} - \oint_{\partial\mathbb{D}} \hat{G}(\boldsymbol{r}, \boldsymbol{r}_B) \boldsymbol{n} \cdot \hat{\boldsymbol{\sigma}} \cdot \nabla \hat{G}(\boldsymbol{r}, \boldsymbol{r}_A) \mathrm{d}^2\boldsymbol{r}. \quad (15)$$

Here we have assumed that both points $\boldsymbol{r}_{A,B}$ are inside $\mathbb{D}$.

Subtracting equation (14) from (15) gives

$$\hat{G}(\boldsymbol{r}_A, \boldsymbol{r}_B) - \hat{G}(\boldsymbol{r}_B, \boldsymbol{r}_A) = \oint_{\partial\mathbb{D}} \Big(\hat{G}(\boldsymbol{r}, \boldsymbol{r}_A) \boldsymbol{n} \cdot \hat{\boldsymbol{\sigma}} \cdot \nabla \hat{G}(\boldsymbol{r}, \boldsymbol{r}_B) - \hat{G}(\boldsymbol{r}, \boldsymbol{r}_B) \boldsymbol{n} \cdot \hat{\boldsymbol{\sigma}} \cdot \nabla \hat{G}(\boldsymbol{r}, \boldsymbol{r}_A) \Big) \mathrm{d}^2\boldsymbol{r}. \quad (16)$$

For two fixed locations, $\boldsymbol{r}_A$ and $\boldsymbol{r}_B$, the left-hand side of equation (16) is fixed, independent of the choice of $\mathbb{D}$, therefore the right-hand side is also fixed and independent of the choice of $\mathbb{D}$. The right-hand side of equation (16) is therefore independent of the size and shape of $\mathbb{D}$ as long as the points $\boldsymbol{r}_{A,B}$ are both inside the volume. When the volume is taken as infinite space the surface integral goes to zero. This is because the Green's function is proportional to the inverse of distance, while its gradient is proportional to the inverse of distance squared; hence, the product goes to zero proportionally to inverse distance cubed and we sum over a spherical surface proportional to only distance squared. Combining this with the value of the left-hand side that is independent of choice of $\mathbb{D}$, implies that the boundary integral is zero for any bounded volume, even when the medium is arbitrarily heterogeneous outside $\mathbb{D}$. This establishes the well-known source-receiver reciprocity relation $\hat{G}(\boldsymbol{r}_A, \boldsymbol{r}_B) = \hat{G}(\boldsymbol{r}_B, \boldsymbol{r}_A)$, and also leads to the relation

$$\oint_{\partial\mathbb{D}} \hat{G}(\boldsymbol{r}, \boldsymbol{r}_A) \boldsymbol{n} \cdot \hat{\boldsymbol{\sigma}} \cdot \nabla \hat{G}(\boldsymbol{r}, \boldsymbol{r}_B) \mathrm{d}^2\boldsymbol{r} = \oint_{\partial\mathbb{D}} \hat{G}(\boldsymbol{r}, \boldsymbol{r}_B) \boldsymbol{n} \cdot \hat{\boldsymbol{\sigma}} \cdot \nabla \hat{G}(\boldsymbol{r}, \boldsymbol{r}_A) \mathrm{d}^2\boldsymbol{r}, \quad (17)$$

which remains valid when both $\boldsymbol{r}_{A,B}$ are outside the volume, because then the left-hand side of equation (16) is always zero. Note that each integral in equation (17) vanishes when the volume is taken as infinite space.

3 GREEN'S FUNCTION RETRIEVAL

Taking the complex-conjugate state for state A is equivalent to taking the time-reversed causal state in the time domain. Using this in equations (12) and (13) leads to expressions involving cross-correlations of quantities in the time-domain. Using this in the frequency-domain and using source-receiver reciprocity, we directly obtain the global interactions by taking the complex-conjugate Green's function for state A in equations (14) and (15), as

$$\hat{G}^*(\boldsymbol{r}_B, \boldsymbol{r}_A) = \int_{\mathbb{D}} (\nabla \hat{G}^*(\boldsymbol{r}, \boldsymbol{r}_A)) \cdot \hat{\boldsymbol{\sigma}} \cdot (\nabla \hat{G}(\boldsymbol{r}, \boldsymbol{r}_B)) \mathrm{d}^3\boldsymbol{r} - \oint_{\partial\mathbb{D}} \hat{G}^*(\boldsymbol{r}, \boldsymbol{r}_A) \boldsymbol{n} \cdot \hat{\boldsymbol{\sigma}} \cdot \nabla \hat{G}(\boldsymbol{r}, \boldsymbol{r}_B) \mathrm{d}^2\boldsymbol{r}, \quad (18)$$

$$\hat{G}(\boldsymbol{r}_B, \boldsymbol{r}_A) = \int_{\mathbb{D}} (\nabla \hat{G}^*(\boldsymbol{r}, \boldsymbol{r}_A)) \cdot \hat{\boldsymbol{\sigma}}^* \cdot (\nabla \hat{G}(\boldsymbol{r}, \boldsymbol{r}_B)) \mathrm{d}^3\boldsymbol{r} - \oint_{\partial\mathbb{D}} \hat{G}(\boldsymbol{r}, \boldsymbol{r}_B) \boldsymbol{n} \cdot \hat{\boldsymbol{\sigma}}^* \cdot \nabla \hat{G}^*(\boldsymbol{r}, \boldsymbol{r}_A) \mathrm{d}^2\boldsymbol{r}. \quad (19)$$

where the superscript $*$ denotes complex conjugation. We extend the domain $\mathbb{D}$ to three-dimensional infinite space $\mathbb{R}^3$ and use the fact that in that case each surface integral goes to zero. We then obtain two integral relations for the Green's function directly as

$$\hat{G}^*(\boldsymbol{r}_B, \boldsymbol{r}_A) = \int_{\mathbb{R}^3} (\nabla \hat{G}^*(\boldsymbol{r}_A, \boldsymbol{r})) \cdot \hat{\boldsymbol{\sigma}} \cdot (\nabla \hat{G}(\boldsymbol{r}_B, \boldsymbol{r})) \mathrm{d}^3\boldsymbol{r}, \quad (20)$$

$$\hat{G}(\boldsymbol{r}_B, \boldsymbol{r}_A) = \int_{\mathbb{R}^3} (\nabla \hat{G}^*(\boldsymbol{r}_A, \boldsymbol{r})) \cdot \hat{\boldsymbol{\sigma}}^* \cdot (\nabla \hat{G}(\boldsymbol{r}_B, \boldsymbol{r})) \mathrm{d}^3\boldsymbol{r}. \quad (21)$$

Interestingly, the only difference between the right-hand sides of equations (20) and (21) is in the complex conductivity. By adding and subtracting equations (20) and (21), we obtain

$$\Im\{\hat{G}(\boldsymbol{r}_B, \boldsymbol{r}_A)\} = - \int_{\mathbb{R}^3} (\nabla \hat{G}^*(\boldsymbol{r}_A, \boldsymbol{r})) \cdot \Im\{\hat{\boldsymbol{\sigma}}\} \cdot (\nabla \hat{G}(\boldsymbol{r}_B, \boldsymbol{r})) \mathrm{d}^3\boldsymbol{r}, \quad (22)$$

finite time window. The sampling rate defines the maximum frequency and the time-window defines the minimum frequency of the experiment. This implies that the measurement can be written in the frequency-domain as

$$\int_{\omega=\omega_{\min}}^{\omega_{\max}} \hat{V}(\omega)\hat{V}^*(\omega)\mathrm{d}\omega = \frac{2}{\pi}k_B T R(\omega_{\max}-\omega_{\min}). \quad (33)$$

This is under the assumption that the resistance is a constant for all frequencies involved and the capacitance plays no role. When the total resistance varies as a function of frequency, equation (33) is modified to

$$\int_{\omega=\omega_{\min}}^{\omega_{\max}} \hat{V}(\omega)\hat{V}^*(\omega)\mathrm{d}\omega = \frac{2}{\pi}k_B T \int_{\omega=\omega_{\min}}^{\omega_{\max}} \Re\{\hat{Z}(\omega)\}\mathrm{d}\omega, \quad (34)$$

where $\hat{Z}$ denotes the impedance of the circuit. In the case of Johnson's experiment the impedance is given by $\hat{Z} = (R^{-1} - \mathrm{i}\omega C)^{-1}$, C being the capacitance of the circuit, and $\Re\{\hat{Z}\} = R/(1+(\omega RC)^2)$; hence, for a non-conductive circuit, $R \to \infty$ leads to $\Re\{\hat{Z}\} \to 0$.

These results were later generalized by Callen and Welton (1951) in the FDT. Using these observations in the general form of FDT for piecewise continuous macroscopic systems, we find that when a scalar observable $\hat{V}$ is related to a field $\hat{I}$ through a linear response function $\hat{R}$ as $\hat{V} = \hat{I}\hat{R}$, the power spectrum of the observable is proportional to the real part of the linear response function $\Re\{\hat{R}\}$. For a general linear medium and the frequency dependent conductivity being a piecewise continuous function of position we can use the same theorem for thermal fluctuations of the electric field vector to satisfy (Landau & Lifshitz, 1960) the relation that is written in vector components as

$$\int_{\boldsymbol{r}'\in\mathbb{R}^3} \hat{E}_k(\boldsymbol{r})\hat{E}_r^*(\boldsymbol{r}')\mathrm{d}^3\boldsymbol{r}' = \frac{2}{\pi}k_B T \Re\{\hat{\zeta}_{kr}(\boldsymbol{r})\}. \quad (35)$$

Only equation (30) can be used for Green's function retrieval using this thermal fluctuational field, because the right-hand side of equation (35) contains the real part of the electric resistivity matrix, which is contained in equation (30). By writing the observation of electric-potential at $\boldsymbol{r}_A$ or $\boldsymbol{r}_B$ as a response to a thermal noise source in accordance with equation (5) as

$$\hat{V}(\boldsymbol{r}_A) = \int_{\boldsymbol{r}\in\mathbb{R}^3} \hat{\boldsymbol{G}}^{VE}(\boldsymbol{r}_A,\boldsymbol{r})\cdot\hat{\boldsymbol{E}}(\boldsymbol{r})\mathrm{d}^3\boldsymbol{r}, \quad (36)$$

$$\hat{V}(\boldsymbol{r}_B) = \int_{\boldsymbol{r}'\in\mathbb{R}^3} \hat{\boldsymbol{G}}^{VE}(\boldsymbol{r}_B,\boldsymbol{r}')\cdot\hat{\boldsymbol{E}}(\boldsymbol{r}')\mathrm{d}^3\boldsymbol{r}', \quad (37)$$

and using equation (35) in the product of $\hat{V}^*(\boldsymbol{r}_A)$ and $\hat{V}(\boldsymbol{r}_B)$ results in

$$\hat{V}(\boldsymbol{r}_A)^*\hat{V}(\boldsymbol{r}_B) = \int_{\boldsymbol{r}\in\mathbb{R}^3}\int_{\boldsymbol{r}'\in\mathbb{R}^3} [\hat{\boldsymbol{G}}^{VE}(\boldsymbol{r}_A,\boldsymbol{r})]^*\cdot\hat{\boldsymbol{E}}^*(\boldsymbol{r}) \hat{\boldsymbol{E}}(\boldsymbol{r}')\cdot\hat{\boldsymbol{G}}^{VE}(\boldsymbol{r}_B,\boldsymbol{r}')\mathrm{d}^3\boldsymbol{r}'\mathrm{d}^3\boldsymbol{r},$$

$$= \frac{2}{\pi}k_B T \int_{\mathbb{R}^3} [\hat{\boldsymbol{G}}^{VE}(\boldsymbol{r}_A,\boldsymbol{r})]^*\cdot\Re\{\hat{\boldsymbol{\zeta}}\}\cdot\hat{\boldsymbol{G}}^{VE}(\boldsymbol{r}_B,\boldsymbol{r})\mathrm{d}^3\boldsymbol{r}, \quad (38)$$

which is equal to the right-hand side of equation (30), apart from the energy factor $2k_BT/\pi$. This gives the desired Green's function retrieval formulation from cross-correlation of the potential measurements between $\boldsymbol{r}_A$ and $\boldsymbol{r}_B$

$$\hat{V}^*(\boldsymbol{r}_A)\hat{V}(\boldsymbol{r}_B) = \frac{2}{\pi}k_B T \Re\{\hat{G}(\boldsymbol{r}_A,\boldsymbol{r}_B)\}. \quad (39)$$

Snieder (2006) was the first to propose a similar expression for the scalar diffusion equation. The Green's function in the right-hand side of equation (39) is the electric potential at $\boldsymbol{r}_A$ due to a current injection at $\boldsymbol{r}_B$. This is an observable for actual dipole current sources and potential differences measured in the field, which are easily obtained by combining different observations.

When the medium is not dissipative everywhere in $\mathbb{R}^3$, the non-dissipative part of the medium can be excluded to allow the boundary to run at the intersection of the dissipative and non-dissipative domain. Under quasi-static electric field conditions, the earth surface is such an interface, and Dirichlet conditions apply to the normal component of the electric current, so that the boundary integrals present in equations (18) and (19) are still zero and equation (23) remains valid in the reduced volume where the medium is dissipative. This implies that the electric response of the earth as a heterogeneous half space can be determined by cross-correlations of thermal fluctuational noise recordings. If other source mechanisms are present, these thermal fluctuations might be too small to be measured, although increasing the measurement time enhances the signal-to-noise ratio in the correlation results.

4.2 Strengths of electric thermal noise signals

The expected strength of the thermal noise fields depends on the thermal energy. Boltzmann's constant is $k_B \approx 1.4\times10^{-23}$ J/K, and for a room temperature of $T \approx 300$ K, we find $k_BT \approx 4.2\times10^{-21}$ J. The total energy delivered between two electrodes is equal to the energy dissipated in the medium by the resistance of the medium, which is related to the location of the two electrodes. This results in $|V|^2/R = 2k_BT\Delta\omega/\pi$, where R is the apparent resistance of the medium and $\Delta\omega$ is the angular frequency bandwidth of the measurement. The energy depends on the bandwidth of the instrument used in the experiment; we assume a frequency bandwidth of $\Delta f = 10kHz$, and use $\Delta\omega = 2\pi\Delta f$, f being natural frequency. The power is $4k_BT\Delta f \approx 1.7\times10^{-16}$ Watt. If the apparent resistance of the measurement is 50 Ω, the mean fluctuation of the squared electric potential difference between these two points is $|V|^2 \approx 0.85\times10^{-14}$ which corresponds to measuring a voltage difference between the two electrodes of $V \approx 90n$V. This is a small number, but certainly within the measurable range of modern equipment. Furthermore, in our estimate we have not made use of any amplification of the recorded signal. If we have a high quality amplifier that has a linear behavior over the whole frequency bandwidth,

flow in the reservoir, thereby obtaining information as if any location of a measurement is a virtual injection or production point. The response to such a virtual source or sink is obtained from cross-correlating recordings of the head differences at any two measurement locations in a well or between two wells. This could then be used to gain a better insight in the reservoir flow properties and in the changes in these properties over sufficiently large production windows.

A third potentially attractive application is the possibility of measuring downhole temperatures using cross-correlations of electric noise measurements. The cross-correlation of the local electric potential difference between two electrodes is equal to the product of the local temperature and the Green's function between the electrodes, which is an apparent resistance. When an active measurement is performed between the same two electrodes to obtain the local apparent resistance value corresponding to that measurement configuration, the ratio of the noise measurement and the active measurement directly gives the temperature scaled by Boltzmann's constant and $2/\pi$. This can be a possible solution for the downhole temperature measurement at many locations inside or outside a well. The practical applicability depends on the strength of the thermal noise signal. This should be such that the necessary time windows, over which the signal should be averaged, are short enough to assume a relatively constant temperature. Calibration and testing of the method under various circumstances could be achieved by simply combining this procedure with independent temperature measurements in or near a well. Combining passive and active measurements at many receiver locations across wells could be used to obtain an estimate of the volumetric temperature distribution. Specimen temperature has been estimated in the lab on an aluminum cylinder from cross-correlations of acoustic thermal noise recordings and calibrating them to active recordings (Weaver & Lobkis, 2003).

Under the assumption of subsurface steady state and thermal equilibrium conditions all three proposed possible applications can have some merit for measurement-and-control type reservoir management systems. More applications are deemed possible.

7 CONCLUSIONS

We have derived interferometric relations to obtain the Green's function of a quasi-static field between two points from the two-point correlation of noise measurements. This has led to representations for the imaginary part and for the real part of the Green's function. The static potential function is the late-time limit of the quasi-static field and is a real function. For this reason the representation for the real part is of interest. We have shown the relationship between the autocorrelation of the electric potential over an electric circuit and the resistance of the circuit. This is extended by the fluctuation-dissipation theorem to arbitrary linear dissipative systems and can be used for Green's function retrieval. We have shown that thermal fluctuations of electric fields have volume-integrated correlations equal to the real part of the local resistivity times the thermal energy. This directly leads to the identity for the cross-correlation of thermal noise measurements at two locations being equal to the Green's function between those two locations.

Based on the analysis for the quasi-static electric field and the general form of the fluctuation-dissipation theorem, we have generalized the quasi-static field Green's function retrieval formulation to any linear system satisfying a similar modified Laplace equation. Subsurface fluid flow was given as an example. According to the fluctuation-dissipation theorem, thermal noise gives the correlation functions of the sources that are required by the Green's function retrieval formulation from the reciprocity theorem.

Finally, we have proposed three possible downhole applications in reservoir environments. Full coverage DC electric resistivity measurements can be generated from correlations of electric noise recordings. A volumetric distribution of flow properties can be determined from correlations of thermal noise measurements of the hydraulic head at all possible well locations. Downhole temperature can be computed from the ratio of cross-correlation of electric potential thermal noise recordings to active resistivity measurements between the same electrodes. These applications depend on the assumption that thermal noise is the major source of fluctuations and requires that the system is in steady-state and in thermal equilibrium.

ACKNOWLEDGMENTS

We are grateful to Ken Larner, Yongxia Liu and Steve Smith for their critical and constructive comments, which greatly improved the manuscript.

REFERENCES

Buckingham, M. J., Berkhout, B. V., & Glegg, S. A. L. 1992. Imaging the ocean with ambient noise. *Nature (London)*, **356**(6367), 327–329.

Callen, H. B., & Welton, T. A. 1951. Irreversibility and Generalized Noise. *Physical Review*, **83**, 34–40.

Einstein, A. 1905. On the motion required by the molecular kinetic theory of heat of small particles suspended in a stationary liquid. *Annalen der Physik*, **17**, 549–560.

Johnson, J. B. 1928. Thermal agitation of electricity in conductors. *Physical Review*, **32**, 97–109.

Landau, L.D., & Lifshitz, E.M. 1960. *Electrodynamics of Continuous Media*. first edn. New York: Pergamon Press.

Nyquist, H. 1928. Thermal Agitation of Electric Charge in Conductors. *Physical Review*, **32**, 110–113.

Controlled source electromagnetic interferometry by multidimensional deconvolution: Spatial sampling aspects

Jürg Hunziker, Evert Slob & Kees Wapenaar
TU Delft, The Netherlands

ABSTRACT
We review electromagnetic interferometry by multidimensional deconvolution (MDD) and investigate its sensitivity to spatial sampling. Two Sea Bed Logging datasets were modeled numerically. One represents a shallow sea situation with a small vertical source-receiver distance and the other a deep sea situation with a large vertical source-receiver distance. The reflection response from below the receivers was retrieved by interferometry by MDD after decomposition of the field into up- and downgoing fields. This reflection response is independent of any effects of the water layer and the air above and consequently the same for the shallow sea and the deep sea situation. We showed, that to decompose the fields and apply MDD successfullyfor a shallow sea situation a denser sampling is necessary than for a deep sea situation.

Key words: Controlled Source Electromagnetics (CSEM), Sea Bed Logging (SBL), Interferometry, Multidimensional Deconvolution (MDD)

1 INTRODUCTION

In seismics, interferometry is known as the process of cross-correlating two traces at two receiver positions to retrieve the Green's function between these two receivers. The theory has been derived by various authors for a lossless medium (Wapenaar (2004), Schuster *et al.* (2004)) and for a dissipative medium (Snieder, 2006) and it has been applied in passive (Draganov *et al.*, 2006) as well as in active seismics (Bakulin & Calvert, 2006). A more complete overview on seismic interferometry can be found in Wapenaar *et al.* (2008c) or Schuster (2009). Interferometry by crosscorrelation has also been derived for electromagnetics (Slob *et al.*, 2007).

It has been shown that the process of cross-correlation can be replaced by a multi-dimensional deconvolution (MDD) in the controlled-source case (Wapenaar *et al.*, 2008b) and in the passive case (Wapenaar *et al.*, 2008a). The advantages of MDD include elimination of the source signature, improved radiation characteristics of the retrieved source and relaxation of the assumption of a lossless medium. On the other hand, MDD is more expensive and the matrix inversion involved may be unstable. Furthermore a decomposition of the measured fields into up- and downgoing fields is necessary. Interferometry by MDD also requires an array or a network of sensors and can not be done with two receivers only, as this is the case in interferometry by cross-correlation.

In this paper Controlled Source Electromagnetic (CSEM) data in a marine environment is considered. This is often referred to as Sea Bed Logging (SBL), where an electric-dipole source is towed behind a boat emitting a low-frequency electric field, which propagates through the subsurface and through the water. The resulting EM-field is recorded at the ocean bottom by horizontal multicomponent receivers as a function of offset. At small source-receiver offsets the field is dominated by the direct field and reflections from the sea surface. At large offsets the refraction from the sea surface (airwave) is very strong (Amundsen *et al.*, 2006). Consequently the recorded signal depends on the thickness of the water layer.

By applying interferometry by MDD the source is redatumed to the receiver level, the direct field is eliminated and the water layer is replaced by a vertically

datasets are decomposed into up- and downgoing fields in the wavenumber-domain. Since the medium is laterally invariant, equation 3 can be solved efficient in the wavenumber-domain, where MDD becomes a simple division. The inverse-Fourier transformed result is equivalent with $\hat{\mathbf{R}}_0^+$ retrieved by MDD. The complete processing flow is shown in figure 2.

4 RESULTS

The magnitude of the two electromagnetic field components H_y and E_x are shown in figure 3 in a semi logarithmic plot. The shallow sea situation is plotted with a gray line and the deep sea situation with a lighter gray line. The slope of the curve representing the shallow sea case is steeper at small offsets for both field components than in the deep sea case, because in the deep sea situation the source is vertically further away from the receivers than in the shallow sea situation. Note that the horizontal tails of the electric field between approximately 3500 m and 5000 m have not a physical origin, but stem from the Fourier Transformation, which requires periodicity of the signal.

As can be seen in figure 4, the steeper field gradients in space-domain for the shallow sea situation correspond in the wavenumber-domain to energy at higher wavenumbers compared to the deep sea situation. In other words, if the source is vertically close to the receivers (shallow sea situation), the data has a higher bandwidth than if the source is vertically further away from the receivers (deep sea situation). In figure 4 it can also be seen that the wavenumber spectra of the magnetic and the electric fields behave similarly. The inlets magnify the fields near the zero wavenumber. The fields differ clearly from each other in this area. These differences, combined with the high amplitude and different phase behavior around small wavenumbers, lead to the pronounced differences between the magnetic and the electric fields in the space-domain.

The reflection response $\hat{\mathbf{R}}_0^+$, which is retrieved after decomposition into up- and downgoing fields and MDD, is shown in figure 5 for the shallow sea (dark gray line) and the deep sea situation (light gray line) as a function of offset for different spacings dx. The total offset is kept constant, therefore with increasing spacing dx the number of samples N decreases. Since MDD replaces the water layer with a halfspace, the reflection responses for the shallow sea and the deep sea situation should be identical (in case of correct sampling). The retrieved reflection responses are compared with a directly modeled reflection response (black solid line), which is the exact response when the water layer is replaced by a halfspace.

In figure 5 a) the spacing dx is equal to 2.5 m. Both retrieved reflection responses and the directly modeled reflection response show exactly the same shape verifying that MDD was successful in removing the imprint of the water layer for both cases. This is also true for a spacing of $dx = 5$ m. A spacing of $dx = 10$ m shows tiny artifacts around zero offset in the shallow sea case, as can be seen in the inlet of figure 5 b). Due to the small amplitude of these artifacts, they can be neglected, but if the spacing is increased further to $dx = 20$ m (figure 5 c), these artifacts at small offsets become more dominant in the shallow sea situation. As seen in figure 3 and mentioned earlier, the electromagnetic fields for the shallow sea case decay faster in the space-domain and have therefore a higher bandwidth in the wavenumber-domain. Increasing the spacing means in the wavenumber-domain to limit the range of wavenumbers. Consequently, a larger spacing introduces aliasing for the high wavenumbers and therefore affects the decomposition algorithm. Improperly decomposed fields lead to artifacts in the retrieved reflection response. A sampling of $dx = 20$ m seems to be too large. For the deep sea situation, the fields decay less strong and therefore this sampling is still sufficient. To detect reservoirs in the subsurface, the small offsets are not of interest, and therefore the artifacts in this region can be ignored. If the spacing is further increased to $dx = 40$ m as shown in figure 5 d), the reflection response for the shallow sea situation is now also for intermediate offsets not retrieved correctly. On the other hand, for the deep sea situation $\hat{\mathbf{R}}_0^+$ could be retrieved perfectly. Further increase of the spacing decreases the quality of $\hat{\mathbf{R}}_0^+$ for the shallow sea situation as expected even more while the reflection response can be retrieved with good quality for the deep sea situation up to a spacing dx equal to 320 m. Artifacts are introduced in the deep sea situation if a spacing of 640 m is reached.

Hunziker *et al.* (2009) show an empirical rule to define the sampling dx as a function of the vertical source-receiver distance z_{sr}. Since the stabilization parameter ε is fixed in their study, but not in this one, their rule can be relaxed. To be precise, the rule presented here is four times less restrictive. Consequently, sampling should be chosen such that $dx \leq z_{sr}/2.5$ to retrieve the reflection response perfectly. If small artifacts around zero offset on $\hat{\mathbf{R}}_0^+$ can be ignored, sampling is sufficient if $dx \leq z_{sr}$. But it should be taken into account, that for bigger sampling distances, the stabilization of the inversion is more difficult. With real data it might not be possible to find the best choice for the stabilization parameter ε and stricter rules should be applied. Fan and Snieder (2009) found a similar rule for electromagnetic fields emitted by a source with a length of 100 m.

5 CONCLUSIONS

SBL data were modeled for a shallow sea and a deep sea situation for a point source. The electromagnetic fields were decomposed and the reflection response $\hat{\mathbf{R}}_0^+$ was retrieved with interferometry by MDD. Different spac-

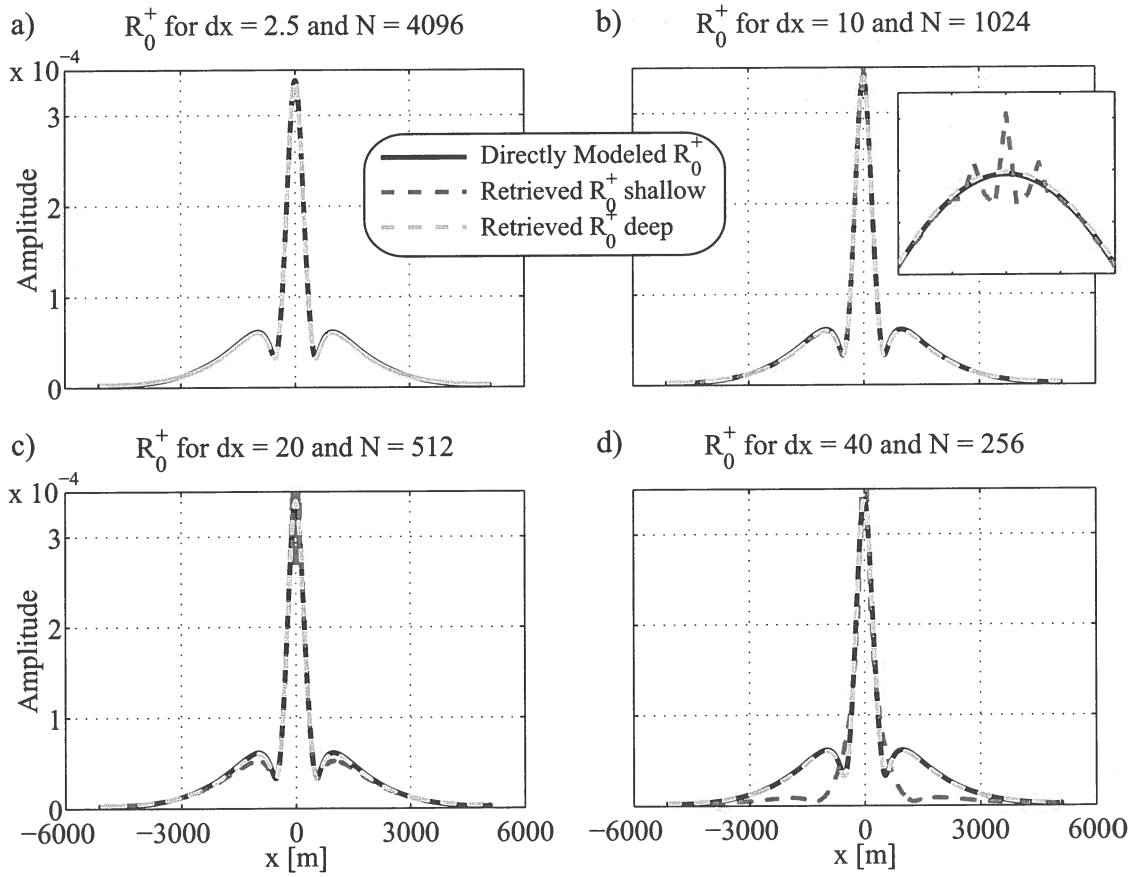

Figure 5. Reflection Responses for different receiver spacings as a function of offset. Spacing dx and the amount of datapoints N is given in the figure captions. The spatial sampling dx is given in meters. The axises span in all plots over the same range. The inlet in subfigure b) magnifies the area between -100 m and 100 m and an amplitude range between 3×10^{-4} and 3.7×10^{-4}.

the Technology Program of the Ministry of Economic Affairs.

REFERENCES

Amundsen, L., Løseth, L., Mittet, R., Ellingsrud, S., & Ursin, B. 2006. Decomposition of electromagnetic fields into upgoing and downgoing components. *Geophysics*, **71**, G211–G223.

Bakulin, A., & Calvert, R. 2006. The virtual source method: Theory and case study. *Geophysics*, **71**, SI139–SI150.

Berkhout, A. J. 1982. *Seismic Migration. Imaging of Acoustic Energy by Wave Field Extrapolation.* Elsevier.

Draganov, D., Wapenaar, K., & Thorbecke, J. 2006. Seismic interferometry: Reconstructing the earth's reflection response. *Geophysics*, **71**, SI61–SI70.

Fan, Y., & Snieder, R. 2009. 3-D Controlled Source Electromagnetic Interferometry by multidimensional deconvolution. *CWP-636, 2009 Annual Project Review Book.*

Hunziker, J., Slob, E., & Wapenaar, K. 2009. Controlled Source Electromagnetic Interferometry by multidimensional deconvolution: spatial sampling aspects in Sea Bed Logging. *71st EAGE Conference and Exhibition, Expanded Abstracts.*

Schuster, G. 2009. *Seismic Interferometry.* Cambridge University Press.

Schuster, G. T., Yu, J., Sheng, J., & Rickett, J. 2004. Interferometric/daylight seismic imaging. *Geophysical Journal International*, **157**, 838–852.

Slob, E. 2009. Interferometry by Deconvolution of Multicomponent Multioffset GPR Data. *IEEE Transactions on Geoscience and Remote Sensing*, **47**, 828–838.

Slob, E., Draganov, D., & Wapenaar, K. 2007. Interferometric electromagnetic Green's functions representations using propagation invariants. *Geophysical Journal International*, **169**, 60–80.

Snieder, R. 2006. Extracting the Green's function of attenuating heterogeneous acoustic media from uncorrelated waves. *Journal of the Acoustical Society of America*, **121**, 2637–2643.

Wapenaar, K. 2004. Retrieving the elastodynamic Green's function of an arbitrary inhomogeneous medium by cross correlation. *Physical Review Letters*, **93**, 254301–1 – 254301–4.

Wapenaar, K., van der Neut, J., & Ruigrok, E. 2008a. Pas-

3-D controlled source electromagnetic interferometry by multidimensional deconvolution

Yuanzhong Fan & Roel Snieder
Department of Geophysics and Center for Wave Phenomena, Colorado School of Mines, Golden, CO 80401, USA

ABSTRACT
Controlled Source Electromagnetic (CSEM) is an important technique in hydrocarbon exploration, because it uses the large contrast in electrical resistivity to distinguishes between water and hydrocarbons. In a shallow sea environment, the airwave that is refracted from the air-water interface dominates the recorded signal at large offsets. Therefore, the hydrocarbon detection ability of the CSEM is weakened, because the airwave is independent on the properties of the subsurface. For a layered earth model, we apply multi-dimensional-deconvolution interferometry to synthetic 3D CSEM data and estimated the reflection response of the subsurface. The difference in the models with and without a resistive layer is significantly increased by the employed interferometric analysis. However, the required receiver spacing is much denser than that of current CSEM surveys. In order to apply this technique in a field survey, we are currently working on how to relax the required receiver criterion for this technique.

Key words: 3-D CSEM, interferometry, airwave

1 THEORY AND MOTIVATION

1.1 Basic theory and history of virtual source technique

The concept of *interferometry* was first introduced to the seismic community by Jon Claerbout in 1968. It became a hot research topic in geophysics in the last decade. The method is also referred to as the *virtual source technique* and in a wider sense *Green's function reconstruction*. In this work, we refer to the same technique using these three terms. The key idea of this technique is the following. The Green's function that describes wave propagation between two receivers can be reconstructed by cross-correlation of the wavefields at two receiver positions provided that the receivers are enclosed by uncorrelated sources on a closed surface. Because of the advantages of this technique and its use in the passive survey, research on seismic interferometry has progressed significantly during the last eight years Lobkis and Weaver (2001); Weaver and Lobkis (2001); Derode et al. (2003); Campillo and Paul (2003); Weaver and Lobkis (2004); Wapenaar (2004); Snieder (2004); Malcolm et al. (2004); Bakulin and Calvert (2004); Calvert et al. (2004); Wapenaar et al. (2005); Shapiro et al. (2005); Roux et al. (2005); Sabra et al. (2005a,b); van Wijk (2006); Larose et al. (2006); Bakulin and Calvert (2006); Snieder (2007); Mehta and Snieder (2008).

Snieder (2006) showed that interferometry can be applied not only to wavefields, but also to diffusive fields. This discovery inspired further research and novel applications to the diffusive fields, as has happened for wave fields. The diffusive fields have a wide range of applications and use in physics, chemistry, medical physics, earth science A.Mandelis (1984); Yodh and Chance (1995); Basser et al. (1994); Mori and Barkar (1999); Koyama et al. (2006); Constable and Srnka (2007). In earth science, diffusive fields are ubiquitous. Examples include heat conduction, flow in porous media, and low-frequency electromagnetic fields in the conductive subsurface. In this work, we focus on the application of interferometry to low-frequency electromagnetic fields in the subsurface. However, we may easily extend the concept to other diffusive fields. Because the electromagnetic field is sensitive to the electric resistivity, it has been used in medical physics and the mining industry for a long time. In recent years, electromagnetic survey became increasingly popular in the petroleum in-

(4) is a discretized version of equation (3) for a sigle source at x_s

$$\begin{pmatrix} U_1 \\ U_2 \\ \vdots \\ U_n \end{pmatrix} = \begin{pmatrix} R_{11}\ R_{12}\ \cdots\ R_{1n} \\ R_{21}\ \cdots\ \cdots\ \cdots \\ \cdots\ \cdots\ \cdots\ \cdots \\ R_{n1}\ \cdots\ \cdots\ R_{nn} \end{pmatrix} \begin{pmatrix} D_1 \\ D_2 \\ \vdots \\ D_n \end{pmatrix}, \quad (4)$$

where the subscript 1 to n of U and D are the discretized sampling points of the surface B_1, R_{ij} denotes the reflection response between the position i and j. The arrays of U and D are the known data and R is the unknown matrix. In general, there is no unique solution for matrix R because there are more unknowns (n^2) than the number of equation (n). Using reciprocity, the number of unknowns can be reduced to $n(n+1)/2$. The expression below is a similar equation but combines sources at position x_s and another position $x_{s'}$

$$\begin{pmatrix} U_1,\ U_1' \\ U_2,\ U_2' \\ \vdots \\ U_n,\ U_n' \end{pmatrix} = \begin{pmatrix} R_{11}\ R_{12}\ \cdots\ R_{1n} \\ R_{21}\ \cdots\ \cdots\ \cdots \\ \cdots\ \cdots\ \cdots\ \cdots \\ R_{n1}\ \cdots\ \cdots\ R_{nn} \end{pmatrix} \begin{pmatrix} D_1,\ D_1' \\ D_2,\ D_2' \\ \vdots \\ D_n,\ D_n' \end{pmatrix}, \quad (5)$$

where U' and D' are the new upgoing and downgoing fields generated by the source at position $x_{s'}$. The matrix R remains the same as it is independent on the source. By increasing the number of sources, the number of columns in U and D increases. The matrix R can be accurately estimated if a sufficient number of sources are used. However, this calculated maxtrix R does not necessarily represent the real medium response R.

When discretizing equation (3), only a finite number of the receivers from a limited range of the surface B_1 can be used. This raises the question how to choose the receiver distribution in order to represent the integral in equation (3) accurately for a band-limited response R (receiver density and the range of the surface where the receiver are located)?

1.2 Why do we apply interferometry in marine CSEM?

Figure 2 shows a typical configuration of an offshore marine CSEM survey. A resistive layer (e.g hydrocarbons) in the subsurface, acts as a secondary source that generates an upgoing EM field. We can distinguish between models with and without the resistive layer from the secondary fields which the subsurface generates. The large difference in the electrical resistivity between water and hydrocarbons makes CSEM an accurate tool to distinguish between these pore fluids. Most of the current successful applications of CSEM are offshore because the water strongly attenuates anthropogenic and natural noise. However, one of the most significant problems in offshore CSEM is the airwave when the water layer is shallow. The airwave is the secondary EM field refracted from the water-air interface as shown in figure

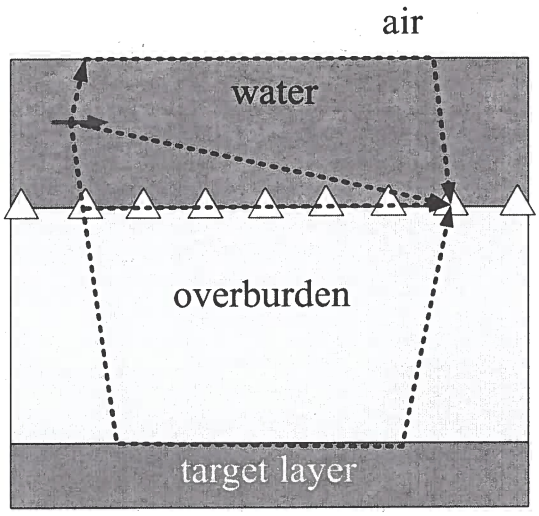

Figure 2. A simple configuration of a offshore CSEM survey in a layered earth model.

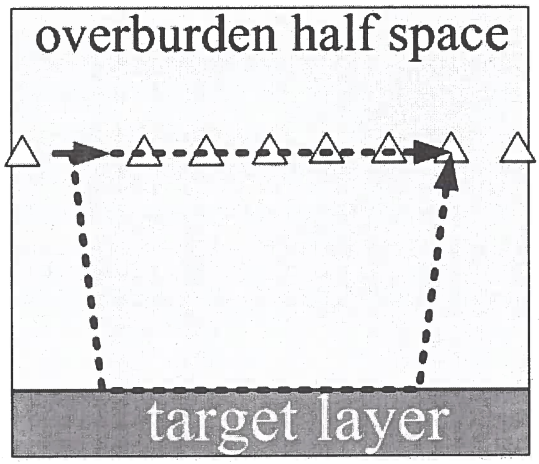

Figure 3. The configuration of CSEM after the application of the multi-dimentional-deconvolution interferometry.

2. The airwave weakens the difference between the signal with a target layer and the signal without a target layer because it is much stronger than the target signal.

If we can successfully apply the multi-dimension-deconvolution interferometry as described in the last section to CSEM, one of the receivers is converted into a source and the overburden is extended upwards to a homogeneous half space Wapenaar et al. (2008). The new configuration after applying this technique is shown in figure 3. In this configuration, the air-water interface and the sea floor are removed, and there is no secondary field is refracted from the medium above the receivers. Note that the sea floor interface may or may not be removed depending on the boundary condition which we use in the decomposition process. Therefore, by ap-

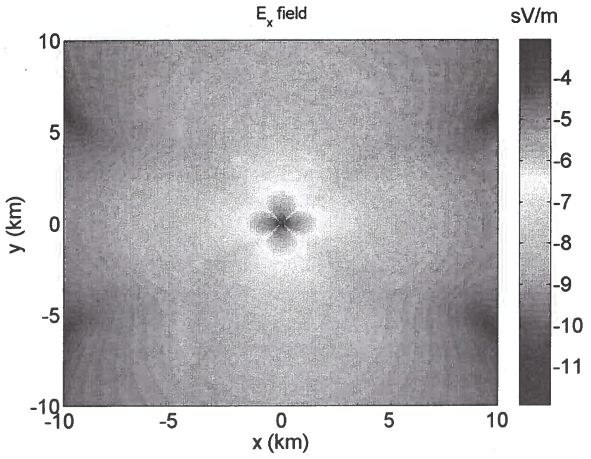

Figure 7. E_x field with target layer in the log10 scale.

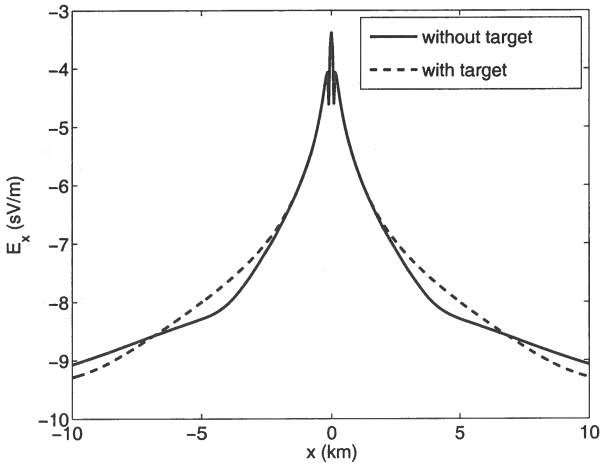

Figure 8. The inline profile of the E_x field in the log10 scale.

almost no difference between these two curves because the direct field dominates. For large offsets (> 7 km), the electric field is strongly influnced by the airwave, which does not depend on the subsurface properties at all. Consequently, targets leave useful imprint only for intermediate offsets (2km to 7km). Because this intermediate range is narrow and the difference between the signals with and without target is weak, it is difficult to interpret the difference between the signals with and without the target, especially in the presence of noise.

We next, apply the multi-dimentional-deconvolution interferometry to these synthetic data. The first step of this technique is to decompose the total field into upgoing and downgoing components. The implementation of the up-down decomposition follows the theory in the appendix of Wapenaar et al. (2008). Note that the up-down decomposed field is the square root of energy flux, not the E (electric) or H (magnetic) field. The input data used in the

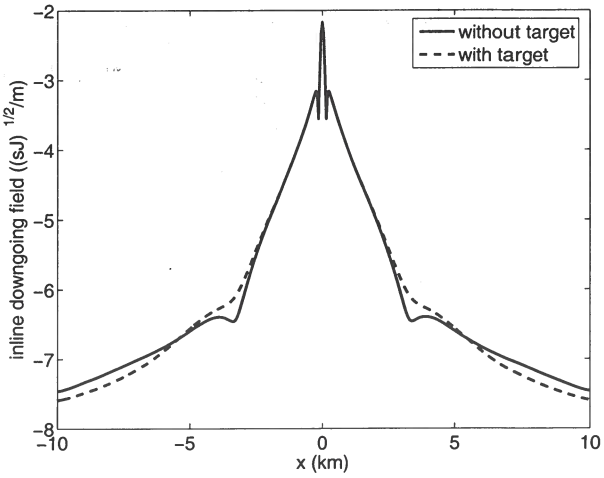

Figure 9. The inline profile of the downgoing fields with and without the target using the water parameters.

decomposition are the horizontal E and H fields. The measured electric and magnetic fields can be related with the upgoing and downgoing flux with the formula

$$P = L^{-1} Q \tag{6}$$

where P is the decomposed upgoing and downgoing potential, normalized to energy flux, Q contains the input horizontal E and H fields and L^{-1} is the conversion operator. Wapenaar et al. (2008) shows a numerical example for a 2D field with a layered model. With an inline dipole source, the physical meaning of $P = [P_d, P_u]'$ is the decomposed energy flux of the TM (transverse magnetic) mode (subscripts d and u represent the downgoing and upgoing, respectivly). The downgoing field is defined as the field which decays downwards and the upgoing field is defined as the field which decays upwards.

In our synthetic example, the field is 3D, hence Q contains four components E_x, E_y, H_x, H_y and P has four components as well $[P_d^1, P_u^1, P_d^2, P_u^2]$.Because the receivers are located at the boundary of the water and the sea floor, we can choose the parameters for L^{-1} from the upper medium (water) or the lower medium (sea floor) in the process of the field decomposition. These two choices of the medium parameters lead to a different physical meaning for the decomposed field. Using the water parameters for the up-down decomposition, we obtain the upgoing and downgoing fields in the water just above the sea bottom. If the sea floor parameters are used, we obtain the upgoing and downgoing fields in the sea bottom just below the acquisition surface. Figures 9 to 12 compare the upoing and downgoing fields in these two choices. For demonstration purposes, only the inline profile of the fields is shown. However, we do need to calculate the upgoing and downgoing fields for all the receivers in the 2D array. When the water parameters are used in the decomposition, the difference

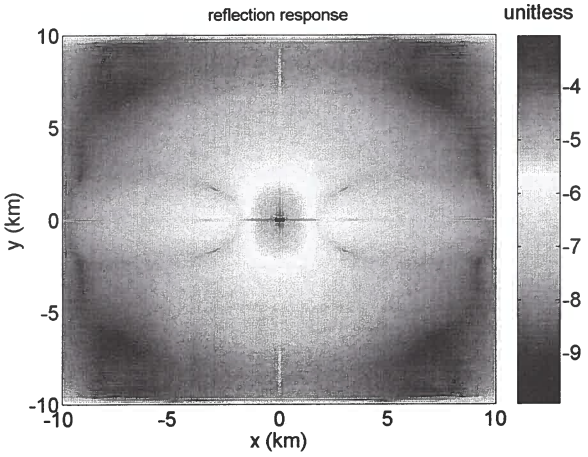

Figure 13. The impulse reflection response R without target in the log10 scale.

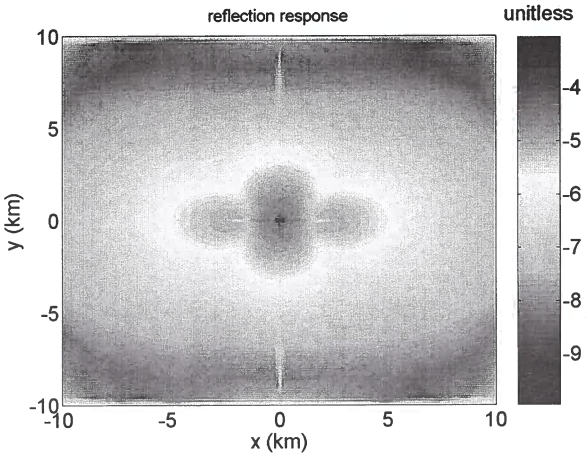

Figure 14. The impulse reflection response R with target in the log10 scale.

used in equation (9) to calculate the impulse response. The calculated impulse responses are shown in figure 13 (without target) and figure 14 (with target). The difference of the impulse response is significant between the two models with and without target. Comparing with the inline profile of the total E_x field (figure 8), the inline profile of the impulse response (figure 15) gives much more pronounced difference between the models with and without the target.

3 DISCUSSION

The 3-D synthetic example in this paper shows that the virtual source technique in CSEM can significantly increase the sensitivity of detecting the high-resistivity layer (such as hydrocarbon reservoir) in the submarine environment. Note that in order to apply this technique

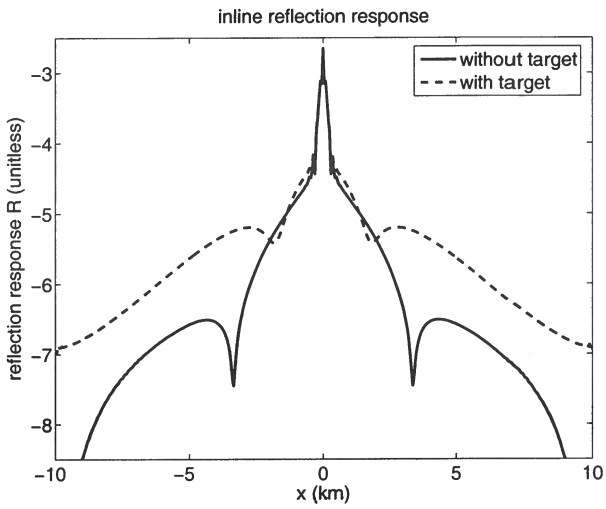

Figure 15. The inline profile of the reflection response R in the log10 scale

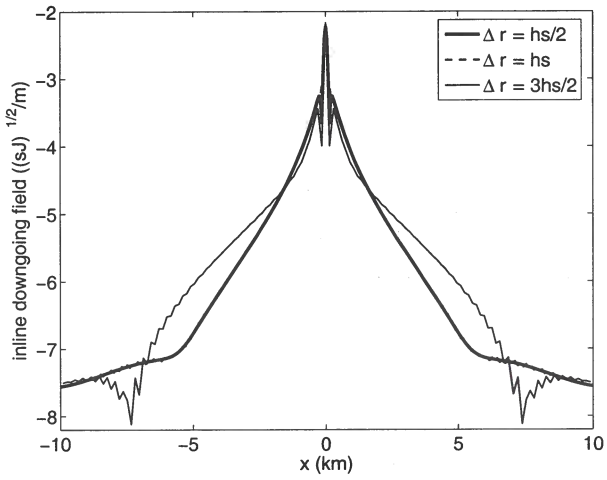

Figure 16. Decomposed downgoing fields using different receiver distributions.

accurately, a dense receiver array is required. We find that the required receiver separation Δr must be less than the height h_s of the dipole source above the sea bottom to adequately carry on the up-down decomposition ($\Delta r < h_s$). The following two figures (figures 16 and 17) demonstrate the effect on the up-down decomposition of the different receive distributions. The thick solid lines shows the downgoing (figure 17) and upgoing field (figure 16) using a over sampled dense receiver array ($\Delta r = h_s/2$). The dashed lines represent decomposed fields using a receiver spacing of $\Delta r = h_s/2$. The oscillations in the dashed lines imply that this spacing is at the edge of the aliasing. When the receiver sampling separation Δr is larger than h_s, the up-down de-

Koyama, T., K. Tamai, and K. Togashi, 2006, Current status of body MR imaging : fast MR imaging and diffusion-weighted imaging: Int. J. Clin. Oncol., **11**, 278–285.

Kwon, M. J. and R. Snieder, 2009, Uncertainty analysis for the integration of seismic and CSEM data: CWP Annul Report.

Larose, E., G. Montaldo, A. Derode, and M. Campillo, 2006, Passive imaging of localized reflectors and interfaces in open media: Appl. Phys. Lett., **88**, 104103.

Lien, M. and T. Mannseth, 2008, Sensitivity study of marine CSEM data for reservoir production monitoring: Geophysics, **73**, F151.

Lobkis, O. I. and R. L. Weaver, 2001, On the emergence of the Green's function in the correlations of a diffuse field: J. Acoust. Soc. Am., **110**, 3011–3017.

Malcolm, A. E., J. A. Scales, and B. A. van Tiggelen, 2004, Extracting the Green function from diffuse, equipartitioned waves: Phys. Rev. E., **70**, 015601.

Mehta, K. and R. Snieder, 2008, Acquisition geometry requirements for generating virtual-source data: The Leading Edge, **27**, 620–629.

Mori, S. and P. B. Barkar, 1999, Diffusion magnetic resonance imaging: its principle and applications: Anat. Rec., **257**, 102–109.

Roux, P., K. G. Sabra, W. A. Kuperman, and A. Roux, 2005, Ambient noise cross correlation in free space: Theoretical approach: J. Acoust. Soc. Am., **117**, 79–84.

Sabra, K. G., P. Gerstoft, P. Roux, W. A. Kuperman, and M. C. Fehler, 2005a, Extracting time-domain Green's function estimates from ambient seismic noise: Geophys. Res. Lett., **32**, L03310.

———, 2005b, Surface wave tomography from microseisms in southern California: Geophys. Res. Lett., **32**, L14311.

Shapiro, N. M., M. Campillo, L. Stehly, and M. H. Ritzwoller, 2005, High-resolution surface-wave tomography from ambient seismic noise: Science, **307**, 1615–1618.

Slob, E., D. Draganov, and K. Wapenaar, 2007, Interferometric electromagnetic Green's functions representations using propagation invariants: Geophys. J. Int., **169**, 60–80.

Snieder, R., 2004, Extracting the Green's function from the correlation of coda waves: A derivation based on stationary phase: Phys. Rev. E, **69**, 046610.

———, 2006, Retrieving the Green's function of the diffusion equation from the response to a random forcing: Phys. Rev. E, **74**, 046620.

———, 2007, Extracting the Green's function of attenuating heterogeneous acoustic media from uncorrelated waves: J. Acoust. Soc. Am., **121**, 2537–2643.

Snieder, R., K. Wapenaar, and U. Wegler, 2007, Unified Green's function retrieval by cross-correlation; connection with energy principles: Phys. Rev. E., **75**, 036103.

van Wijk, K., 2006, On estimating the impulse response between receivers in a controlled ultrasonic experiment: Geophysics, **71**, SI79–SI84.

Wapenaar, K., 2004, Retrieving the elastodynamic Green's function of an arbitrary inhomogeneous medium by cross correlation: Phys. Rev. Lett., **93**, 254301–4.

Wapenaar, K., J. Fokkema, and R. Snieder, 2005, Retrieving the Green's function in an open system by cross-correlation : a comparison of approaches: J. Acoustic. Soc. Am., **118**, 2783–2786.

Wapenaar, K., E. Slob, and R. Snieder, 2008, Seismic and electromagnetic controlled-source interferometry in dissipative media: Geophys. Prospect., **56**, 419–434.

Weaver, R. L. and O. I. Lobkis, 2001, Ultrasonics without a source: Thermal fluctuation correlations at MHz frequencies: Phys. Rev. Lett., **87**, 134301.

———, 2004, Diffuse fields in open systems and the emergence of the Green's function.: J. Acoust. Soc. Am., **116**, 2731–2734.

Yodh, A. and B. Chance, 1995, Spectroscopy and imaging with diffusing light: Physics Today, **48**, 34–40.

Uncertainty analysis for the integration of seismic and CSEM data

Myoung Jae Kwon & Roel Snieder
Center for Wave Phenomena, Colorado School of Mines

ABSTRACT

Geophysical inverse problems consist of three stages: the forward problem, optimization, and appraisal. We study the appraisal problem for the joint inversion of seismic and controlled source electro-magnetic (CSEM) data and utilize rock-physics models to integrate these two disparate data sets. The appraisal problem is solved by adopting a Bayesian model and we incorporate four representative sources of uncertainty. These are uncertainties in (1) seismic wave velocity, (2) electric conductivity, (3) seismic data, and (4) CSEM data. The uncertainties in porosity and water saturation are quantified by a posterior random sampling in the model space of porosity and water saturation of a marine one-dimensional structure. We study the relative contributions from the four individual sources of uncertainty by performing several statistical experiments. The uncertainties in the seismic wave velocity and electric conductivity play a more significant role on the variation of posterior uncertainty than do the seismic and CSEM data noise. The numerical simulations also show that the assessment of porosity is most affected by the uncertainty in seismic wave velocity and the assessment of water saturation is most influenced by the uncertainty in electric conductivity. The framework of the uncertainty analysis presented in this study can be utilized to effectively reduce the uncertainty of the porosity and water saturation derived from integration of seismic and CSEM data.

Key words: uncertainty analysis, Metropolis-Hastings algorithm, CSEM

1 INTRODUCTION

Currently, there is an increasing interest in the integration of the seismic and controlled source electromagnetic (CSEM) method in deep marine exploration (Harris & MacGregor, 2006). Although the CSEM method has less resolution than the seismic method, it provides extra information about, for example, electric conductivity. This property is important for the economic evaluation of reservoirs. Therefore, the CSEM method is considered an effective complementary tool when combined with seismic exploration.

The seismic and CSEM methods are disparate exploration techniques that are sensitive to different medium properties: the seismic method is sensitive to density and seismic wave velocity and the CSEM method to electric conductivity. There have been several approaches for joint inversion that integrate disparate data sets. Some of them assume a common structure (Musil *et al.*, 2003) or similar structural variations of different medium properties (Gallardo & Meju, 2004). More recently, the application of rock-physics models for joint inversion has been studied (Hoversten *et al.*, 2006). Rock-physics models enable us to interrelate seismic wave velocity and electric conductivity with the reservoir parameters such as porosity, water saturation, or permeability. The main advantage of the approach is that the reservoir parameters have great economic importance. The application of a rock-physics model is limited, however, by the fact that such a model is site-specific and there are not yet any universal solutions to the inverse problem. Furthermore, even for any particular area of interest, any rock-physics model is generally described as a cloud of samples. These limitations

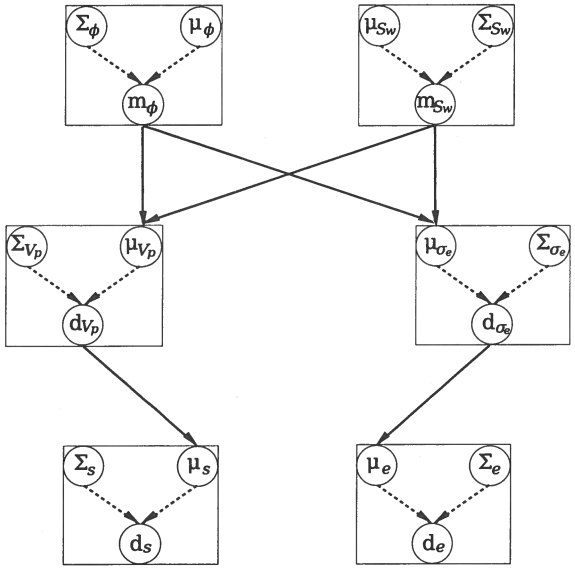

Figure 2. A hierarchical dependency structure represented by a directed graph. The nodes represent stochastic variables, the dashed arrows represent probability dependencies, and the solid arrows represent deterministic relationships. μ and $\mathbf{\Sigma}$ denote expectation vectors and covariance matrices, respectively. $\mathbf{m}_\phi$ and $\mathbf{m}_{S_w}$ represent two reservoir parameters: medium porosity and water saturation. $\mathbf{d}_{V_p}$ and $\mathbf{d}_{\sigma_e}$ denote P-wave velocity and logarithm of electric conductivity, respectively. $\mathbf{d}_s$ and $\mathbf{d}_e$ represent two different data sets: seismic and CSEM data.

as follows:

$$\begin{aligned} & \pi_{post}(\mathbf{m}_\phi, \mathbf{m}_{S_w} | \mathbf{d}_{V_p}, \mathbf{d}_{\sigma_e}, \mathbf{d}_s, \mathbf{d}_e) \\ \propto\ & \pi(\mathbf{m}_\phi, \mathbf{m}_{S_w}, \mathbf{d}_{Vp}, \mathbf{d}_{\sigma_e}, \mathbf{d}_s, \mathbf{d}_e) \\ =\ & \pi_{prior}(\mathbf{m}_\phi)\pi_{prior}(\mathbf{m}_{S_w}) \\ \times\ & f(\mathbf{d}_{V_p}|\mathbf{m}_\phi, \mathbf{m}_{Sw}) f(\mathbf{d}_{\sigma_e}|\mathbf{m}_\phi, \mathbf{m}_{Sw}) \\ \times\ & f(\mathbf{d}_s|\mathbf{d}_{Vp}) f(\mathbf{d}_e|\mathbf{d}_{\sigma_e}). \end{aligned} \tag{3}$$

Equation (3) indicates that the posterior probability is proportional to the product of individual priors and likelihoods.

In statistics, the central limit theorem states that the sum of a sufficiently large number of identically distributed independent random variables follow a normal distribution. This implies that the normal distribution is a reasonable choice for describing probability. Therefore, throughout this project, we assume the priors and likelihoods to follow multivariate Gaussian distribution with expectation vector μ and covariance matrix $\mathbf{\Sigma}$, such that

$$f(\mathbf{x}) = \frac{1}{\sqrt{(2\pi)^n |\mathbf{\Sigma}|}} \exp\left[-\frac{1}{2}(\mathbf{x}-\mu)^T \mathbf{\Sigma}^{-1}(\mathbf{x}-\mu)\right], \tag{4}$$

where $\mathbf{x}$ denotes data or model and n denotes the dimension of $\mathbf{x}$. The covariance matrix is modeled as a diagonal matrix as follows:

$$\mathbf{\Sigma} = \text{diag}\ \{\sigma_1^2, \sigma_2^2, \cdots, \sigma_n^2\}, \tag{5}$$

where σ_i^2 denote the variance value of a datum or model parameter. If the error structure is apparently different from Gaussian, another appropriate probability function should be modeled. Equation (4) expresses the general form of the probability function used in this project and the covariance matrices for individual prior and likelihoods are discussed later. Note that since the forward operations in this project (solid arrows in Figure 2) are nonlinear, the posterior distributions are not necessarily Gaussian.

2.2 Prior and likelihood model

In the Bayesian context, there are several approaches to represent prior information (Scales & Tenorio, 2001). The prior model encompasses all the information we have before the data sets are acquired. In practice, the prior information includes the definition of the model parameters, geologic information about the investigation area, and preliminary investigation results. Therefore, the prior model is the starting point of a Bayesian approach, and we expect to have a posterior probability distribution with less uncertainty than the prior probability. The prior model also plays an important role in Bayesian inversion to eliminate unreasonable models that fit the data (Tenorio, 2001). Obvious prior information we have is the definition of the porosity and water saturation, such that $0 \leq m_{\phi_i} \leq 1$ and $0 \leq m_{S_{w_i}} \leq 1$. This implies that the prior distributions of the porosity and water saturation are intrinsically non-Gaussian. However, when the variances of the distributions are sufficiently small, the deviation from the Gaussian approximation is negligible. We adopt this assumption and take the Gaussian approximations for the modeling of the prior probabilities. We further assume that the covariance matrices $\mathbf{\Sigma}_\phi$ and $\mathbf{\Sigma}_{S_w}$ (Figure 2) are diagonal and that the diagonal elements within each covariance matrix are identical.

For the hierarchical Bayesian model shown in Figure 2, there are four elementary likelihoods. Each of these likelihoods describes how well any rock-physics model or geophysical forward modeling fits with the rock-physics experiment results or the noisy observations. The details of the likelihood modeling are covered in the modeling procedure section.

2.3 MCMC sampling

The assessment of the posterior probability requires great computational resources and, in most cases, it is still impractical for 3-D inverse problems. Pioneering studies about the assessment were performed for 1-D seismic waveform inversion (Gouveia & Scales, 1998; Mosegaard *et al.*, 1997). The posterior model space of this project encompasses porosity and water saturation of several layers. We use a Markov-Chain Monte Carlo

	ϕ (%)	S_w (%)	V_p (km/s)	σ_e (S/m)
soft shale layer	35	90	2.30	0.430
gas saturated sandstone layer	25	10	3.57	0.003
hard shale layer	10	50	4.86	0.018

Table 1. Ground truth values of the porosities ϕ, water saturations S_w, P-wave velocities V_p, and electric conductivities σ_e of the 1-D model shown in Figure 4.

clay mineral	CEC (coulomb/kg)
kaolinite	2,000 - 10,000
illite	10,000 - 38,000
montmorillonite	67,000 - 77,000
smectite	77,000 - 144,000

Table 2. Typical ranges of the cation exchange capacity (CEC) value for authigenic forms of the clay minerals.

2004) as follows:

$$K = K_d + \frac{(1 - \frac{K_d}{K_0})^2}{\frac{\phi}{K_f} + \frac{1-\phi}{K_0} - \frac{K_d}{K_0^2}}, \tag{8}$$

where K_d, K_0, and K_f are the bulk modulus of the dry rock, mineral material, and pore fluid, respectively. We model two phases of pore fluid: water and gas. A mixture of two different pore fluids can be regarded as an effective fluid model and the bulk modulus is derived from Wood's equation (Batzle & Wang, 1992) as follows:

$$\frac{1}{K_f} = \frac{S_w}{K_w} + \frac{1 - S_w}{K_g}, \tag{9}$$

where K_w and K_g are the bulk modulus of the water and gas phase. One more factor that has significant effect on the P-wave velocity of a medium is the clay content. Han's empirical relations (Mavko *et al.*, 1998) state that the clay content c reduces the P-wave velocity. Applying a Han's empirical relation, we derive the P-wave velocity as

$$V_p = \sqrt{\frac{K + \frac{4}{3}\mu}{\rho}} - 2.18c \text{ km/s}, \tag{10}$$

where the bulk modulus K and shear modulus μ are in GPa and density ρ is in g/cc. In this project, the clay contents are assumed to be constant (20%, 1%, and 10% for the soft shale, sandstone, and hard shale layer, respectively).

The relationship between the reservoir parameters (porosity ϕ and water saturation S_w) and electric conductivity is given by Archie's second law (Mavko *et al.*, 1998), which describes the electric conductivity in clean sands. The electric conductivity in shaley sands is complicated by the presence of clays and is described by Waxman-Smits formula (Revil *et al.*, 1998; Waxman & Smits, 1968):

$$\sigma_e = \phi^m S_w^n \left[\sigma_w + \frac{BQ_v}{S_w}\right], \tag{11}$$

where m is cementation exponent, n is saturation exponent, and σ_w is electric conductivity of pore fluid. Empirically, the cementation and saturation exponents are close to 2 for most sedimentary rocks (Mavko *et al.*, 1998), and this value is used in this project. The parameter B is an equivalent counterion mobility and Q_v is the excess of surface charge per unit pore volume. The parameter B is given empirically at 25°C by

$$B = B_0 \left[1 - 0.6 \exp\left(-\frac{\sigma_w}{0.0013}\right)\right], \tag{12}$$

where σ_w is in S/m and the maximum counterion mobility B_0 is given by 4.78×10^{-8} m^2/volt/s (Revil *et al.*, 1998). The parameter Q_v is related to the grain density ρ_g (in kg/m^3) and the cation exchange capacity (CEC) (Waxman & Smits, 1968) by

$$Q_v = \rho_g \frac{1 - \phi}{\phi} \text{CEC}. \tag{13}$$

The CEC is usually significant only for clay minerals and the vaules for the representative clay minerals are shown in Table 2. As is indicated in the table, the variation of the CEC for the different clay mineral is dramatic. For a mixture of sand grains and clay minerals, the CEC of the sediment is calculated by

$$\text{CEC} = f_c \sum_i \chi_i \text{ CEC}_i, \tag{14}$$

where f_c is the mass fraction of clay minerals, χ_i are the relative fractions of each clay minerals in the shale fraction, and CEC_i is the cation exchange capacity of each of these clay minerals. Because of the large grain size, the CEC of the quartz grains can be neglected. In this project, we simplify the contribution of the clay contents on the electric conductivity and assume that the clay content in the shale fraction is only composed of kaolinite.

We assume that the distribution of P-wave velocity follows a Gaussian distribution. In contrast, considering that the electric conductivity exhibits exponential variation in most geologic environments, we assume that the electric conductivity follows a lognormal distribution. The P-wave velocity and electric conductivity are derived from equations (10) - (11), and Gaussian and

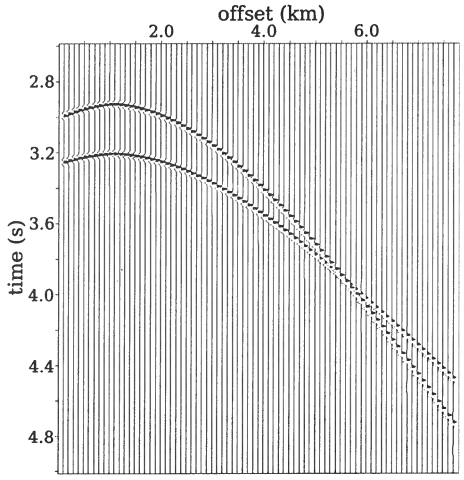

Figure 9. Ray tracing based seismic traces for the 1-D model shown in Figure 4. The modeled reflection events are generated on the top and bottom boundaries of the gas saturated sandstone. The central frequency of the source wavelet is 30 Hz and the time sampling interval is 3 ms.

method is effective for the least-squares misfit optimization for the velocities (Jannane *et al.*, 1989; Snieder *et al.*, 1989). Seismic waveform data is synthesized by a ray-tracing algorithm (Docherty, 1987) and we model the primary reflections of the P-wave from the top and bottom boundaries of the target sandstone layer. Figure 9 shows the representative time traces simulated from the 1-D model shown in Figure 4. Typical reflection parabola and phase shift at post-critical incidence (Aki & Richards, 2002) are observed. In this project, we use the time series data that corresponds to 2 km source-receiver offset and add random noise to the synthesized data.

There are many sources of seismic noise in a marine environment: ambient noise, guided waves, tail-buoy noise, shrimp noise, and side-scattered noise (Yilmaz, 1987). We model the seismic noise by adding band-limited noise as shown in Figure 10. The frequency band of the noise is between 10 and 55 Hz, and the central frequency of the source wavelet is 30 Hz. Figure 11 shows a realization of noisy seismic data that is contaminated by band-limited noise. The maximum amplitude of the noise is 30% of the maximum amplitude of the noise-free signal.

We assume that the seismic data likelihood probability $f(\mathbf{d}_s|\mathbf{d}_{V_p})$ follows the multivariate Gaussian distribution (equation (4)). For the calculation of the likelihood, it is necessary to evaluate the covariance matrix $\mathbf{\Sigma}_s$ (Figure 2). For band-limited noise, the covariance matrix follows from the power spectrum of the band-pass filter and the resulting covariance matrix is not diagonal. We approximate the covariance matrix of a band-limited noise as the covariance matrix of a white

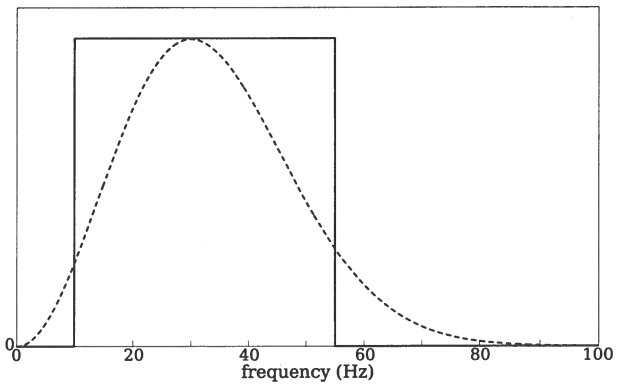

Figure 10. Band-width of the noise (solid line) and amplitude spectrum of the source wavelet (dashed curve). The amplitude spectra are normalized for comparison.

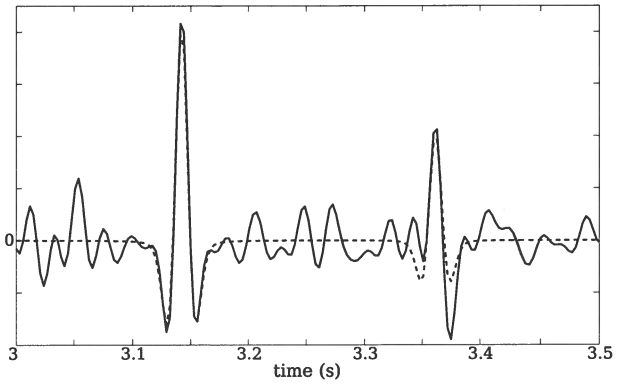

Figure 11. Time trace of a data contaminated by the band-limited white noise (solid curve) and noise free data (dashed curve). The exact P-wave velocities are used for the seismic data calculation shown here.

noise. We therefore model the covariance matrix as a diagonal matrix as shown in equation (5), where the variance values $\sigma_i^2(d_s)$ are identical.

3.3 CSEM data likelihood modeling

The controlled source electo-magnetic (CSEM) method has been studied for the last few decades (Cox *et al.*, 1978) and the feasibility for the delineation of a hydrocarbon reservoir has recently been discussed (Mehta *et al.*, 2005). There are several data acquisition geometries in the CSEM method and horizontal electric dipole transmitter and radial electric field response is generally preferred (Chave & Cox, 1982).

Contrary to seismic wave propagation, EM energy transport within the earth is diffusive and the EM field strength decreases to $1/e$ order in a length called skin depth (Jackson, 1999), defined as

$$\delta = \sqrt{\frac{2}{\mu_m \sigma_e \omega}} \approx 0.503 \sqrt{\frac{1}{\sigma_e f}} \text{ km}, \tag{15}$$

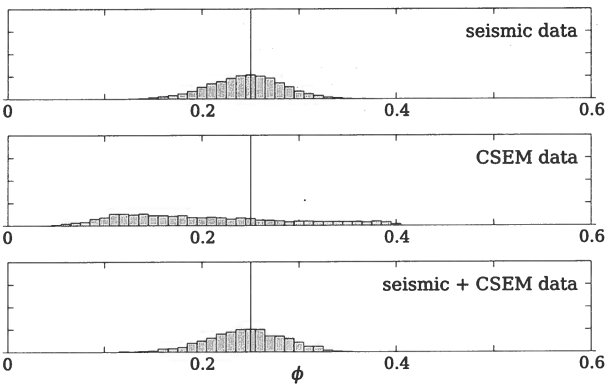

Figure 15. Histograms of posterior porosity (ϕ) samples of the sandstone layer. Vertical line indicates the ground truth value.

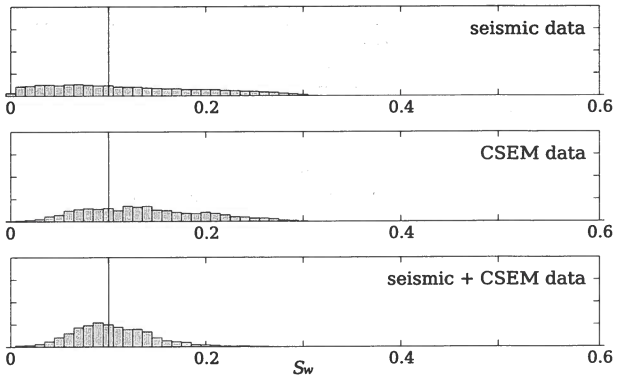

Figure 16. Histograms of posterior water saturation (S_w) samples of the sandstone layer. Vertical line indicates the ground truth value.

The CSEM data we utilize consists of the real and imaginary parts of the CSEM signal. We design the CSEM noise from the amplitude of the CSEM response and then add the noise to the real and imaginary parts of the response. The CSEM noise is categorized as systematic and non-systematic noise as shown in Figure 13. The systematic noise includes the instrument noise and the positioning error. We assume the systematic noise to be proportional to the amplitude of the CSEM signal whereas the non-systematic noise is independent of the signal. A realization of noisy CSEM data is shown in Figure 14, where the systematic noise is 5% of each noise-free amplitude and the non-systematic noise is 5×10^{-14} V/m. The CSEM signal decreases with frequency and the CSEM noise is more obvious.

We assume the CSEM data likelihood probability $f(\mathbf{d}_e|\mathbf{d}_{\sigma_e})$ to follow the multivariate Gaussian distribution (equation (4)). For the calculation of the likelihood, we assume that the CSEM data noise is independent. We model the covariance matrix $\mathbf{\Sigma}_e$ (Figure 2) as a diagonal matrix shown in equation (5). Assuming that the systematic and non-systematic noise are uncorrelated, the diagonal elements of the covariance matrix is derived as

$$\sigma_i^2(d_e) = \sigma_i^2(\varepsilon_{\text{sys}}) + \sigma_i^2(\varepsilon_{\text{nonsys}}), \tag{16}$$

where ε_{sys} and $\varepsilon_{\text{nonsys}}$ denote the systematic and non-systematic noise, respectively. Note that $\sigma_i^2(\varepsilon_{\text{sys}})$ values vary with frequency whereas $\sigma_i^2(\varepsilon_{\text{nonsys}})$ is independent of frequency.

4 UNCERTAINTY ANALYSIS

4.1 Histogram analysis of posterior distributions

We perform MCMC sampling to describe the posterior probability distribution (equation (3)). The random sampling is performed within a six dimensional model space that accounts for porosity or water saturation of soft shale, sandstone, and hard shale layers (Figure 4). The random samples of the porosity and water saturation are retrieved from the posterior probability distribution of three different cases: using seismic data only, CSEM data only, and both seismic and CSEM data. The uncertainty levels applied to the comparison are summarized as the base state variances in Table 3. The posterior distributions of the porosity and water saturation of the target sandstone layer are summarized as histograms as shown in Figures 15 and 16. Note that for the given uncertainties of rock-physics model and data noise levels, the histograms show that the single interpretations weakly constrain porosity and water saturation. However, the histograms from the joint interpretation exhibit a narrower sample distribution of the porosity and water saturation. The figures also show that the seismic data is more sensitive to the porosity than to the water saturation. This is connected with the rock-physics models in Figures 5 and 6 which show that the P-wave velocity has weaker correlation with the water saturation than with porosity. The relatively poor resolution from the CSEM data is attributed to the fact that the sandstone layer is electrically shielded by the more conductive overburden (soft shale layer). These examples illustrate the strength and limitation of both seismic and CSEM methods and explain the motivation of the joint interpretation of seismic and CSEM data. The histograms of the joint interpretation show smaller posterior uncertainty than do the single interpretations. The reduction of uncertainty is more pronounced for the water saturation than for the porosity.

We next compare the histograms that describe the posterior probabilities of different layers. Figure 17 shows the joint posterior distributions of the porosity of three layers. The posterior distribution for the soft shale layer is less constrained than that of the other layers. This is a consequence of the relatively weak correlation between the porosity and P-wave velocity of the soft

tude value, and the CSEM data uncertainty is defined as a sum of systematic and non-systematic noise. Figures 17 and 18 represent the posterior probability for the base uncertainty level. The histograms for the improved uncertainty level are shown in Figures 19 and 20. The reduced uncertainty level leads, of course, to a sharper posterior probability distribution than the base state and thus enhances the assessment of porosity and water saturation. This stronger constraint is more obvious for porosity than for water saturation. This is due to the smaller resolution of the CSEM method compared to the seismic method.

4.2 Different scenarios for uncertainty reduction

In the previous section, we presented histograms that characterize the posterior uncertainty. As stated before, we assume the multivariate Gaussian distribution (equation (4)) for the calculation of prior and likelihood. However, there are several factors that make the distribution of the posterior samples non-Gaussian. First, the porosity or water saturation have values between 0 and 1. Second, the porosity sampling is bounded by the critical porosity ϕ_c. The critical porosity is the threshold value between the suspension and the load-bearing domain and denotes the upper porosity limit of the range where the rock-physics model can be applied (Mavko *et al.*, 1998). The critical porosity values we apply for the soft shale, sandstone, and hard shale layer are 0.6, 0.4, and 0.4, respectively. These bounds can lead to skewed sample distributions. If the sample distributions are significantly skewed, another appropriate probability distribution should be applied for the probability assessment of the random samples. In this project, the distributions of the samples shown in Figure 17 through 20 do not display hard bounds or skewed distribution and indicate that the Gaussian distribution is a good approximation. The posterior distributions, however, do not necessarily follow the Gaussian distribution because of the nonlinearity of the forward models. The posterior uncertainty can generally be assessed by sample mean and sample variance. For reasons of clarity, we use the Gaussian curves for the representation of the sample mean and sample variance.

In this project, we model four factors of uncertainty: rock-physics model uncertainties of the P-wave velocity and electric conductivity, and noise of the seismic and CSEM data. The posterior probabilities of the porosity and water saturation for the base and improved uncertainty levels (Table 3) are discussed in the previous section (Figures 17 - 20). We perform the following numerical experiments to quantify the contributions of the four possible sources of uncertainty. The initial simulation is performed based on the base uncertainty level. For the analysis of the contributions of each of the factors on the posterior uncertainties, six subsequent simulations are performed with reduced uncertainty levels of one or two of the four factors of uncertainty. We perform the last simulation based on reduced uncertainty levels of all factors of uncertainty (improved level). These eight numerical experiments are summarized in Table 4. We compare the posterior distributions from different treatments with the base and improved level, and deduce how much a treatment contributes on the overall change of the sample variances. The posterior distributions of the porosity and water saturation are shown in Figures 21 - 26.

	uncertainty of the individual factors
base level	none of the factors are improved
treatment-1	only reducing P-wave velocity uncertainty
treatment-2	only reducing electric conductivity uncertainty
treatment-3	only reducing seismic noise level
treatment-4	only reducing CSEM noise level
treatment-5	reducing P-wave velocity uncertainty and seismic noise level
treatment-6	reducing electric conductivity uncertainty and CSEM noise level
improved level	reducing all of the four uncertainty factors

Table 4. Eight numerical experiments for the analysis of the contributions of four possible factors of uncertainty. Two states of uncertainty for the individual factors are listed in Table 3.

Figures 21 and 22 show the posterior probability distributions for the treatments 1 and 2. When we reduce uncertainty levels of P-wave velocity or electric conductivity the resultant posterior distributions exhibit smaller sample variances than the base level. Furthermore, the sample means generally are closer to the ground truth values as we reduce the individual uncertainty levels. The probability density distribution for porosity of the sandstone layer (Figure 21) reveals that the P-wave velocity uncertainty plays a significant role on the overall uncertainty reduction of the porosity and the contribution of the electric conductivity uncertainty is limited. In contrast, Figure 22 shows that the overall uncertainty variation of the water saturation is more strongly influenced by the uncertainty of the electric conductivity than by the uncertainty of the P-wave velocity. This is consistent with the simulated rock-physics models shown in Figures 5 - 8. From the rock-physics models, we can deduce that the porosity strongly influences both the P-wave velocity and electric conductivity. The rock-physics models also show that the water saturation strongly influences the electric conductivity while its influence on the P-wave velocity is limited.

The posterior probability distributions for the treatments 3 and 4 are shown in Figures 23 and 24. When we reduce the noise levels of the seismic or CSEM data, the improvements of the posterior uncertainties of

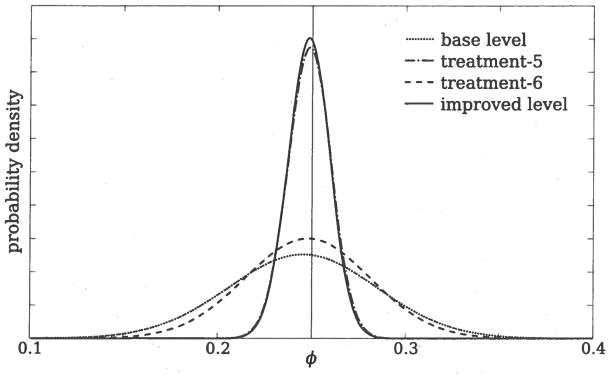

Figure 25. Posterior probability distributions of porosity ϕ of the sandstone layer. The distributions from the treatments 5 and 6 (Table 4) are compared with those from the base and improved levels. Vertical line indicates the true porosity value.

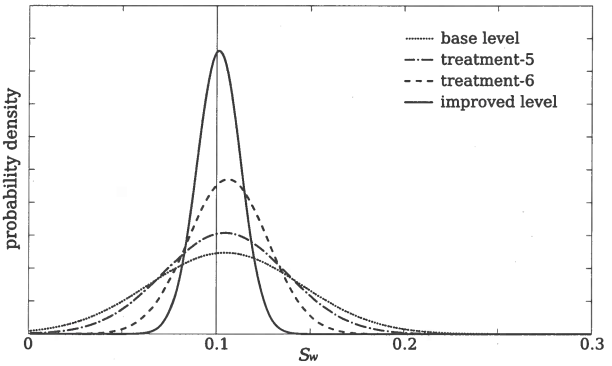

Figure 26. Posterior probability distributions of water saturation S_w of the sandstone layer. The distributions from the treatments 5 and 6 (Table 4) are compared with those from the base and improved levels. Vertical line indicates the true water saturation value.

the water saturation, the acquisition of more detailed electric conductivity information and the suppression of CSEM data noise will be preferred.

5 CONCLUSIONS

We have shown that the posterior probability random sampling based on the Metropolis-Hastings algorithm is capable of assessing the multi-dimensional probability distribution of the porosity and water saturation. We have also shown that the joint inversion of the seismic and CSEM data can be achieved by introducing rock-physics models that interconnect the P-wave velocity and electric conductivity. There are four representative sources of uncertainty that influence the posterior probability density of the porosity and water saturation. These uncertainties are related to seismic wave velocity, electric conductivity, seismic data, and CSEM data.

sample variance ($\times 10^{-3}$)	$S^2(\phi)$	$S^2(S_w)$
base level	1.56	1.63
treatment-1	0.13	1.38
treatment-2	1.24	0.50
treatment-3	1.19	1.16
treatment-4	1.44	1.27
treatment-5	0.13	1.06
treatment-6	1.11	0.45
improved level	0.12	0.13

Table 5. Sample variances S^2 of porosity ϕ and water saturation S_w of the sandstone layer. The details about the treatments are in Table 4.

Even when the single interpretations poorly constrain the posterior distributions of the porosity and water saturation, the distributions from the joint interpretation are well constrained and exhibit reduced uncertainty.

Assuming two levels of overall uncertainty, we study the relative contributions from the four individual sources of uncertainty. The numerical simulations show that rock-physics model uncertainties play a more significant role on the overall uncertainty variation than do seismic and CSEM data noise. The numerical experiment also suggests different ways of accomplishing uncertainty reduction depending on whether our interests focus on porosity or on water saturation. When porosity is our prime concern, we can effectively accomplish uncertainty reduction by acquiring more precise P-wave velocity information and suppressing the seismic data noise. On the other hand, if we need a more accurate assessment of water saturation, the acquisition of more detailed electric conductivity information and the suppression of CSEM data noise are desirable.

It is necessary to emphasize that the conclusions explained above depend on the parameters chosen in this project. Furthermore, there are many sources of uncertainty that we do not take into account such as lithologic variation, variation of mineralogical composition of clay, depth of layers. The methodology of the uncertainty analysis presented in this project can, however, be extended to a specific problem. The employed method can be used for experimental design, and for targeting the source of error that constributes most to the posterior uncertainty.

ACKNOWLEDGMENTS

This work was supported by the Consortium Project on Seismic Inverse Methods for Complex Structures at Center for Wave Phenomena (CWP). We thank Alan D. Chave (Woods Hole Oceanographic Institution) for providing his CSEM code, which was critically important for the success of this study. We acknowledge Inge Myrseth (Norwegian University of Science and Technol-

Iterative extended Born approximation based on CG-FFT integral equation method for low-frequency 3D modeling

A. Moradi Tehrani & E. Slob
Delft University of Technology

ABSTRACT
We present a fast method for modeling three-dimensional low frequency controlled source electro-magnetic (CSEM) problems. We apply the method to the marine controlled source electromagnetic (MCSEM) exploration situation where conductivity and permittivity are different from the known background medium. For 3D problems fast computational methods are relevant for both forward and inverse modeling studies. Since this problem involves a large number of unknowns, it has to be solved efficiently so that the results can be obtained in a timely manner, without compromising accuracy. For this reason, the Born approximation (BA), extended Born approximation (EBA) and iterative extended Born approximation (IEBA) are implemented and compared with the full solution of the conjugate gradient fast Fourier transformation method (CG-FFT). These methods are based on an electric field domain integral equation formulation. It is shown here how well the IEBA method performs in terms of both accuracy and speed with different configurations and different source positions. For forward modeling the solution at the sea bottom is of interest because that is where the receivers are usually located. But for inverse modeling, the accuracy of the solution in the target zone is important to be able to obtain reasonably accurate conductivity values from the inversion using this approximate solution method. Our modeling studies show that the IEBA method is suitable for both forward and inverse modeling.

Key words: CSEM, Modeling, Iterative Extended Born Approximation, Integral Equation, Low Frequency

1 INTRODUCTION

For three-dimensional diffusive electromagnetic modeling problems, local methods seem to have outperformed global methods in terms of memory requirements and computational efforts. The main reason for pursuing integral equation methods for modeling is that for a large class of problems the modeling domain can be reduced to the target volume. For such problems integral equations are useful, because they are based on primary-secondary, or direct-scattered field separation and allow for several types of suitable approximations. The integral equation uses the unperturbed field as a kernel multiplying the unknown perturbation on one side, with the source of the perturbation on the other side. Fast forward modeling solution algorithms are especially important for solving a parametric inverse problem. Examples of inverse scattering solutions using integral equations can be found in Abubakar & van den Berg (2004) and Gribenko & Zhadnov (2007). A modification to the original CG method (Hestenes & Stiefel, 1952) is an efficient way for solving integral equation problems (van den Berg, 1984). An additional advantage in computational efficiency is achieved when the background medium can be chosen as a homogeneous space or a horizontally layered earth. Then the convolutional structure of the system matrix is exploited by using the FFT routine for fast computation of the discrete convolutions while the background medium is homogeneous (Zwamborn &

where $\underline{x} \in \mathbb{D}^{sc}$.

We can solve this integral equation of the second kind through reducing the integral equation to a linear system of algebraic equation, then discretizing this system and approximating the unknown total electric field.

Once the total field has been found for all points inside the reservoir, we can compute the total field at the receiver,

$$\hat{E}_k^t(\underline{x}, \underline{x}^S) = \hat{E}_k^i(\underline{x}, \underline{x}^S) + \hat{E}_k^{sc}(\underline{x}, \underline{x}^S). \tag{7}$$

The incident field can be found from equation (2), whereas the scattered field can be written as the following representation,

$$\hat{E}_k^{sc}(\underline{x}, \underline{x}', s) = \int_{x' \in \mathbb{D}^{sc}} G_{kr}^{EJ}(\underline{x}, \underline{x}', s)\chi^{\sigma}(x')\hat{E}_r(\underline{x}', s)d^3\underline{x}' \tag{8}$$

where $\underline{x} \in \mathbb{D}_1$.

For low frequencies, small contrasts and a scattering domain that is small compared to the total domain, we can show that approximating the total internal electric field by the background field gives us almost the same accuracy. The scattered field is then computed at low computational cost. Thus analysis of the Born and extended Born approximations are of interest. In cases where the scattered field only consists of inductive effects at low frequencies, the Born approximation works well and there is no need to use more complex methods with many terms to converge.

If we consider

$$E_k^{(0)}(x, s) = E_k^i(x, s), \tag{9}$$

which means total field strength inside the scatterer equals to the background field then we are using the Born approximation (BA).

On the other hand,

$$\begin{aligned} E_k^{(1)}(x, s) &= E_k^i(x, s) \\ &+ \int_{\underline{x}' \in D^{sc}} G_{kr}^{EJ}(x, x', s)\chi^{\sigma}(\underline{x}')E_s^{(0)}(\underline{x}', s)dv, \end{aligned} \tag{10}$$

and iterative Born approximation would be as follow,

$$\begin{aligned} E_k^{(n)}(x, s) &= E_k^i(x, s) \\ &+ \int_{\underline{x}' \in D^{sc}} G_{kr}^{EJ}(x, x', s)\chi^{\sigma}(\underline{x}')E_s^{(n-1)}(\underline{x}', s)dv, \end{aligned} \tag{11}$$

In the following expression which is the so-called Extended Born approximation (EBA) the method is based on dominant contribution of the integral equation at locations where the Green's function is singular, leading to

$$E_s^{(0)}(\underline{x}, s) = L_{sk}^{(\underline{x})} E_k^i(\underline{x}, s), \tag{12}$$

where

$$L_{sk} M_{kr} = \delta_{sr} \tag{13}$$

and

$$M_{kr} = \delta_{kr} - \int_{\underline{x}' \in \mathbb{D}^{sc}} G_{kr}^{EJ}(\underline{x}, \underline{x}', s)\chi^{\sigma}(\underline{x}')d^3\underline{x}'. \tag{14}$$

According to Eq.(12) the iterative form of approximating the scattered field while using extended Born approximation would be,

$$E_k^{(n)}(\underline{x}, s) = E_k^i(\underline{x}, s) + K E_{kr}^{(n-1)}(\underline{x}, s), \tag{15}$$

where

$$K = \int_{\underline{x}' \in \mathbb{D}^{sc}} G_{kr}^{EJ}(\underline{x}, \underline{x}', s)\chi^{\sigma}(\underline{x}')d^3\underline{x}'. \tag{16}$$

The accuracy of EBA can be increased iteratively as formulated in Eq.(12). Notice that the iterative form of the Born approximation requires the full volume integration over the scattering domain, while the iterative form of the extended Born approximation as formulated in equation (15) only requires a local update at every location in the scattering domain which makes it essentially as fast as the EB method itself. This is why our formulation of the iterative extended Born approximation is so fast. We will investigate on this approach by numerical computations in the next section.

On the other hand the Born approximation is computed at the cost of zero iterations and EBA is computed at the cost of one iteration compared to the full solution with a large number of iterations. The iterative extended Born approximation requires a computational cost of just one iteration of the operator just as the EBA, then we need only local iterations so it has almost the same speed as EBA. We must consider that we have different processing time for the first iteration and the iterations afterward.

2.1 Numerical results

2.1.1 Accuracy of IEBA and the number of the iterations

We use the configurations depicted in Figure 2 for the three dimensional numerical examples.

Figure 2 shows a layered earth of air, sea and ground with an assumed reservoir. The background conductivity in the ground is 1 S/m and the reservoir's conductivity is 0.02 S/m. Air and sea have conductivity of 0 and 3 S/m respectively. The source is located above the center of the reservoir and situated 25 m above the sea bottom, whereas the receivers are spread in the area of 8×16 km. Depth of water is 1 km and the reservoir is located at the depth of 1 km below the sea bed. Dimensions of the reservoir are 4000×2000×300 m^3. A single frequency of 1 Hz is used in this example.

In this section we investigate the accuracy of the approximation at the receiver level. Later the accuracy of the method will be investigated at the reservoir level where we need high level of the accuracy for inverse modeling.

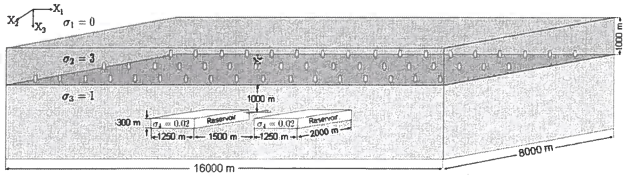

Figure 5. Diffusive fields present in a three media configuration with two reservoirs.

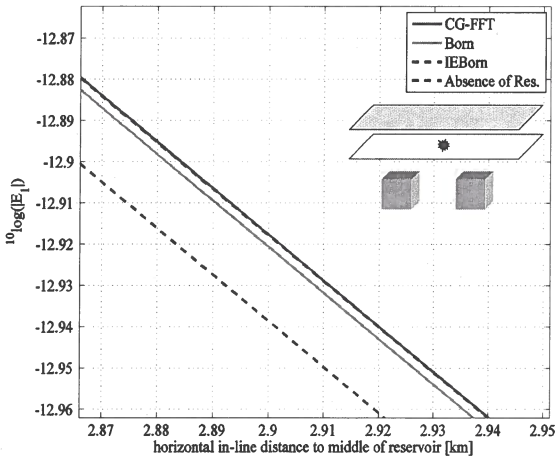

Figure 6. 3D electric scattered field at the receiver level with two assumed reservoirs and source is located 25 m above the sea bed at top of the middle of two reservoirs. The full solution is compared with solutions using the Born approximation, extended Born approximation and iterative extended Born approximation.

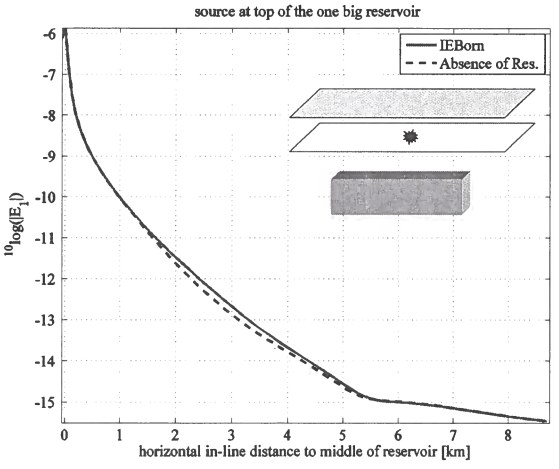

Figure 7. 3D electric scattered field at the receiver level with one assumed reservoir and source is located 25 m above the sea bed at top of the middle of the reservoir. Iterative extended Born approximation is compared with electric field in absence of the reservoir.

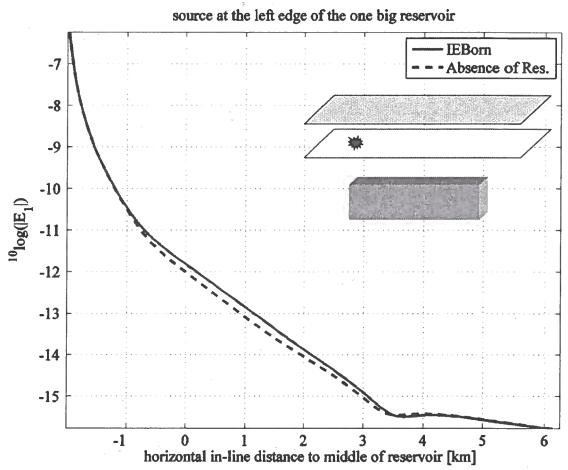

Figure 8. 3D electric scattered field at the receiver level with one assumed reservoir and source is located 25 m above the sea bed at top of the left edge of the reservoir (2 Km in the left-hand side of the center of the configuration). Iterative extended Born approximation is compared with electric field in absence of the reservoir.

Figures 7,8,9 and 10 aim to show the sensitivity of the method for both aforementioned examples as a function of horizontal source position along the x-axis. Figure 7 shows the scattered 3D electric field at the receiver level in the case of one assumed reservoir and source located 25 m above the sea bed in the middle of the reservoir. The iterative extended Born approximation result is compared with the electric field in absence of the reservoir. Figure 8 shows the 3D scattered electric field at the receiver level with one assumed reservoir and the source located 25 m above the sea bed at the left edge of the reservoir, which means 2 km away from the center of the configuration at the left hand side. The iterative extended Born approximation result is compared with the electric field in absence of the reservoir. Also Figure 9 shows the 3D scattered electric field at the receiver level with two assumed reservoirs and the source is located 25 m above the sea bed above the middle of the reservoirs. Iterative extended Born approximation is compared with electric field in absence of the reservoir.

It can be seen in Fig 8 where we have the source at the edge of the reservoir we have more response compared to the others in Figures 7,9 and 10.

So in more detail the configuration shown in figure 11 gives the biggest response as we mentioned before, but if the source is located above the middle of the reservoir (Figure 12) we have less response.

The minimum response comes from the case when we have two reservoirs and the source is located above the middle in between them (Figure 13).

The reason is that the strong direct incident field from source to the receivers along the x-axis does not

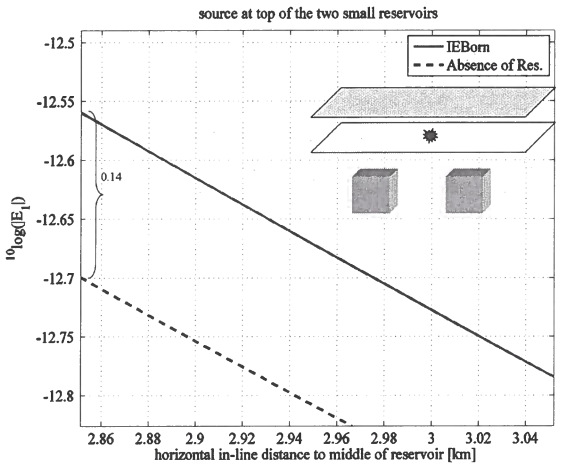

Figure 13. 3D electric scattered field at the receiver level with two assumed reservoirs and source is located 25 m above the sea bed at top of the middle of the reservoirs. Iterative extended Born approximation is compared with electric field in absence of the reservoir in more details.

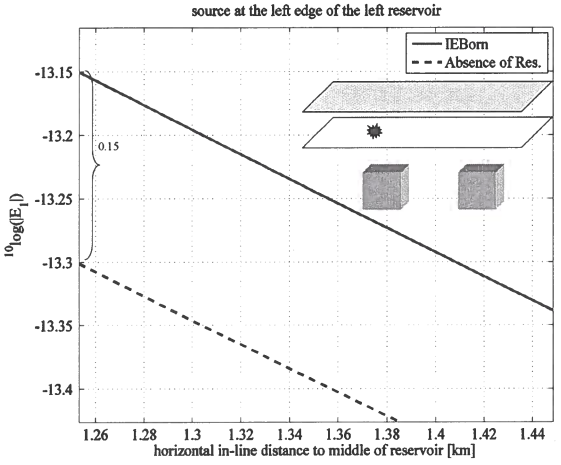

Figure 14. 3D electric scattered field at the receiver level with two assumed reservoirs and source is located 25 m above the sea bed at top of the left edge of the left reservoir (2 Km in the left-hand side of the center of the configuration). Iterative extended Born approximation is compared with electric field in absence of the reservoir in more details.

Also high order solutions have been implemented successfully for low frequency inversion of 3D buried objects (Cui *et al.*, 2006). Now we investigate the accuracy of the iterative extended Born approximation. In Figure 15 and 16 we can see that IEBA gives accurate result at the reservoir level along the x-axis while y=0 and the center along the vertical direction of the reservoir z is 1150 m from the sea floor.

Figure 15 shows the scattered field responses of the

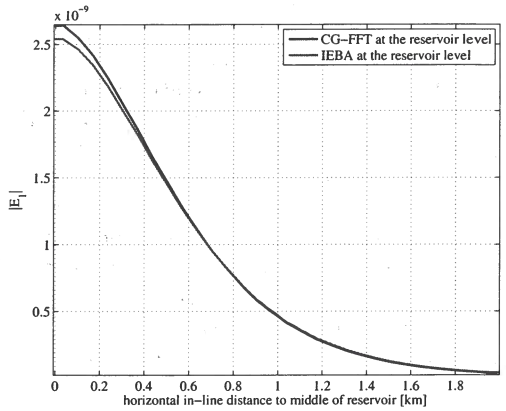

Figure 15. Scattered field responses of full solution and approximation at the reservoir level for one single reservoir.

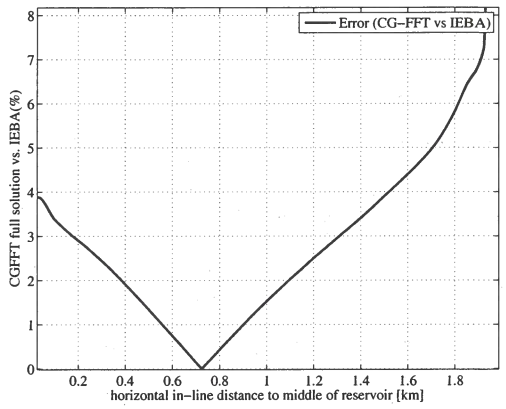

Figure 16. CGFFT vs. IEBA at the reservoir level.

full solution and the approximation at the reservoir level for one single reservoir.

In this figure the cross plots are along the source in x-direction and the source is located 25 m above the sea bed above the middle of the reservoir.

In Figure 16 the normalized difference in percent; between the CG-FFT result and the iterative extended Born approximation result along the line shown in Figure 15. The normalized error is in average less than four percent, while the maximum error is less than ten percent. It means this method can work well also for inverse modeling.

3 CONCLUSIONS

An iterative extended Born approximation is proposed here to solve 3D diffusive electromagnetic field scattering problems based on the integral equation method. Theoretical formulations and numerical results, where the unknown object is an modeled reservoir in the lay-

Feasibility of borehole radar measurements to monitor water/steam fronts in enhanced oil recovery applications

Mattia Miorali[1], Evert Slob[1] & Rob Arts[1,2]
[1] *Department of Geotechnology, Delft University of Technology, 2600 GA Delft, The Netherlands*
[2] *TNO, PO Box 80015, 3508 TA Utrecht, The Netherlands*

ABSTRACT

A technique capable of capturing the dynamics of reservoir fluids in the proximity of production wells would provide enormous benefits to the reservoir management. In fact, monitoring can be used to develop a feedback loop between measurements and control technologies to optimize production. This paper examines the feasibility of a borehole radar tool for near-wellbore imaging. Modeling results show that the maximum imaging range depends mainly on the conductivity of the formation in which the radar borehole system lies. Another constraint is given by the operating frequency of the system. Too low frequencies compromise the electromagnetic wave propagation in favor of diffusion phenomena and too high frequencies drastically attenuate the signal. In case of a relatively low conductive reservoir and a limited band of frequencies higher than 100 MHz, we have defined the optimal imaging capacity of the radar system to be in the order of ten of meter. We suggest borehole radar measurements as a promising approach to monitor steam chamber growth in Steam Assisted Gravity Drainage (SAGD) processes and to prevent water encroachment in thin oil rims. The penetration capacity of a radar system fits the required imaging depth for these environments.

Key words: electromagnetic (EM), borehole radar, Enhanced Oil Recovery (EOR), thin oil rim, Steam Assisted Gravity Drainage (SAGD)

1 INTRODUCTION

In this last decade an important innovation in the oil industry has been the development of a new generation of wells called smart wells. These wells are equipped with down-hole sensors to monitor well and reservoir conditions and with valves to control the inflow of fluids from the reservoir into individual well segments (Robison, 1997). Figure 1 shows a schematic representation of a smart horizontal well (Jansen *et al.* (2008)). The combination of monitoring and control has the potential to significantly improve oil and gas recovery (Glandt, 2005). In fact, the adjustable settings of the inflow control valves (ICVs) can be varied to optimize the inflow profile along the well in response to monitoring data obtained from down-hole sensors. Addiego-Guevara *et al.* (2008) have demonstrated that control strategies always enhance production and mitigate reservoir uncertainty; a typical application is the management of undesired fluid to prevent early breakthrough within the production wells. Currently the most used permanent down-hole sensors measure pressure and temperature, but give a poor description of the fluid reservoir conditions outside the well. There is an intense research effort to discover new monitoring techniques that could capture the fluid dynamics at larger distances from the well. For example, Saunders *et al.* (2008) have suggested that electrokinetic potential measurements should be sensitive to the movement of an approaching water front

frequencies.

We have used a volumetric model to get effective values of relative permittivity ϵ_{eff}, therefore the dielectric properties of a rock are based on the relative volumes of the different components and their individual dielectric characteristics. The Complex Refractive Index Model (CRIM), proposed by Birchak *et al.* (1974), is the most used mixing model in the radar range of frequency, since it is the one that better fits laboratory measurements (Roth *et al.* (1990) and Seleznev *et al.* (2004)); in case of three components it is given by the following formula:

$$\epsilon_{eff}^{1/2} = (1-\phi)\epsilon_s^{1/2} + \theta\epsilon_w^{1/2} + (\phi-\theta)\epsilon_o^{1/2}, \quad (5)$$

where ϵ_s, ϵ_w and ϵ_o are respectively the relative permittivity of the solid, the water and the oil, ϕ is the porosity and θ is the volumetric water content. To get effective values of conductivity we have used the classic Archie's law (Archie, 1942). These effective EM properties of a rock are mainly controlled by the amount of pore water. In fact, the relative permittivity of water is much higher than the one of the other reservoir components ($\epsilon_w = 80$, $\epsilon_o = 2-3$ and $\epsilon_s = 4-10$) and just the electrical conductivity of water can reach values that would have strong impact on the EM wave propagation ($\sigma > 0.1$ S/m), σ_o is lower than 10^{-6} and σ_s is scattered over several orders of magnitude but for reservoir material it does not exceed 10^{-4}. The EM properties of water, instead, can be strongly affected by temperature and salinity. As temperature increases, thermal agitation reduces the interaction between the dipoles and the electric field, while it facilitates the movement of the ions, so the overall effect is a reduction of ϵ_w and an increase of σ_w. The addition of salt to water decreases ϵ_w, since the amount of the molecules able to polarize is reduced. The electrical conductivity, instead, is directly proportional to the total dissolved salt ions, since the conduction of current in an electrolyte depends on the concentration of ionic species. Consequently, both temperature and saline concentration have a relevant influence on the effective EM properties of a rock.

As an example, we present in figure 3 attenuation and phase distortion for three frequencies (10, 100 and 300 MHz). Analysis shows, that for the given range of medium parameters, wave propagation starts to dominate around 100 MHz; at lower frequencies the phase distortion is not tolerable (fig. 3d), and, on the other side, higher frequencies make the attenuation increase (fig. 3c). The effect of phase distortion can be clearly seen in the time domain. Figure 4 shows that for a fixed propagation distance there is an additional time delay for higher values of PH_{err}. This compromises a localization of a water/steam front, since the interface would appear at higher distance than what it actually is. Time delay of 3 ns corresponds to approximately 30 cm for a typical EM velocity of high resistive medium (9×10^7 m/s), which reflects the formation around the production well where the borehole radar system would be located. For $PH_{err} = 2$, it can be seen that the time delay is already bigger that 3 ns, so a shift of approximately 50 cm would occur. This is already too much in an environment where the investigation depth can be only 5 m. Moreover, higher PH_{err} values reduce the resolution of the wave and consequently the ability to distinguish multiple reflections. Another observation that can be deduced from figure 3 is the strong effect of conductivity on both attenuation and phase distortion: increase of σ makes ATT and PH_{err} raise, hampering the wave propagation domain. Therefore, we conclude that a borehole radar system should operate above 100 MHz and that the natural regime for EM propagation would be favorable in reservoirs with $\sigma < 0.03$ S/m.

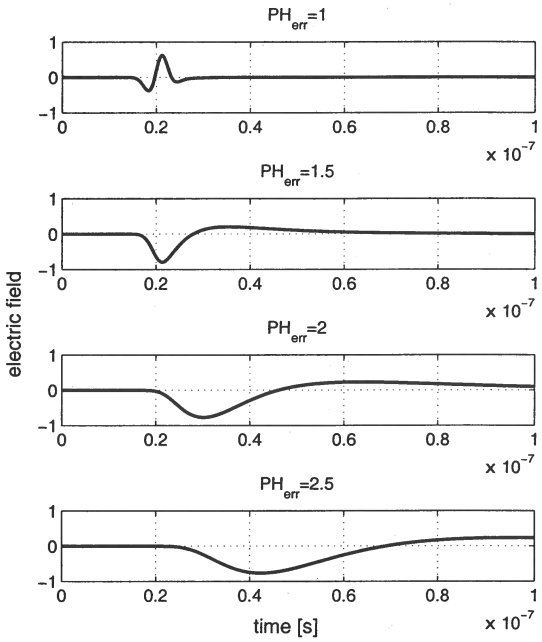

Figure 4. Electric field in the time domain for waves that travel the same distance but with different value of phase distortion: $PH_{err} = 1$, $PH_{err} = 1.5$, $PH_{err} = 2$, $PH_{err} = 2.5$.

3 REFLECTIVITY OF WATER/STEAM FRONT

Another important parameter to be considered for a feasibility study of borehole radar is the reflectivity of medium discontinuities: if the reflectivity of an interface is weak, a radar system may not be able to detect the reflection from the interface. The reflectivity expresses the amount of reflected energy and it depends on the reflection coefficient, which can be split into a transverse electric (TE) mode and into a transverse magnetic mode

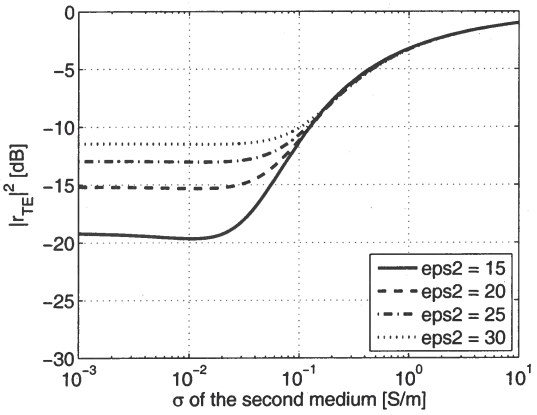

(a)

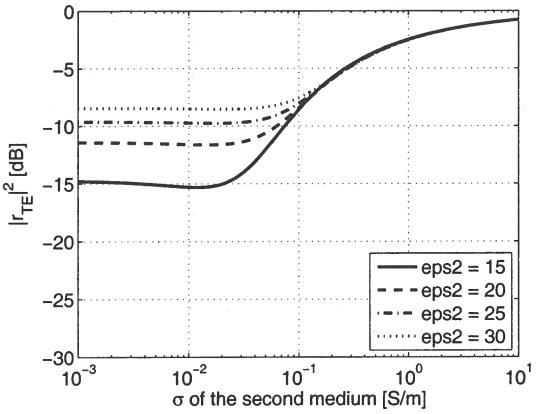

(b)

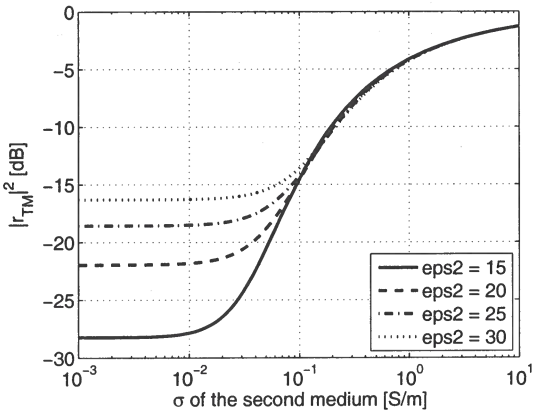

(c)

Figure 5. Reflectivity of a single planar interface with varying properties of medium 2 at 100 MHz. Medium 1 has fixed properties: $\epsilon_r = 10$ and $\sigma = 0.01$ S/m. Fig. 5a and 5b shows $|r_{TE}|^2$ when the angle of incidence θ is respectively 0 and 45 degrees; fig. 5c shows $|r_{TM}|^2$ when θ is 45 degrees.

minimum detectable signal and depends on technical features of the system: transmitting and receiving antenna directional gains, transmitting and receiving antenna coupling efficiencies an transmitted power. On the right hand side are the medium and target-dependent parameters: attenuation α, wavelength λ, reflectivity Γ and maximum penetration depth $R_{\max}$. Using equation (8), it is possible to estimate the SP that a radar system must satisfy to detect interfaces between two media with different EM properties and for different penetration depths. A broad range of EM contrasts at oil-water and oil-steam interfaces in oilfield conditions have been considered, and the calculated SP values are shown in figure 6. Medium 1 has been modeled with proper ϵ_r and σ of high oil saturation rock, while we have allowed the EM properties of medium 2 to assume a broad range of values characteristic of rock saturated by undesired fluids like water or steam. It seems that permittivity variations of the remote medium do not affect the SP (fig. 6a); instead, conductivity variations of the remote medium affect the SP and a conductivity increase causes a reduction of the SP needed to detect the same interface (fig. 6b). Therefore, in case of favorable EM properties of the first medium, larger penetration depths can be reached if the discontinuity has a strong conductivity contrast. Moreover, it seems that investigation depths in the order of ten meters can be achieved with typical SP of current radar systems being around 160 dB and an operating frequency of 100 MHz.

5 MODELING RESULTS

In order to evaluate the most significant parameters for the feasibility of a borehole radar tool, we have modeled the electric field reflected by transitions between oil-rich zones to water/steam-rich zones. We have used the reflection operator approach given in Nguyen *et al.* (1998). This technique requires a layered configuration embedded in two half spaces. Every layer has relative permittivity ϵ_{ri}, conductivity σ_i , relative magnetic permeability $\mu_{ri} = 1$ and propagation constant $\gamma_i = i\omega/c\sqrt{\epsilon_{ri} - (i\sigma/\epsilon_0\omega)}$ with $i = 1, ..., N$. Based on the wave equation and the boundary conditions at each of the N layers, the reflection operator can be expressed by the following recursion formula:

$$\hat{R} = \frac{r_n + R_{n+1}\exp\left(-2\gamma_{n+1}h_{n+1}\right)}{1 + r_n R_{n+1}\exp\left(-2\gamma_{n+1}h_{n+1}\right)}, \quad n = 0, ..., N \quad (9)$$

where $h_{n+1} = z_{n+1} - z_n$ is the thickness of each layer and $r_n = (\gamma_n - \gamma_{n+1})/(\gamma_n + \gamma_{n+1})$ is the reflection coefficient of each interface. Source and receiver are located in the upper half space, so once the reflector operator at the first interface $\hat{R}_0$ is known, it is possible to calculate the scattered electric field E^s at the position of the receiver z:

$$E^s(z, \omega) = \hat{R}_0 E_{inc}\exp(-\gamma_0 z), \quad (10)$$

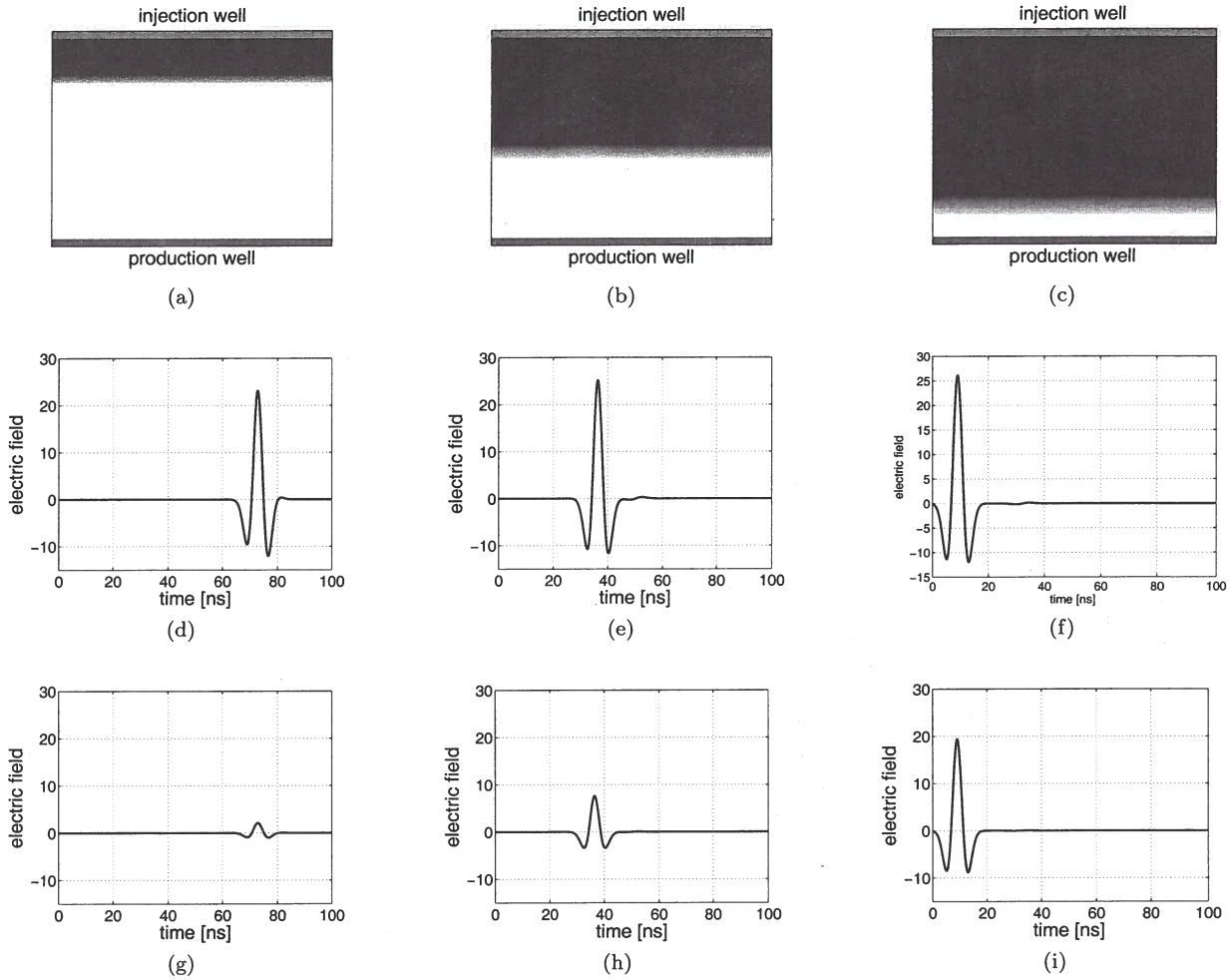

Figure 7. Modeled reflected electric field as a function of time for three sequent positions of a steam front in a SAGD process. In fig. 7a, 7b and 7c the three different geometries of the process are shown: the black color represents the steam rich zone, the gray color the transition zone and the white color the oil rich zone. The gray layers at the top and at the bottom of the figures represent respectively the injection and the production well. Source and receiver are located in the production well. Two different conductivity of formation water are considered: 0.01 S/m (7d,7e,7f) and 1 S/m (7g,7h,7i)

Chen, Y. H., & Oristaglio, M. L. 2002. A modeling study of borehole radar for oil-field applications. *Geophysics*, **67**, 1486–1494.

Glandt, C. A. 2005. Reservoir management employing smart wells: a review. *SPE Drilling and Completion*, **20**, 281–288.

Jansen, J. D., O. H. Bosgra, & van den Hof, P. M. 2008. Model-based control of multiphase flow in subsurface oil reservoirs. *Journal of Process Control*, **18**, 846–855.

Nguyen, B. L., J. Bruining, & Slob, E. C. 1998. Delineation of air/capillary transition zone from GPR data. *SPE Reservoir Evaluation and Engineering*, 319–327.

Noon, D. A., G. F Stickley, & Longstaff, D. 1998. A frequency-independent characterization of GPR penetration and resolution performance. *Journal of Applied Geophysics*, **40**, 127–137.

Robison, C. E. 1997. Overcoming the challenges associated with the life-cycle management of multilaterals wells: assessing moves towards the intelligent completion. *SPE Offshore Europe Conference*, 269–276.

Roth, K., H. Schulin H. Fluhler, & Attinger, W. 1990. Calibration of time domain reflectometry for water content measurements using a composite dielectric approach. *Water Resources Research*, **26**.

Saunders, J. H., M. D. Jackson, & Pain, C. C. 2008. Fluid flow monitoring in oil fields using downhole measurements of electrokinetic potential. *Geophysics*, **73**, 165–180.

Seleznev, N. V., A. Body T. Habashy, & Luthi, S. 2004. Dielectric mixing laws for partially saturated carbonate rocks. 45^{th} *Annual Logging SPWLA Symposium.*

Facing the main challenges in carbon capture and sequestration

Roel Snieder and Terry Young
Department of Geophysics, Colorado School of Mines

ABSTRACT
We discuss the main hurdles in implementing carbon capture and sequestration, these are (1) reducing the cost to a level that is comparable with the cost of steps towards energy efficiency and conservation, (2) upscaling the current technology with a factor 1000, and (3) monitoring leakage rates less than a percent per year. Unless we are able to address these question in a satisfactory way, carbon carbon and sequestration holds little promise for being helping curb anthropogenic global warming.

Key words: carbon capture and sequestration

Anthropogenic emission of greenhouse gases, notably CO_2, contributes significantly to global warming (Pachauri & Reisinger, 2007). Economic growth in developing countries, increasing reliance on non-conventional oil, and use of coal as a power source are all leading to increased emissions of CO_2 (Kerr, 2008). Carbon Capture and Sequestration (CCS) is viewed by some as a panacea. The US Department of Energy (DOE) made \$3.4 billion available for fossil fuel research, a significant fraction for CCS (Charles, 2009), and DOE supports a number of trial projects for CO_2 sequestration (Litynski *et al.*, 2008).

Injecting CO_2 in the subsurface has an out-of-sight, out-of-mind appeal because the CO_2 is prevented from entering the atmosphere. This approach is, however, not without its drawbacks and research needs to focus on making CCS effective both technically and economically on the scale needed to mitigate anthropogenic contributions to global warming. In order to assess this issue it is essential to look at the numbers involved in CCS.

Let us assume that in order for CCS to have a significant effect, we sequester worldwide about 4 $GtCO_2$/year. This is about 1/6th of the current global production, and it is roughly the same as the amount of CO_2 sequestered as one of the seven steps needed for capping the CO_2 concentration at 550 ppm(Pacala & Socolow, 2004) (twice the pre-industrial level of CO_2). To put this in perspective, this is the same mass as the total annual global oil production (Central Intelligence Agency, 2009). To sequester such an amount in the subsurface takes an infrastructure that is comparable to the one used now for petroleum production worldwide.

Currently, CO_2 is injected at a number of pilot projects in countries that include Canada (Weyburn), the Norway (Sleipner), and Algeria (In Salah). In the multiple pilot projects supported by DOE in the continental USA, typically about 1 $MtCO_2$/year is to be injected. Therefore, the pilot-project technology currently used must be replicated or up-scaled by a factor of 1000 to be effective for mitigating global climate change. The current cost of CCS is between 40-70 \$/ton CO_2 (Metz *et al.*, 2005). The annual cost of sequestering 4 $GtCO_2$/year at a cost of \$50/ton CO_2 is 200 billion \$/year. Even though this amount is not large compared to the global expenditure for energy, one may question whether society is willing to cover an expense of this magnitude in order to mitigate climate change. Moreover, the recent McKinsey report *Reducing U.S. greenhouse emissions: How much at what cost?* (McKinsey&Company, 2007) showed that the USA can avoid about 40% of its CO_2 emissions by taking actions such as driving more efficient cars and trucks, and implementing combined heat and power generation. Most of these actions are cheaper than CCS and actually pay for themselves in the long-term. Over the time-scale of several hundred years, CO_2 has the potential to react with the host rock in some geologic formations and to become permanently stored in the subsurface (Metz *et al.*, 2005). In order for CCS to be effective, CO_2 must be sequestered for several hundred years. Losing 0.5% of the

Influence of background heterogeneity on traveltime shifts for compacting reservoirs

Rodrigo F. Fuck[1], Ilya Tsvankin[1] & Andrey Bakulin[2]
[1] *Center for Wave Phenomena, Colorado School of Mines, Golden, CO*
[2] *WesternGeco, Houston, Texas*

ABSTRACT

Compaction induced by pore-pressure decrease inside a reservoir can be monitored by measuring traveltime shifts of reflection events on time-lapse seismic data. Recently we presented a perturbation-based formalism to describe traveltime shifts caused by the 3D stress-induced velocity field around a compacting reservoir. Application of this method to homogeneous background models showed that the offset variation of traveltime shifts is controlled primarily by the anisotropic velocity perturbations and can provide valuable information about the shear and deviatoric stresses.
Here, we model and analyze traveltime shifts for reservoirs whose elastic properties before compaction are different from those of the surrounding medium. For such models, the excess stress is influenced primarily by the contrast in the rigidity modulus μ across the reservoir boundaries. Synthetic examples demonstrate that a significant (25% or more) contrast in μ enhances the isotropic velocity perturbations outside the reservoir. Nevertheless, the influence of background heterogeneity is mostly confined to the reservoir and its immediate vicinity, and the anisotropic velocity changes are still largely responsible for the offset dependence of traveltime shifts. If the reservoir is stiffer than the host rock, the background heterogeneity reduces anisotropic velocity perturbations inside the reservoir, but increases them in the overburden. As a result, in that case the magnitude of the offset variation of traveltime shifts is generally higher for reflections from interfaces above the reservoir.

We also studied compaction-induced stress/strain and traveltime shifts for a stiff reservoir embedded in a softer layered model based on velocity profiles from Valhall Field in the North Sea. Despite producing discontinuities in strain across medium interfaces, horizontal layering does not substantially alter the overall behavior of traveltime shifts. The most pronounced offset variation of traveltime shifts is observed for overburden events recorded at common midpoints close to the reservoir edges. On the whole, prestack analysis of traveltime shifts should help to better constrain compaction-induced velocity perturbations in the presence of realistic background heterogeneity.

Key words: time-lapse seismic, traveltime shifts, prestack time shifts, heterogeneity, compacting reservoirs, excess stress, stress-induced anisotropy.

1 INTRODUCTION

Traveltime shifts (i.e., the differences in traveltime for the same reflector measured between time-lapse seismic surveys) have become a common tool for monitoring dynamic changes in hydrocarbon reservoirs caused by depletion. For example, Guilbot and Smith (2002) employ traveltime shifts to detect and monitor reservoir

by

$$\Delta e_{kk} \propto \frac{\alpha\,\Delta P}{\rho V_P^2}\frac{g}{(3-4g)} \approx \frac{\alpha\,\Delta P}{\rho V_P^2}\frac{g}{3}\left(1+\frac{4g}{3}\right), \quad (3)$$

where $g = (V_P/V_S)^{-2}$. Since typically $g \ll 1$, Δe_{kk} is inversely proportional both to V_P^2 and V_P^2/V_S^2.

2.2 Traveltime shifts

To give an analytic description of P-wave traveltime shifts above a compacting reservoir, Fuck et al. (2009) assume the compaction-induced velocity changes to be small. Traveltime shifts are then obtained from the first-order perturbation of traveltimes along reference rays traced in the background model. The approximation of Fuck et al. (2009) includes two terms, one of which is "geometric" (i.e., the time shift related to the displacement of the sources, receivers and interfaces), while the other depends on the velocity perturbations along the ray. Since the compaction-related displacements in the elastic regime yield relatively small traveltime shifts, the geometric term can be neglected.

Using the nonlinear theory of elasticity, the stiffness tensor c_{ijkl} of the deformed medium can be represented as

$$c_{ijkl} = c^{\circ}_{ijkl} + c_{ijklmn}\,\Delta e_{mn}\,, \quad (4)$$

where c°_{ijkl} is the stiffness tensor of the background medium, c_{ijklmn} is the strain-sensitivity tensor, and Δe_{mn} is the tensor of the elastic strains induced by the reservoir compaction. Hereafter, the summation convention over repeated indices is assumed.

It is convenient to rewrite equation 4 by employing Voigt notation, which maps each pair of indices ij to a single index α:

$$\alpha = i\delta_{ij} + (9-i-j)\,(1-\delta_{ij})\,, \quad (5)$$

where δ_{ij} is Kronecker's symbol. The strain tensor Δe_{mn} then becomes a vector (denoted by ΔE_γ), and equation 4 takes a concise matrix form (Fuck and Tsvankin, 2009):

$$C_{\alpha\beta} = C^{\circ}_{\alpha\beta} + C_{\alpha\beta\gamma}\Delta E_\gamma\,. \quad (6)$$

A detailed analysis of the symmetry of the deformed medium based on equation 4 can be found in Fuck and Tsvankin (2009).

Assuming both the background stiffness tensor and the strain-sensitivity tensor to be isotropic, the velocity-related P-wave traveltime shifts are obtained as (Fuck et al., 2009) ¶:

$$\delta t = -\frac{1}{2}\int_{\tau_1}^{\tau_2}\Big[\underbrace{B_1\Delta e_{kk}}_{\text{volumetric}} + \underbrace{B_2\big(\mathbf{n}^{\mathrm{T}}\Delta\epsilon\,\mathbf{n}\big)}_{\text{deviatoric}}\Big]\mathrm{d}\tau\,, \quad (7)$$

where $\mathbf{n}$ is the unit slowness vector of the reference ray, and τ is the time along the ray. The constants B_1 and B_2 are given by

$$B_1 = \frac{C_{111}+2C_{112}}{3C^{\circ}_{33}}\,, \quad (8)$$

$$B_2 = \frac{4C_{155}}{C^{\circ}_{33}}\,. \quad (9)$$

Since $C_{155} = (C_{111}-C_{112})/4$, traveltime shifts in equation 7 depend on just two combinations of the three linearly independent elements $C_{\alpha\beta\gamma}$ of the isotropic tensor c_{ijklmn}. Equation 7 separates the velocity-related traveltime shifts into the isotropic term, which depends on the volumetric strain (Δe_{kk}) and the anisotropic term associated with the deviatoric strain elements ($\Delta\epsilon_{ij}$).

3 MODELING METHODOLOGY

Following Fuck et al. (2009), we employ a three-step procedure to simulate depletion-related traveltime shifts. First, the excess stress and strain fields are computed for several 2D models with a heterogeneous background. We use finite elements (COMSOL™ package) to solve for the displacements, stresses and strains caused by a pore-pressure drop inside a rectangular reservoir. The modeling is carried out in 2D by assuming a plane-strain model (i.e., there is no deformation in the x_2-direction). The accuracy of the numerical solutions is checked by comparing the results for a homogeneous model with those obtained from the analytic expressions of Hu (1989). The top of the model is specified as a free surface; to avoid artifacts due to the finite model dimensions, the model's height and width are 10 times larger than those of the reservoir.

At the second step, we compute the stiffness and velocity perturbations from the strain changes using equation 6. Finally, the traveltime shifts are obtained either from approximation 7 or by subtraction of the exact (ray-traced) traveltimes calculated for the perturbed and background velocity models. The anisotropic ray-tracing algorithm is based on the equations of Červený (2001) for heterogeneous anisotropic media, which are solved by the fifth-order Runge-Kutta method (Press et al., 1992). To avoid errors in traveltime shifts caused by smoothing of velocity models, we account for reflection/transmission at interfaces using Snell's law.

¶Here, we express the traveltime shifts in terms of the deviatoric strain rather than deviatoric stress to facilitate comparison between the contributions of the isotropic and anisotropic velocity changes.

deviatoric strains observed above a more rigid reservoir (compare Figures 3b and 3c) produce larger traveltime shifts with more pronounced offset variation. Traveltime shifts beneath the reservoir are strongly dependent on the strains accumulated inside it. In particular, the reduction in the volumetric strain and increase in the deviatoric strains inside a softer reservoir result in a more pronounced offset variation of traveltime shifts for deep reflectors (Figures 4a and 4b).

Figures 8 and 9 illustrate how the contrast in μ influences the behavior and composition of traveltime shifts. In general, traveltime shifts vary more rapidly with offset, if the contrast in μ increases the deviatoric strains above the reflector. On the whole, offset-dependent traveltime shifts for this group of models are governed primarily by the anisotropic velocity perturbations.

4.2 Layered model

Next, we examine a model that consists of eight horizontal layers whose parameters were adapted from velocity profiles estimated at Valhall Field in the North Sea (Figure 10). The components of the strain-sensitivity tensor are taken from the measurements for North Sea shales made by Prioul et al. (2004) under two different ranges of hydrostatic load. Taking into account the weight of the overburden, the layers above 2 km were assigned the values of C_{ijk} for the load ranging from 5 MPa to 30 MPa [except for the water (0–0.1 km) where $C_{ijk} = 0$]; the deeper layers were assigned C_{ijk} measured for the load between 30 MPa and 100 MPa. To obtain the static velocity values similar to those published by Herwanger and Horne (2005) for their Valhall model, the seismic velocities were reduced by 40%.

4.2.1 Stress/strain modeling

Apart from the discontinuities in strain across the layer boundaries, the compaction-induced strains for the layered model are generally similar to those observed for the simpler models investigated above. For example, since the reservoir is stiffer than the rocks of the overburden, the deviatoric strains tend to concentrate around the reservoir rather than spread through the upper part of the model (Figure 11). Also, as predicted by equation 2, the deviatoric strains are smaller beneath the reservoir than above it because of the higher P-wave velocities in the two bottom layers (Figures 11a–c).

The volumetric strain Δe_{kk} is largely confined to the reservoir, where it exceeds the deviatoric strain $\Delta\epsilon_{ij}$. Outside the reservoir, however, the deviatoric strains dominate the strain field (compare Figures 11a and 11d). Some of the features of the distribution of the volumetric strain can be explained using equation 3. For instance, because Δe_{kk} is inversely proportional to V_P^2/V_S^2, the largest volumetric strain outside the reservoir is accumulated in the seventh layer, which has a small value of $V_P/V_S = 1.6$.

Figure 12 summarizes the influence of the compaction-induced strains on the velocity perturbations. As expected from our previous results (Fuck et al., 2009), the initially isotropic velocity model composed of homogeneous layers becomes anisotropic with a heterogeneous velocity field inside each layer. For our 2D model, velocity anisotropy in all layers is elliptical with a tilted symmetry axis (in 3D the symmetry becomes orthorhombic). Because the strain-sensitivity elements C_{ijk} are much larger for the shallow layers (down to 2 km), the velocity perturbations are restricted primarily to the upper part of the model (Figure 12a). The sign of the Thomsen anisotropy parameter $\varepsilon = \delta$ indicates that the horizontal velocity is higher than the vertical velocity outside the reservoir ($\varepsilon > 0$) and smaller inside it ($\varepsilon < 0$, Figure 12a). The rotation of the symmetry axis from the vertical (caused by the shear strain) does not exceed 1°.

4.2.2 Offset variation of traveltime shifts

Figure 13 displays ray-traced and approximate traveltime shifts for a range of reflector depths and a CMP located above the reservoir center. In contrast to the results of Fuck et al. (2009) for the homogeneous model, approximation 7 is more accurate for deeper reflectors because the largest velocity perturbations are concentrated in the upper part of the model.

Another factor contributing to the poor performance of the linearized approximation for reflectors at the shallow depths (0.85 km, 1.5 km, and 2 km) is significant ray bending, which is not taken into account by equation 7. Ray bending makes the traveltimes more sensitive to the horizontal and shear components of the deviatoric strain tensor, which increases the offset variation of the exact (ray-traced) shifts. Also, the approximation deteriorates for common midpoints near the edges of the reservoir due to the pronounced accumulation of the shear strain around the reservoir corners (Figure 11b). For example, the difference between the ray-traced and approximate traveltime shifts for reflectors above the reservoir increases as the CMP approaches the reservoir edge located at $x = 1$ km.

Since the compaction-induced velocity perturbations occur mostly above the reservoir, the largest shifts (as well as their most pronounced offset variation) are observed for the overburden events, especially in common midpoints located above the reservoir corner (Figure 14). As was the case for the "homogeneous host rock" models with a relatively rigid reservoir, the reflections from the base of the reservoir and interfaces close to it exhibit the smallest offset variation of the shifts, particularly if the CMP is above the reservoir center (Figure 13c). The near-offset traveltime shifts for the

6 CONCLUSIONS

We studied the influence of heterogeneity of the background velocity model on compaction-related traveltime shifts and their variation with offset. The main goal of our numerical simulations was to verify whether prestack analysis of traveltime shifts provides useful information for reservoir characterization in the presence of background heterogeneity.

When the reservoir is embedded in a medium with different elastic properties, the contrast in the rigidity modulus μ may cause substantial changes in the compaction-related strains. In particular, the contrast in μ influences the relative magnitude of the deviatoric strains responsible for the anisotropic velocity perturbations. Still, the most pronounced isotropic velocity changes (which are related to the volumetric strain), are largely restricted to the reservoir itself. Therefore, as was the case for homogeneous background models, offset-dependent traveltime shifts are mainly governed by the anisotropic velocity perturbations. Thus, the offset variation of traveltime shifts estimated from prestack data can provide useful information about the compaction-induced deviatoric strains.

The numerical experiments allowed us to formulate some simple "rules of thumb" about the properties of the strain field and traveltime shifts. For example, if the reservoir is more rigid than the host rock, the deviatoric strains tend to increase (compared with the homogeneous background model) outside the reservoir and decrease inside it. Hence, the largest offset variation of traveltime shifts for a rigid reservoir is observed for reflectors in the overburden.

The geomechanical modeling for a realistic layered background medium indicates that vertical heterogeneity does not dramatically alter the compaction-induced strain. For example, the magnitude of the deviatoric strains in each layer is inversely proportional to the squared P-wave velocity, while the magnitude of the volumetric strain is also inversely proportional to the squared P-to-S velocity ratio. Moreover, despite the strain discontinuities across layer boundaries, the spatial distribution of strain is generally similar to that for models with a simpler background. For instance, because the reservoir in the layered model is more rigid than the overburden, the volumetric strain dominates inside the reservoir, while the deviatoric strains accumulate mostly above it. The deeper layers are stiffer and less strain-sensitive than the rest of the background model, which also contributes to the concentration of the strain-induced velocity perturbations in the upper part of the section. Therefore, the most pronounced offset variation of traveltime shifts is observed for overburden reflections, especially if the CMP is located close to the reservoir edge.

We also showed that reservoirs that have rectangular and elliptical cross-sections with the same area and aspect ratio produce similar spatial distributions of compaction-induced strains. As a result, the magnitude and offset variation of traveltime shifts are insensitive to such differences in the reservoir shape.

References

Červený, V., 2001, Seismic ray theory: Cambridge University Press.

Chin, L. Y., and N. B. Nagel, 2004, Modeling of subsidence and reservoir compaction under waterflood operations: International Journal of Geomechanics, **4**, 28–34.

Downes, J. R., D. A. Faux, and E. P. O'Reilly, 1997, A simple method for calculating strain distributions in quantum dot structures: Journal of Applied Physics, **81**, 6700–6702.

Faux, D. A., J. R. Downes, and E. P. O'Reilly, 1997, Analytic solutions for strains distributions in quantum-wire structures: Journal of Applied Physics, **82**, 3754–3762.

Fuck, R. F., A. Bakulin, and I. Tsvankin, 2009, Theory of traveltime shifts around compacting reservoirs: 3D solutions for heterogeneous anisotropic media: Geophysics, **74**, D25–D36.

Fuck, R. F., and I. Tsvankin, 2009, Analysis of the symmetry of a stressed medium using nonlinear elasticity: Geophysics. In print.

Geertsma, J., 1973, Land subsidence above compacting oil and gas reservoirs: Journal of Petroleum Technology, **25**, 734–744.

Glas, F., 1991, Coherent stress relaxation in half space: modulated layers, inclusions, steps, and a general solution: Journal of Applied Physics, **70**, 3556–3571.

Guilbot, J., and B. Smith, 2002, 4D constrained depth conversion for reservoir compaction estimation: Application to Ekofisk field: The Leading Edge, **21**, 302–308.

Gutierrez, M. S., and R. W. Lewis, 2002, Coupling of fluid flow and deformation in underground formations: Journal of Engineering Mechanics, **128**, 779–787.

Hatchell, D. P. J., and S. J. Bourne, 2005a, Measuring reservoir compaction using time-lapse timeshifts: Annual International Meeting, Expanded Abstracts, 2500–2503.

Hatchell, P., and S. Bourne, 2005b, Rocks under strain: strain-induced time-lapse time-shifts are observed for depleting reservoirs: The Leading Edge, **24**, 1222–1225.

Herwanger, J., and S. Horne, 2005, Predicting time-lapse stress effects in seismic data: The Leading Edge, **24**, 1234–1242.

Hodgson, N., C. MacBeth, L. Duranti, J. Rickett, and K. Nihei, 2007, Inverting for reservoir pressure change using time-lapse time strain: application to Genesis field, Gulf of Mexico: The Leading Edge, **26**, 649–652.

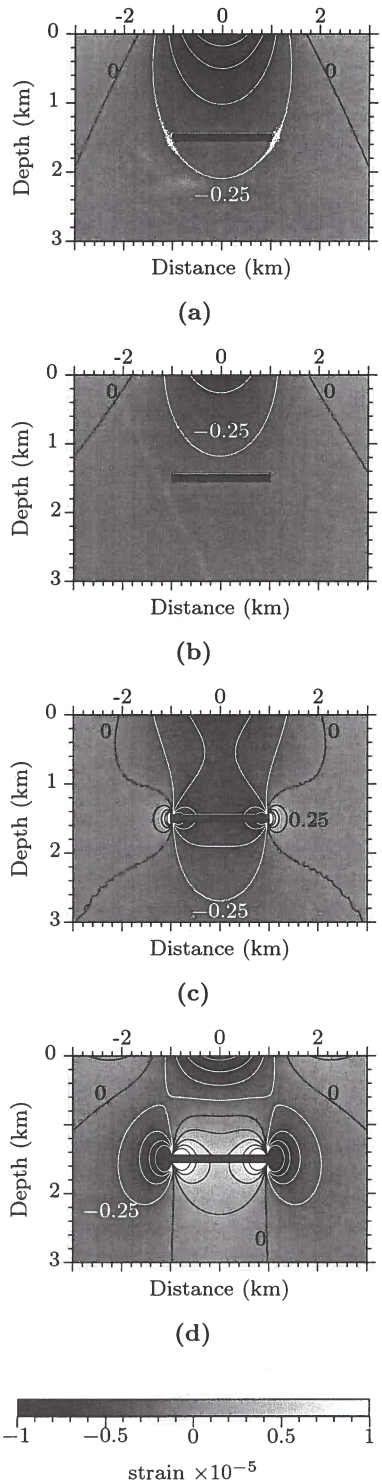

Figure 2. Compaction-related volumetric strain Δe_{kk} for models with different elastic contrast between the reservoir and host rock. (a) No elastic contrast across the reservoir boundaries; b) the velocity V_P is 25% higher outside the reservoir; c) the velocity V_S is 20% lower outside the reservoir; d) V_S is 20% higher outside the reservoir. Negative values are contoured in white, zero and positive values are in black. The contour step is 0.25 $\times 10^{-5}$.

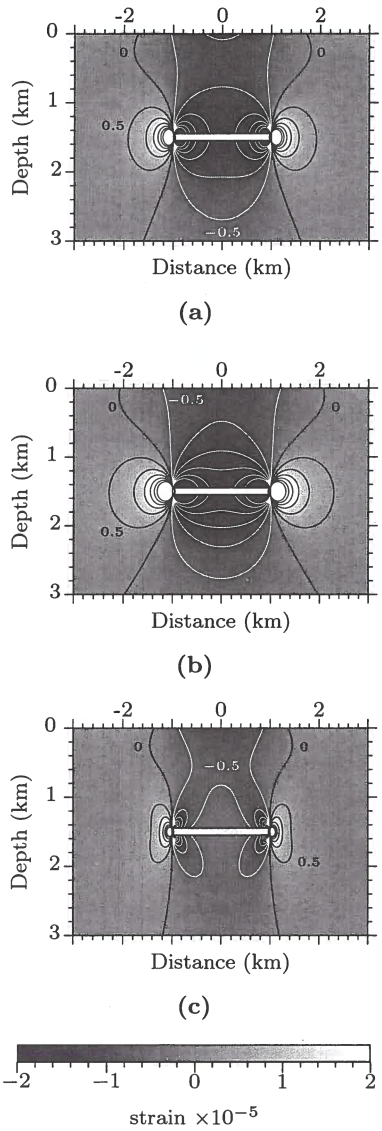

Figure 3. Influence of the contrast in the rigidity modulus μ on the compaction-related horizontal deviatoric strain Δe_{11}. (a) No elastic contrast across the reservoir boundaries; b) the velocity V_S is 20% lower outside the reservoir; d) V_S is 20% higher outside the reservoir. The contrast in V_S is equivalent to the contrast in μ because the density is held constant. The contour step is 0.5 $\times 10^{-5}$.

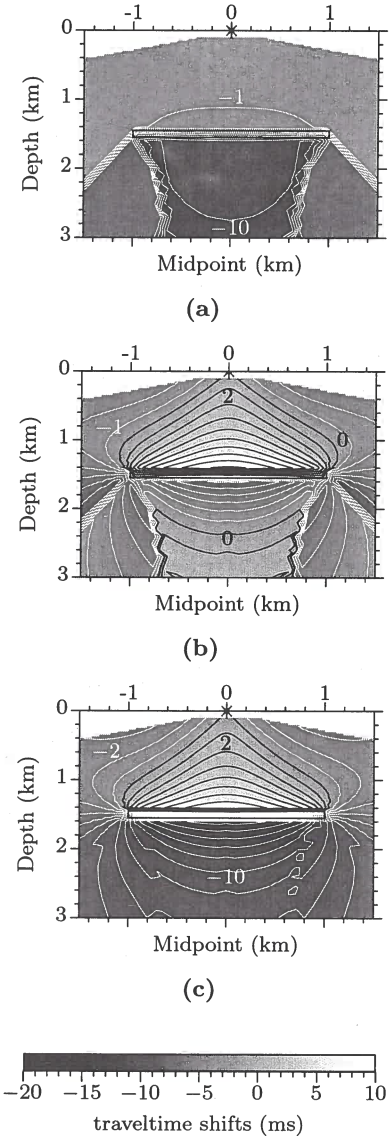

Figure 6. Approximate traveltime shifts for a shot above the center of the reservoir. The background velocity V_S is 20% smaller outside the reservoir. Traveltime shifts caused by the a) isotropic and b) anisotropic velocity changes; c) the total shifts.

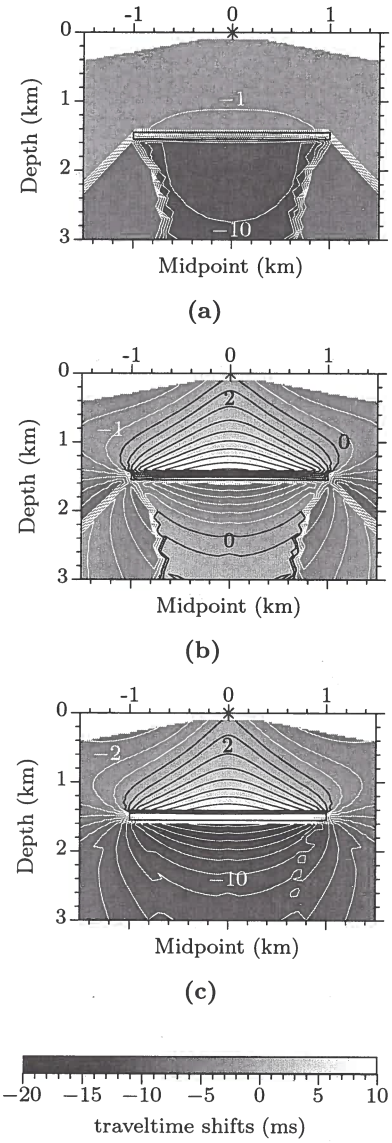

Figure 7. Approximate traveltime shifts for a shot above the center of the reservoir. The background velocity V_S is 20% smaller outside the reservoir. Traveltime shifts caused by the a) isotropic and b) anisotropic velocity changes; c) the total shifts.

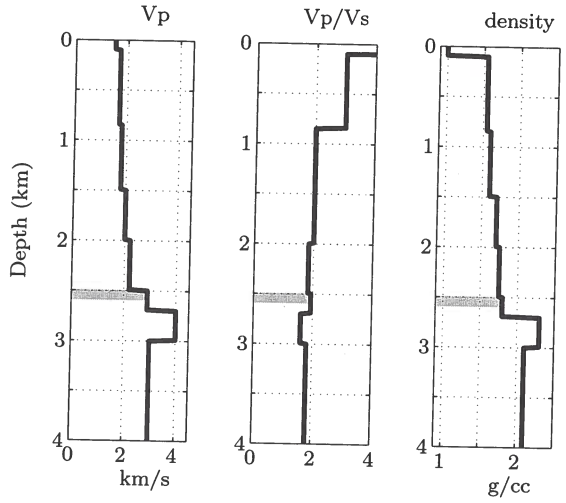

Figure 10. Velocity and density profiles adapted from published results for Valhall Field in the North Sea. The model is composed of eight homogeneous layers, and the rectangular reservoir (gray bar) is located inside layer 6. The ocean depth (i.e., the thickness of the first layer) is 100 m, with $C_{ijk} = V_S = 0$. For layers two through four, $C_{111} = -11300$ GPa, $C_{112} = -4800$ GPa, and $C_{123} = 5800$ GPa. For layers five through eight, $C_{111} = -3100$ GPa, $C_{112} = -800$ GPa, and $C_{123} = 40$ GPa.

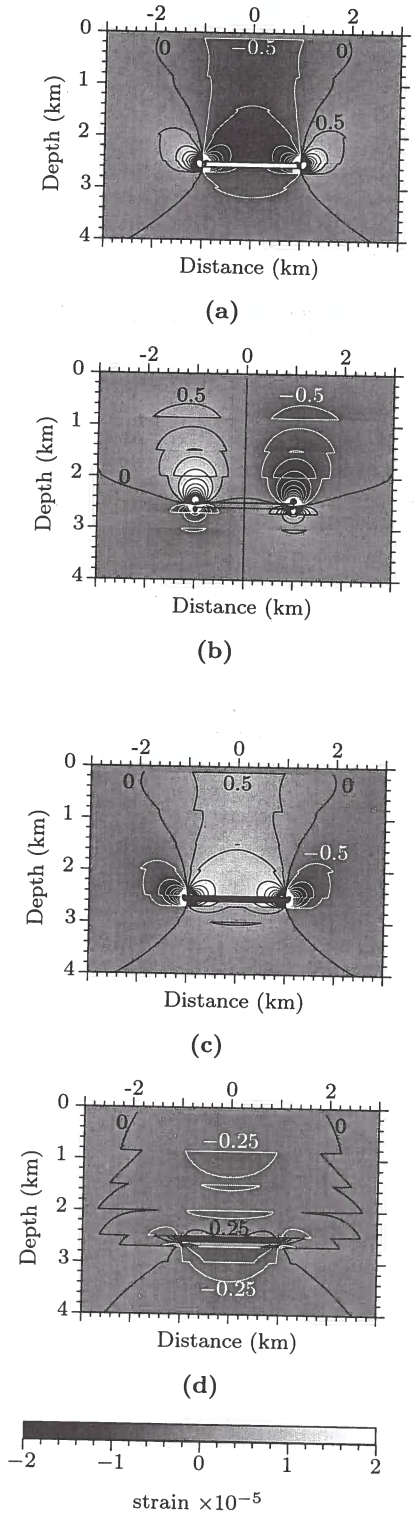

Figure 11. Deviatoric and volumetric strains caused by the pore-pressure drop $\Delta p = -2.5$ MPa inside the reservoir for the model from Figure 10. The deviatoric strains a) $\Delta\epsilon_{11}$; b) $\Delta\epsilon_{13}$; c) $\Delta\epsilon_{33}$; and d) the volumetric strain Δe_{kk}. Negative strain values are contoured in white, positive values in black. The contour step is 0.5×10^{-5} in (a), (b), and (c), and 0.25×10^{-5} in (d). The color scale is clipped for better contrast. At the center of the reservoir (0 km, 2.55 km), $\Delta\epsilon_{11} = 1.2 \times 10^{-4}$, $\Delta\epsilon_{33} = -2.5 \times 10^{-4}$, and $\Delta e_{kk} = -3.9 \times 10^{-4}$.

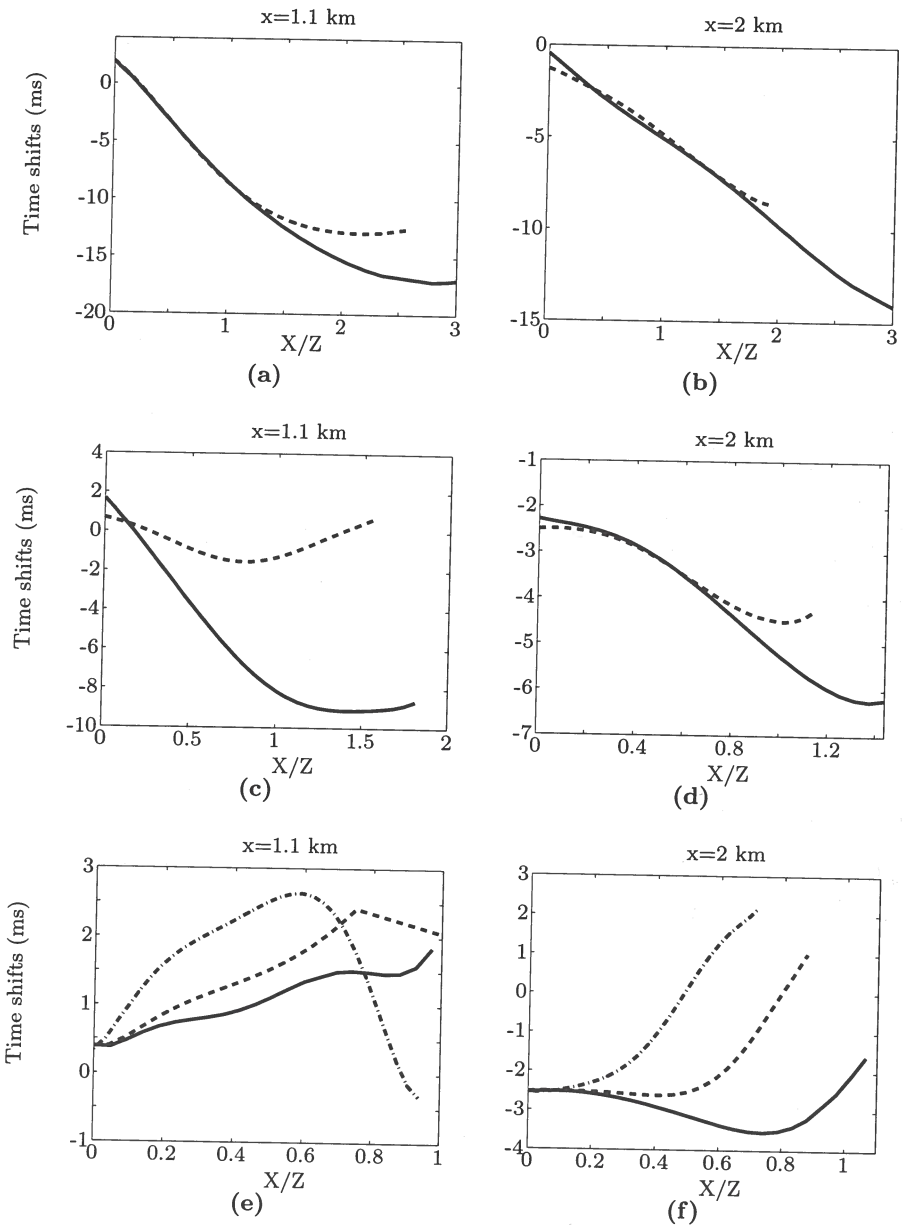

Figure 14. Ray-traced traveltime shifts for common midpoints located at $x = 1.1$ km (above the reservoir edge, left column) and at $x = 2$ km (right column). The reflector depth in a) and b) is 0.85 km (solid lines) and 1.5 km (dashed); in c) and d), the depth is 2 km (solid) and 2.5 km (dashed); and in e) and f) the depth is 2.7 km (solid), 3 km (dashed) and 4 km (dash-dotted).

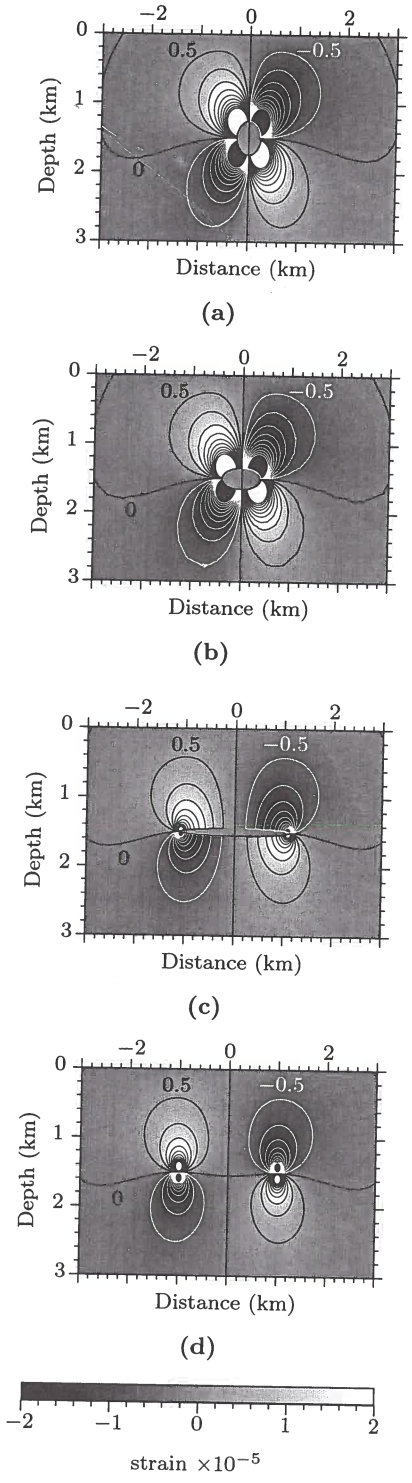

Figure 17. Shear strain $\Delta\varepsilon_{13}$ around compacting reservoirs of different shapes. The reservoir cross-section is a) circular; b) elliptical with the aspect ratio 1/4; c) elliptical with the aspect ratio 1/20; and d) rectangular with the aspect ratio 1/20; the area of the cross-sections is fixed. The model parameters are taken from Figure 1, with no elastic contrast between the reservoir and host rock (i.e., the background is homogeneous).

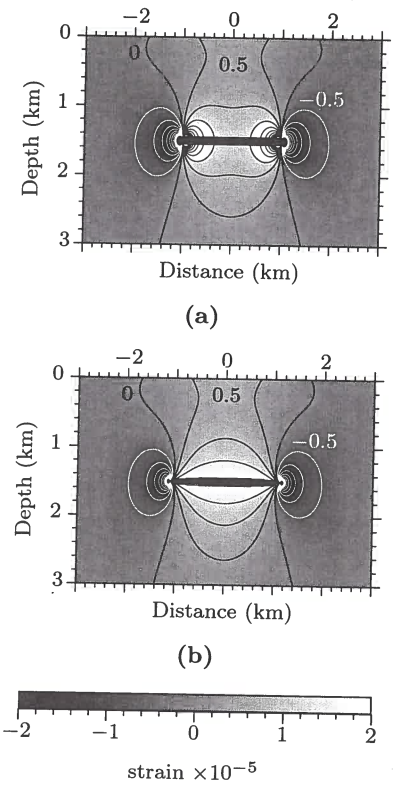

Figure 18. Vertical deviatoric strain $\Delta\varepsilon_{33}$ for reservoirs with a) rectangular; and b) elliptical cross-sections. The area of the cross-section and its aspect ratio (1/20) are the same. The model parameters are taken from Figure 1.

Analysis of the symmetry of a stressed medium using nonlinear elasticity

Rodrigo Felício Fuck & Ilya Tsvankin
Center for Wave Phenomena, Colorado School of Mines, Golden, CO 80401

ABSTRACT

Velocity variations caused by subsurface stress changes play an important role in monitoring compacting reservoirs and in several other applications of seismic methods. The most general way of describing stress-induced (or, equivalently, strain-induced) velocity fields is by employing the theory of nonlinear elasticity, which operates with third-order elastic (TOE) tensors. These sixth-rank strain-sensitivity tensors, however, are difficult to manipulate because of the large number of terms involved in the algebraic operations. Thus, even evaluation of the anisotropic symmetry of a medium under stress/strain proves to be a challenging task. Here, we employ a matrix representation of TOE tensors that allows computation of strain-related stiffness perturbations from a linear combination of 6×6 matrices scaled by the components of the strain tensor. In addition to streamlining the numerical algorithm, this approach helps to predict the strain-induced symmetry using relatively straightforward algebraic considerations. For example, our analysis shows that a transversely isotropic (TI) medium acquires orthorhombic symmetry if one of the principal directions of the strain tensor is aligned with the symmetry axis. Otherwise, the strained TI medium can become monoclinic or even triclinic.

Key words: anisotropic symmetry, nonlinear elasticity, stress-induced anisotropy, stiffness tensor, third-order elastic tensor, time-lapse seismic.

1 INTRODUCTION

Monitoring subsurface stress/strain fields and their time-lapse variations is an important research area with applications in velocity model-building (e.g., Sengupta and Bachrach, 2008) and reservoir geophysics (e.g., Fuck et al., 2009). For example, pore-pressure drop due to hydrocarbon production leads to reservoir compaction, which produces excess stress and strain not only in the reservoir itself, but also in the surrounding rock mass.

Seismic velocities can help to monitor subsurface stress and strain fields because numerous laboratory experiments have demonstrated that the stiffness tensor changes under stress/strain (Eberhart-Phillips et al., 1989; Prasad and Manghnani, 1997). In the elastic regime, stress stiffens grain contacts and closes fractures, making rocks more rigid and increasing P- and S-wave velocities. Therefore, some theoretical models describe the stress/strain sensitivity of seismic velocities through the stiffening of grain contacts (e.g., Gassman and Hertz-Mindlin models discussed in Mavko et al., 1998), while others relate the velocity variation to closing (or opening) of microcracks (e.g., Mavko et al., 1995; Sayers, 2006).

An alternative approach that has been successfully applied to this problem is based on the nonlinear theory of elasticity (e.g. Sinha and Kostek, 1996; Winkler et al., 1998; Sinha and Plona, 2001). In contrast to the Hertz-Mindlin theory, it employs a Taylor series expansion that yields the full elastic tensor of the strained medium (Thurston, 1974, p. 276). Unlike fracture-based models, nonlinear elasticity operates not with the fracture orientations and compliances, but with a third-order elastic (TOE) tensor responsible for the strain sensitivity of the rock mass.

We start by reviewing the nonlinear theory of elasticity and application of TOE tensors to model stress-

for all possible symmetry classes. Here, we use their results to construct the matrix representation for several symmetries relevant in the context of exploration geophysics. We proceed from the lowest possible symmetry (triclinic), which is characterized by the absence of any symmetry elements (i.e., symmetry axes or planes), to the isotropic tensor, which is invariant with respect to any coordinate transformation. A more detailed analysis of the matrices $C_{\alpha\beta\gamma}$ for various symmetry classes can be found in Appendix A.

3.1 Triclinic symmetry

Although the triclinic TOE tensor contains no symmetry elements, only 56 out of a total of $3^6 = 729$ elements are independent (equation 6). All six matrices that form the vector $C_{\alpha(\beta\gamma)}$ in equation ?? are symmetric because the indices β and γ can be interchanged:

$$C_{\alpha(\beta\gamma)} = \begin{pmatrix} C_{\alpha11} & C_{\alpha12} & C_{\alpha13} & C_{\alpha14} & C_{\alpha15} & C_{\alpha16} \\ C_{\alpha12} & C_{\alpha22} & C_{\alpha23} & C_{\alpha24} & C_{\alpha25} & C_{\alpha26} \\ C_{\alpha13} & C_{\alpha23} & C_{\alpha33} & C_{\alpha34} & C_{\alpha35} & C_{\alpha36} \\ C_{\alpha14} & C_{\alpha24} & C_{\alpha34} & C_{\alpha44} & C_{\alpha45} & C_{\alpha46} \\ C_{\alpha15} & C_{\alpha25} & C_{\alpha35} & C_{\alpha45} & C_{\alpha55} & C_{\alpha56} \\ C_{\alpha16} & C_{\alpha26} & C_{\alpha36} & C_{\alpha46} & C_{\alpha56} & C_{\alpha66} \end{pmatrix}; \tag{7}$$

$\alpha = 1, 2 \ldots, 6$.

3.2 Monoclinic symmetry

The matrix representation of monoclinic TOE tensors can be derived from equation 7 by defining either a plane of mirror symmetry or a 2-fold symmetry axis (Winterstein, 1990).† The independent elements $C_{\alpha\beta\gamma}$ are invariant with respect to rotation by $\theta = \pi$ around the symmetry axis; the same set of independent $C_{\alpha\beta\gamma}$ can be obtained by using a symmetry plane perpendicular to this axis. If the horizontal plane $[x_1, x_2]$ is the plane of symmetry, the monoclinic TOE matrices for $\alpha = 1$, 2, 3, and 6 have the following form (Appendix A):

$$C_{\alpha(\beta\gamma)} = \begin{pmatrix} C_{\alpha11} & C_{\alpha12} & C_{\alpha13} & 0 & 0 & C_{\alpha16} \\ C_{\alpha12} & C_{\alpha22} & C_{\alpha23} & 0 & 0 & C_{\alpha26} \\ C_{\alpha13} & C_{\alpha23} & C_{\alpha33} & 0 & 0 & C_{\alpha36} \\ 0 & 0 & 0 & C_{\alpha44} & C_{\alpha45} & 0 \\ 0 & 0 & 0 & C_{\alpha45} & C_{\alpha55} & 0 \\ C_{\alpha16} & C_{\alpha26} & C_{\alpha36} & 0 & 0 & C_{\alpha66} \end{pmatrix}. \tag{8}$$

†A direction is called a k-fold symmetry axis when a tensor is invariant with respect to rotations by $\theta = 2\pi/k$ around it (Helbig, 1994).

When $\alpha = 4$ or 5,

$$C_{\alpha(\beta\gamma)} = \begin{pmatrix} 0 & 0 & 0 & C_{\alpha14} & C_{\alpha15} & 0 \\ 0 & 0 & 0 & C_{\alpha24} & C_{\alpha25} & 0 \\ 0 & 0 & 0 & C_{\alpha34} & C_{\alpha35} & 0 \\ C_{\alpha14} & C_{\alpha24} & C_{\alpha34} & 0 & 0 & C_{\alpha46} \\ C_{\alpha15} & C_{\alpha25} & C_{\alpha35} & 0 & 0 & C_{\alpha56} \\ 0 & 0 & 0 & C_{\alpha46} & C_{\alpha56} & 0 \end{pmatrix}. \tag{9}$$

Interestingly, the matrices described by equation 8 have the same structure (i.e., the same nonzero elements) as the matrix representing the monoclinic SOE tensor (e.g., Helbig, 1994). The matrices in equation 9, however, contain nonzero elements in place of the vanishing elements in equation 8. According to equations 8 and 9, the total number of independent elements $C_{\alpha\beta\gamma}$ for monoclinic symmetry is 32.

3.3 Orthorhombic symmetry

Orthorhombic symmetry is characterized by three orthogonal 2-fold symmetry axes, or, correspondingly, by three orthogonal mirror symmetry planes (Helbig, 1994). Because orthorhombic symmetry is a special case of the monoclinic model, the matrix representation of the orthorhombic TOE tensor can be obtained from equations 8 and 9 by requiring invariance with respect to rotations by $\theta = \pi$ around the x_1- and x_2-axes. These constraints reduce the number of independent elements to 20, and, when $\alpha = 1$, 2, and 3, the orthorhombic matrices $C_{\alpha\beta\gamma}$ can be written as (see Appendix A)

$$C_{\alpha(\beta\gamma)} = \begin{pmatrix} C_{\alpha11} & C_{\alpha12} & C_{\alpha13} & 0 & 0 & 0 \\ C_{\alpha12} & C_{\alpha22} & C_{\alpha23} & 0 & 0 & 0 \\ C_{\alpha13} & C_{\alpha23} & C_{\alpha33} & 0 & 0 & 0 \\ 0 & 0 & 0 & C_{\alpha44} & 0 & 0 \\ 0 & 0 & 0 & 0 & C_{\alpha55} & 0 \\ 0 & 0 & 0 & 0 & 0 & C_{\alpha66} \end{pmatrix}. \tag{10}$$

For $\alpha = 4$, 5, and 6,

$$C_{4(\beta\gamma)} = \begin{pmatrix} 0 & 0 & 0 & C_{144} & 0 & 0 \\ 0 & 0 & 0 & C_{244} & 0 & 0 \\ 0 & 0 & 0 & C_{344} & 0 & 0 \\ C_{144} & C_{244} & C_{344} & 0 & 0 & 0 \\ 0 & 0 & 0 & 0 & 0 & C_{456} \\ 0 & 0 & 0 & 0 & C_{456} & 0 \end{pmatrix}, \tag{11}$$

$$C_{5(\beta\gamma)} = \begin{pmatrix} 0 & 0 & 0 & 0 & C_{155} & 0 \\ 0 & 0 & 0 & 0 & C_{255} & 0 \\ 0 & 0 & 0 & 0 & C_{355} & 0 \\ 0 & 0 & 0 & 0 & 0 & C_{456} \\ C_{155} & C_{255} & C_{355} & 0 & 0 & 0 \\ 0 & 0 & 0 & C_{456} & 0 & 0 \end{pmatrix}, \tag{12}$$

and

$$C_{4(\beta\gamma)} = \begin{pmatrix} 0 & 0 & 0 & C_{144} & 0 & 0 \\ 0 & 0 & 0 & C_{155} & 0 & 0 \\ 0 & 0 & 0 & C_{155} & 0 & 0 \\ C_{144} & C_{155} & C_{155} & 0 & 0 & 0 \\ 0 & 0 & 0 & 0 & 0 & C_{456} \\ 0 & 0 & 0 & 0 & C_{456} & 0 \end{pmatrix}, \tag{28}$$

where (Thurston and Brugger, 1964)

$$C_{111} = C_{123} + 6C_{144} + 8C_{456}\,, \tag{29}$$
$$C_{112} = C_{123} + 2C_{144}\,, \tag{30}$$
$$C_{155} = C_{144} + 2C_{456}\,. \tag{31}$$

The remaining matrices can be obtained from the following permutations:

$$C_{2(\beta\gamma)} = \mathcal{R}_1 C_{1(\beta\gamma)} \mathcal{R}_1\,, \quad C_{3(\beta\gamma)} = \mathcal{R}_2 C_{1(\beta\gamma)} \mathcal{R}_2\,, \tag{32}$$
$$C_{5(\beta\gamma)} = \mathcal{R}_1 C_{4(\beta\gamma)} \mathcal{R}_1\,, \quad C_{6(\beta\gamma)} = \mathcal{R}_2 C_{4(\beta\gamma)} \mathcal{R}_2\,. \tag{33}$$

The matrix $\mathcal{R}_2$ has the same block structure as $\mathcal{R}_1$ from equation 25, but with P_1 substituted by P_2, a matrix that interchanges the first and third rows or columns of 3×3 matrices:

$$P_2 = \begin{pmatrix} 0 & 0 & 1 \\ 0 & 1 & 0 \\ 1 & 0 & 0 \end{pmatrix}. \tag{34}$$

4 SYMMETRY OF THE DEFORMED MEDIUM

The matrix representation of the TOE tensor helps to devise an algebraic procedure to evaluate the symmetry of a medium under stress/strain. Using Voigt notation, equation 3 can be expressed in terms of the TOE matrix $C_{\alpha\beta\gamma}$:

$$C_{\beta\gamma} = C^{\circ}_{\beta\gamma} + C_{\alpha\beta\gamma}\, \Delta E_\alpha\,, \tag{35}$$

where the vector $\Delta E_\alpha = (e_{11}, e_{22}, e_{33}, 2e_{23}, 2e_{13}, 2e_{12})^{\mathsf{T}}$ is obtained from the symmetric strain tensor Δe_{mn} by applying Voigt notation. Hereafter, the strain tensor with vanishing off-diagonal components ΔE_4, ΔE_5 and ΔE_6 will be called *diagonal*. If the elements ΔE_1, ΔE_2 and ΔE_3 of a diagonal strain tensor are equal, such a tensor represents *volumetric strain change* (Fuck et al., 2009).

Each perturbation stiffness element $\Delta C_{\beta\gamma} = C_{\alpha\beta\gamma}\, \Delta E_\alpha$ in equation 35 is obtained as a linear combination of the $C_{\alpha(\beta\gamma)}$ matrices scaled by the components of the vector ΔE_α. Due to the significant difference in the structure of the matrices $C_{\alpha(\beta\gamma)}$ for $\alpha = 1, 2, 3$ and $\alpha = 4, 5, 6$, it is possible to separate the contributions of the normal (diagonal) and shear (off-diagonal) strain components in equation 35. Next, we analyze the symmetry of the perturbation matrix $\Delta C_{\alpha\beta}$ using the results of the previous section. The structure of the resulting stiffness matrix $C_{\beta\gamma}$ is defined by the stiffnesses of the undeformed medium and the nonzero elements of $\Delta C_{\beta\gamma}$.

4.1 Isotropic TOE tensor

When the TOE tensor is isotropic, the symmetry of the matrix $\Delta C_{\alpha\beta}$ is entirely controlled by the structure of the strain tensor. This can be proved by substituting the matrix representation of the isotropic TOE tensor into equation 35.

For a volumetric strain change ($\Delta E_1 = \Delta E_2 = \Delta E_3$; $\Delta E_4 = \Delta E_5 = \Delta E_6 = 0$), the term $C_{\alpha\beta\gamma}\, \Delta E_\alpha$ reduces to the sum of the matrix $C_{1(\beta\gamma)}$ from equation 27 and its two permutations, $C_{2(\beta\gamma)}$ and $C_{3(\beta\gamma)}$, multiplied by the normal strain ΔE_1. The resulting tensor $\Delta C_{\alpha\beta}$ is isotropic:

$$\Delta C_{11} = \Delta C_{22} = \Delta C_{33} = (C_{111} + 2C_{112})\, \Delta E_1\,, \tag{36}$$
$$\Delta C_{44} = \Delta C_{55} = \Delta C_{66} = (C_{144} + 2C_{155})\, \Delta E_1\,, \tag{37}$$
$$\Delta C_{12} = \Delta C_{13} = \Delta C_{23} = \Delta C_{11} - 2\Delta C_{44} = (C_{123} + 2C_{111})\, \Delta E_1\,. \tag{38}$$

This confirms our expectation that any object undergoing volumetric change will remain just a scaled version of itself by conserving its original shape or symmetry.

If the applied strain is uniaxial, then the stiffness perturbation from equation 35 is transversely isotropic (TI). For example, the vertical strain ΔE_3 yields the tensor $\Delta C_{\alpha\beta}$ with VTI symmetry:

$$\Delta C_{11} = \Delta C_{22} = C_{112}\, \Delta E_3\,; \tag{39}$$
$$\Delta C_{33} = C_{111}\, \Delta E_3\,; \tag{40}$$
$$\Delta C_{44} = \Delta C_{55} = C_{155}\, \Delta E_3\,; \tag{41}$$
$$\Delta C_{66} = C_{144}\, \Delta E_3\,; \tag{42}$$
$$\Delta C_{12} = \Delta C_{11} - 2\Delta C_{66} = C_{123}\, \Delta E_3\,; \tag{43}$$
$$\Delta C_{13} = \Delta C_{23} = C_{112}\, \Delta E_3\,. \tag{44}$$

When the strain tensor is diagonal, each matrix $C_{\alpha(\beta\gamma)}$ ($\alpha = 1, 2, 3$) is multiplied with a different normal strain component, which results in the stiffness perturbation that has orthorhombic symmetry:

$$\Delta C_{\alpha\beta} = \begin{pmatrix} \Delta C_{11} & \Delta C_{12} & \Delta C_{13} & 0 & 0 & 0 \\ \Delta C_{12} & \Delta C_{22} & \Delta C_{23} & 0 & 0 & 0 \\ \Delta C_{13} & \Delta C_{23} & \Delta C_{33} & 0 & 0 & 0 \\ 0 & 0 & 0 & \Delta C_{44} & 0 & 0 \\ 0 & 0 & 0 & 0 & \Delta C_{55} & 0 \\ 0 & 0 & 0 & 0 & 0 & \Delta C_{66} \end{pmatrix}. \tag{45}$$

Furthermore, if the TOE tensor is isotropic, the symmetry of $\Delta C_{\alpha\beta}$ is always orthorhombic or higher, with the principal directions of the strain tensor defining the 2-fold symmetry axes of the deformed medium.

ing perturbation tensor is triclinic. Likewise, for a monoclinic TOE tensor, any shear strain not defined in the symmetry plane (i.e., in the plane perpendicular to the 2-fold symmetry axis) produces a triclinic perturbation $\Delta C_{\alpha\beta}$. Therefore, misalignment of the principal strain directions with the symmetry elements of the TOE tensor lowers the symmetry of $\Delta C_{\alpha\beta}$.

Finally, if the TOE tensor is triclinic (i.e., with no symmetry axes or planes), the stiffness perturbation always has triclinic symmetry as well, regardless of the structure of the strain tensor.

4.4 Symmetry of the resulting stiffness tensor

The above discussion was focused on the symmetry of the perturbation stiffness matrix $\Delta C_{\beta\gamma} = C_{\alpha\beta\gamma}\,\Delta E_\alpha$ in equation 35. Once this matrix has been obtained, it is straightforward to evaluate the symmetry of the effective elastic tensor $C_{\alpha\beta}$ which describes the medium after deformation. In principle, the symmetry of the strained medium should not be higher than that of either $C^\circ_{\alpha\beta}$ or $\Delta C_{\alpha\beta}$. There might be situations, however, in which some of the off-diagonal terms in $C^\circ_{\alpha\beta}$ and $\Delta C_{\alpha\beta}$ cancel out, resulting in the deformed medium with a higher symmetry than those of the background model and the stiffness perturbation. Although this issue should be studied further, such strain-induced compensation of intrinsic anisotropy seems unlikely.

5 CONCLUSIONS

Using the theory of nonlinear elasticity based on third-order elastic (TOE) tensors, we analyzed the symmetry of a medium under stress/strain. Application of Voigt notation leads to a convenient representation of the TOE tensor c_{ijklmn} in terms of a $6 \times 6 \times 6$ matrix $C_{\alpha\beta\gamma}$. The strain-induced stiffness perturbation $\Delta C_{\beta\gamma}$ is then obtained by summing 6×6 TOE submatrices scaled by the components of the strain tensor. This formalism provides a direct way to assess the contribution of each strain component to the stiffness perturbation for a given symmetry of the TOE tensor. In particular, our approach helps to separate the influence of the normal and shear strains on the symmetry of the perturbed medium.

In the simplest case of a purely isotropic TOE tensor, the perturbation $\Delta C_{\beta\gamma}$ always has orthorhombic or higher symmetry with the the 2-fold symmetry axes defined by the principal directions of the strain tensor. When the strain is uniaxial, the stiffness perturbation is transversely isotropic, and the symmetry axis is parallel to the strain direction. The deformed medium remains isotropic only if an isotropic TOE tensor is combined with volumetric strain (i.e., the strain tensor has only identical diagonal elements).

When the TOE tensor is hexagonal (transversely isotropic), a uniaxial strain applied in the direction of the symmetry axis conserves TI symmetry. If the strain tensor is diagonal or a uniaxial strain is confined to the plane orthogonal to the symmetry axis, the stiffness perturbation becomes orthorhombic. The influence of the off-diagonal (shear) strains may lower the symmetry of $\Delta C_{\beta\gamma}$ to monoclinic or even triclinic.

On the whole, our algebraic procedure significantly facilitates application of TOE tensors to analysis of strain-induced velocity perturbations. The formalism introduced here is as intuitive as that describing the strain sensitivity of seismic velocities through closing or opening of microcracks. Our results should be helpful in modeling and inversion of anisotropic velocity fields caused by excess strains/stresses near salt bodies and compacting hydrocarbon reservoirs.

6 ACKNOWLEDGMENTS

We are grateful to our colleagues in the Center for Wave Phenomena (CWP) at Colorado School of Mines (CSM) for helpful discussions. The constructive suggestions of the reviewers of *Geophysics* helped to improve the paper. This work was supported by the Consortium Project on Seismic Inverse Methods for Complex Structures at CWP.

References

Barsch, G. R., and Z. Chang, 1968, Second- and higher-order effective elastic constants of cubic crystals under hydrostatic pressure: Journal of Applied Physics, **39**, 3276–3284.

Eberhart-Phillips, D., D.-H. Han, and M. D. Zoback, 1989, Empirical relations among seismic velocity, effective pressure, porosity and clay content in sandstone: Geophysics, **54**, 82–89.

Fuck, R. F., A. Bakulin, and I. Tsvankin, 2009, Theory of traveltime shifts around compacting reservoirs: 3D solutions for heterogeneous anisotropic media: Geophysics, **74**, D25–D36.

Fumi, F. G., 1951, Third-orer elastic coefficients of crystals: Physical Review, **83**, 1274–1275.

——— 1952, Third-order elastic coefficients in trigonal and hexagonal crystals: Physical Review, **86**, 561.

Goldstein, H., 1980, Classical mechanics: Addison-Wesley, 2nd ed. edition.

Hearmon, R. F. S., 1953, Third-order elastic coefficients: Acta Crystallographica, **6**, 331–340.

Helbig, K., 1994, Foundations of anisotropy for exploration seismics: Pergamon.

Johnson, P. A., and P. N. J. Rasolofosaon, 1996, Nonlinear elasticity and stress-induced anisotropy in rock: Journal of Geophysical Research, **101**, 3113–3124.

Mavko, G., T. Mukerji, and J. Dvorkin, 1998, The rock physics handbook, tools for seismic analysis in

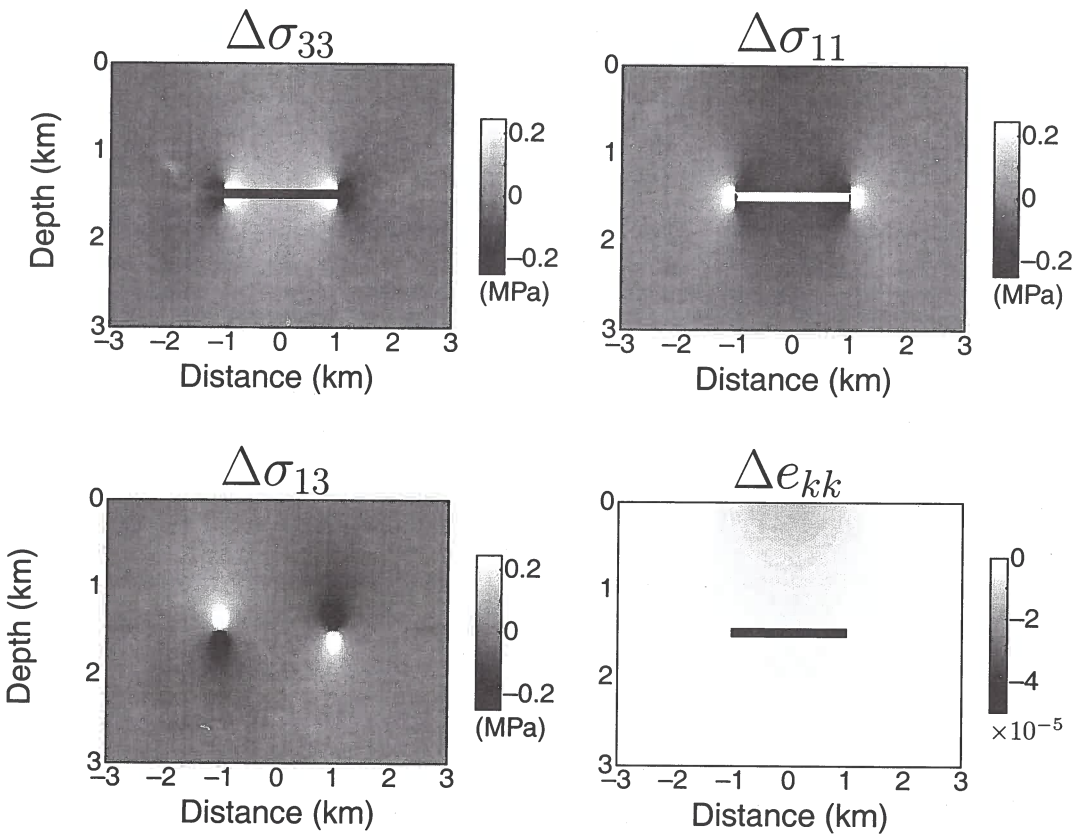

Figure 1. 2D stress and strain changes due to a 5 MPa drop in pore pressure inside a compacting rectangular reservoir (after Fuck et al., 2009). $\Delta\sigma_{33}$ and $\Delta\sigma_{11}$ are the normal deviatoric stresses, $\Delta\sigma_{13}$ is the shear deviatoric stress, and Δe_{kk} is the trace of the strain tensor. Negative values imply compression for stress and contraction (shortening) for strain. Inside the reservoir the maximum stresses are $\Delta\sigma_{33} = -2.2$ MPa and $\Delta\sigma_{11}$=1.7 MPa, while the volumetric change is constant: $\Delta e_{kk} = -4.6 \times 10^{-4}$. The plots were clipped for better visualization.

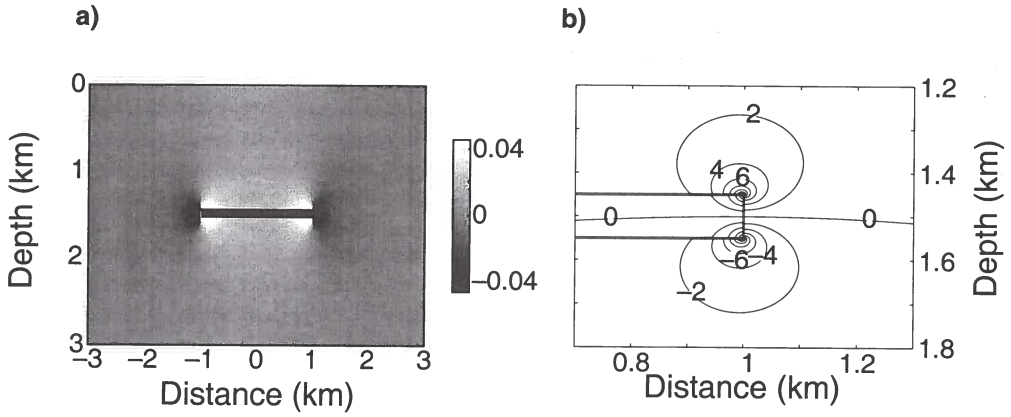

Figure 2. Anisotropy parameters and the symmetry-axis orientation of the strain-induced TI medium for the reservoir model from Figure 1 (after Fuck et al., 2009). a) The anisotropy parameter $\delta = \epsilon$ (color scale is clipped); b) contours of the angle between the symmetry axis and the vertical (positive angles correspond to clockwise axis rotation) near the right edge of the reservoir (gray rectangle). Inside the reservoir $\delta = -0.18$, while the tilt of the symmetry axis at the reservoir corners (where the shear strains become infinite) approaches $\pm 45°$ (for more details, see Fuck et al., 2009).

A5 Isotropy

A simple way of making the TOE tensor isotropic is to require that the 10 independent elements of the hexagonal tensor remain unchanged for arbitrary rotation around any axis. For example, c_{ijklmn} should stay the same when we interchange any two indices. Hence,

$$C_{111} = C_{222} = C_{333}; \tag{A7}$$

$$C_{112} = C_{133} = C_{223} = C_{113} = C_{122} = C_{233}; \tag{A8}$$

$$C_{144} = C_{255} = C_{366}; \tag{A9}$$

$$C_{155} = C_{266} = C_{344} = C_{166} = C_{244} = C_{355}; \tag{A10}$$

Taking into consideration the constraints in equations 14–22, the identities in equations A7–A10 also imply that

$$C_{112} = C_{123} + 2C_{144}\,, \tag{A11}$$

$$C_{111} = C_{123} + 6C_{144} + 8C_{456}\,. \tag{A12}$$

Therefore, the isotropic TOE tensor is completely defined by three independent constants (C_{123}, C_{144} and C_{456}), as shown in several publications (e.g. Barsch and Chang, 1968). The matrix representation of the isotropic TOE tensor is given in equations 27–33.

Role of the inhomogeneity angle in anisotropic attenuation analysis

Jyoti Behura & Ilya Tsvankin
Center for Wave Phenomena, Geophysics Department, Colorado School of Mines, Golden, Colorado 80401

ABSTRACT

The inhomogeneity angle (the angle between the real and imaginary parts of the wave vector) is seldom taken into account in estimating attenuation coefficients from seismic data. Wave propagation through the subsurface, however, can result in relatively large inhomogeneity angles ξ, especially for models with significant attenuation contrasts across layer boundaries. Here, we study the influence of the angle ξ on phase and group attenuation in arbitrarily anisotropic media using the first-order perturbation theory verified by exact numerical modeling.

Application of the spectral-ratio method to transmitted or reflected waves yields the normalized group attenuation coefficient $\mathcal{A}_g$, which is responsible for the amplitude decay along seismic rays. Our analytic solutions show that for a wide range of inhomogeneity angles the coefficient $\mathcal{A}_g$ is close to the normalized *phase* attenuation coefficient $\mathcal{A}$ computed for $\xi = 0^\circ$ ($\mathcal{A}|_{\xi=0^\circ}$). The coefficient $\mathcal{A}|_{\xi=0^\circ}$ can be inverted directly for the attenuation-anisotropy parameters, so no knowledge of the inhomogeneity angle is required for attenuation analysis of seismic data. This conclusion remains valid even for uncommonly high attenuation with the quality factor Q less than 10 and strong velocity and attenuation anisotropy. However, the relationship between the group and phase attenuation coefficients becomes more complicated for relatively large inhomogeneity angles approaching so-called "forbidden directions." We also demonstrate that the velocity function remains practically independent of attenuation for a wide range of small and moderate angles ξ.

In principle, estimation of the attenuation-anisotropy parameters from the coefficient $\mathcal{A}|_{\xi=0^\circ}$ requires computation of the phase angle, which depends on the anisotropic velocity field. For moderately anisotropic models, however, the difference between the phase and group directions should not significantly distort the results of attenuation analysis.

Introduction

In attenuative media, the direction of maximum attenuation of a plane wave can differ from the propagation direction. This implies that the real part of the wave vector $\mathbf{k}^R$ ("propagation vector") deviates from the imaginary part $\mathbf{k}^I$ ("attenuation vector"), as illustrated in Figure 1. The angle between the vectors $\mathbf{k}^R$ and $\mathbf{k}^I$ is called the "inhomogeneity angle," denoted here by ξ. When $\xi = 0^\circ$, the plane wave is often characterized as "homogeneous;" when $\xi \neq 0^\circ$, it is called "inhomogeneous." For plane-wave propagation, ξ represents a free parameter except for certain "forbidden directions" (Krebes & Le, 1994; Carcione & Cavallini, 1995; Červený & Pšenčík, 2005a,b) where solutions of the wave equation do not exist. If the wavefield is excited by a point source, the inhomogeneity angle is determined by the medium properties including the boundary conditions (Zhu, 2006; Vavryčuk, 2007).

Alternatively, the wave vector in attenuative media can be parameterized in terms of the "inhomogeneity parameter" D (Boulanger & Hayes, 1993; Declercq *et al.*, 2005; Červený & Pšenčík, 2005a):

$$\mathbf{k} = \omega(\sigma\mathbf{n} + iD\mathbf{m})\,, \tag{1}$$

such that

$$\mathbf{m}\cdot\mathbf{n} = 0\,, \tag{2}$$

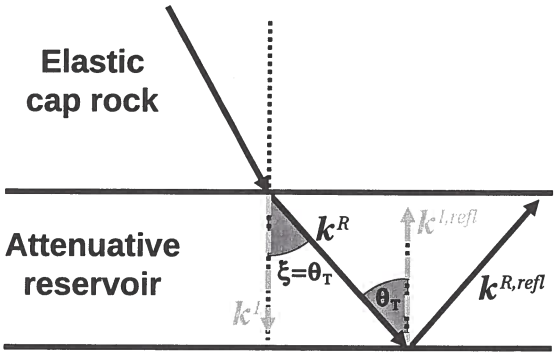

Figure 2. Illustration of the reflection/transmission problem at the interface between a purely elastic cap rock and an attenuative reservoir. $\mathbf{k}^R$ and $\mathbf{k}^I$ are the real and imaginary parts of the wave vector of the transmitted wave, while $\mathbf{k}^{R,refl}$ and $\mathbf{k}^{I,refl}$ correspond to the reflected wave. As discussed in the text, the inhomogeneity angle ξ of the transmitted wave is equal to the transmission angle θ_T.

tion is measured along the raypath, which deviates from the phase direction $\mathbf{k}^R$ when the medium is anisotropic.

Attenuation is commonly computed from seismic data using the spectral-ratio method (e.g., Johnston & Toksöz, 1981; Tonn, 1991), which has been extended to anisotropic media (Zhu *et al.*, 2007). If two receivers record the same event at two different locations along a raypath, the attenuation coefficient can be estimated from the ratio S of the measured amplitude spectra:

$$\ln S = \ln \mathcal{G} - k_g^I \, l, \tag{4}$$

where $\mathcal{G}$ contains the reflection/transmission coefficients, source/receiver radiation patterns, and geometrical spreading along the raypath, k_g^I is the average group attenuation coefficient, and l is the distance between the two receivers. Assuming that the medium between the receivers is homogeneous, equation 4 can be rewritten in terms of the group velocity V_g and traveltime t:

$$\ln S = \ln \mathcal{G} - k_g^I \, V_g \, t,$$

$$= \ln \mathcal{G} - \omega \, \mathcal{A}_g \, t, \tag{5}$$

where ω is the angular frequency and $\mathcal{A}_g = k_g^I / k_g^R = k_g^I / (\omega / V_g)$ is the normalized group attenuation coefficient. It follows from equation 5 that by estimating the slope of $\ln S$ expressed as a function of ω, we can compute the group attenuation along the raypath, if the traveltime t is known. Therefore, $\mathcal{A}_g$ is the measure of attenuation obtained from seismic data.

If the medium is anisotropic (or isotropic, but the inhomogeneity angle is large, as discussed below), the group-velocity vector $\mathbf{V}_g$ deviates from the phase direction parallel to $\mathbf{k}^R$. To simplify the analytic development, we choose a coordinate frame in which $\mathbf{k}^R$ coincides with the axis x_3 and $\mathbf{k}^I$ is confined to the $[x_1, x_3]$-plane (Figure 3). The group attenuation coefficient k_g^I can be found by projecting the phase attenuation vector $\mathbf{k}^I$ onto the group direction:

$$k_g^I = \frac{1}{V_g} \left(\mathbf{k}^I \cdot \mathbf{V}_g \right), \tag{6}$$

$$= k^I (\cos\xi \cos\psi + \sin\xi \sin\psi \cos\phi), \tag{7}$$

where ψ is the angle between $\mathbf{k}^R$ and $\mathbf{V}_g$ (group angle) and ϕ is the azimuth of $\mathbf{V}_g$ with respect to the $[x_1, x_3]$-plane (Figure 3). If the vectors $\mathbf{V}_g$, $\mathbf{k}^R$, and $\mathbf{k}^I$ lie in the same plane (i.e., $\phi = 0$), k_g^I is given by

$$k_g^I = k^I \cos(\xi - \psi). \tag{8}$$

Using equation 7, the normalized group attenuation coefficient $\mathcal{A}_g$ can be represented as

$$\mathcal{A}_g = \frac{k_g^I}{k_g^R} = \frac{k^I \cos\xi \cos\psi \, (1 + \tan\xi \tan\psi \cos\phi)}{\omega / V_g}. \tag{9}$$

The group velocity can be obtained from the well-known relation (e.g., Červený & Pšenčík, 2006):

$$\frac{1}{\omega} \mathbf{k}^R \cdot \mathbf{V}_g = 1, \tag{10}$$

or

$$\frac{\omega}{V_g} = k^R \cos\psi. \tag{11}$$

Substituting equation 11 into equation 9 yields

$$\mathcal{A}_g = \frac{k^I}{k^R} \cos\xi \, (1 + \tan\xi \tan\psi \cos\phi). \tag{12}$$

Equation 12 can be used to compute the exact coefficient $\mathcal{A}_g$ for arbitrarily anisotropic, attenuative media and any angle ξ. If the group-velocity vector is confined to the plane formed by $\mathbf{k}^R$ and $\mathbf{k}^I$ (see above), $\cos\phi = 1$ and equation 12 becomes

$$\mathcal{A}_g = \frac{k^I}{k^R} \frac{\cos(\xi - \psi)}{\cos\psi}. \tag{13}$$

For a zero inhomogeneity angle, the coefficient $\mathcal{A}_g$ reduces to

$$\mathcal{A}_g(\xi = 0^\circ) = \left. \frac{k^I}{k^R} \right|_{\xi = 0^\circ} = \mathcal{A}|_{\xi = 0^\circ}. \tag{14}$$

Equation 14 demonstrates that even for arbitrary anisotropy, the group attenuation coefficient coincides with the phase attenuation coefficient for $\xi = 0^\circ$ (Zhu, 2006). It is unclear, however, how $\mathcal{A}_g$ is related to phase attenuation for a nonzero ξ and what role is played by the inhomogeneity angle in the estimation of the attenuation coefficient.

2 ISOTROPIC MEDIA

To evaluate the influence of the inhomogeneity angle on velocity and attenuation in isotropic media, we obtain the real and imaginary parts of the vector $\mathbf{k}$ from the

$$k^I = \frac{\omega}{V\sqrt{2Q\cos\xi}}\left(1 - \frac{Q\cos\xi}{2}\right). \tag{24}$$

Dropping quadratic and higher-order terms in $Q\cos\xi$, we find

$$\mathcal{A} = \frac{k^I}{k^R} = 1 - Q\cos\xi. \tag{25}$$

The velocity of wave propagation, determined by the denominator of the expression for k^R (equation 23), is proportional to $\sqrt{Q\cos\xi}$ and goes to zero when the inhomogeneity angle approaches 90°.

When $\xi \to 90°$, the influence of the inhomogeneity angle on the group quantities ψ, V_g, and $\mathcal{A}_g$ is no longer negligible. The group angle for large inhomogeneity angles becomes (Appendix A)

$$\tan\psi = \frac{1}{Q} - \cos\xi. \tag{26}$$

Equation 26 demonstrates that for strong attenuation (small Q) the group-velocity vector deviates from the phase direction.

The coefficient $\mathcal{A}_g$ for large angles ξ can be obtained by substituting equations 25 and 26 into equation 12:

$$\mathcal{A}_g = (1 - Q\cos\xi)\left[\cos\xi + \left(\frac{1}{Q} - \cos\xi\right)\sin\xi\right]. \tag{27}$$

Linearizing equation 27 in $\cos\xi$ yields

$$\mathcal{A}_g = \frac{1}{Q} - \cos\xi. \tag{28}$$

Equation 28 shows that the group attenuation coefficient $\mathcal{A}_g$ for large inhomogeneity angles reduces to just $\tan\psi$ (see equation 26). Therefore, whereas the real and imaginary parts of the wave vector (equations 23 and 24) become infinite as $\xi \to 90°$, the group attenuation coefficient approaches $1/Q$ and is about twice as large as $\mathcal{A}|_{\xi=0°}$ (Figure 4). Hence, for large angles ξ close to 90°, seismic attenuation measurements in isotropic media *do not* provide a direct estimate of the quality factor because $\mathcal{A}_g$ rapidly increases with ξ from $1/(2Q)$ to $1/Q$.

Although the presence of anisotropy makes treatment of wave propagation in attenuative media much more complicated, several key conclusions drawn above prove to be valid for models with anisotropic velocity and attenuation functions.

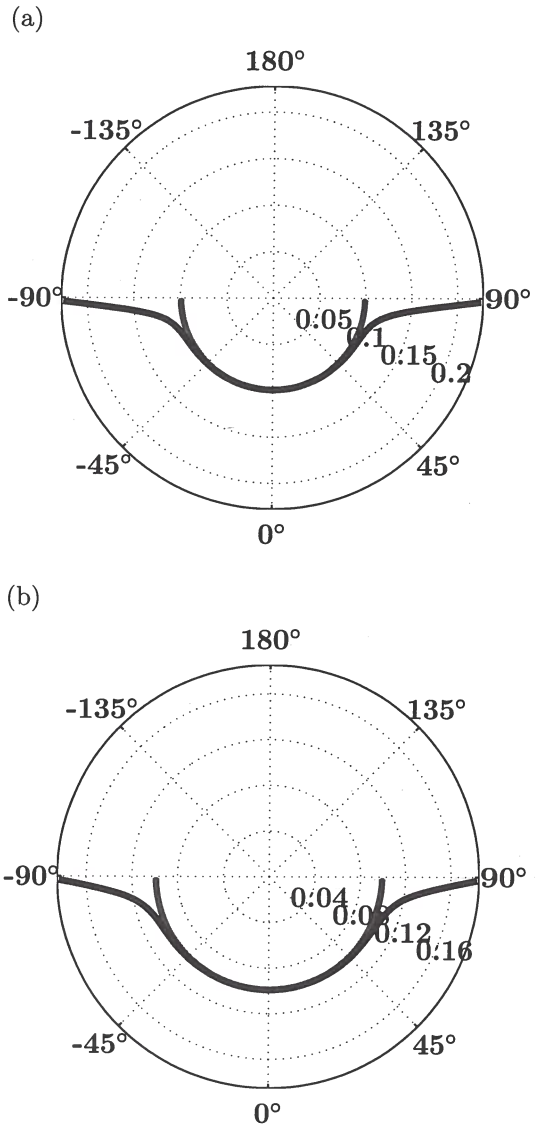

Figure 4. Exact P-wave (a) and S-wave (b) coefficient $\mathcal{A}|_{\xi=0°}$ (equation 3, red curve) and the normalized group attenuation $\mathcal{A}_g$ (equation 12, blue curve) in isotropic media as a function of the inhomogeneity angle ξ (numbers on the perimeter). The quality factors are $Q_P = Q_S = 5$.

3 ANISOTROPIC MEDIA

The dependence of attenuation on the inhomogeneity angle ξ in anisotropic media is influenced by the angular variation of the phase quantities and by the difference between the group and phase directions. Using the Christoffel equation B1, the phase attenuation coefficient $\mathcal{A}$ can be computed for arbitrary values of the angle ξ. Then general group-velocity equations (e.g., Tsvankin, 2005) can be employed to obtain the group attenuation coefficient. It would be useful, however, to develop analytic expressions for phase and group attenuation that provide physical insight into the contribution of the inhomogeneity angle. To derive analytic expressions for $\mathbf{k}^R$, $\mathbf{k}^I$, and $\mathcal{A}_g$ in arbitrarily anisotropic media, we use the first-order perturbation theory, as discussed in Appendix A. The analytic development is supported by numerical modeling based on exact solutions.

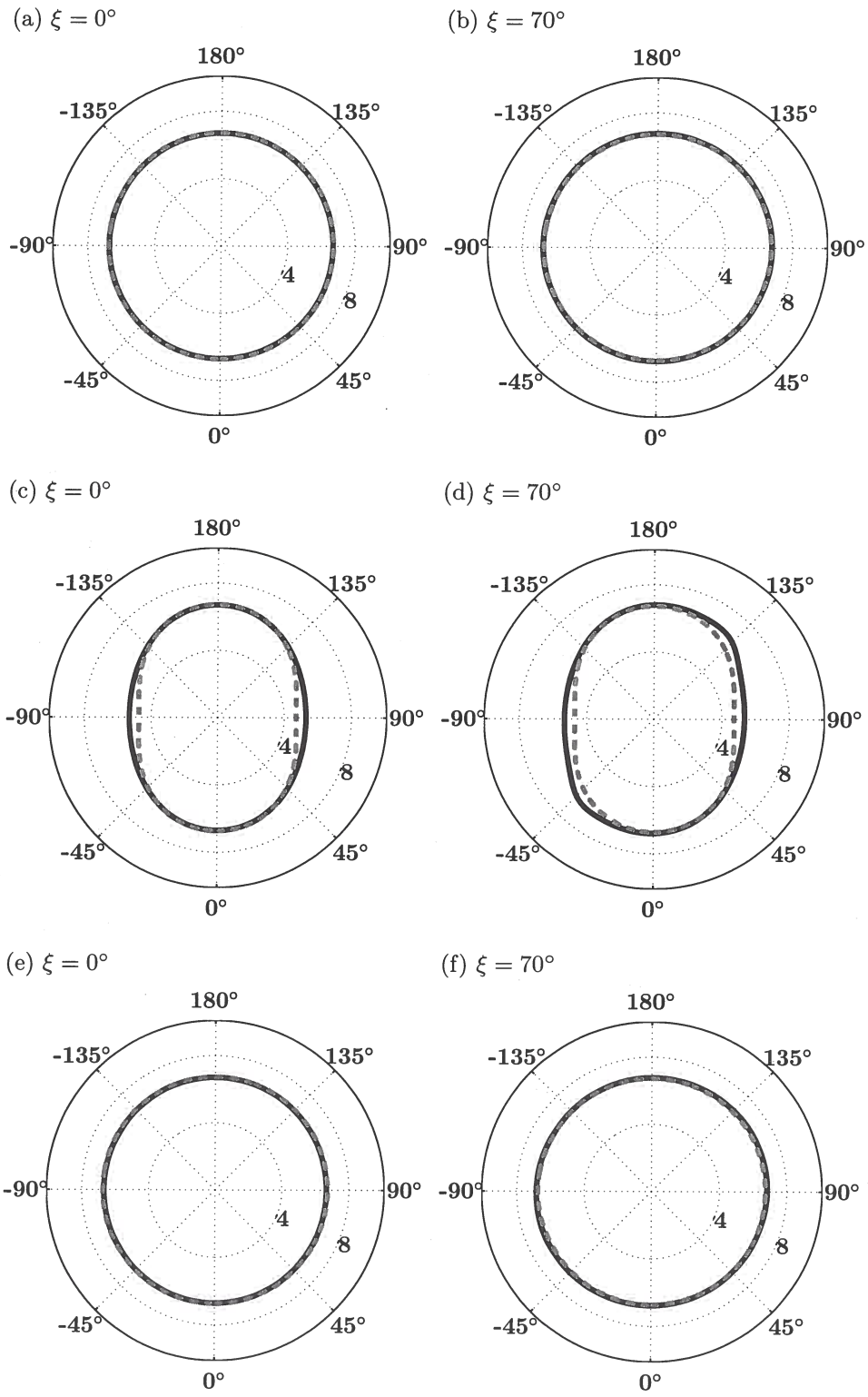

Figure 5. Exact real part k^R (in 100 m^{-1}) of the P-wave vector $\mathbf{k}$ (solid lines) and approximate $k^R = k^{R,0} + \Delta k^R$ from equation 29 (dashed lines) for $\xi = 0°$ (a,c,e) and $\xi = 70°$ (b,d,f) as a function of the phase angle (numbers on the perimeter). The model in (a,b) is isotropic; in (c,d) it is anisotropic in terms of velocity but has isotropic attenuation, while in (e,f) it has isotropic velocity and anisotropic attenuation (Table 1). The frequency is 30 Hz.

	ξ	ϵ	δ	γ	Q_{P0}	Q_{S0}	ϵ_Q	δ_Q	γ_Q
Figs. 5a,b	0°, 70°	0	0	0	10	10	0	0	0
5c,d	0°, 70°	0.3	0.2	0	10	10	0	0	0
5e,f	0°, 70°	0	0	0	10	10	0.6	0.4	0
Figs. 6a,b,c	0°, 45°, 70°	Same as in Figures 5a,b							
6d,e,f	0°, 45°, 70°	Same as in Figures 5c,d							
6g,h,i	0°, 45°, 70°	Same as in Figures 5e,f							
Fig. 7a	0°	0.3	0.2	0	10	10	0.6	0.4	0
7b	0°	0	0	0.3	10	10	0	0	0.5
Fig. 8	-	0.3	0.2	0	5	5	0.6	0.4	0
Fig. 9a	60°	0	0	0	10	10	0	0	0
9b	60°	0.3	0.2	0	10	10	0	0	0
9c	60°	0.6	0.4	0	10	10	0	0	0
9d	60°	0	0	0	10	10	0.6	0.4	0
Fig. 10a,b	60°	0.6	0.4	0	10	10	0.6	0.4	0
10c,d	60°	0	0	0.5	10	10	0	0	0.5
Fig. 11	-	0	0	0.3	5	5	0	0	0.5
Fig. 12a	-	0	0	1	5	5	0	0	-0.5
12b	-	0	0	0.3	5	5	0	0	-0.5

Table 1. Medium parameters used in the numerical tests. For all models, the P- and S-wave symmetry-direction velocities (V_{P0} and V_{S0}) are 2800 m/s and 1700 m/s, respectively.

and attenuation-anisotropy parameters to obtain

$$\mathcal{A}_{g,P} = \frac{1}{2Q_{P0}} \left(1 + \delta_Q \sin^2\theta \cos^2\theta + \epsilon_Q \sin^4\theta\right). \qquad (34)$$

Similar approximate expressions for the group attenuation coefficient of SV- and SH-waves are given in Appendix C (equations C10 and C11).

Therefore, the inhomogeneity angle has no influence on the approximate group attenuation coefficient. Furthermore, $\mathcal{A}_{g,P}$ in equation 34 coincides with the linearized P-wave phase attenuation coefficient for a zero inhomogeneity angle ($\mathcal{A}|_{\xi=0°}$) derived by Zhu and Tsvankin (2006). Equation 34 deviates from the exact $\mathcal{A}_g$ only when the angle ξ approaches forbidden directions (Figure 8); the behavior of $\mathcal{A}_g$ for large inhomogeneity angles is analyzed in more detail below.

Note that the linearized $\mathcal{A}_g$ (equations 34, C10, and C11) is controlled by attenuation anisotropy and does not depend on the velocity-anisotropy parameters. This conclusion is confirmed by the exact modeling results in Figures 9a and 9b where the coefficient $\mathcal{A}_g$ remains insensitive even to strong velocity anisotropy with $\epsilon = 0.6$ and $\delta = 0.4$ when $\xi = 60°$ (Figure 9c). The presence of attenuation anisotropy, on the other hand, results in a substantial change in $\mathcal{A}_g$ (Figure 9d).

3.3 Relationship between group and phase attenuation

The normalized phase attenuation coefficient $\mathcal{A}|_{\xi=0°}$ can be obtained from the Christoffel equation and expressed through the attenuation-anisotropy parameters (Zhu & Tsvankin, 2006). As shown above, the coefficient $\mathcal{A}_g$ coincides with $\mathcal{A}|_{\xi=0°}$ for a wide range of ξ in isotropic media and for $\xi = 0°$ in anisotropic media.

Using perturbation analysis, we obtained closed-form expressions for the coefficient $\mathcal{A}|_{\xi=0°}$ in arbitrarily anisotropic media linearized in Δa_{ij} (Appendix B). For P-waves,

$$\mathcal{A}|_{\xi=0°,P} = \frac{1}{2Q_{P0}} - \frac{1}{2V_{P0}^2}\left(\frac{\Delta a_{33}^R}{Q_{P0}} - \Delta a_{33}^I\right). \qquad (35)$$

Similar expressions for S_1- and S_2-waves are given in Appendix B. Comparison of equations 33 and 35 shows that for a wide range of angles ξ (except for values close to 90°; see below), the linearized coefficient $\mathcal{A}_g$ coincides with $\mathcal{A}|_{\xi=0°}$. This conclusion is also valid for S_1- and S_2-waves (compare equations B30 and B31 with equations B24 and B25).

The approximate P-wave phase attenuation coefficient for TI media can be found as a simple function of the attenuation-anisotropy parameters (Zhu & Tsvankin, 2006):

$$\mathcal{A}|_{\xi=0°,P} = \frac{1}{2Q_{P0}} \left(1 + \delta_Q \sin^2\theta \cos^2\theta + \epsilon_Q \sin^4\theta\right). \qquad (36)$$

Zhu & Tsvankin (2006) also provide similar linearized expressions for SV- and SH-waves reproduced in Appendix B. As is the case for arbitrary ansisotropy, the coefficient $\mathcal{A}|_{\xi=0°}$ in equation 36 coincides with $\mathcal{A}_g$ in equation 34.

Figures 10a and 10b demonstrate that the maximum difference between the exact coefficients $\mathcal{A}_g$ and $\mathcal{A}|_{\xi=0°}$ does not exceed 10% even for strong attenuation ($Q_{33} = 10$) and uncommonly large anisotropy parameters ($\epsilon = \epsilon_Q = 0.6$ and $\delta = \delta_Q = 0.4$). The coefficients $\mathcal{A}_g$ and $\mathcal{A}|_{\xi=0°}$ are also close for SV- and SH-waves, which confirms the analytic results of Appendix C (Figures 10c and 10d).

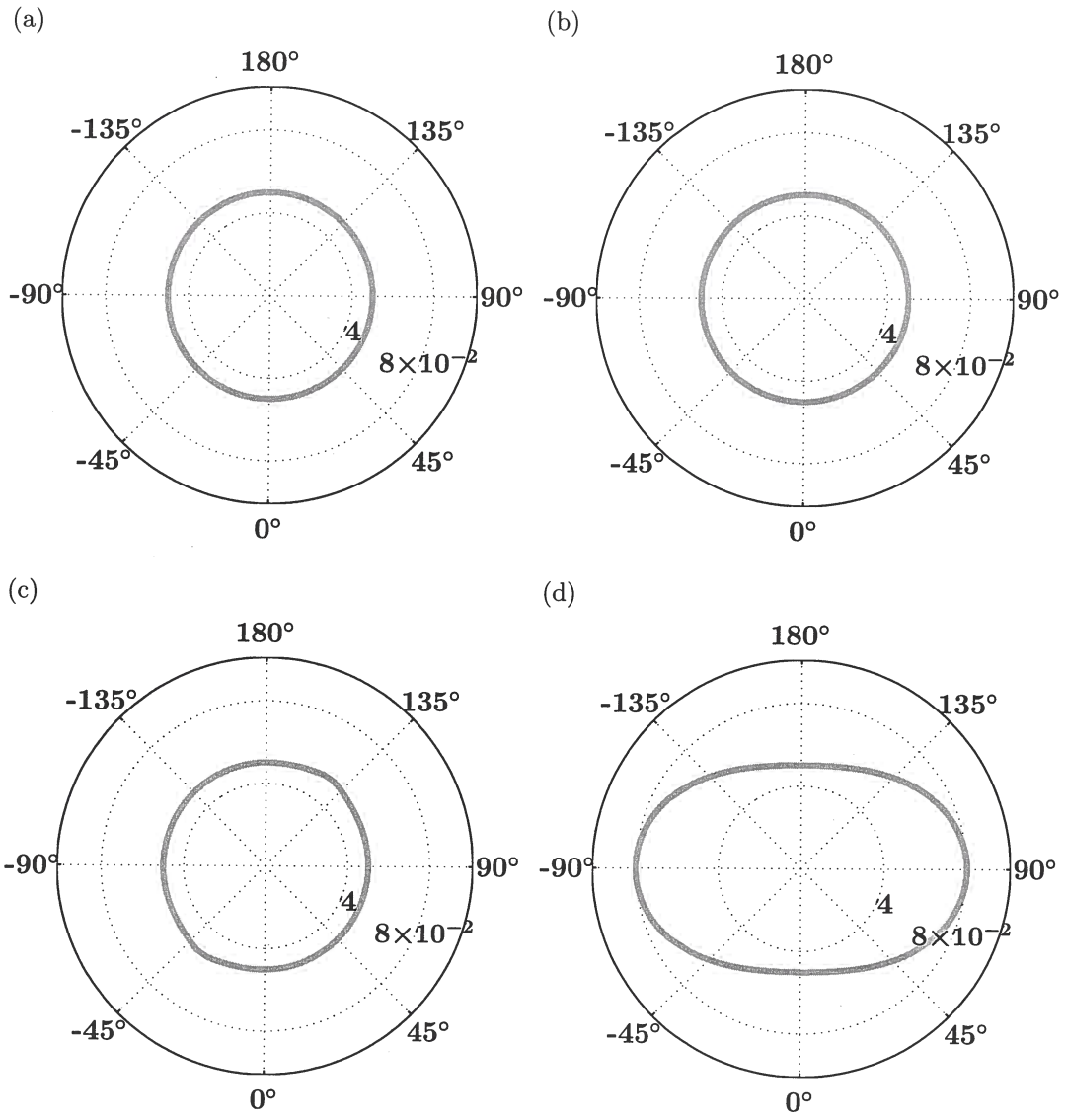

Figure 9. Exact P-wave group attenuation coefficient $\mathcal{A}_g$ for $\xi = 60°$ in isotropic (a) and TI (b,c,d) media. In (b,c) only velocity varies with angle, while attenuation is isotropic; in (d) attenuation varies with angle, while velocity is isotropic. The model parameters are given in Table 1.

and

$$\beta = \cos^{-1}\left(\frac{\gamma_Q \cos 2\theta}{4Q_{S0}}\right). \tag{40}$$

Equivalent expressions for the bounds on ξ for SH-wave propagation in the symmetry plane of a monoclinic medium are given by Červený & Pšenčík (2005a) in terms of the inhomogeneity parameter D.

For wave propagation along the symmetry axis or perpendicular to it ($\theta = 0°$ or $90°$), the angle $\alpha = 0°$ and the bounds on ξ are symmetric with respect to $\xi = 0°$ (equations 38 and 40; Figure 11). It is also clear from equation 40 that $\beta \approx 90°$ because the ratio γ_Q/Q_{S0} typically is small. Hence, for $\theta = 0°$ and $90°$ anisotropy does not signficantly change the bounds on ξ, which remain close to $\pm 90°$. As was the case for isotropic media, when the angle ξ approaches the "forbidden directions," the group attenuation coefficient $\mathcal{A}_g$ rapidly increases with $|\xi|$ and reaches values approximately twice as large as $\mathcal{A}|_{\xi=0°}$ (Figure 11).

For oblique propagation angles, α does not vanish, and the bounds on ξ become asymmetric with respect to $\xi = 0°$. This asymmetry is controlled by the velocity-anisotropy coefficient γ and reaches its maximum for the phase angle $\theta = 45°$ (equation 39). The model in Figure 12a, taken from Carcione & Cavallini (1995), has an uncommonly large parameter γ equal to unity, and for

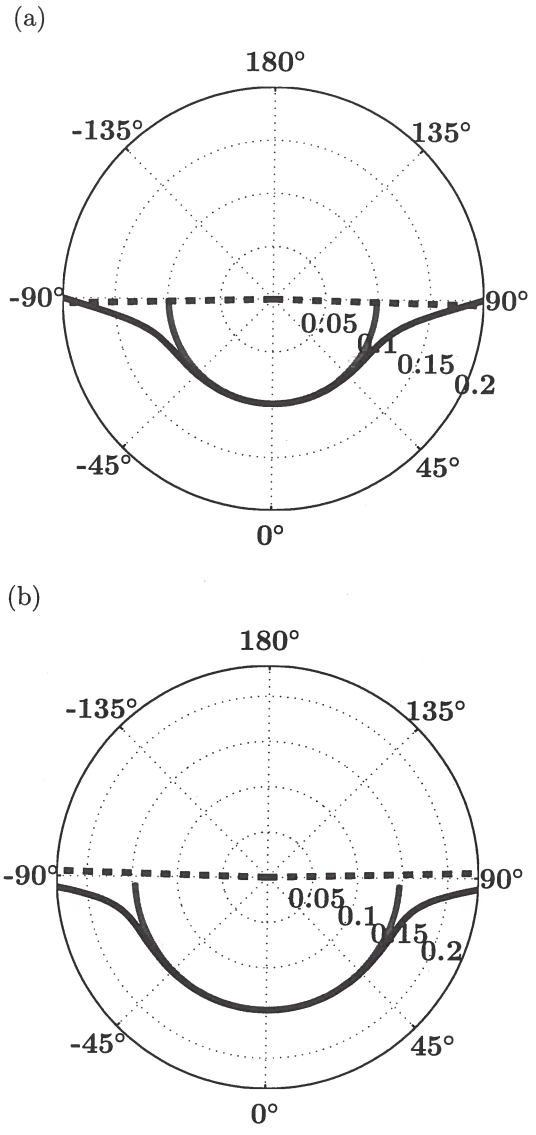

Figure 11. Exact SH-wave coefficients $\mathcal{A}|_{\xi=0^\circ}$ (red curve) and $\mathcal{A}_g$ (blue curve) in TI media for propagation in the directions $\theta = 0^\circ$ (a) and $\theta = 90^\circ$ (b) plotted as a function of the inhomogeneity angle ξ (numbers on the perimeter). The black dashed line marks the bounds of ξ computed from equations 38–40. The model parameters are listed in Table 1.

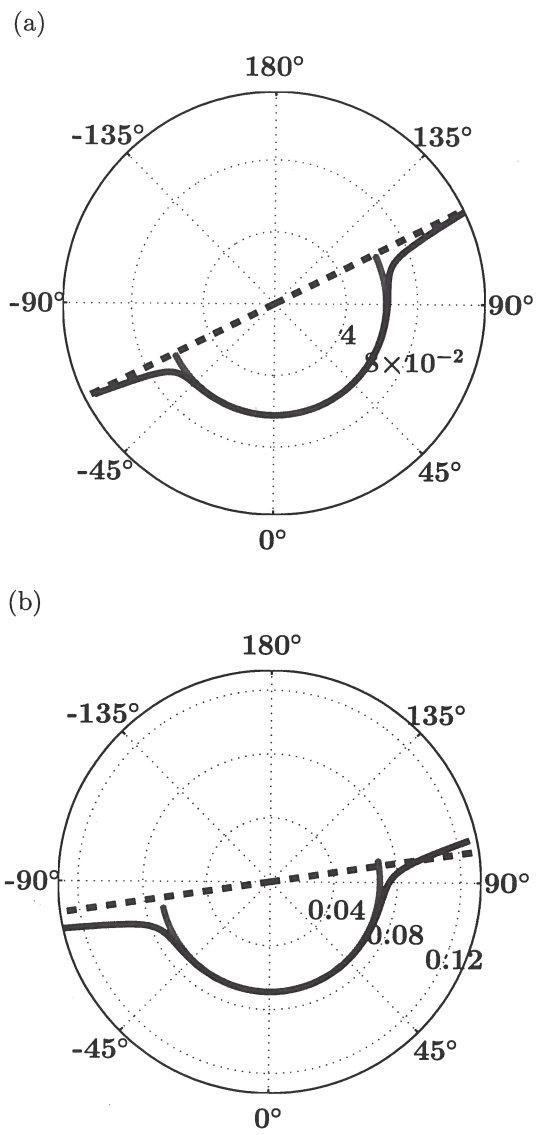

Figure 12. Exact SH-wave coefficients $\mathcal{A}|_{\xi=0^\circ}$ (red curve) and $\mathcal{A}_g$ (blue) as a function of ξ (numbers on the perimeter) for $\theta = 45^\circ$ and $\gamma = 1.0, \gamma_Q = -0.5$ (a) and $\gamma = 0.3, \gamma_Q = -0.5$ (b). The black dashed line marks the bounds of ξ computed from equations 38–40. The model parameters are listed in Table 1.

plitudes practically coincide even at large offsets where the inhomogeneity angle reaches 60°.

The coefficient $\mathcal{A}|_{\xi=0^\circ}$ in TI and orthorhombic media can be inverted for the Thomsen-style attenuation-anisotropy parameters using the formalism developed by Zhu & Tsvankin (2006, 2007). Note that estimation of the attenuation-anisotropy parameters from $\mathcal{A}|_{\xi=0^\circ}$ requires computation of the corresponding phase angle, which depends on the anisotropic velocity field. Even in strongly anisotropic models, however, the influence of attenuation on velocity is of the second order (see above), which implies that velocity analysis can be performed using existing methods. The reconstructed velocity field can then be employed to recompute the known group direction into the phase direction needed in the inversion for the attenuation-anisotropy parameters. Furthermore, given the large uncertainty of amplitude measurements, the difference between the phase and group directions for moderately anisotropic models should not significantly distort the results of attenuation analysis.

anelastic media. *Journal of Geophysical Research*, **99**(B12), 899–919.

Tonn, R. 1991. The determination of the seismic quality factor Q from VSP data: A comparison of different computational methods. *Geophysical Prospecting*, **39**(1), 1–27.

Tsvankin, I. 1995. *Seismic Wavefields in Layered Isotropic Media.* Samizdat Press.

Tsvankin, I. 2005. *Seismic Signatures and Analysis of Reflection Data in Anisotropic Media.* 2 edn. Elsevier Science.

Vavryčuk, V. 2007. Ray velocity and ray attenuation in homogeneous anisotropic viscoelastic media. *Geophysics*, **72**(6), D119–D127.

Vavryčuk, V. 2008. Velocity, attenuation, and quality factor in anisotropic viscoelastic media: A perturbation approach. *Geophysics*, **73**(5), D63–D73.

Zhu, Y. 2006. *Seismic wave propagation in attenuative anisotropic media.* Ph.D. thesis, Colorado School of Mines.

Zhu, Y., & Tsvankin, I. 2006. Plane-wave propagation in attenuative transversely isotropic media. *Geophysics*, **71**(2), T17–T30.

Zhu, Y., & Tsvankin, I. 2007. Plane-wave attenuation anisotropy in orthorhombic media. *Geophysics*, **72**(1), D9–D19.

Zhu, Y., Tsvankin, I., Dewangan, P., & van Wijk, K. 2007. Physical modeling and analysis of P-wave attenuation anisotropy in transversely isotropic media. *Geophysics*, **72**(1), D1–D7.

APPENDIX A: COMPLEX WAVE VECTOR FOR ISOTROPIC ATTENUATIVE MEDIA

We consider a harmonic plane wave with an arbitrary inhomogeneity angle ξ propagating in isotropic attenuative media:

$$A(\mathbf{x},t) = A_0\, e^{i(\omega\, t\, -\, \mathbf{k}\cdot\mathbf{x})}\,, \tag{A1}$$

where ω is the angular frequency and $\mathbf{k} = \mathbf{k}^R - i\,\mathbf{k}^I$ is the complex wave vector responsible for the velocity and the attenuation coefficient. Substitution of the plane wave A1 into the acoustic wave equation results in

$$k_1^2 + k_2^2 + k_3^2 = \frac{\omega^2}{V^2\left(1+\dfrac{i}{Q}\right)}\,, \tag{A2}$$

where V is the real part of the medium velocity, and Q is the quality factor. Dropping quadratic and higher-order terms in $1/Q$, we rewrite equation A2 as

$$(k^R)^2 - 2\,i\,\mathbf{k}^R\cdot\mathbf{k}^I - (k^I)^2 = \frac{\omega^2}{V^2}\left(1-\frac{i}{Q}\right); \tag{A3}$$

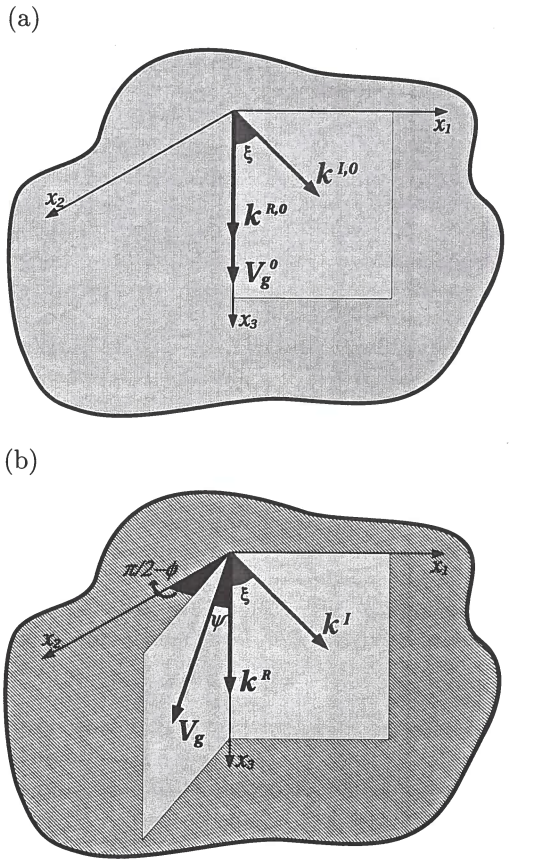

Figure A1. Isotropic attenuative background medium (a) is perturbed to make it anisotropic (b). $\mathbf{k}^{R,0}$ and $\mathbf{k}^{I,0}$ are the real and imaginary parts of the wave vector in the background, and $\mathbf{k}^R = \mathbf{k}^{R,0} + \Delta\mathbf{k}^R$ and $\mathbf{k}^I = \mathbf{k}^{I,0} + \Delta\mathbf{k}^I$ form the wave vector in the perturbed medium; ξ is the inhomogeneity angle. The vectors $\mathbf{k}^{R,0}$ and $\mathbf{k}^R$ are parallel to the vertical x_3 direction while $\mathbf{k}^{I,0}$ and $\mathbf{k}^I$ are confined to the $[x_1, x_3]$-plane. $\mathbf{V}_g^0$ is the group velocity in the background; ψ is the polar group angle after the perturbation, and ϕ is the azimuth of the perturbed vector $\mathbf{V}_g$ with respect to the $[x_1, x_3]$-plane.

$k^R = |\mathbf{k}^R|$ and $k^I = |\mathbf{k}^I|$. Equation A3 can be separated into the real and imaginary parts:

$$(k^R)^2 - (k^I)^2 = \frac{\omega^2}{V^2}\,, \tag{A4}$$

$$\mathbf{k}^R\cdot\mathbf{k}^I = \frac{\omega^2}{2V^2\,Q}\,. \tag{A5}$$

When the medium is non-attenuative and $1/Q = 0$, the right-hand side of equation A5 vanishes. Then the vectors $\mathbf{k}^R$ and $\mathbf{k}^I$ of an inhomogeneous (evanescent) plane wave have to be orthogonal, with the relationship between k^R and k^I determined by equation A4.

Because the factor Q responsible for attenuation is positive, equation A5 can be satisfied only if $\mathbf{k}^R\cdot\mathbf{k}^I > 0$, which requires that $\cos\xi > 0$ and $\xi < 90°$. (We make

imaginary (Δk^I) parts of the wave vector. Because the inhomogeneity angle ξ is a free parameter, we choose not to perturb it when making the medium anisotropic. This implies that the vectors $\mathbf{k}^R$ and $\mathbf{k}^{R,0}$, as well as $\mathbf{k}^I$ and $\mathbf{k}^{I,0}$, are parallel.

We choose $\mathbf{k}^0$ such that $\mathbf{k}^{R,0}$ coincides with the axis x_3 and $\mathbf{k}^{I,0}$ lies in the $[x_1, x_3]$-plane (Figures A1a and A1b). This approach differs from the one adopted by Jech & Pšenčík (1989), Červený & Pšenčík (2008b), and Vavryčuk (2008), who used a fixed reference frame. To compute the perturbations for a different vector $\mathbf{k}$ in the same medium, we rotate the coordinate frame such that $\mathbf{k}^R$ coincides with the axis x_3 and $\mathbf{k}^I$ lies in the $[x_1, x_3]$-plane. This approach involves the rotation of the density-normalized stiffness tensor a_{ijkl} but obviates the need for introducing two additional angles needed to define the orientations of $\mathbf{k}^R$ and $\mathbf{k}^I$.

B1 Real and imaginary parts of the wave vector

We start with the Christoffel equation in the perturbed medium:

$$(G_{ik} - \delta_{ik})\, g_k = 0\,, \tag{B1}$$

where $G_{ik} = a_{ijkl}\, p_j\, p_l$ is the Christoffel matrix, $\mathbf{p}$ is the complex slowness vector, and $\mathbf{g}$ is the polarization vector of the plane wave. Perturbation of equation B1 yields

$$\left(G^0_{ik} + \Delta G_{ik} - \delta_{ik}\right)\left(g^0_k + \Delta g_k\right) = 0\,, \tag{B2}$$

which can be linearized to obtain

$$\left(G^0_{ik} - \delta_{ik}\right)\Delta g_k + \Delta G_{ik}\, g^0_k = 0\,, \tag{B3}$$

where $\mathbf{g}^0$ is the plane-wave polarization in the background and $\Delta\mathbf{g}$ is the perturbation of the polarization vector. The polarization $\mathbf{g}^0$ defines whether the wave mode is P, SV, or SH. The mode obtained by perturbing the SV-wave will be denoted S_1, and the perturbed SH-wave will be denoted S_2. Multiplying equation B3 with g^0_i (Jech & Pšenčík, 1989) reduces equation B3 to

$$\Delta G_{ik}\, g^0_i\, g^0_k = 0\,, \tag{B4}$$

with

$$\Delta G_{ik} = \Delta a_{ijkl}\, p^0_j\, p^0_l + 2a^0_{ijkl}\, \Delta p_j\, p^0_l\,, \tag{B5}$$

where a^0_{ijkl} and $\mathbf{p}^0$ are defined in the isotropic background, and Δa_{ijkl} and $\Delta\mathbf{p}$ are the perturbations. The tensors a^0_{ijkl} and Δa_{ijkl} are given by

$$a^0_{ijkl} = a^{R,0}_{ijkl} + i a^{I,0}_{ijkl} = a^{R,0}_{ijkl}\left(1 + \frac{i}{Q^0_{ijkl}}\right), \tag{B6}$$

$$\Delta a_{ijkl} = \Delta a^R_{ijkl} + i\Delta a^I_{ijkl}\,, \tag{B7}$$

where the superscripts "R" and "I" denote the real and imaginary parts, and Q^0_{ijkl} is the ratio a^R_{ijkl}/a^I_{ijkl}. The background slowness $\mathbf{p}^0$ and its perturbation $\Delta\mathbf{p}$ can be expressed as

$$\mathbf{p}^0 = \left[-ip^{I,0}\sin\xi,\ 0,\ p^{R,0} - ip^{I,0}\cos\xi\right], \tag{B8}$$

$$\Delta\mathbf{p} = \left[-i\Delta p^I\sin\xi,\ 0,\ \Delta p^R - i\Delta p^I\cos\xi\right], \tag{B9}$$

where $p^{R,0}$, $p^{I,0}$ and Δp^R, Δp^I are the magnitudes of the real and imaginary parts of $\mathbf{p}^0$ and $\Delta\mathbf{p}$, respectively.

Assuming $(Q^0\cos\xi) \gg 1$, we solve equation B4 for $\Delta k^R = \omega\Delta p^R$ and $\Delta k^I = \omega\Delta p^I$:

$$\frac{\Delta k^R}{k^{R,0}} = -\frac{\chi^R}{2} - \frac{\chi^I}{2Q^0}\left(1 - \frac{\sec^2\xi}{2}\right), \tag{B10}$$

$$\frac{\Delta k^I}{k^{I,0}} = -\frac{\chi^R}{2} + Q^0\chi^I, \tag{B11}$$

where χ^R and χ^I are the real and imaginary parts of $\chi = \Delta a_{ijkl} p^0_j p^0_l g^0_i g^0_k$. The above analysis is valid for all three modes (P-, S_1-, and S_2-waves). By choosing the corresponding $\mathbf{k}^0$ and χ, we can compute the perturbations of the complex wave vector for any of the three modes. The term χ for P-, S_1-, and S_2-waves has the form

$$\chi_P = \frac{1}{V^2_{P0}}\left(\Delta a^R_{33} + \frac{\Delta a^I_{33}}{Q_{P0}} + \frac{2\Delta a^I_{35}}{Q_{P0}}\tan\xi\right) + i\,\frac{1}{V^2_{P0}}\left(-\frac{\Delta a^R_{33}}{Q_{P0}} + \Delta a^I_{33} - \frac{2\Delta a^R_{35}}{Q_{P0}}\tan\xi\right), \tag{B12}$$

$$\chi_{S_1} = \frac{1}{V^2_{S0}}\left(\Delta a^R_{55} + \frac{\Delta a^I_{55}}{Q_{S0}} + \frac{\Delta a^I_{15} - \Delta a^I_{35}}{Q_{S0}}\tan\xi\right) + i\,\frac{1}{V^2_{S0}}\left(-\frac{\Delta a^R_{55}}{Q_{S0}} + \Delta a^I_{55} - \frac{\Delta a^R_{15} - \Delta a^R_{35}}{Q_{S0}}\tan\xi\right), \tag{B13}$$

and

$$\chi_{S_2} = \frac{1}{V^2_{S0}}\left(\Delta a^R_{44} + \frac{\Delta a^I_{44}}{Q_{S0}} + \frac{\Delta a^I_{46}}{Q_{S0}}\tan\xi\right) + i\,\frac{1}{V^2_{S0}}\left(-\frac{\Delta a^R_{44}}{Q_{S0}} + \Delta a^I_{44} - \frac{\Delta a^R_{46}}{Q_{S0}}\tan\xi\right); \tag{B14}$$

Q_{P0} and Q_{S0} are the P- and S-wave quality factors in the background medium. Substituting equations B12–B14 into equations B10 and B11 and retaining only the terms linear in Δa_{ij} yields

$$\frac{\Delta k^R_P}{k^{R,0}_P} \approx -\frac{1}{V^2_{P0}}\left[\frac{\Delta a^R_{33}}{2} + \frac{\Delta a^I_{33}}{Q_{P0}}\left(1 - \frac{\sec^2\xi}{4}\right) + \frac{\Delta a^I_{35}}{Q_{P0}}\tan\xi\right], \tag{B15}$$

$$\frac{\Delta k^I_{SV}}{k^{I,0}_{SV}} = (\epsilon_Q - \delta_Q)\frac{g^2}{g_Q}\sin^2\theta\cos^2\theta + \sigma\frac{2-3g_Q}{g_Q}\sin^2\theta\cos^2\theta - \sigma\sin 2\theta\cos 2\theta\tan\xi\,, \tag{C2}$$

$$\frac{\Delta k^R_{SH}}{k^{R,0}_{SH}} = -\gamma\sin^2\theta\,, \tag{C3}$$

$$\frac{\Delta k^I_{SH}}{k^{I,0}_{SH}} = \gamma_Q\sin^2\theta - \gamma\sin^2\theta - \gamma\sin 2\theta\tan\xi\,, \tag{C4}$$

where $g = V_{P0}/V_{S0}$, the parameter $\sigma = g^2(\epsilon - \delta)$ controls the SV-wave phase velocity, $g_Q = Q_{P0}/Q_{S0}$, and the parameters γ and γ_Q are responsible for the SH-wave velocity and attenuation anisotropy, respectively (Zhu & Tsvankin, 2006).

The normalized SV- and SH-wave phase attenuation coefficients for $\xi = 0°$ can be found from equations B24 and B25:

$$\mathcal{A}|_{\xi=0°,SV} = \frac{1}{2Q_{S0}}\left(1+\sigma_Q\sin^2\theta\cos^2\theta\right), \tag{C5}$$

$$\mathcal{A}|_{\xi=0°,SH} = \frac{1}{2Q_{S0}}\left(1+\gamma_Q\sin^2\theta\right), \tag{C6}$$

where the parameter σ_Q (Zhu & Tsvankin, 2006) controls the SV-wave attenuation coefficient:

$$\sigma_Q = \frac{1}{g_Q}\left[2\sigma(1-g_Q) + g^2(\epsilon_Q - \delta_Q)\right]. \tag{C7}$$

To obtain the linearized shear-wave group angles in TI media, we use equations B27 and B28 (see also Tsvankin, 2005):

$$\tan\psi_{SV}\cos\phi_{SV} = \sigma\sin 2\theta\cos 2\theta \tag{C8}$$

and

$$\tan\psi_{SH}\cos\phi_{SH} = \gamma\sin 2\theta\,. \tag{C9}$$

Substituting the anisotropy parameters into equations B30 and B31 yields the following group attenuation coefficients:

$$\mathcal{A}_{g,SV} = \frac{1}{2Q_{S0}}\left(1+\sigma_Q\sin^2\theta\cos^2\theta\right), \tag{C10}$$

$$\mathcal{A}_{g,SH} = \frac{1}{2Q_{S0}}\left(1+\gamma_Q\sin^2\theta\right). \tag{C11}$$

APPENDIX D: ATTENUATION FOR LARGE INHOMOGENEITY ANGLES

Here, we develop closed-form expressions for the wave vector $\mathbf{k}$ and group attenuation coefficient $\mathcal{A}_g$ for large angles ξ. For simplicity, we analyze only S_2-waves; expressions for P- and S_1-waves can be derived using the same procedure. The development follows the same approach as that described in Appendix B. The group angle ψ^0 in the background, however, does not vanish (equation 26), and the background vector $\mathbf{k}^0 = \mathbf{k}^{R,0} - i\mathbf{k}^{I,0}$ is given by equations 23 and 24. (Note that for small and moderate angles ξ considered in Appendix B, the group angle ψ^0 was zero.) For large ξ, the real ($k^{R,0}$) and imaginary ($k^{I,0}$) parts of the background wave vector are related by (equation 25)

$$\frac{k^{I,0}}{k^{R,0}} = 1 - Q^0\cos\xi\,, \tag{D1}$$

and the group angle ψ^0 is expressed as (equation 26)

$$\tan\psi^0 = \frac{1}{Q^0} - \cos\xi\,, \tag{D2}$$

where Q^0 is the background quality factor. The perturbation produces a change in both the wave vector ($\Delta k^R - i\Delta k^I$) and the group direction.

First, we obtain k^R and k^I by solving equation B4 and linearizing the result in Δa_{ij}. Eliminating terms quadratic or higher-order in $Q^0\cos\xi$ and those proportional to $\Delta a_{ij}Q^0\cos\xi$, as well as setting terms quadratic in $\sin\xi$ to one, we find

$$\frac{k^R_{S_2}}{k^{R,0}_{S_2}} = \frac{k^I_{S_2}}{k^{I,0}_{S_2}} = 1 - \frac{1}{2V^2_{S0}}\left(\Delta a^R_{46} + \frac{\Delta a^I_{46}}{Q_{S0}}\right)\tan\xi + \frac{1}{4V^2_{S0}\cos\xi}\left(\Delta a^I_{44} - \frac{\Delta a^R_{44}}{Q_{S0}} - \Delta a^I_{66} + \frac{\Delta a^R_{66}}{Q_{S0}}\right). \tag{D3}$$

For the special case of TI media, the S_2-mode becomes the SH-wave, and equation D3 (after eliminating terms proportional to γ/Q^2_{S0} and γ_Q/Q^2_{S0}) takes the form

$$\frac{k^R_{S_2}}{k^{R,0}_{S_2}} = \frac{k^I_{S_2}}{k^{I,0}_{S_2}} \approx 1 + \frac{\gamma\sin 2\theta}{2}\tan\xi - \frac{\gamma_Q\cos 2\theta}{4Q_{S0}}\frac{1}{\cos\xi}. \tag{D4}$$

The product $\tan\psi\cos\phi$ needed to find $\mathcal{A}_g$ can be obtained from equation A16:

$$\tan\psi\cos\phi = \frac{1}{Q_{S0}} - \cos\xi - \frac{1}{4V^2_{S0}}\left[\frac{2\Delta a^I_{46}}{Q_{S0}} - 6\Delta a^R_{46} + \left(\frac{3\Delta a^R_{44}}{Q_{S0}} + \frac{\Delta a^R_{66}}{Q_{S0}} + \Delta a^I_{44} - 5\Delta a^I_{66}\right)\sin\xi\right]. \tag{D5}$$

The group attenuation coefficient $\mathcal{A}_g$ is found by

Multi-azimuth prestack time migration for anisotropic weakly heterogeneous media

Walter Söllner[1], Ilya Tsvankin[2], & Eduardo Filpo Ferreira da Silva[3]
[1] *Petroleum Geo-Services, Lysaker, Norway*
[2] *Center for Wave Phenomena, Colorado School of Mines, Golden, CO*
[3] *Petrobras, Rio de Janeiro, Brazil*

ABSTRACT

Conventional prestack time-migration velocity analysis is designed to estimate diffraction time functions in a fixed azimuthal direction from narrow-azimuth reflection data. Therefore, it can build accurate 3D migration operators only if the subsurface is isotropic (or azimuthally isotropic) and laterally homogeneous. Here, we extend time-migration methodology to multi-azimuth or wide-azimuth data from azimuthally anisotropic, weakly heterogeneous media.
We derive the azimuthally varying diffraction time function from the most general form of Hamilton's principal equation and apply a Taylor series expansion to the traveltime in the vicinity of the image ray. This approach helps to relate the Taylor series coefficients to the corresponding multi-azimuth imaging parameters. The second-order coefficients, which define the "migration-velocity ellipse," are obtained from time-migration velocity analysis in at least three distinct azimuthal directions. Our multi-azimuth prestack time migration (MAPSTM) solves the mismatch problem that occurs in conventional processing when the same depth point creates different time images in different azimuths. The algorithm is successfully tested on synthetic data for a horizontally layered azimuthally anisotropic model and an isotropic medium with a dipping interface.

Key words: time migration, velocity analysis, azimuthal anisotropy, NMO ellipse, image ray, multi-azimuth surveys.

1 INTRODUCTION

Conventional prestack time-migration operators are derived from analytic diffraction time functions. The diffraction times for any source and receiver position are defined solely by a single average velocity (i.e., the RMS velocity) at the image point instead of the true velocity field above the reflector. The time-migration velocity is obtained by focusing analyses on prestack time-migrated gathers. This approach generally proved to be robust for narrow-azimuth 2D and 3D seismic data, particularly when the subsurface is not structurally complex.

However, the limitations of the conventional time-migration methodology have become obvious with the advent of multi-azimuth and wide-azimuth seismic surveys. The most important advantages of multi-azimuth data acquisition are improved noise suppression, multiple attenuation and target illumination (Manning *et al.*, 2007); wide azimuthal coverage can also help in anisotropic parameter estimation. As discussed by Keggin *et al.* (2007), one of the the biggest problems in conventional processing of multi-azimuth data is that summation of signals acquired at different azimuths does not account for traveltime differences due to azimuthal anisotropy and/or lateral velocity variation.

Time imaging for orthorhombic symmetry, which adequately describes fracture-induced azimuthal anisotropy, is discussed by Grechka & Tsvankin (1999). They show that all P-wave time processing steps (normal-moveout and dip-moveout corrections, prestack and poststack time migration) for a laterally homogeneous orthorhombic medium above a dipping

paraxial matrices (Moser & Červený, 2007), which describe the transmission of the central ray between the anterior and posterior surfaces:

$$\begin{pmatrix} \mathbf{x}' \\ \mathbf{p}' - \mathbf{p}'_0 \end{pmatrix} = \begin{pmatrix} \mathbf{A}_0 & \mathbf{B}_0 \\ \mathbf{C}_0 & \mathbf{D}_0 \end{pmatrix} \begin{pmatrix} \mathbf{x} \\ \mathbf{p} - \mathbf{p}_0 \end{pmatrix}. \quad (2)$$

Given the deviations from the central ray in the initial position ($\mathbf{x}$) and slowness ($\mathbf{p} - \mathbf{p}_0$) vectors, equation 2 yields the corresponding vectors at the posterior surface, if the matrices $\mathbf{A}_0$, $\mathbf{B}_0$, $\mathbf{C}_0$, and $\mathbf{D}_0$ are known. The surface-to-surface paraxial matrix $\mathbf{T}$ can also be computed from the paraxial ray propagator matrix using surface transformation matrices (Hubral *et al.*, 1992; Červený, 2001; Moser & Červený, 2007).

Assuming the existence of the inverse matrix $\mathbf{B}_0^{-1}$, equation 2 can be rewritten after simple algebraic operations as

$$\mathbf{p} = \mathbf{p}_0 + \mathbf{B}_0^{-1}\,\mathbf{x}' - \mathbf{B}_0^{-1}\mathbf{A}_0\,\mathbf{x}, \quad (3)$$

and

$$\mathbf{p}' = \mathbf{p}'_0 + \mathbf{C}_0\,\mathbf{x} - \mathbf{D}_0\,\mathbf{B}_0^{-1}\mathbf{A}_0\,\mathbf{x} + \mathbf{D}_0\,\mathbf{B}_0^{-1}\mathbf{x}'. \quad (4)$$

Therefore, the initial and final slowness vectors of any transmitted ray in the vicinity of the central ray can be computed from equations 3 and 4, respectively.

2.2 Traveltime of transmitted events

The traveltime difference between the central ray and a ray displaced at the anterior surface by $d\tilde{\mathbf{x}}$ and at the posterior surface by $d\tilde{\mathbf{x}}'$ can be found from Hamilton's principal equation as the total differential,

$$dt(\tilde{\mathbf{x}}, \tilde{\mathbf{x}}') = \tilde{\mathbf{p}}' \cdot d\tilde{\mathbf{x}}' - \tilde{\mathbf{p}} \cdot d\tilde{\mathbf{x}}. \quad (5)$$

Hamilton's equation was originally derived from general variational principles. For example, the proof of equation 5 for anisotropic media in Buchdahl (1970) is based on Fermat's principle. The partial derivatives ($\tilde{\mathbf{p}}'$ and $-\tilde{\mathbf{p}}$) of the total differential dt in equation 5 lead to the fundamental relationship between phase and group velocity for arbitrarily anisotropic media. Within the framework of our approximation, it is possible to replace the three-component vectors in equation 5 by their two-component counterparts (Bortfeld, 1989):

$$dt(\mathbf{x}, \mathbf{x}') = \mathbf{p}' \cdot d\mathbf{x}' - \mathbf{p} \cdot d\mathbf{x}. \quad (6)$$

Equation 6 preserves the general form of Hamilton's equation for the two-component position and slowness vectors.

Substituting equations 3 and 4 into equation 6 and integrating the resulting expression, we obtain:

$$t(\mathbf{x}, \mathbf{x}') = t_0 - \mathbf{p}_0 \cdot \mathbf{x} + \mathbf{p}'_0 \cdot \mathbf{x}' + \frac{1}{2}\mathbf{x}' \cdot \mathbf{D}_0\,\mathbf{B}_0^{-1}\mathbf{x}'$$

$$+ \frac{1}{2}\mathbf{x} \cdot \mathbf{B}_0^{-1}\mathbf{A}_0\,\mathbf{x} - \mathbf{x} \cdot \mathbf{B}_0^{-1}\,\mathbf{x}'; \quad (7)$$

t_0 is the exact one-way traveltime along the central ray. Equation 7, also known as Hamilton's point characteristic, yields the traveltimes of paraxial rays transmitted through an anisotropic heterogeneous medium between the anterior ($\mathbf{x}$) and posterior ($\mathbf{x}'$) surfaces. If known, the special form of Hamilton's point characteristic allows one to determine the complete seismic system. This property is very important for model parameter estimation.

2.3 Multi-azimuth prestack time migration

Time migration moves a weighted sum of the wavefield amplitudes measured at the diffraction time surface to the two-way traveltimes at the emerging point of the image ray. An image ray is a transmitted ray that originates at the surface with the slowness vector parallel to the surface normal and ends at the reflection point (Hubral & Krey, 1980). The diffraction time surface is obtained as the ensemble of the transmitted times from all source-receiver combinations to the reflection point. This type of migration is also called "diffraction stack" or "Kirchhoff-type migration."

The weighting functions are commonly applied to preserve the amplitude behavior of reflected waves, or in some cases even to compensate the amplitude for losses caused by geometrical spreading (Schleicher *et al.*, 2007). For example, simplified versions of such weights valid for horizontally layered media are often applied in time migration and are considered as known here.

To define the migration operator, we still need to obtain the diffraction time function of a hypothetical diffractor at the reflection point, the associated image ray and the two-way traveltime along that ray. Since the reflection point is generally unknown, neither traveltime can be found. To overcome this difficulty, we reformulate the problem by starting from the migrated volume. The amplitude at each time sample is considered to belong to a time image point built by stacking along the diffraction times of a diffractor at the endpoint of the image ray. If no reflector was found at the endpoint of the image ray, the amplitude of the corresponding time image sample is expected to vanish. A different approach that leads (theoretically) to the same migration result operates in the vicinity of the normal ray (see Appendix A).

We consider an arbitrary image ray (coveniently treated as the central ray) and build the diffraction time function for every time sample. Parameters related to this central ray will be denoted by the subscript "I." For example, the traveltime of the ray that connects the receiver $\mathbf{x}_r$ and the diffraction point $\mathbf{x}'$ at the reflector is obtained from Hamilton's point characteristic for transmitted rays (equation 7) by employing the image ray condition $\mathbf{p}_I = \mathbf{0}$ (Bortfeld, 1989; Hubral *et al.*,

an intermediate plane dipping interface (Figure 2). The synthetic volume included two 3D data sets with the acquisition azimuths in the dip and strike directions of the interface. Conventional prestack time migration including common-image-gather (CIG) velocity analysis was applied to each data set separately. Figure 3 shows image gathers for the horizontal reflector beneath the dipping interface computed in the dip and strike directions. Although the gathers obtained with the best-fit velocity in each direction are flat, they show a time difference sufficient to degrade the quality of stacking. This difference, caused by the 30°-dip of the intermediate interface (i.e., by lateral heterogeneity), is the reason for destructive intereference on time-migration stacks often observed in multi-azimuth time imaging.

For isotropic media, conventional processing leads to distortions when the overburden is laterally heterogeneous and the image point is located outside the incidence (sagittal) plane. The presence of heterogeneity requires application of an azimuthally-dependent migration operator, while out-of-plane image rays correspond to azimuthal imaging angles (i.e., the angles between the x-axis and the lines from the source/receiver positions to the emergence point of the image ray) different from the source-receiver azimuth. In our simple example, the image rays for reflections recorded on the strike line deviate from the incidence plane, which distorts the migration result obtained using a single best-fit velocity.

Next, the same image gathers in dip and strike directions were computed by our multi-azimuth prestack time migration, which takes the azimuthal velocity variation into account (Figure 4). After application of the optimal migration-velocity ellipse, flat gathers from different azimuthal directions are recorded at the same time and can be stacked to obtain a high-quality final image.

We also tested our algorithm on a laterally homogeneous azimuthally anisotropic model that includes an HTI layer sandwiched between two isotropic layers. The parameter $\delta^{(V)}$, which determines the elongation of the P-wave NMO ellipse in HTI media (Tsvankin, 1997), was intentionally chosen to be uncommonly large by absolute value. The synthetic data were generated with anisotropic ray tracing code ANRAY developed by Gajewski & Pšenčík (1987). Figure 5 shows several input common-offset, common-azimuth sections for the reflection from the bottom of the HTI layer.

The substantial time difference between the reflections in the planes parallel and perpendicular to the symmetry axis is caused by the pronounced azimuthal anisotropy (here associated with the parameter $\delta^{(V)}$). This difference would result in a significant imaging mismatch after conventional time migration, if a single velocity is used for both principal azimuthal directions. Note that image rays excited in either vertical symmetry plane of the HTI layer do not deviate from the incidence plane. Therefore, for this model it is possible to avoid the mismatch by migrating narrow-azimuth data for each symmetry plane with the best-fit velocity estimated for that plane by the conventional algorithm (i.e., the approach that failed for the isotropic model discussed above).

To carry out multi-azimuth time-migration velocity analysis, we used equation 12. The time-migration velocity ellipse was estimated by flattening the common-image gathers for the available offsets and azimuths. Because the symmetry-axis orientation is assumed to be known, velocity analysis has to be applied only in the principal directions of the model. The time-migrated images of the azimuth-offset sections from Figure 5 are displayed in Figure 6. Clearly, the reflection from the bottom of the HTI layer is imaged at the same position using all azimuth-offset combinations in the input data. Figure 7 shows the time-migration response of one of the constant-azimuth, constant-offset volumes in the form of a time-slice, as well as in-line and cross-line sections.

4 CONCLUSIONS

We introduced a method for multi-azimuth prestack time migration (MAPSTM) based on the azimuthally-dependent diffraction time function. Hamilton's principal equation helped to obtain a relationship between azimuthally varying time-migration velocities and 3D prestack time-migration operators for arbitrarily anisotropic, weakly heterogeneous media. The current version of the method employs a second-order traveltime approximation, which makes the MAPSTM operator sufficiently accurate only for small- and moderate-offset data. The operator depends on three independent parameters that form the "time-migration velocity ellipse." The ellipse is obtained from time-migrated multi-azimuth data by flattening common-image gathers for all available offsets and azimuths. In contrast to existing migration methods for azimuthally anisotropic (e.g., orthorhombic) media, our algorithm does not require estimation of the normal-moveout velocities and relevant anisotropy parameters.

To compare MAPSTM with conventional processing, we generated multi-azimuth synthetic data for two models, one of which is isotropic but laterally heterogeneous (it contains a dipping interface), while the other includes an HTI layer with strong azimuthal anisotropy. Although conventional migration may produce flat gathers in the principal azimuthal directions, the time of migrated events varies with azimuth. This time difference is sufficient to cause destructive intereference on time-migration stacks often observed in multi-azimuth time imaging. The time mismatch problem was fully resolved for both models by applying MAPSTM with the best-fit time-migration velocity ellipse.

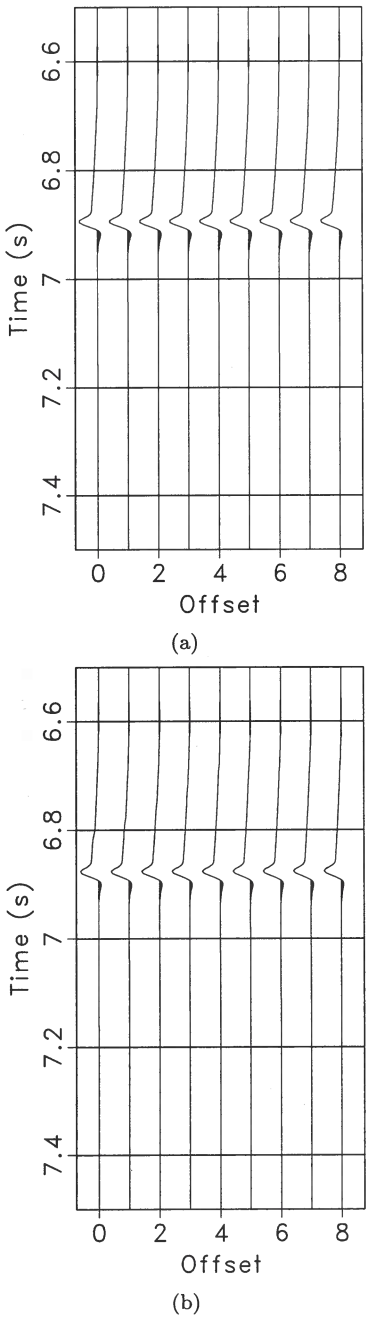

Figure 3. Conventional CIG gathers in the dip (a) and strike (b) directions for the isotropic model from Figure 2. The gathers are computed with the optimal migration velocity for each direction.

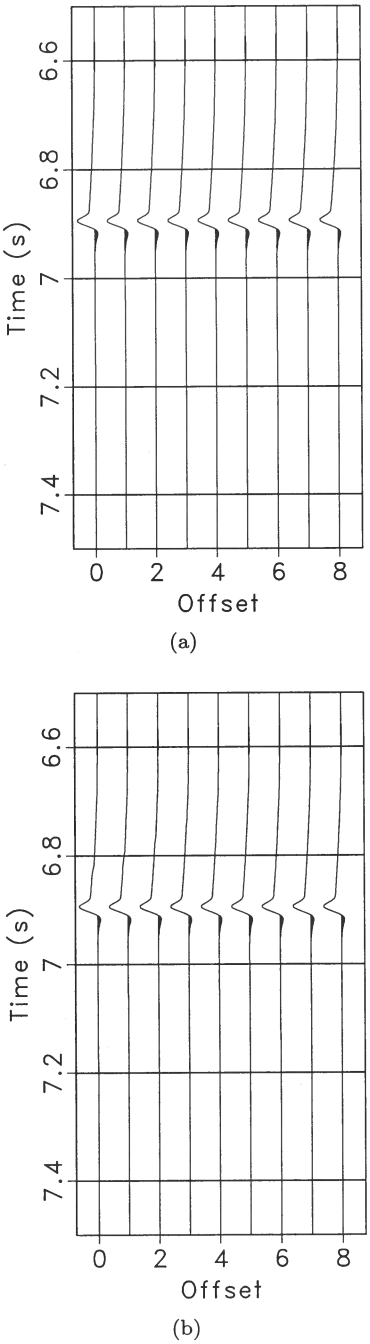

Figure 4. Multi-azimuth CIG gathers in the dip (a) and strike (b) directions for the isotropic model from Figure 2. Both gathers are computed with the optimal migration-velocity ellipse. The first offset and the offset increment in the CIG are 400 m.

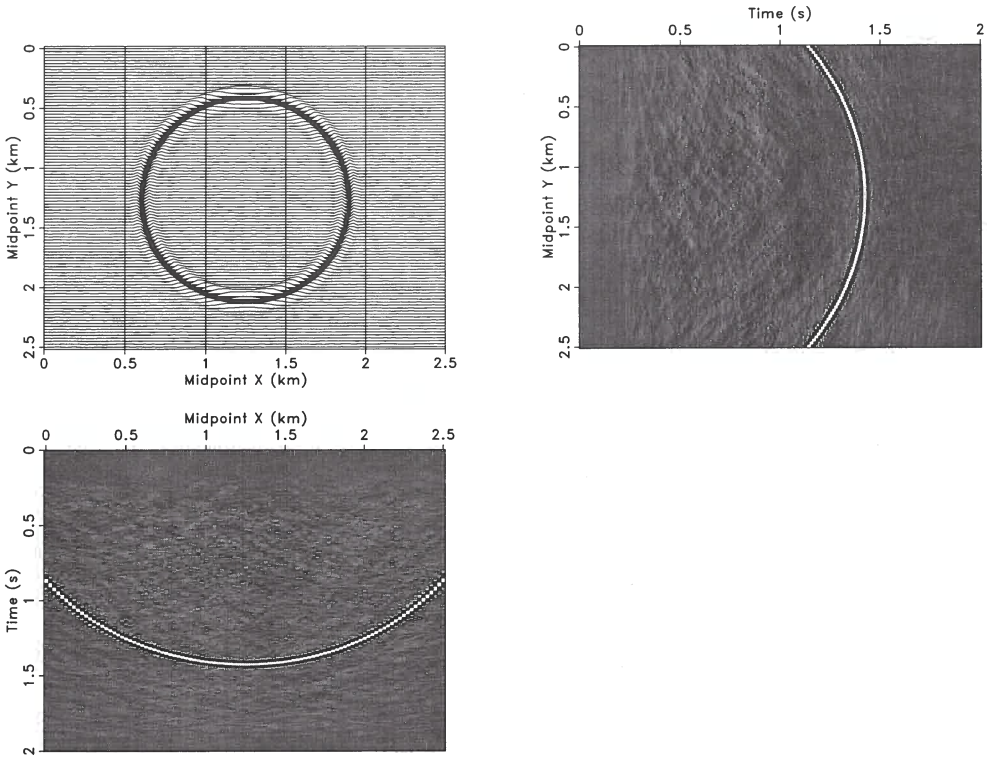

Figure 7. Multi-azimuth time-migration response for the input data with the azimuth 90° and offset 1000 m. The time slice at 1.3 s (top left); the inline section at y=1.25 km (top right); and the cross-line section at x=1.25 km (bottom).

the midpoint at the origin of the coordinate system is obtained from equation A2 by setting $\frac{1}{2}(\mathbf{x}_r + \mathbf{x}_s)=\mathbf{0}$:

$$T^2(\mathbf{x}_r, \mathbf{x}_s) = T_0^2 + 2T_0 \frac{1}{2}(\mathbf{x}_r - \mathbf{x}_s)\cdot\mathbf{B}_0^{-1}\mathbf{A}_0\frac{1}{2}(\mathbf{x}_r - \mathbf{x}_s). \quad \text{(A3)}$$

We denote the three independent elements of the symmetric 2×2 matrix $\mathbf{B}_0^{-1}\mathbf{A}_0$ by W_{11}, W_{12}, W_{22}, and express the offset vector $\mathbf{x}_r - \mathbf{x}_s$ through its magnitude h and angle α with the x-axis. After carrying out the vector-matrix operations, equation A3 becomes:

$$T^2(\mathbf{x}_r, \mathbf{x}_s) = T_0^2 + \frac{T_0}{2}(W_{11}\cos^2\alpha + 2W_{12}\cos\alpha\sin\alpha + W_{22}\sin^2\alpha)\,h^2 = T_0^2 + \frac{h^2}{V_{\text{nmo}}^2(\alpha)}, \quad \text{(A4)}$$

where

$$V_{\text{nmo}}^{-2}(\alpha) = \frac{T_0}{2}(W_{11}\cos^2\alpha + 2W_{12}\cos\alpha\sin\alpha + W_{22}\sin^2\alpha). \quad \text{(A5)}$$

Equations A4 and A5 are equivalent to the equation of the NMO ellipse derived by Grechka & Tsvankin (1998). The parameters W_{11}, W_{12}, and W_{22} of the global matrix combination $\mathbf{B}_0^{-1}\mathbf{A}_0$ define the NMO ellipse and can be estimated from hyperbolic moveout analysis for at least three distinct azimuths of the CMP line. The NMO-velocity equations A4 and A5 appear to be similar to equations 10 and 11 for the azimuthally-varying time-migration velocity. However, NMO and time-migration velocities are identical only in the special case when the normal and image rays coincide, which happens in horizontally layered media. In order to derive a time-migration operator from NMO velocities (around the normal ray), it will be necessary to add dip information.

A1 Time migration based on NMO velocities

To develop a time-migration formalism using the normal ray and NMO velocities, we use an approach different from the one described in the main text. As before, we consider the diffraction time function of a hypothetical diffractor at the reflection point. But here we start from the normal ray (instead of the image ray) treating every time sample along the normal ray as a possible reflection point and stacking along the corresponding diffraction time function. The stacked amplitude value is assigned to the image time (two-way traveltime along the image ray). The image ray is the transmitted ray between the earth's surface and the reflection point, whose initial slowness vector is perpendicular to the surface. If no reflector is found at the endpoint of the normal ray, the amplitude obtained by summation is expected to vanish.

The diffraction time function of a diffractor at the endpoint ($\mathbf{x}' = \mathbf{0}$ and $\mathbf{p}'_0 = \mathbf{0}$) of the normal ray (in this case chosen as the central ray) is obtained from Hamilton's point characteristic in equation 7. For example, the traveltime from the receiver $\mathbf{x}_r$ to the diffraction point is

$$t(\mathbf{x}_r, \mathbf{x}' = \mathbf{0}) = t_0 - \mathbf{p}_0\cdot\mathbf{x}_r + \frac{1}{2}\mathbf{x}_r\cdot\mathbf{B}_0^{-1}\mathbf{A}_0\,\mathbf{x}_r\,, \quad \text{(A6)}$$

where t_0 is the exact one-way traveltime along the central ray; the initial slowness vector $\mathbf{p}_0$ and the product $\mathbf{B}_0^{-1}\mathbf{A}_0$ also correspond to that ray. The second-order (hyperbolic) approximation is obtained by squaring both sides of equation A6 and dropping third- and higher-order terms:

$$t^2(\mathbf{x}_r, \mathbf{x}' = \mathbf{0}) = [t_0 - \mathbf{p}_0\cdot\mathbf{x}_r]^2 + t_0\,\mathbf{x}_r\cdot\mathbf{B}_0^{-1}\mathbf{A}_0\,\mathbf{x}_r\,. \quad \text{(A7)}$$

The three independent elements W_{11}, W_{12}, W_{22} of the 2×2 symmetric matrix $\mathbf{B}_0^{-1}\mathbf{A}_0$ can be found from azimuthal moveout analysis, as discussed above (equations A4 and A5). Finally, the diffraction time function is obtained by substituting the NMO ellipse into equation A7 and adding a similar traveltime term for the transmitted ray from the source position $\mathbf{x}_s$:

$$T_D = \sqrt{[t_0 - \mathbf{p}_0\cdot\mathbf{x}_r]^2 + \frac{l_r^2}{V_{\text{nmo}}^2(\phi)}} + \sqrt{[t_0 - \mathbf{p}_0\cdot\mathbf{x}_s]^2 + \frac{l_s^2}{V_{\text{nmo}}^2(\gamma)}}. \quad \text{(A8)}$$

The distances l_r and l_s are measured from the normal ray (where the NMO ellipse is determined), and γ and ϕ are the azimuths to the source and receiver, respectively. Given the NMO ellipse and the initial slowness vector of the central ray, equation A8 yields the diffraction times for any source-receiver combination in the prestack data. The final image time and image position are found by simply searching for the shortest two-way time among all rays transmitted from the surface to the diffraction point.

Equation A8 helps us understand the difference between the two time-migration approaches discussed here. Whereas the algorithm based on the image-ray parameters (equation 12) requires only the time-migration velocities, time migration operating with the normal-ray parameters (equation A8) needs not just the NMO ellipse but also the initial slowness vector $\mathbf{p}_0$ (i.e., the horizontal slowness) of the normal ray. However, with the vector $\mathbf{p}_0$ estimated from zero-offset time slopes, the two approaches produce equivalent time-migration operators (in the second-order approximation). A post-stack version of time migration based on NMO velocities and zero-offset slopes is used in Söllner & Andersen (2005) for 3D kinematic imaging.

Stacking-velocity tomography with borehole constraints for tilted TI media

Xiaoxiang Wang & Ilya Tsvankin
Center for Wave Phenomena, Geophysics Department, Colorado School of Mines, Golden, Colorado 80401

ABSTRACT
Transversely isotropic models with a tilted symmetry axis (TTI) play an increasingly important role in seismic imaging, especially near salt bodies and in active tectonic areas. Here, we present a 2D parameter-estimation methodology for TTI media based on combining P-wave normal-moveout (NMO) velocities, zero-offset traveltimes, and reflection time slopes with borehole data that include the vertical group velocities as well as the reflector depths and dips.
For a dipping TTI layer with the symmetry axis confined to the dip plane of the reflector, estimation of the symmetry-direction velocity V_{P0}, the anisotropy parameters ϵ and δ, and the tilt ν of the symmetry axis proves to be ambiguous despite the borehole constraints. If the symmetry axis is orthogonal to the reflector (a model typical for dipping shale layers), V_{P0} and δ can be recovered with high accuracy, even when the symmetry axis deviates by $\pm 5^\circ$ from the reflector normal. The parameter ϵ, however, cannot be constrained for dips smaller than 60° without using nonhyperbolic moveout.
To invert for the interval parameters of layered TTI media, we apply 2D stacking-velocity tomography supplemented with the same borehole constraints. The dip planes in all layers are assumed to be aligned; also, the symmetry axis is set orthogonal to the reflector in each layer, which helps to avoid ambiguity caused by an unknown tilt ν. Synthetic tests confirm that estimation of the interval parameters V_{P0} and δ remains stable in the presence of Gaussian noise in the input data. Our algorithm can be used to build an accurate initial TTI model for post-migration reflection tomography and other techniques that employ migration velocity analysis.

Key words: transverse isotropy, tilted axis, TTI, moveout inversion, interval parameters, stacking velocity, dipping reflectors, tomography, borehole data

1 INTRODUCTION

Ignoring anisotropy in P-wave processing causes imaging and interpretation errors, such as mispositioning of horizontal and dipping reflectors (e.g., Alkhalifah & Larner, 1994; Alkhalifah *et al.*, 1996; Vestrum *et al.*, 1999). While many widely used migration algorithms have been extended to transversely isotropic (TI) media, constructing an accurate anisotropic velocity model remains a challenging problem. For TI models with a vertical symmetry axis (VTI), the depth-domain P-wave velocity field is controlled by the vertical velocity V_{P0} and the Thomsen (1986) parameters ϵ and δ. To resolve all three parameters individually, P-wave moveout typically has to be combined with shear modes (SS- or PS-waves) or borehole data (Tsvankin & Grechka, 2000; Sexton & Williamson, 1998).

Vertical transverse isotropy has proved to be adequate for most horizontally stratified, unfractured sediments. However, in progradational clastic or carbonate sequences, as well as in the presence of obliquely dipping fractures, the symmetry axis is tilted (Figure 1). Also, TI with a tilted symmetry axis (TTI) is an appropriate model for dipping shale layers near salt domes and in fold-and-thrust belts such as the Canadian Foothills (Isaac & Lawton, 1999; Vestrum *et al.*, 1999; Charles

flector depths, but also with the dips of all interfaces. First, we introduce a semi-analytic inversion procedure for a single TTI layer above a dipping interface and show that the medium parameters cannot be resolved without constraining the tilt of the symmetry axis. Then we develop joint tomographic inversion of moveout and borehole data for a stack of TTI layers with the symmetry axis orthogonal to the layer boundaries. Synthetic tests with a realistic level of Gaussian noise illustrate the stability of estimating the interval parameters V_{P0}, ϵ, and δ.

2 INVERSION FOR A SINGLE TTI LAYER

We start by considering the simple model of a homogeneous TTI layer above a planar dipping reflector. To make the problem 2D, the symmetry axis is assumed to be confined to the dip plane. The tilt angle ν is taken positive, if the symmetry axis is rotated counterclockwise from the vertical. P-wave surface data provide the zero-offset reflection time t_0, the reflection slope (horizontal slowness) p on the zero-offset time section, and the NMO velocity $V_{\rm nmo}$. Because the layer is homogeneous, it is sufficient to have the estimates of t_0, p, and $V_{\rm nmo}$ for a single common midpoint (CMP). At a location where a vertical well is available, we can measure the P-wave vertical group velocity along with the depth and dip of the reflector.

2.1 Arbitrary axis orientation

2.1.1 Inversion methodology

The exact P-wave phase-velocity function in TI media expressed through the Thomsen parameters is given by (Tsvankin, 1996, 2005)

$$\frac{V^2}{V_{P0}^2} = 1 + \epsilon \sin^2\theta - \frac{f}{2} + \frac{f}{2}\sqrt{1 + \frac{4\sin^2\theta}{f}(2\delta\cos^2\theta - \epsilon\cos 2\theta) + \frac{4\epsilon^2\sin^4\theta}{f^2}}, \tag{1}$$

where θ is the phase angle with the symmetry axis (assumed to be positive for counter-clockwise rotation), V_{P0} is the symmetry-direction velocity, and

$$f \equiv 1 - \frac{V_{S0}^2}{V_{P0}^2}; \tag{2}$$

V_{S0} is the symmetry-direction velocity of S-waves. Because the influence of V_{S0} on P-wave kinematics is negligible, the value of f can be set to a constant using a typical V_{P0}/V_{S0} ratio (e.g., $V_{P0}/V_{S0} = 2$). Therefore, the phase velocity V represents a function of the four medium parameters (V_{P0}, ϵ, δ, and ν) and the phase angle $\tilde{\theta}$ with the vertical:

$$V = f_1(V_{P0}, \epsilon, \delta, \tilde{\theta}, \nu); \tag{3}$$

the phase angle with the symmetry axis in equation 1 is $\theta = \tilde{\theta} - \nu$.

For the zero-offset reflection, the phase-velocity (slowness) vector is perpendicular to the reflector, and the phase angle with the vertical $\tilde{\theta}$ is equal to the dip ϕ_w (Figure 3a; the subscript "w" denotes well data). The phase velocity for the zero-offset reflection can be computed through the known values of ϕ_w and p as

$$V_{\phi_w} = \frac{\sin\phi_w}{p}. \tag{4}$$

Substituting equation 4 into equation 3 yields

$$f_1(V_{P0}, \epsilon, \delta, \phi_w, \nu) = \frac{\sin\phi_w}{p}. \tag{5}$$

The P-wave group velocity V_G in TI media can be found as a function of the phase velocity V and its derivative with respect to θ (e.g., Tsvankin, 2005):

$$V_G = V\sqrt{1 + \left(\frac{1}{V}\frac{dV}{d\theta}\right)^2}. \tag{6}$$

Therefore, V_G represents a function (different from f_1) of the parameters V_{P0}, ϵ, δ, $\tilde{\theta}$, and ν:

$$V_G = f_2(V_{P0}, \epsilon, \delta, \tilde{\theta}, \nu). \tag{7}$$

The P-wave group angle ψ with the symmetry axis is also controlled by the angle-dependent phase velocity (e.g., Tsvankin, 2005):

$$\tan\psi = \frac{\tan\theta + \frac{1}{V}\frac{dV}{d\theta}}{1 - \frac{\tan\theta}{V}\frac{dV}{d\theta}}. \tag{8}$$

Therefore, the angle $\tilde{\psi}$ with the vertical in a TTI layer can be rewritten as

$$\tilde{\psi} = f_3(V_{P0}, \epsilon, \delta, \tilde{\theta}, \nu). \tag{9}$$

For the zero-offset reflection, the phase angle $\tilde{\theta} = \phi_w$ (Figure 3a), so

$$V_{G0} = f_2(V_{P0}, \epsilon, \delta, \phi_w, \nu), \tag{10}$$

and the group angle with the vertical is

$$\tilde{\psi}_0 = f_3(V_{P0}, \epsilon, \delta, \phi_w, \nu). \tag{11}$$

The length of the zero-offset raypath (AB in Figure 3a) can be calculated from the vertical thickness z_w of the layer and the angles ϕ_w and $\tilde{\psi}_0$ (Figure 3a). AB can also be expressed through the two-way zero-offset reflection time t_0 and the group velocity given by equation 10:

$$\frac{z_w\cos\phi_w}{\cos(\tilde{\psi}_0 - \phi_w)} = \frac{V_{G0}\,t_0}{2}; \tag{12}$$

$\tilde{\psi}_0$ is found from equation 11. Note that if the CMP is displaced from the well by a known distance, equation 12 can be modified accordingly. Hence, we have constructed two equations (5 and 12) for the four unknown parameters.

	Actual	Estimated	
		mean	sd
V_{P0} (km/s)	2.50	2.92	0.25
ϵ	0.25	0.15	0.77
δ	0.10	-0.14	0.14
ν (°)	50	-20	33
Dip (°)	30	–	–
Depth (km)	1	–	–

Table 1. Actual and estimated parameters of a TTI layer. The dip and depth are measured at the well location. The input data were contaminated by Gaussian noise with the standard deviations equal to 1% for p and t_0, and 2% for $V_{\rm nmo}$ and V_{Gw}. The standard deviations and mean values of the inverted parameters are denoted by "sd" and "mean," respectively.

to be highly unstable, with small errors in the data producing large distortions in the estimated parameters. This instability is partially caused by the nonlinear dependence of the phase velocity V on the tilt ν (Grechka *et al.*, 2002a). Similar results were obtained for a wide range of model parameters.

2.2 Symmetry axis orthogonal to the reflector

If TTI symmetry is associated with dipping shale layers, the symmetry axis is typically orthogonal to the layer boundaries (Isaac & Lawton, 1999; Vestrum *et al.*, 1999; Charles *et al.*, 2008). Fixing the orientation of the symmetry axis helps to overcome the nonuniqueness of the inversion procedure (Grechka *et al.*, 2002a; Zhou *et al.*, 2008; Behera & Tsvankin, 2009).

2.2.1 Inversion methodology

If the symmetry axis is orthogonal to the reflector, the tilt ν is equal to the reflector dip ϕ_w measured in the well. Also, the phase-velocity vector of the zero-offset reflection is parallel to the symmetry axis, and the velocity V_{P0} can be obtained directly from surface data and the dip ϕ_w:

$$V_{P0} = \frac{\sin\phi_w}{p}\,. \tag{22}$$

The NMO velocity for $\nu = \phi_w$ is given by the isotropic cosine-of-dip relationship (Tsvankin, 2005):

$$V_{\rm nmo} = \frac{V_{\rm nmo}(0)}{\cos\phi_w}\,, \tag{23}$$

where $V_{\rm nmo}(0) = V_{P0}\sqrt{1+2\delta}$. Since V_{P0} is already known, equation 23 constrains the parameter δ.

Because the group and phase velocities in the symmetry direction coincide, equation 18 contains only known quantities and can be used to check the validity of the model. Therefore, the inverse problem reduces to estimating the parameters ϵ and $\tilde{\theta}_w$ from the vertical group velocity (i.e., from equations 19 and 20):

$$f_2(V_{P0}, \epsilon, \delta, \tilde{\theta}_w, \phi_w) = V_{Gw}\,; \tag{24}$$

$$f_3(V_{P0}, \epsilon, \delta, \tilde{\theta}_w, \phi_w) = 0\,. \tag{25}$$

Evidently, when $\nu = \phi_w$, the inversion equations do not include z_w and are independent of the CMP location. Moreover, if the well is not vertical but its inclination is known, equations 24 and 25 retain the same form with a nonzero group angle on the right-hand side of equation 25.

2.2.2 Synthetic examples

First, we perform a test on noise-contaminated data for a model with $\nu = \phi_w = 30°$ and typical values of the Thomsen parameters (Figure 4a). The parameters V_{P0} and δ can be estimated with high accuracy; the mean value of V_{P0} is 2.50 km/s with the standard deviation 1%; the mean value of δ is 0.10 with the standard deviation 0.03. However, the parameter ϵ is practically unconstrained (the standard deviation is 1.37). The instability in estimating ϵ can be explained using the linearized weak-anisotropy approximation. For weak anisotropy, the phase and group velocities coincide (Thomsen, 1986), and for the vertical ray

$$V_{Gw} = V_{P0}(1 + \delta\sin^2\phi_w\cos^2\phi_w + \epsilon\sin^4\phi_w)\,. \tag{26}$$

For moderate dips, such as $\phi_w = 30°$ used in the test, the contribution of ϵ is much smaller than that of δ because ϵ is multiplied with $\sin^4\phi_w$.

We repeated the test for a range of dips with the results listed in Table 2. The estimates of V_{P0} and δ are sufficiently accurate, with small (and practically constant) standard deviations for all dips. The errors in the parameter ϵ, however, are much larger; to resolve ϵ from the vertical group velocity, the dip (and tilt) should reach at least 60°. Our algorithm operates with NMO velocity, which controls reflection moveout for offset-to-depth ratios limited by unity. If long-spread P-wave data (with the offset-to-depth ratio reaching two) are available, it is possible to estimate ϵ from nonhyperbolic moveout (Behera & Tsvankin, 2009).

If the symmetry axis is not orthogonal to the reflector, the algorithm based on setting $\nu = \phi_w$ produces errors in the inverted parameters. However, for typical moderate magnitudes of ϵ and δ ($|\epsilon| \le 0.5$; $|\delta| \le 0.3$), the errors in V_{P0} and δ remain small, if the symmetry axis deviates from the reflector normal by less than 5° and the dip ranges from 5° to 50° (Table 3). For example, we computed the input data with the actual tilt $\nu = 15°$ and dip $\phi_w = 20°$, then obtained the parameters $V_{P0} = 2.5$ km/s and $\delta = 0.11$ under the as-

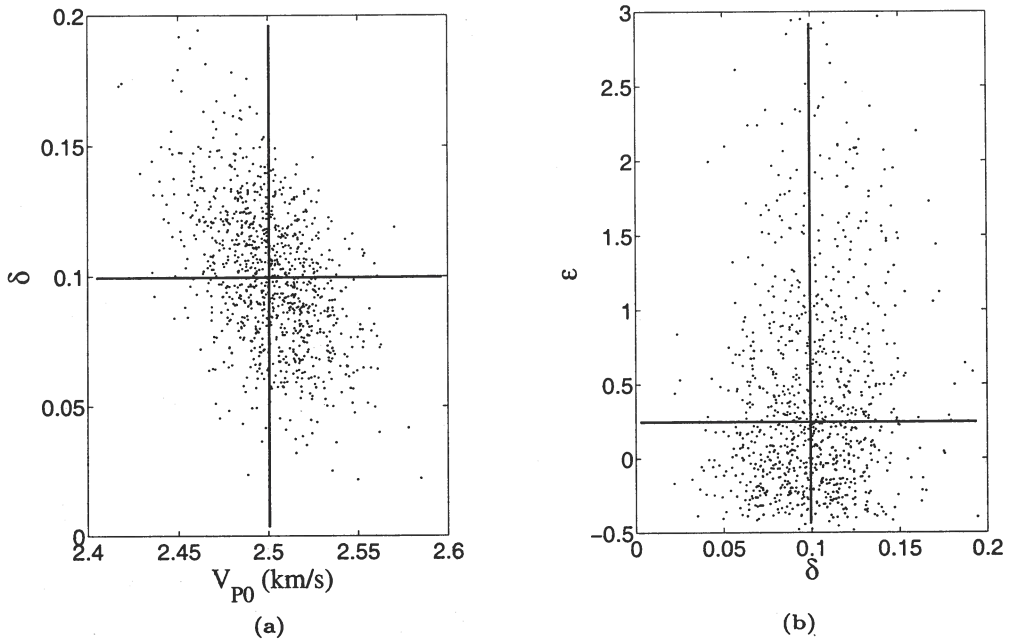

Figure 4. Inversion results (dots) for a TTI layer with the symmetry axis orthogonal to its bottom. The inversion was carried out for 1000 realizations of input data contaminated by Gaussian noise with the standard deviations equal to 1% for the reflection slope p and 2% for $V_{\rm nmo}$ and V_{Gw}. Due to the large standard deviation (1.37) of ϵ, the ϵ-axis on plot (b) is clipped. The actual parameter values are marked by the crosses. The starting model was isotropic.

also obtained by ray tracing in the trial model. Fitting the interval velocity $V_{Gw}^{(n)}$ is equivalent to solving equations 24 and 25 for a single layer because the phase angle $\tilde{\theta}_w$ for the vertical ray is obtained from the trial medium parameters.

Reflection slopes in layered media cannot yield the interval symmetry-direction velocities directly (as in equation 22). Instead, we use the slopes $p(n)$ and zero-offset traveltimes $t_0(n)$ (equation 28) to construct the one-way zero-offset rays for the trial TTI parameters and compute the "trial" reflector depths in the well. For the first layer, the vertical slowness of the zero-offset ray and the slowness vector as a whole can be computed from the trial parameters $\tilde{m}_1$ and the horizontal slowness $p(1)$ using the Christoffel equation. The group-velocity vector (zero-offset ray) in the first layer is then calculated from the slowness vector. The zero-offset reflection point is found from the traveltime $t_0(1)$, which allows us to compute the depth of the first reflector $z_{\rm calc}^{(1)}$ at the well location. After the first interface has been reconstructed, we repeat the same procedure for the second interface by tracing "back" the zero-offset ray with the slope $p(2)$ (see Grechka *et al.*, 2002b). Continuing this procedure downward yields the estimated reflector depths $z_{\rm calc}^{(n)}$, which can be compared with the measured values.

The interval parameters $V_{P0}^{(n)}, \epsilon^{(n)}, \delta^{(n)}$ are estimated by minimizing the following objective function that contains the differences between the calculated ("calc") and measured quantities:

$$\mathcal{F}(\tilde{m}) \equiv \sum_{n=1}^{N} \Big(\big\| V_{\rm nmo,calc}(n) - V_{\rm nmo}(n) \big\| + \big\| z_{w,\rm calc}^{(n)} - z_w^{(n)} \big\| + \big\| V_{Gw,\rm calc}^{(n)} - V_{Gw}^{(n)} \big\| \Big). \tag{29}$$

Grechka *et al.* (2002b) fit only P-wave NMO ellipses in their objective function, because their input data did not include borehole information. Our algorithm operates with 2D data, so we use a single NMO velocity instead of the three parameters of the NMO ellipse. However, we also add two quantities ($z_w^{(n)}$ and $V_{Gw}^{(n)}$) measured from borehole data. Note that the dips $\phi_w^{(n)}$ have been used to constrain the tilt $\nu^{(n)}$ of the symmetry axis in each layer.

For a single layer, the parameter ϵ is constrained only by equations 24 and 25. However, for layered TTI media, $\epsilon^{(n)}$ also contributes to $z_{\rm calc}^{(n)}$ and $V_{\rm nmo,calc}(n)$ (except for $n = 1$). Therefore, although we established that $\epsilon^{(n)}$ cannot be resolved from conventional-spread P-wave data for dips smaller than 60°, it has to be estimated together with $V_{P0}^{(n)}$ and $\delta^{(n)}$. This tomographic inversion can be applied to a single CMP since each layer is laterally homogeneous with planar boundaries.

It should be emphasized that we invert for all interval parameters simultaneously without employing layer

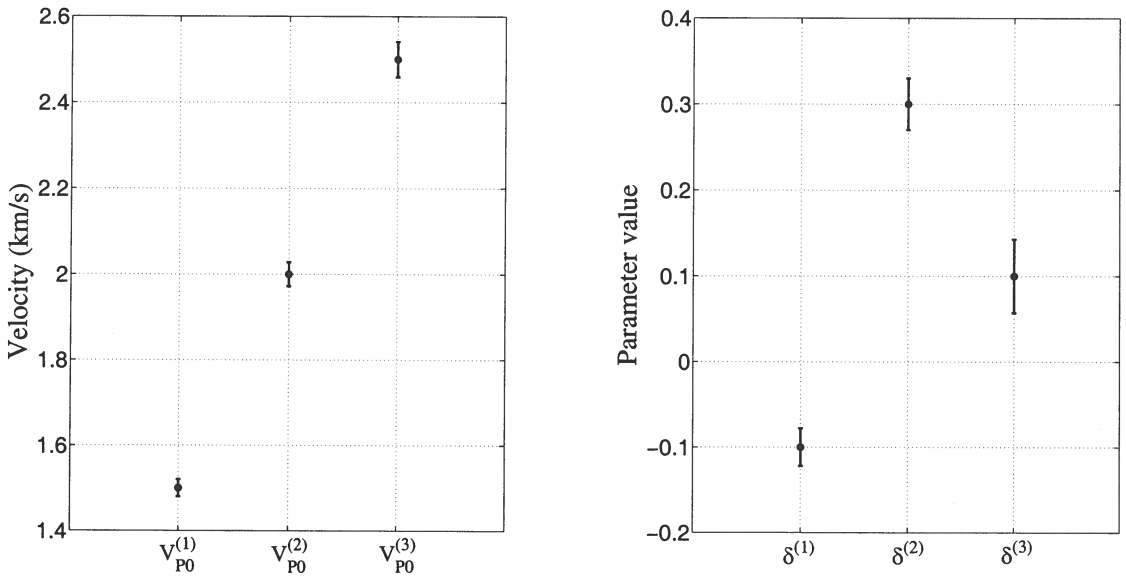

Figure 6. a) Interval symmetry-direction velocities $V_{P0}^{(n)}$ and b) anisotropy parameters $\delta^{(n)}$ $(n = 1, 2, 3)$ estimated by the tomographic inversion for the model from Figure 5 and Table 4. The dots mark the exact values, and the bars correspond to the $\pm$ standard deviation in each parameter.

reflector depth. By performing the inversion for all layers simultaneously, the algorithm mitigates error accumulation with depth. As is the case for a single layer, V_{P0} and δ are well-resolved, while ϵ is poorly constrained for small and moderate reflector dips. If long-spread P-wave data are available, ϵ can be obtained from nonhyperbolic moveout inversion.

Our algorithm can be extended in a straightforward way to 3D wide-azimuth P-wave data by replacing the NMO velocities in the objective function with the NMO ellipses. If the dip and strike of each reflector are measured in the borehole, the orientation of the symmetry axis in each layer is known. Therefore, wide-azimuth data provide additional information for estimating the same interval TTI parameters (V_{P0}, ϵ, and δ), which should enhance the stability of the inversion procedure and reduce errors caused by the deviation of the symmetry axis from the reflector normal.

Stacking-velocity tomography, possibly supplemented with nonhyperbolic moveout inversion for ϵ, represents an efficient tool for building an initial model for migration velocity analysis (MVA) and post-migration reflection tomography. After carrying out the interval parameter estimation at well locations, the V_{P0}- and δ-fields can be computed by interpolation between the wells. An accurate initial TTI model is critically important to ensure the convergence of MVA-based algorithms.

5 ACKNOWLEDGMENTS

We are grateful to Andrey Bakulin (WesternGeco), Paul Fowler (WesternGeco), Vladimir Grechka (Shell), and Andres Pech (IPN, Mexico) for making available their codes and numerous helpful suggestions. We are also grateful to our colleagues from the Center for Wave Phenomena (CWP) for valuable discussions and technical help. This work was supported by the Consortium Project on Seismic Inverse Methods for Complex Structures at CWP.

References

Alkhalifah, T., & Larner, K. 1994. Migration error in transversely isotropic media. *Geophysics*, **59**, 1405–1418.

Alkhalifah, T., Tsvankin, I., Larner, K., & Toldi, J. 1996. Velocity analysis and imaging in transversely isotropic media: Methodology and a case study. *The Leading Edge*, **15**, 371–378.

Behera, L., & Tsvankin, I. 2009. Migration velocity analysis for tilted TI media. *Geophysical Prospecting*, **57**, 13–26.

Charles, S., Mitchell, D. R., Holt, R. A., Lin, J., & Mathewson, J. 2008. Data-driven tomographic velocity analysis in tilted transversely isotropic media: A 3D case history from the Canadian Foothills. *Geophysics*, **73**, VE261–VE268.

Elastic wave mode separation for TTI media

Jia Yan and Paul Sava
Center for Wave Phenomena, Colorado School of Mines

ABSTRACT
The separation of wave modes for isotropic elastic wavefields is typically done using Helmholtz decomposition. However, Helmholtz decomposition using conventional divergence and curl operators does not give satisfactory results in anisotropic media and leaves the different wave modes only partially separated. The separation of anisotropic wavefields requires the use of more sophisticated operators which depend on local material parameters. Wavefield separation operators for TI (transverse isotropic) models can be constructed based on the polarization vectors evaluated at each point of the medium by solving the Christoffel equation using local medium parameters. These polarization vectors can be represented in the space domain as localized filters, which resemble conventional derivative operators. The spatially-variable "pseudo" derivative operators perform well in 2D heterogeneous TI media even at places of rapid variation. Wave separation for 3D TI media can be performed in a similar way. In 3D TI media, P and SV waves are polarized only in symmetry planes, and SH waves are polarized orthogonal to symmetry planes. Using the mutual orthogonality property between these modes, we only need to solve for the P wave polarization vectors from the Christoffel equation, and SV and SH wave polarizations can be constructed using the relationship between these three modes. Synthetic results indicate that the operators can be used to separate wavefields for TI media with arbitrary strength of anisotropy.

Key words: elastic, imaging, TTI, heterogeneous

1 INTRODUCTION

wave-equation migration for elastic data usually consists of two steps. The first step is wavefield reconstruction in the subsurface from data recorded at the surface. The second step is the application of an imaging condition which extracts reflectivity information from the reconstructed wavefields.

The elastic wave-equation migration for multicomponent data can be implemented in two ways. The first approach is to separate recorded elastic data into the compressional and transverse (P and S) modes and use these separated modes for acoustic wave-equation migration respectively. This acoustic imaging approach to elastic waves is used most frequently, but it is fundamentally based on the assumption that P and S data can be successfully separated on the surface, which is not always true (Etgen, 1988; Zhe & Greenhalgh, 1997). The second approach is to not separate P and S modes on the surface, extrapolate the entire elastic wavefield at once, then separate wave modes prior to applying an imaging condition. The reconstruction of elastic wavefields can be implemented using various techniques, including reconstruction by time reversal (RTM) (Chang & McMechan, 1986, 1994) or by Kirchhoff integral techniques (Hokstad, 2000).

The imaging condition applied to the reconstructed vector wavefields directly determines the quality of the images. The conventional cross-correlation imaging condition does not separate the wave modes and cross-correlates the Cartesian components of the elastic wavefields. In general, the various wave modes (P and S) are mixed on all wavefield components and cause crosstalk and image artifacts. Yan & Sava (2008b) suggest using imaging conditions based on elastic potentials, which require cross-correlation of separated modes. Potential-based imaging condition creates images that have a clear physical meaning, in contrast to images obtained with Cartesian wavefield components, thus justifying the need for wave mode separation.

As the need for anisotropic imaging increases, processing and migration are performed more frequently based on anisotropic acoustic one-way wave equations (Alkhalifah, 1998, 2000; Shan, 2006; Shan & Biondi, 2005; Fletcher et al., 2008). However, less research has been done on anisotropic elastic migration based on two-way wave equations. Elastic Kirch-

medium in the symmetry plane, and they can change from location to location according to the material parameters.

The separation of P and SV wavefields can be similarly accomplished for both VTI and TTI media. However, the filters for TTI and VTI media are different. The main difference is that for VTI media, waves propagating in all vertical planes are simply P and SV wave modes. However, for TTI media, only P and SV wave modes are polarized in the vertical symmetry plane, and SH waves are decoupled from P and SV modes, while in other vertical planes, the propagating waves are a mix of P, SV, and SH modes. Therefore, the 2D wave mode separation works for the vertical symmetry plane or other non-vertical symmetry planes of TTI media.

For a medium with arbitrary anisotropy, we obtain the polarization vectors $\mathbf{U}(\mathbf{k})$ by solving the Christoffel equation (Aki & Richards, 2002; Tsvankin, 2005):

$$\left[\mathbf{G} - \rho V^2 \mathbf{I}\right] \mathbf{U} = 0\,, \tag{3}$$

where $\mathbf{G}$ is the Christoffel matrix with $G_{ij} = c_{ijkl} n_j n_l$, in which c_{ijkl} is the stiffness tensor, n_j and n_l are the normalized wave vector components in the j and l directions with $i, j, k, l = 1, 2, 3$. The parameter V corresponds to the eigenvalues of the matrix $\mathbf{G}$ and represents the phase velocities of different wave modes as functions of the wave vector $\mathbf{k}$ (corresponding to n_j and n_l in the matrix $\mathbf{G}$). For plane waves propagating in a symmetry plane of a TTI medium, since qP and qSV modes are decoupled from the SH mode and polarized in the symmetry planes, we can set $k_y = 0$ and get

$$\begin{bmatrix} G_{11} - \rho V^2 & G_{12} \\ G_{12} & G_{22} - \rho V^2 \end{bmatrix} \begin{bmatrix} U_x \\ U_z \end{bmatrix} = 0\,, \tag{4}$$

where

$$G_{11} = c_{11} k_x^2 + 2c_{15} k_x k_z + c_{55} k_z^2\,, \tag{5}$$

$$G_{12} = c_{15} k_x^2 + (c_{13} + c_{55})\, k_x k_z + c_{35} k_x^2\,, \tag{6}$$

$$G_{22} = c_{55} k_x^2 + 2c_{35} k_x k_z + c_{33} k_z^2\,. \tag{7}$$

This equation allows us to compute the polarization vectors $\mathbf{U}_P = \{U_x, U_z\}$ and $\mathbf{U}_{SV} = \{-U_z, U_x\}$ (the eigenvectors of the matrix) for P and SV wave modes given the stiffness tensor at every location of the medium. Here, the symmetry axis of the TTI medium is not aligned with vertical axis of the Cartesian coordinates, and the TTI Christoffel matrix takes a different form than the VTI form.

Figure 2(b) shows the z and x components of the P wave polarization vectors of a TTI medium with a 30° tilt angle, and Figure 2(c) shows the polarization vectors projected onto the symmetry axis and the isotropy plane (30° and -60°). Comparing Figure 2(a) and 2(c), we see that the polarization vectors of this TTI medium are rotated 30° from those of the VTI medium. However, notice that: the z and x components of the polarization vectors for the VTI medium, Figure 2(a), are symmetric with respect to x and z axes, respectively; while the polarization vector components for the TTI medium, Figure 2(c), are not.

In order to maintain the continuity at the negative and positive Nyquist wavenumbers, $-\pi$ and π radians, we apply a taper to the vector components. For VTI media, a taper corresponding to the function (Yan & Sava, 2008a)

$$f(k) = -\frac{8\sin(k)}{5k} + \frac{2\sin(2k)}{5k} - \frac{8\sin(3k)}{105k} + \frac{\sin(4k)}{140k} \tag{8}$$

can be applied to the x and z components of the polarization vectors. The taper ensures that the Fourier domain derivatives are 0 at the positive and negative Nyquist wavenumbers in the derivative directions. They are also continuous in the z and x directions, respectively, due to the symmetry. The taper applied to isotropic polarization vectors $\mathbf{k}$ leads to the normal finite difference operators in the space domain (Yan & Sava, 2008a). Therefore, the VTI operators degenerate to normal derivatives $\frac{\partial}{\partial x}$ and $\frac{\partial}{\partial z}$ when the anisotropic parameters ϵ and δ are both zero.

For TTI media, due to the asymmetry of the Fourier domain derivatives, we need to apply a rotational symmetric taper to the polarization vector components. A simple Gaussian taper

$$f(k) = Exp\left[-\frac{||\mathbf{k}||^2}{2\sigma^2}\right] \tag{9}$$

can be applied to both components of TTI media polarization vectors. We choose a standard deviation of $\sigma = 1$. In this case, at the positive and negative Nyquist wavenumbers ($-\pi$ and π radians), the magnitude of this taper is about 3% of the peak value, and the components can be safely assumed to be continuous across the Nyquist wavenumbers. However, after applying this taper, even for isotropic media, the space domain derivatives are not the conventional finite difference operators. Compared to conventional finite difference operators which are 1D stencils, the derivatives constructed after the application of the Gaussian taper are represented by 2D stencils.

Figure 3 illustrates the application of the Gaussian taper to the polarization vectors shown in Figure 2. Figures 3(a), 4(a) and Figures 3(b), 4(b) are the k and x domain representations of the polarization vector components for the VTI medium and the TTI medium after applying the Gaussian taper, respectively; Figures 3(c) and 4(c) are the polarization vectors projected on the symmetry axis and isotropy plane of the TTI medium. We see that the derivatives in the k domain are now continuous across the Nyquist wavenumbers in both x and z directions, and that the x domain derivatives are 2D compared to the conventional 1D finite difference operators.

We can apply the procedure described here to heterogeneous media by computing two different operators, namely U_x and U_z, at every grid point. In any symmetry plane of a TTI medium, the operators are 2D and depend on the local values of the stiffness coefficients. For each point, we pre-compute the polarization vectors as a function of the local medium parameters and transform them to the space domain to obtain the wave mode separators. We assume that the medium parameters vary smoothly (locally homogeneous), but even for complex media, the localized operators work similarly as the long finite difference operators would work for locations where medium parameters change rapidly.

If we represent the stiffness coefficients using Thomsen

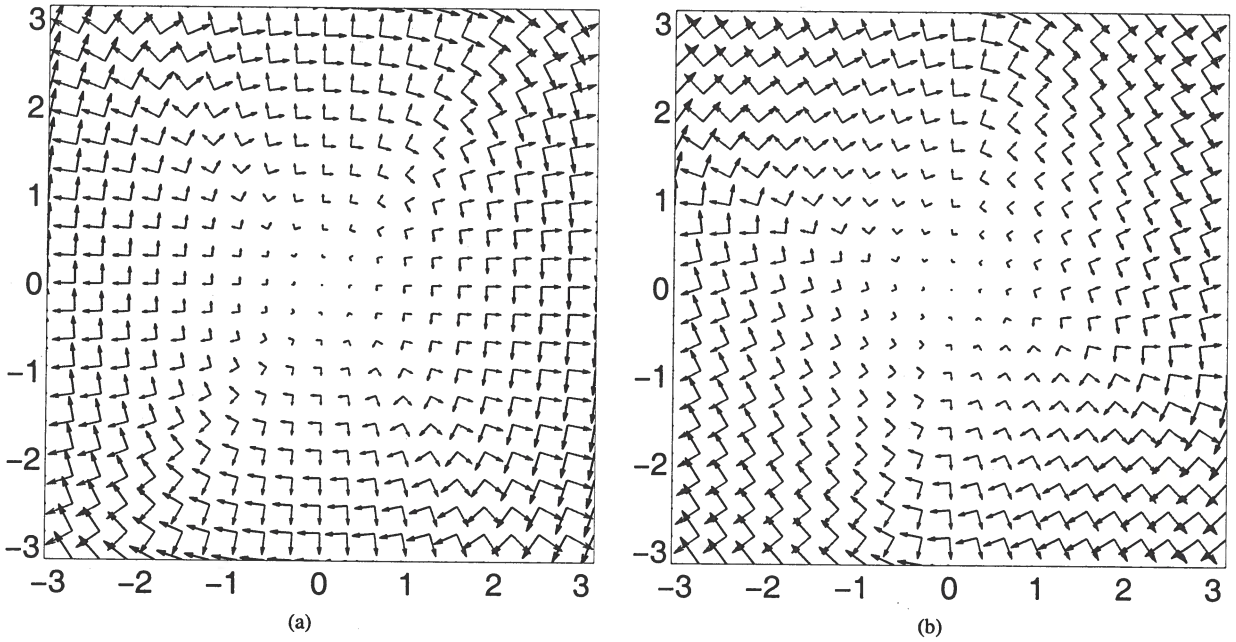

Figure 1. The qP and qS polarization vectors as a function of normalized wavenumbers k_x and k_z ranging from -1 to $+1$ cycles, for (a) a VTI model with $V_{P0} = 3$ km/s, $V_{S0} = 1.5$ km/s, $\epsilon = 0.25$ and $\delta = -0.29$ (b) a TTI model with the same model parameters as (a) and a symmetry axis tilt $\nu = 30°$. The arrows in almost radial directions are the qP wave polarization vectors, and the arrows in almost tangential directions are the qS wave polarization vectors.

the SV wave is obtained by

$$\begin{aligned} \widetilde{qSV} &= i\,\mathbf{U}_{SV}(\mathbf{k}) \cdot \widetilde{\mathbf{W}} \\ &= -i\,U_x U_z\,\widetilde{W}_x - i\,U_y U_z\,\widetilde{W}_y + i\,(U_x^2 + U_y^2)\,\widetilde{W}_z \\ &= SV\sqrt{U_x^2 + U_y^2}\,, \end{aligned} \tag{25}$$

and the SH wave is obtained by

$$\begin{aligned} \widetilde{qSH} &= i\,\mathbf{U}_{SH}(\mathbf{k}) \cdot \widetilde{\mathbf{W}} \\ &= -i\,U_y\,\widetilde{W}_x + i\,U_x\,\widetilde{W}_y \\ &= SH\sqrt{U_x^2 + U_y^2}\,. \end{aligned} \tag{26}$$

We can see that SV and SH waves are scaled differently than the P wave. The SV and SH waves are scaled by the magnitude $\sqrt{U_x^2 + U_y^2}$, which more or less characterizes wave propagation directions. This scaling factor goes from zero in the vertical propagation direction to unity in the horizontal propagation directions.

For general 3D TI media whose symmetry axis has non-zero tilt and azimuth, we simply need to represent the symmetry-axis vector as $\{\sin\nu\cos\alpha, \sin\nu, \sin\alpha, \cos\nu\}$, where ν and α are the symmetry axis tilt and azimuth angles, respectively (Figure 5(b)). The P wave polarization can be computed from the TTI Christoffel equation, and SH and SV wave polarizations can be calculated from P wave polarization and the symmetry axis vector using the orthogonality between these modes.

The wave polarization vectors for P, SV, and SH waves can be brought to space domain to construct spatial filters for 3D heterogeneous TI media. Therefore, wave mode separation would work for models that have complex structures and tributary tilts of TI symmetry.

4 EXAMPLES

We illustrate the anisotropic wave mode separation with a simple fold synthetic example and a more challenging elastic model based on the elastic Marmousi II model (Bourgeois et al., 1991). We then show the wave mode separation for a 3D isotropic model and a 3D VTI model.

4.1 2D TTI fold model

We consider the 2D TTI model shown in Figure 7. Panels 7(a) to 7(f) shows the P and S wave velocities along the local symmetry axis, parameters ϵ, δ and the local tilts ν of the model, respectively. The symmetry axis is orthogonal to the reflectors throughout the model. Figure 8 illustrates the pseudo-derivative operators obtained at different locations in the model defined by the intersections of x coordinates 0.15, 0.3, 0.45 km and z coordinates 0.15, 0.3, 0.45 km, shown by the dots in Figure 7(f). The operators are projected onto their local symmetry axis and the isotropy plane (the direction orthogonal to it). Since the operators correspond to different combinations of V_P/V_S ratio along the symmetry axis and parameters ϵ, δ and tilt angle ν, they have different forms.

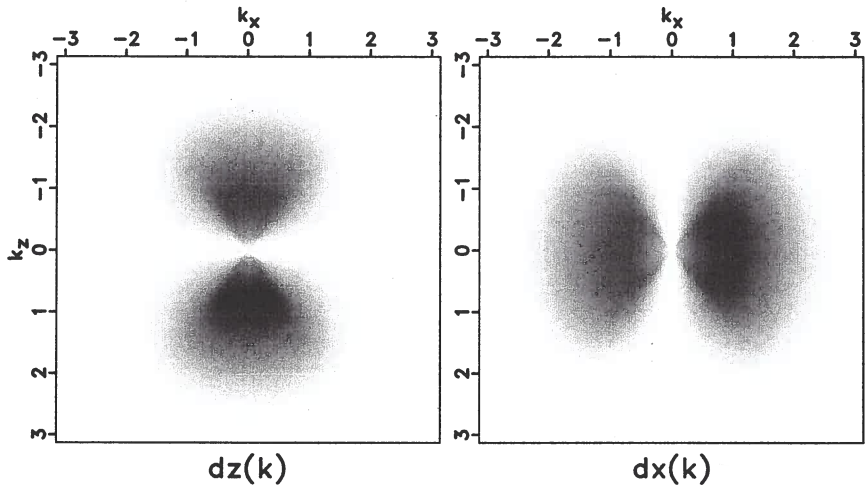

(a)

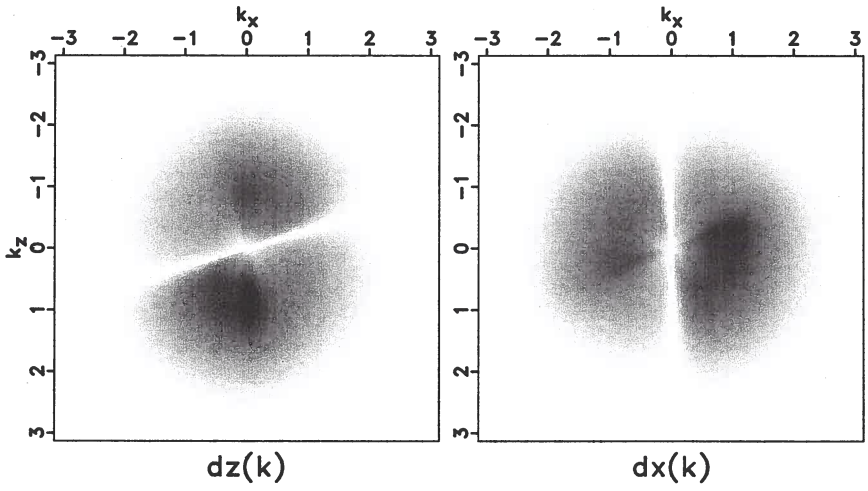

(b)

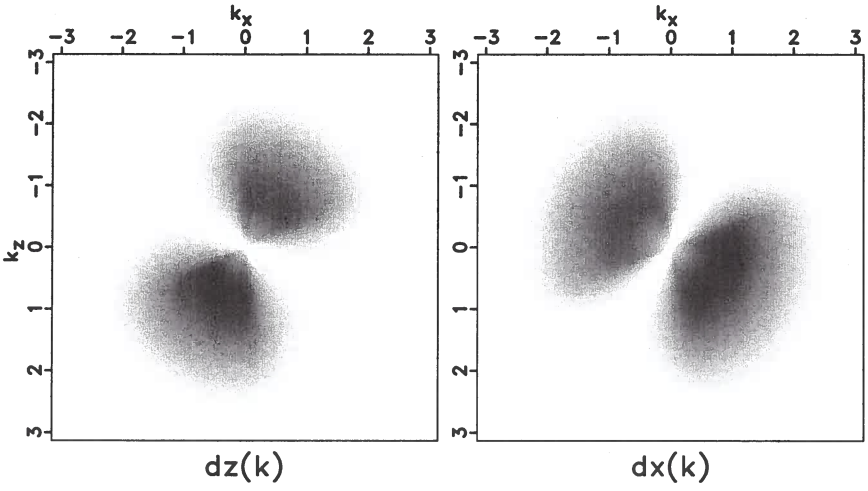

(c)

Figure 3. The polarization vectors in the wavenumber domain for the models shown in Figure 2. The wavenumber domain vectors are tapered by the function $Exp\left[-\frac{k_x^2+k_z^2}{2}\right]$ to avoid Nyquist discontinuity. Panel (a) corresponds to the VTI medium, panel (b) corresponds to the TTI medium, and panel (c) is the projection of the polarization vectors shown in (b) on the tilt axis and the isotropy plane.

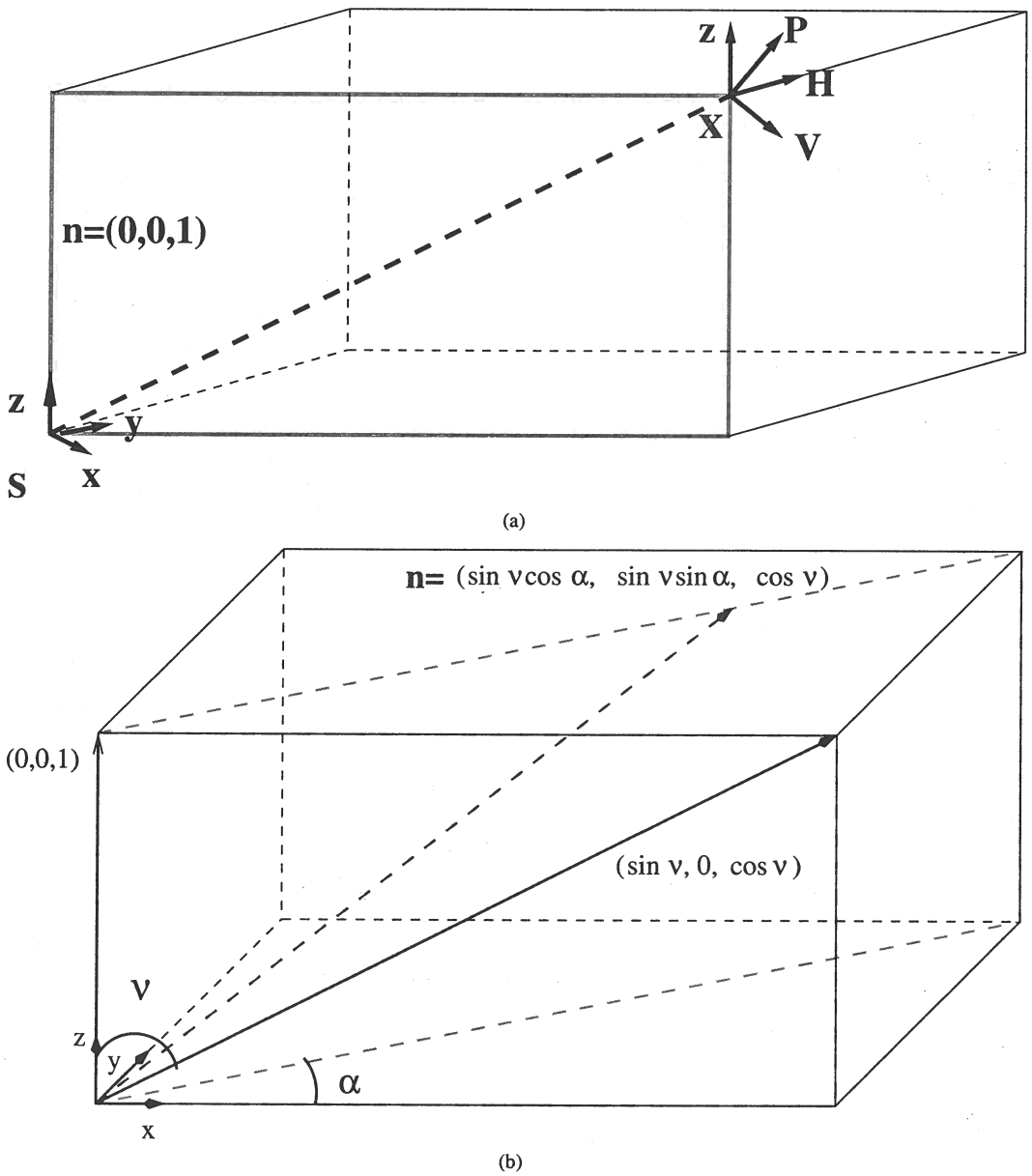

Figure 5. (a) A schematic showing the elastic wave modes polarization in a 3D VTI medium. S is the source, and x represents the coordinates of a spatial point. $\mathbf{n} = \{0, 0, 1\}$is the symmetry axis of the VTI medium. The wave mode P is polarized in the direction $\{U_x, U_y, U_z\}$, the wave mode SV is polarized in the direction $\{-U_x U_z, -U_y U_z, U_x^2 + U_y^2\}$, and the wave mode SH wave is polarized in the direction $\{-U_y, U_x, 0\}$. (b) A schematic showing the symmetry axis for a general TTI medium whose tilt and symmetry axis are both non-zero. The symmetry axis $=\{\sin\nu\cos\alpha, \sin\nu, \sin\alpha, \cos\nu\}$.

As we can see, the orientation of the operators conforms to the corresponding tilts at the locations shown by the dots in Figure 7(f).

Figure 9(a) shows the vertical and horizontal components of one snapshot of the simulated elastic anisotropic wavefield; Figure 9(b) shows the separation to qP and qS modes using VTI filters, i.e., by assuming zero tilt throughout the model; and Figure 9(c) shows the mode separation obtained with the correct TTI operators constructed using the local medium parameters with correct tilts. A comparison of Figure 9(b) and 9(c) indicates that the spatially-varying derivative operators with correct tilts successfully separate the elastic wavefields into qP and qS modes, while the VTI operators only work in the part of the model where it is locally VTI. The separation using VTI filters fails at locations where the local dip is large. For example, at coordinates $x = 0.42$ km and $z = 0.1$ km, we see strong S wave residual in the qP panel; and at coordinates

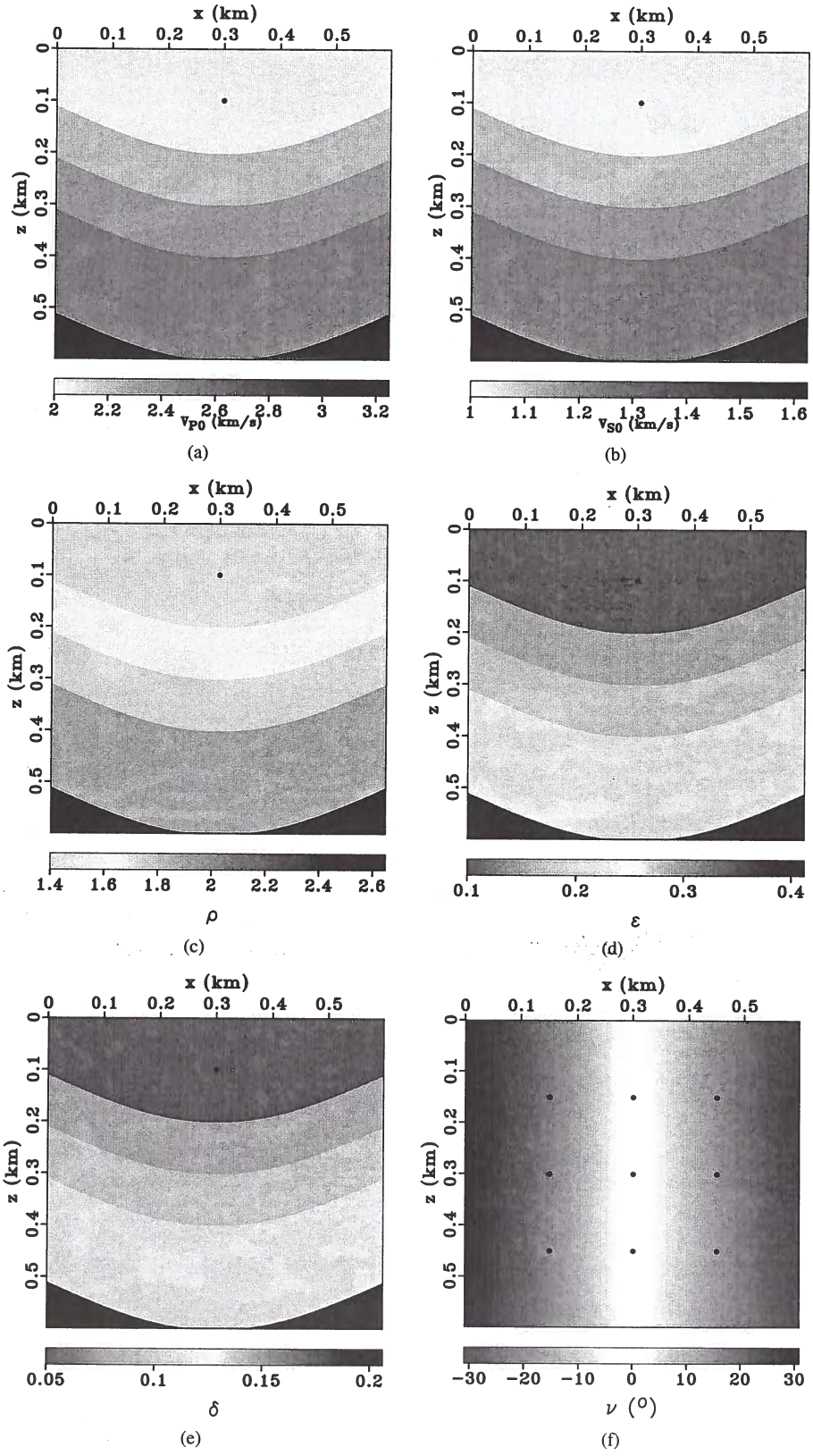

Figure 7. A fold model with parameters (a) P wave velocity along the local symmetry axis, (b) S wave velocity along the local symmetry axis, (c) density, (d) ϵ, (e) δ, and (f) tilt angle ν. A vertical point force source is located at $x = 0.3$ km and $z = 0.1$ km shown by the dot in panel (b) to (f). The dots in panel (f) correspond to the locations of the anisotropic operators shown in Figure 8.

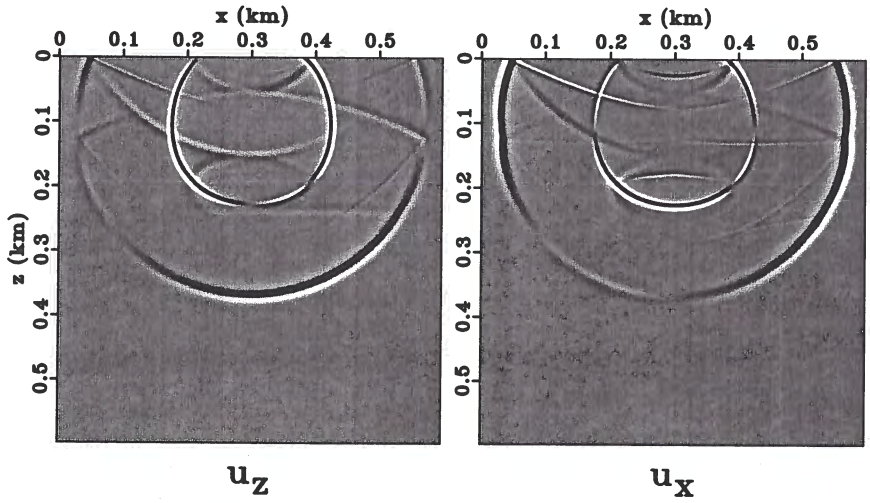

(a)

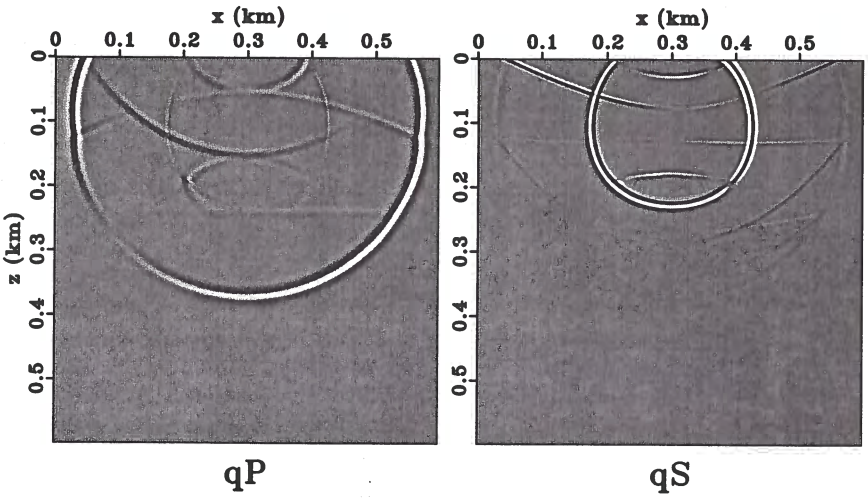

(b)

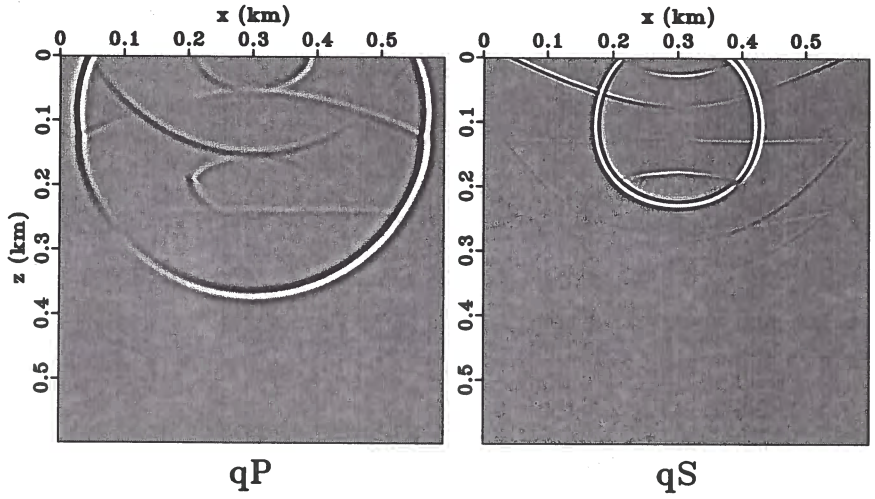

(c)

Figure 9. (a) A snapshot of the anisotropic wavefield simulated with a vertical point displacement source at $x = 0.3$ km and $z = 0.1$ km for the model shown in Figure 7, (b) anisotropic qP and qS modes separated using VTI pseudo-derivative operators and (c) anisotropic qP and qS modes separated using TTI pseudo-derivative operators. The separation of wavefields into qP and qS modes in (b) is not complete, which is visible such as at coordinates $x = 0.4$ km and $z = 0.9$ km. In contrast, the separation in (c) is better, because the correct anisotropic derivative operators are used.

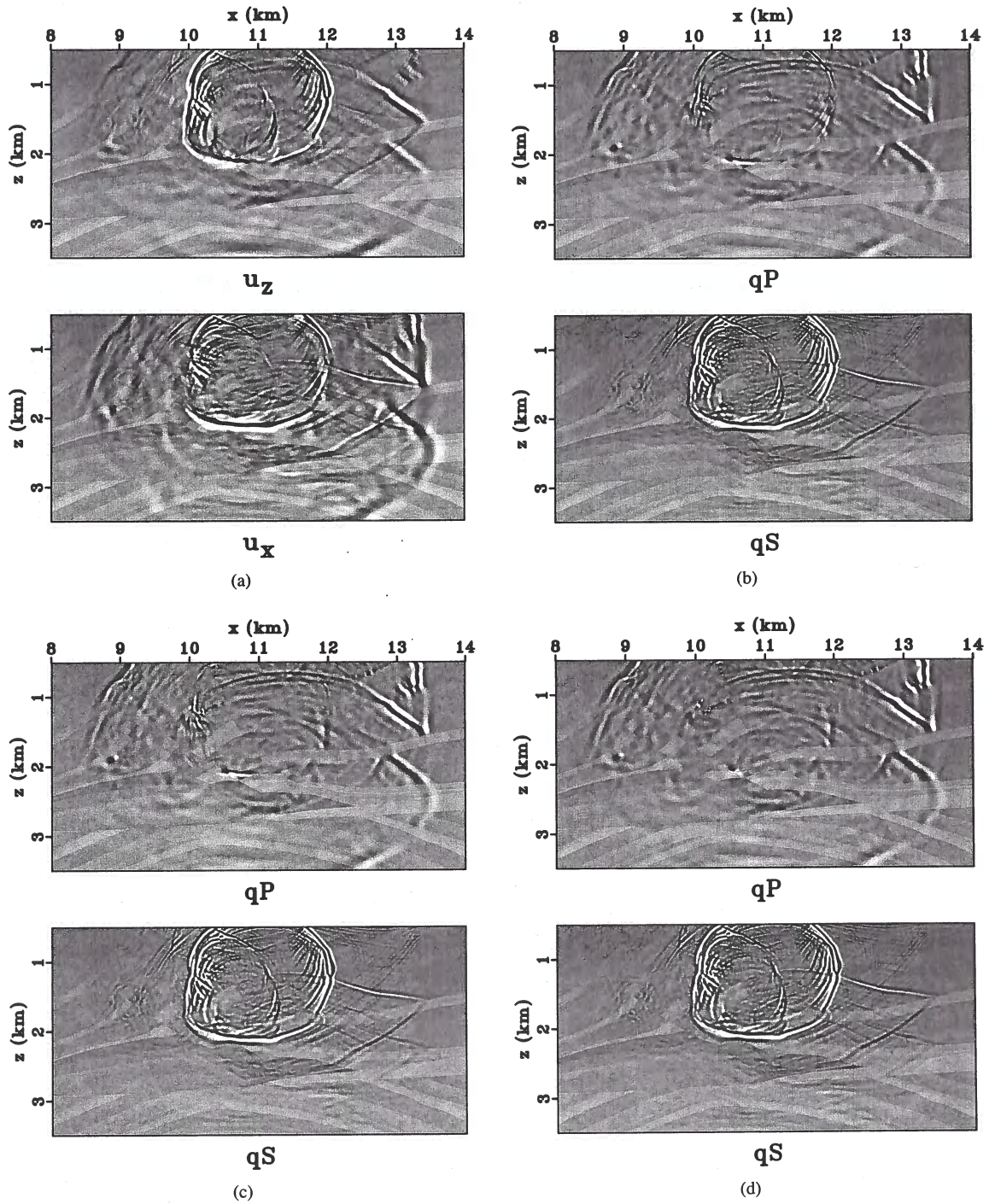

Figure 11. (a) A snapshot of the vertical and horizontal displacement wavefield simulated for model shown in Figure 10. Panels (b) to (c) are the P and SV wave separation using $\nabla \cdot$ and $\nabla \times$, VTI separators and TTI separators, respectively. The separation is incomplete in panel (b) and (c) where the model is strongly anisotropic and where the model tilt is large, respectively. Panel (d) shows the best separation among all.

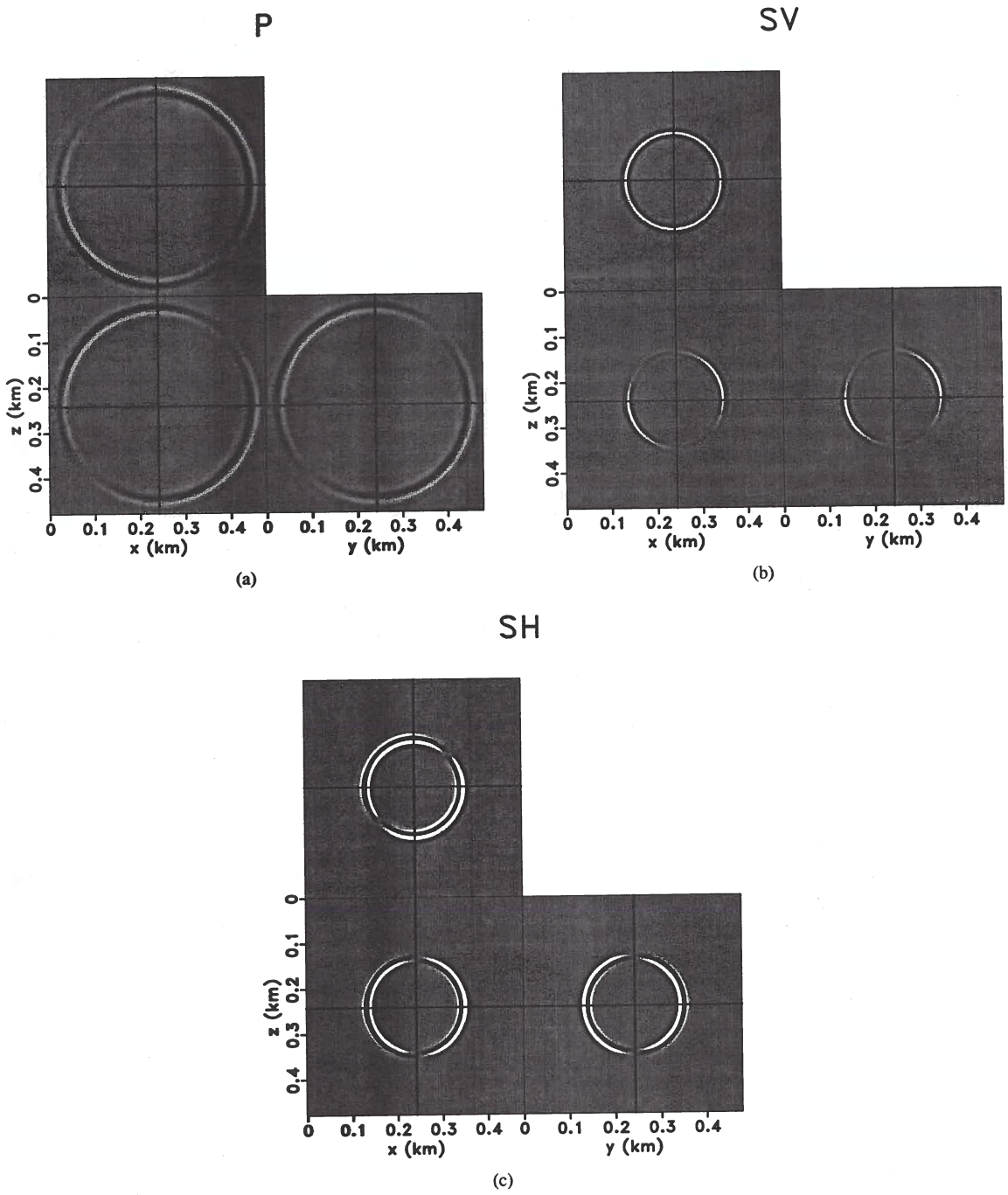

Figure 13. Separated P, SV and SH wave modes for the elastic wavefields shown in Figure 12. P, SV, and SH are well separated from each other.

5. 2 S mode amplitudes

Although the procedure used here to separate S waves into SV and SH modes is simple, the amplitudes of S modes are not correct due to the scaling factors in Equations 25 and 26. The amplitudes of S modes obtained in this way are zero in the symmetry axis direction and gradually increase to one in the symmetry plane. However, since the symmetry axis direction usually corresponds to normal incidence of the elastic waves, it is important to obtain more accurate S wave amplitudes in this direction. The main problem that impedes us from construct 3D global S-wave separators is that the SV and SH polarization vectors are singular in the symmetry axis direction, i.e., they are defined by plane-wave solution to the TI elastic wave equation. Various studies (Kieslev & Tsvankin,

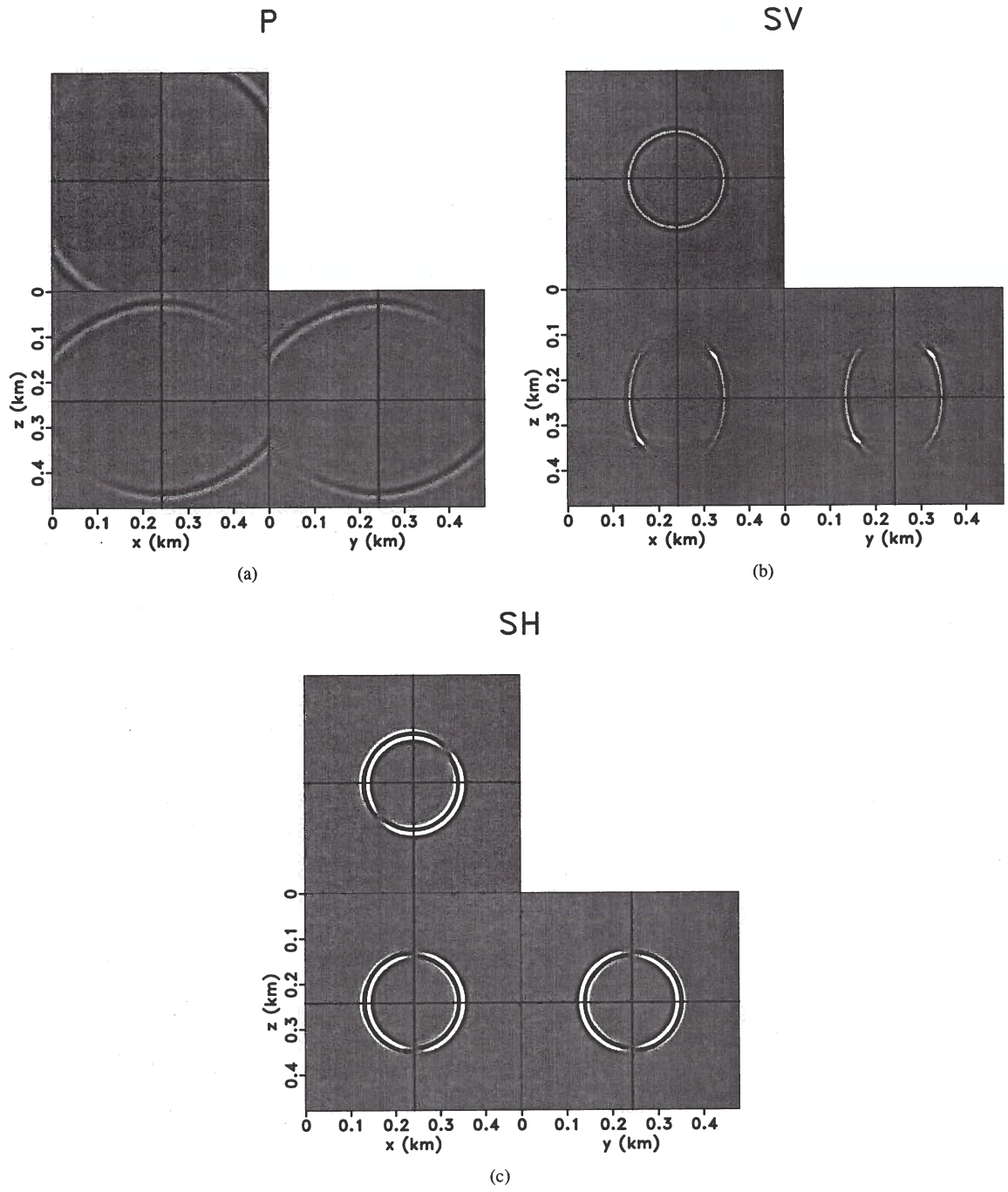

Figure 15. Separated P, SV and SH wave modes for the elastic wavefields shown in Figure 14. P, SV, and SH are well separated from each other.

of the quasi-ellipse of the S-wave polarization, which can be obtained incorporating the first-order term in the ray tracing method.

6 CONCLUSIONS

We present a method of obtaining spatially-varying derivative operators for TI models, which can be used to separate elastic wave modes in complex media. The main idea is to utilize polarization vectors constructed in the wavenumber domain using the local medium parameters and then transform these vectors back to the space domain. The main advantage of ap-

Moveout analysis of wave-equation extended images

Tongning Yang and Paul Sava
Center for Wave Phenomena, Colorado School of Mines

ABSTRACT
Conventional velocity analysis applied to images produced by wave-equation migration with a cross-correlation imaging condition makes use either of moveout information from space-lags or of focusing information from time-lags. However, more robust velocity estimation methods can be designed to take advantage simultaneously of the moveout and focusing information provided by the migrated images. Such joint velocity estimation requires characterization of the moveout surfaces defined jointly for space- and time-lag common-image gathers. Such surfaces estimated for single events (shots) are non-planar but they reduce naturally to the conventional space-lag and time-lag moveout functions. The superposition of those surfaces for many experiments (shots) in a common-image gather forms a shape which can be characterized as a "light-cone" in the lag space. When imaged with correct velocity, the focus of the light cone is located at the correct image depth and at zero space- and time-lags. When imaged with incorrect velocity, the focus of the light cone shifts both in depth and along the time-lag axis. The characteristics of the light cones are directly related to the quality of the velocity model, thus their analysis provides a rich source of information for velocity model building. Joint migration velocity analysis technique exploiting the entire information provided by the extended imaging condition has the potential to benefit from the combination of the robustness of depth focusing analysis and of the high resolution of conventional semblance analysis.

Key words: wave-equation, extended imaging, focusing, semblance

1 INTRODUCTION

A key challenge for imaging in complex geology is an accurate determination of the velocity model in the area under investigation. Migration velocity analysis is based on the principle that image accuracy indicators are optimized when data are correctly imaged. A common procedure for migration velocity analysis is to examine the alignment of images created with data from many complementary experiments. An optimal choice for image analysis in complex areas is the angle domain which is free of complicated artifacts present in surface offset gathers (Stolk & Symes, 2004). If images constructed by illuminating a point from various directions are aligned, then the velocity model used for imaging is said to be accurate. This idea is usually referred to as the *semblance principle* (Yilmaz, 2001) and it represents the foundation of most velocity analysis methods in use today.

Often, semblance analysis is performed in the angle domain. Several methods have been proposed for angle decomposition (Sava & Fomel, 2003b,a; Fomel, 2004; Biondi & Symes, 2004). All these procedures require decomposition of extrapolated wavefields or of migrated images in components that are related to the reflection angles. This imaging procedure requires the application of an *extended imaging condition* (Sava & Fomel, 2006) which implements a point-by-point comparison of the source and receiver wavefields extrapolated from the surface. In general, the comparison is done using simple image processing procedures applied at every location in the subsurface. If the source and receiver wavefields match each-other, then their cross-correlation maximizes at zero lag in space and time; otherwise, their cross-correlation does not maximize at zero lag indicating wavefield reconstruction error which may have different causes, e.g., velocity inaccuracy.

The source and receiver wavefields used for imaging are 4D objects, function of space coordinates and time (or frequency). For simplicity, we discuss in this paper only time-domain imaging, although our analysis applies equally well to frequency domain imaging. For such 4D objects, the images obtained by extended imaging conditions are characterized in general by a 3D space-lag vector and a 1D time-lag. The

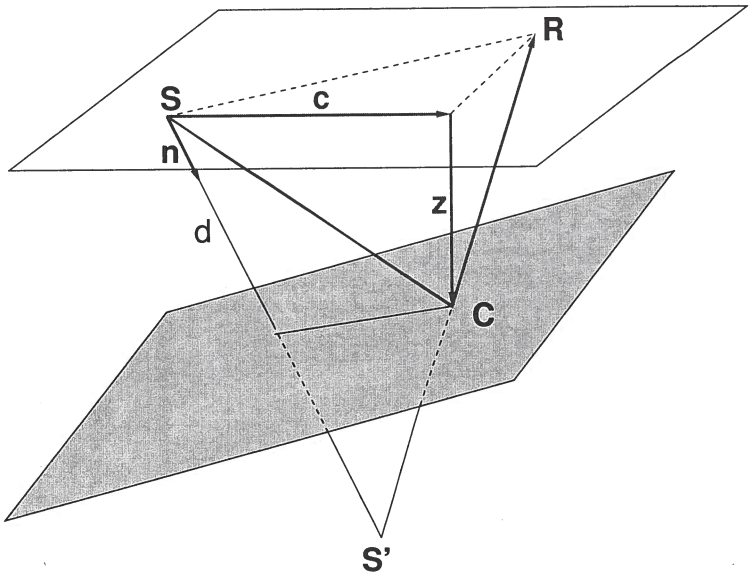

Figure 1. Geometry of a reflection experiment. **S**, **R** and **C** identify the positions of the source, receiver and image, respectively. The reflector is located at distance d from the source position in the direction of the vector **n**. The position of the CIG relative to the source is indicated by the vectors **c** and **z**.

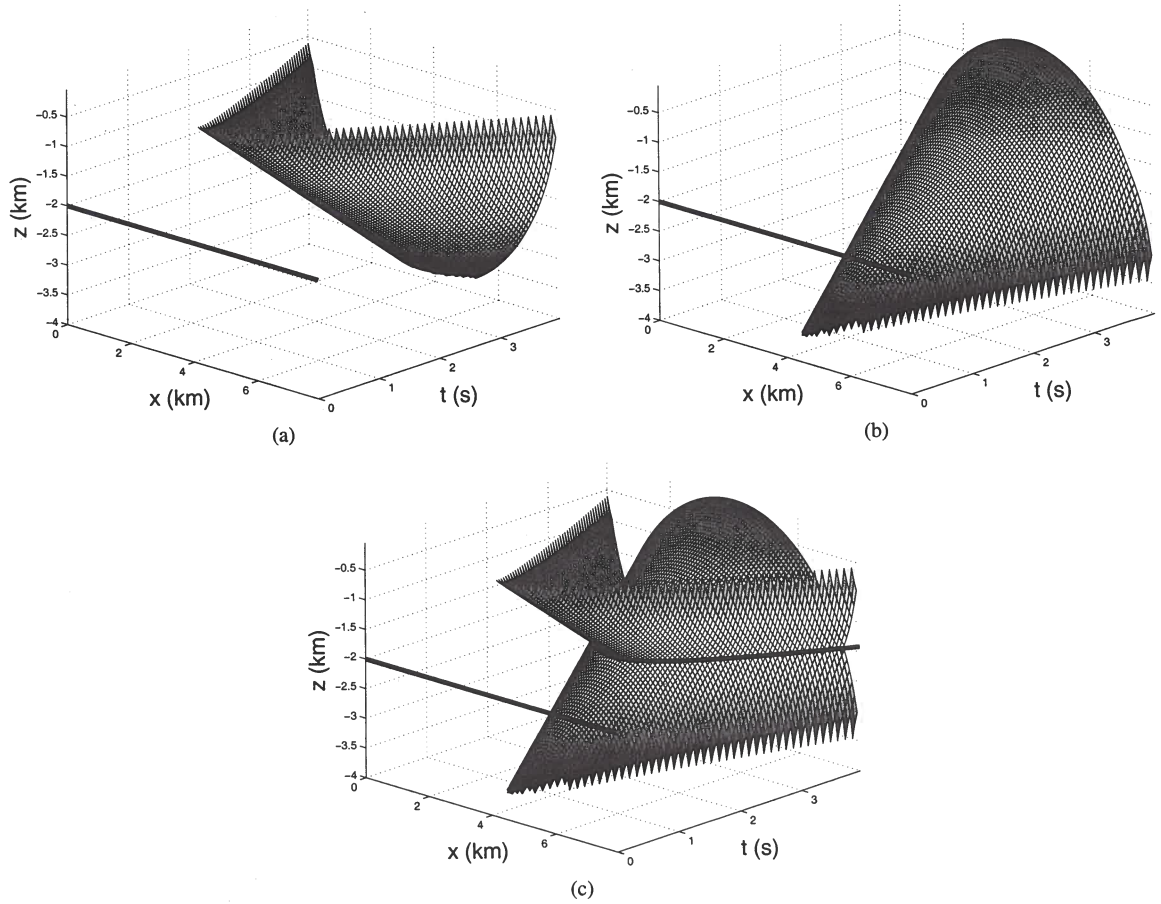

Figure 2. (a) Source wavefield in a homogeneous medium represented by a cone in space-time. (b) Receiver wavefield in a homogeneous medium represented by the mirror image of the source wavefield relative to the reflector. (c) Intersections of the source and receiver wavefields reconstructed with correct velocity. The projection of the intersection onto Cartesian spatial coordinates indicates the position of the reflector.

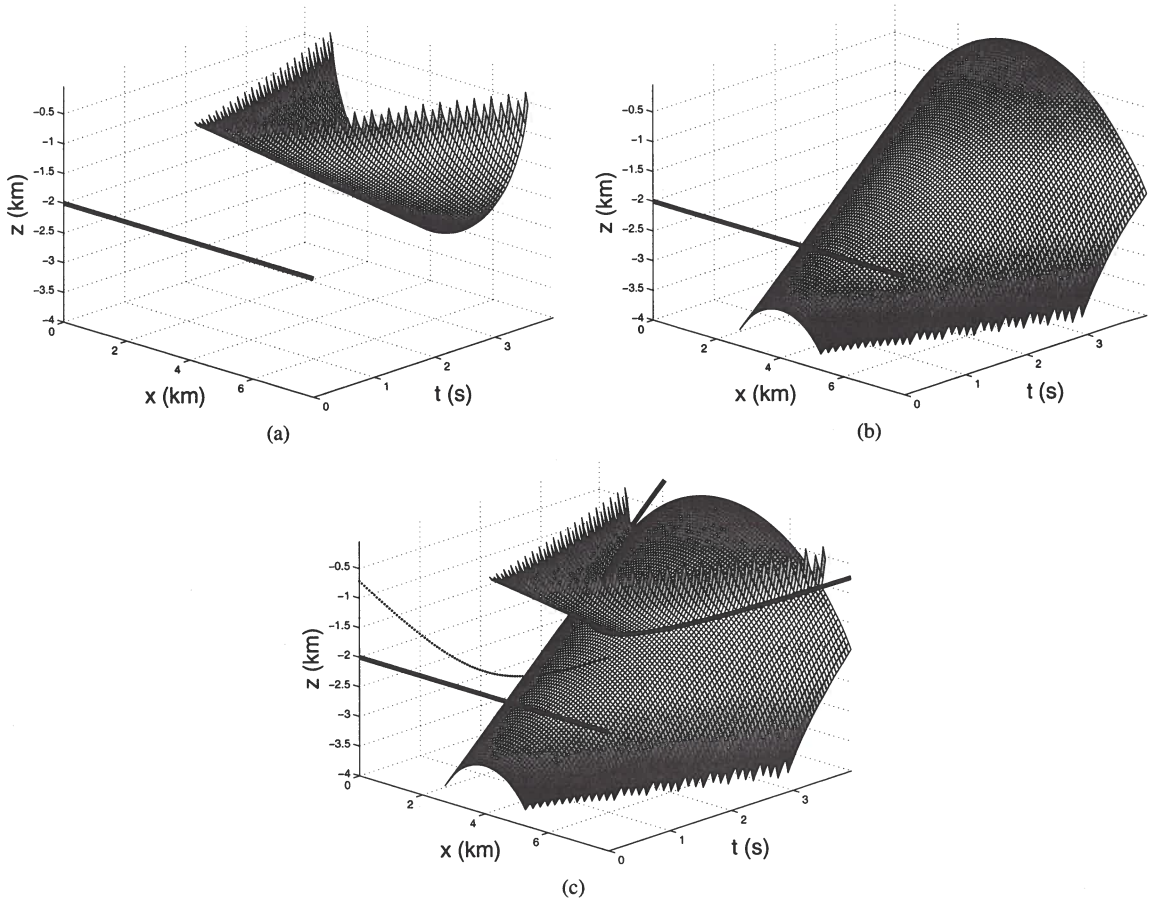

Figure 3. (a) Source wavefield in a homogeneous medium constructed using an incorrect velocity. The wavefield forms a cone in space-time and has a different shape compared with the wavefield constructed with the correct velocity model. (b) Receiver wavefield in a homogeneous medium constructed using an incorrect velocity. The wavefield forms a cone in space-time and has a different shape relative to the wavefield constructed in the correct velocity, and is also shifted along the time axis. (c) Intersections of the source and receiver wavefields reconstructed with incorrect velocity. The curved dash line, which is the projection of the intersection onto Cartesian spatial coordinates, indicates the position of the reflector. The image is distorted compared to the case when the correct velocity model is used.

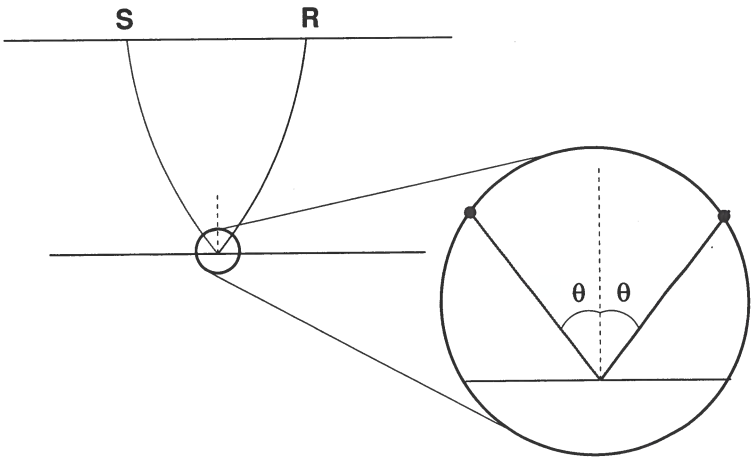

Figure 4. Cartoon describing wave propagation in an inhomogeneous medium. The wavepaths in the local region around the reflection point can be approximated with straight lines.

which characterizes the moveout at an image point function of space- and time-lags.

On the other hand, we have the following relations for the reflection geometry:

$$\mathbf{p}_s - \mathbf{p}_r = 2\mathbf{n}cos\theta\,, \tag{25}$$

$$\mathbf{p}_s + \mathbf{p}_r = 2\mathbf{q}sin\theta\,, \tag{26}$$

where $\mathbf{n}$ and $\mathbf{q}$ are unit vectors normal and parallel to the reflection plane, and θ is the reflection angle. Combining equations 24-25-26, we obtain a simplified moveout function for plane-waves:

$$z\left(\boldsymbol{\lambda},\tau\right) = d_0 - \frac{tan\theta\left(\mathbf{q}\cdot\boldsymbol{\lambda}\right)}{n_z} + \frac{v\tau}{n_z cos\theta}\,. \tag{27}$$

The quantity d_0 is defined as

$$d_0 = \frac{d - \left(\mathbf{c}\cdot\mathbf{n}\right)}{n_z}\,, \tag{28}$$

which represents the depth of the reflection corresponding to the chosen CIG location. Thus the quantity is invariant for different plane-waves, and it is used as a constant here.

When incorrect velocity is used for imaging, based on the analysis in the preceding section, we can obtain the moveout function

$$z\left(\boldsymbol{\lambda},\tau\right) = d_{0f} - \frac{tan\theta_m\left(\mathbf{q}_m\cdot\boldsymbol{\lambda}\right)}{n_{mz}} + \frac{v_m\left(\tau - t_d\right)}{n_{mz}cos\theta_m}\,, \tag{29}$$

where d_{0f} is the focusing depth of the corresponding reflection point, v_m is the migration velocity, t_d is the focusing delay, $\mathbf{n}_m$ and $\mathbf{q}_m$ are the new normal and parallel vector to the reflector.

In this analysis, we derive the moveout functions describing the extended images for a single seismic experiment. However, typical imaging employs multi-shot seismic experiments for better illumination of subsurface and analysis of the imaging redundancy which indicates velocity accuracy. Thus, it is important to understand the characteristics of the extended images in such situations and understand the moveout functions characterizing reflection experiments.

Since the wave equation is a linear partial differential equation, its solutions comply with the linear superposition principle . This is also true for the extended images, thus for multi-shot experiments the total extended images are the linear superimposition of the extended images from all the individual single-shot experiments. In this case, the moveout surface represents the envelope of the surfaces characterizing individual seismic experiments.

According to the definition, the envelope of a family of curves is obtained by setting both the implicit definition of the family and the derivative with respect to index parameter equal zero, and solving the system of equations. Therefore, the envelope representing a multi-shot image in extended CIGs with space-lag $\boldsymbol{\lambda}$ and time-lag τ is given by the system

$$G\left(z,\boldsymbol{\lambda},\tau,\theta\right) = 0\,, \tag{30}$$

$$\frac{\partial G\left(z,\boldsymbol{\lambda},\tau,\theta\right)}{\partial\theta} = 0\,, \tag{31}$$

where G represents the moveout function 27 for correct velocity and 29 for incorrect velocity, respectively. Solving the envelope system yields the following solutions:

$$z\left(\boldsymbol{\lambda},\tau\right) = d_0 + \frac{v\tau}{n_z}\sqrt{1 - \left(\frac{n_z\left(\mathbf{q}\cdot\boldsymbol{\lambda}\right)}{v\tau}\right)^2} \tag{32}$$

for correct velocity, and

$$z\left(\boldsymbol{\lambda},\tau\right) = d_{0f} + \frac{v_m\left(\tau - t_d\right)}{n_{mz}}\sqrt{1 - \left(\frac{n_{mz}\left(\mathbf{q}_m\cdot\boldsymbol{\lambda}\right)}{v_m\left(\tau - t_d\right)}\right)^2} \tag{33}$$

for incorrect velocity.

Analyzing the envelope functions for the cases of correct and incorrect velocities, we note that both envelope functions share a similar form, thus they should have similar properties. The envelope functions become singular when $\tau = 0$ or $\tau = t_d$, because at these special time-lags, all the individual surfaces corresponding to various experiments intersect at the same location. Mathematically, the envelope function is equivalent to a delta function at this τ, which represents a singularity. Also, the square-root term in the formula contains a subtraction, thus we have to ensure that the content under the square-root is non-negative otherwise the formula fails. This implies that the range of variable $\boldsymbol{\lambda}$ is limited which suggests

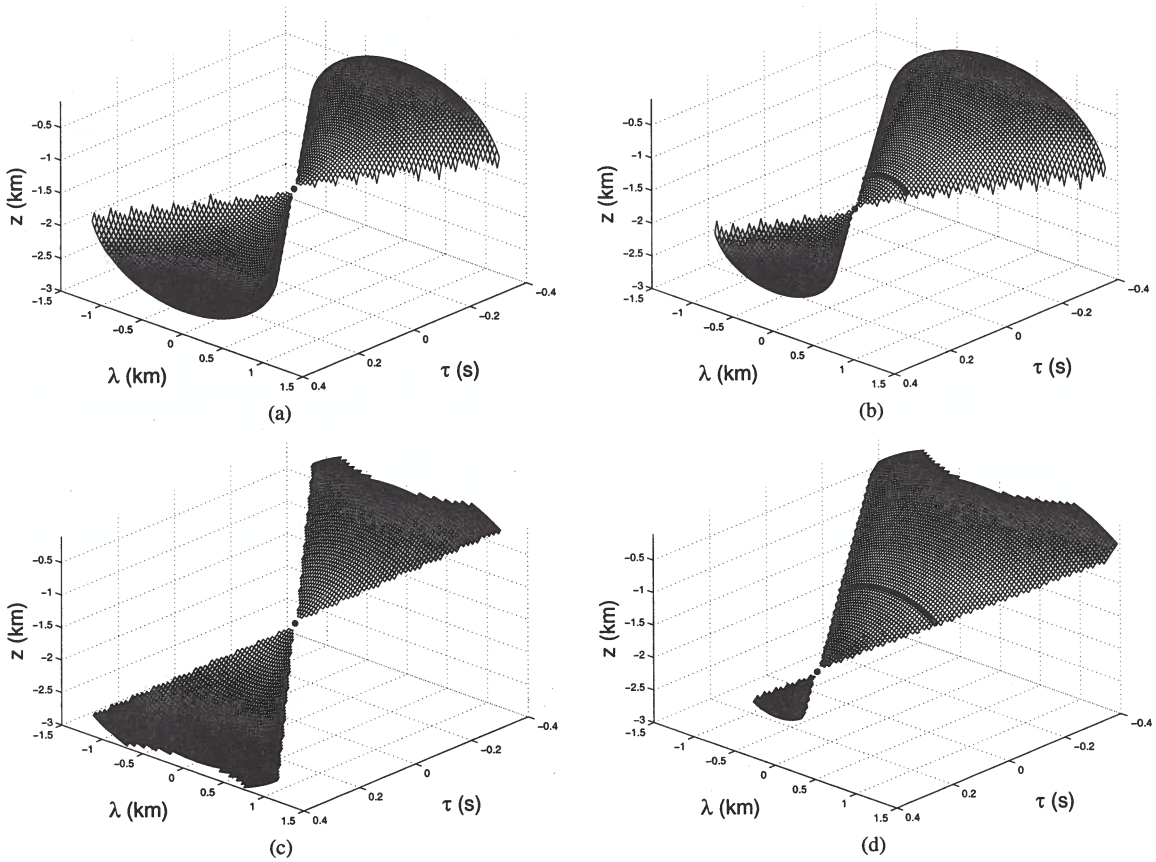

Figure 5. Light cone formed by the envelope of the moveout surfaces corresponding to individual plane-waves for a horizontal reflector in (a) the correct velocity case, the focus of the cone occurs at zero space- and time-lags and (b) the incorrect velocity case, the focus of the cone shifts to a nonzero time-lag. Light cone formed by the envelope of the moveout surfaces corresponding to individual plane-waves for a dipping reflector in (c) the correct velocity case, the focus of the cone occurs at zero space- and time-lags and (d) the incorrect velocity case, the focus of the cone shifts to a nonzero time-lag. The thick line corresponds to the slice of the cone cut at zero time-lag.

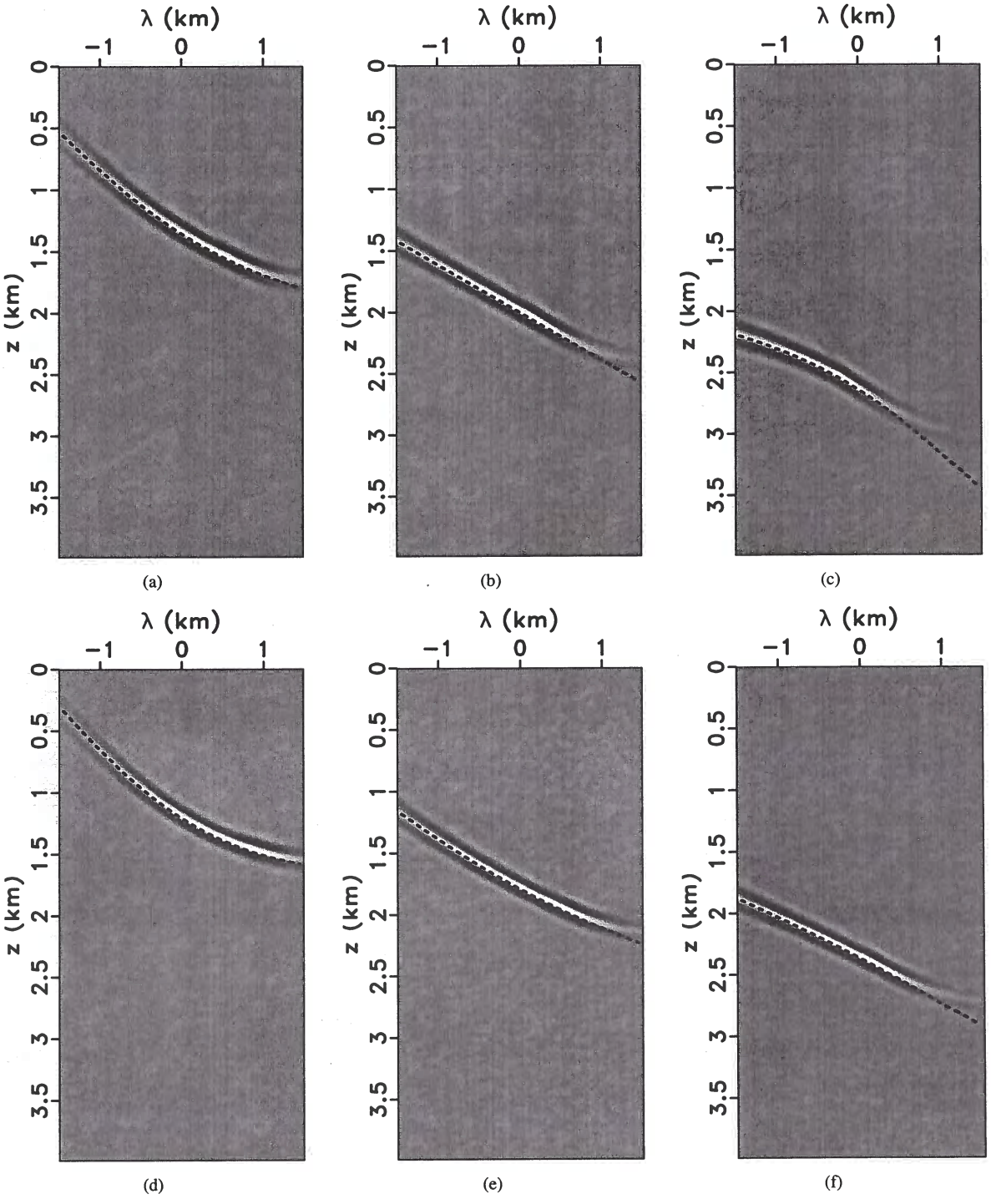

Figure 7. Space-lag CIGs for $\tau = \{-0.20, 0, +0.20\}$ s. Panels (a)-(c) correspond to correct velocity. Panels (d)-(f) correspond to incorrect velocity. The dash line overlain corresponds to the derived analytic function.

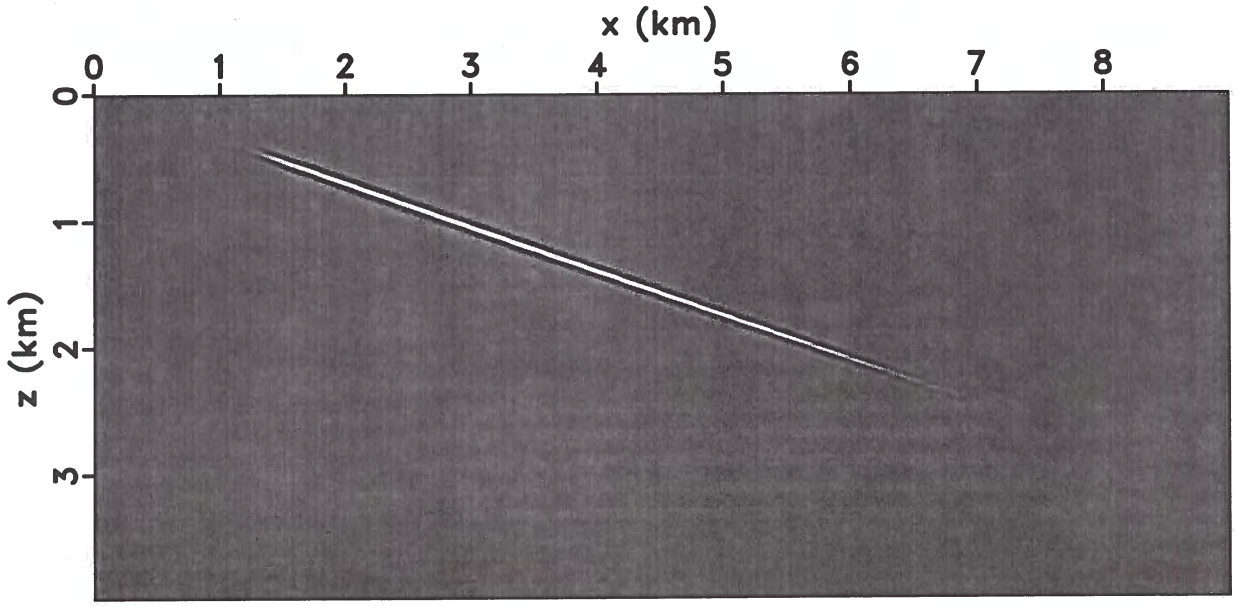

(a)

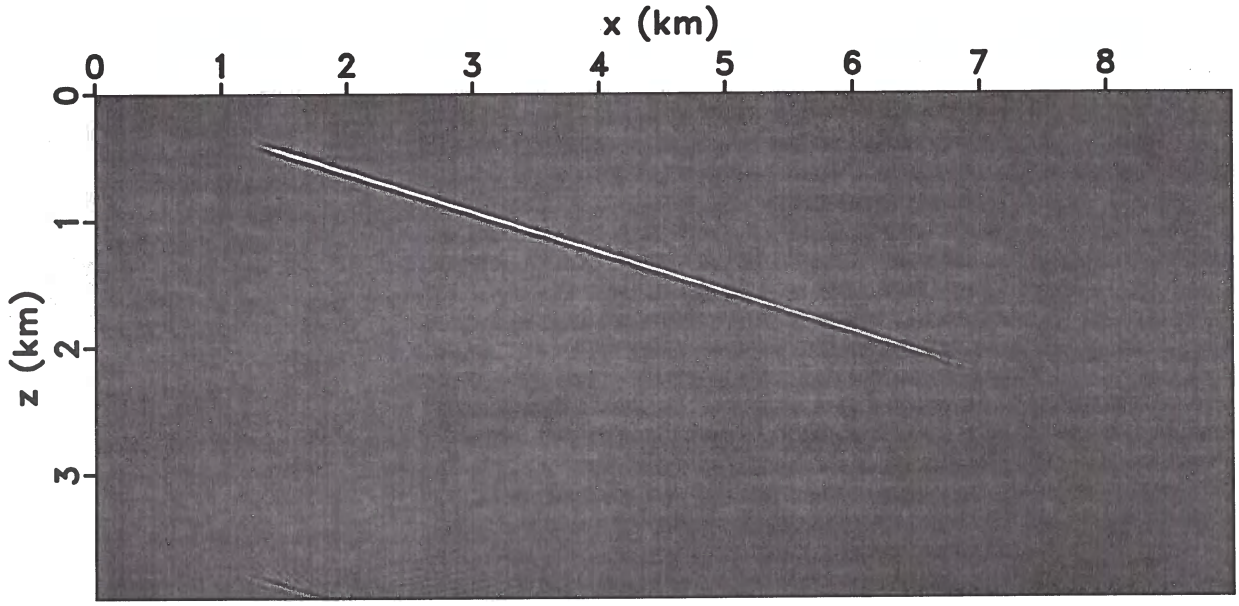

(b)

Figure 9. Migrated image corresponding to (a) correct velocity and (b) incorrect velocity.

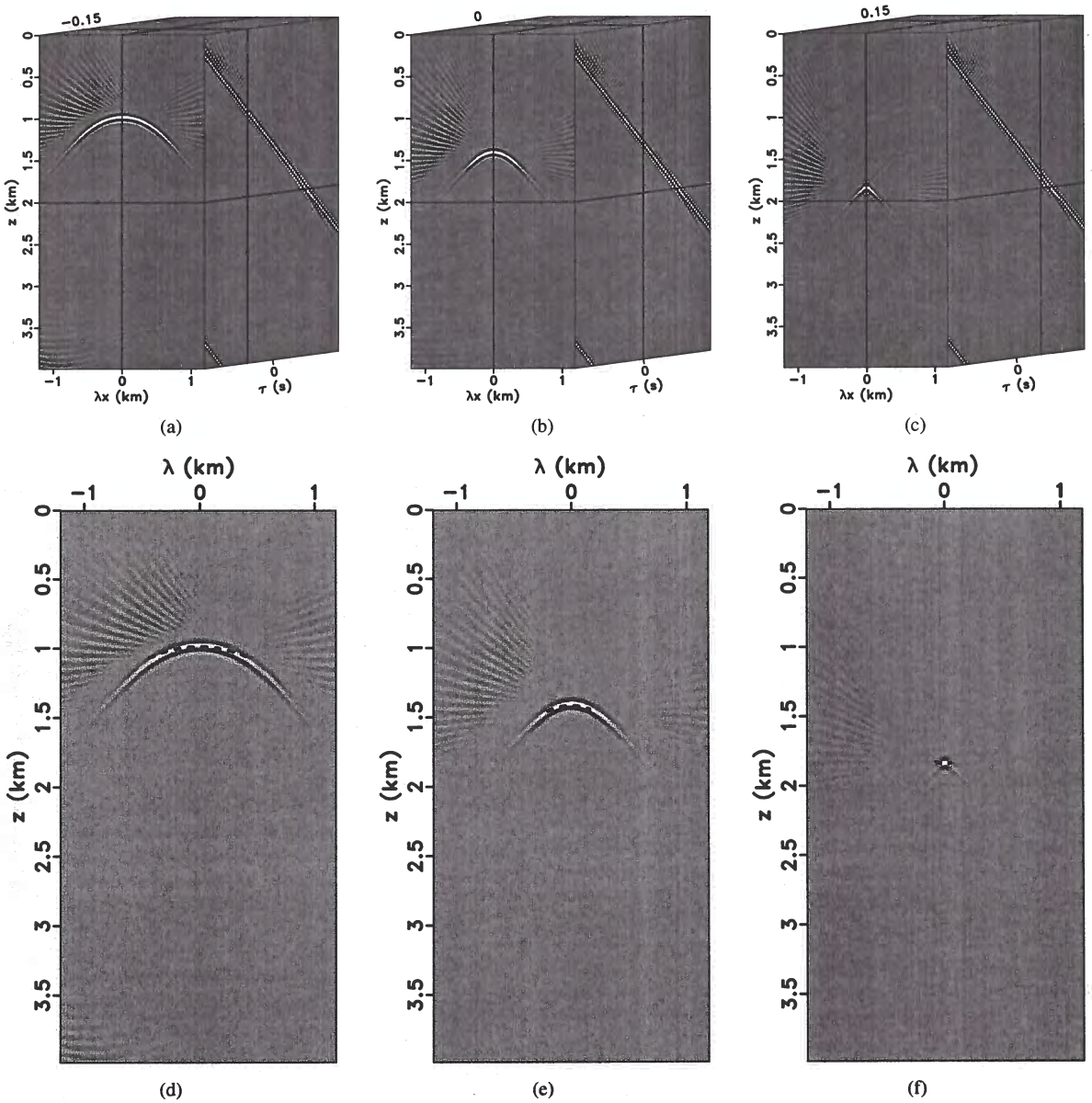

Figure 11. Envelope of the moveout surface at different time-lag for incorrect velocity. Panels (a)-(c) correspond slices to $\tau = \{-0.15, 0, +0.15\}$ s, respectively. Panels (d)-(f) show the same slices overlain by the derived analytic envelope function.

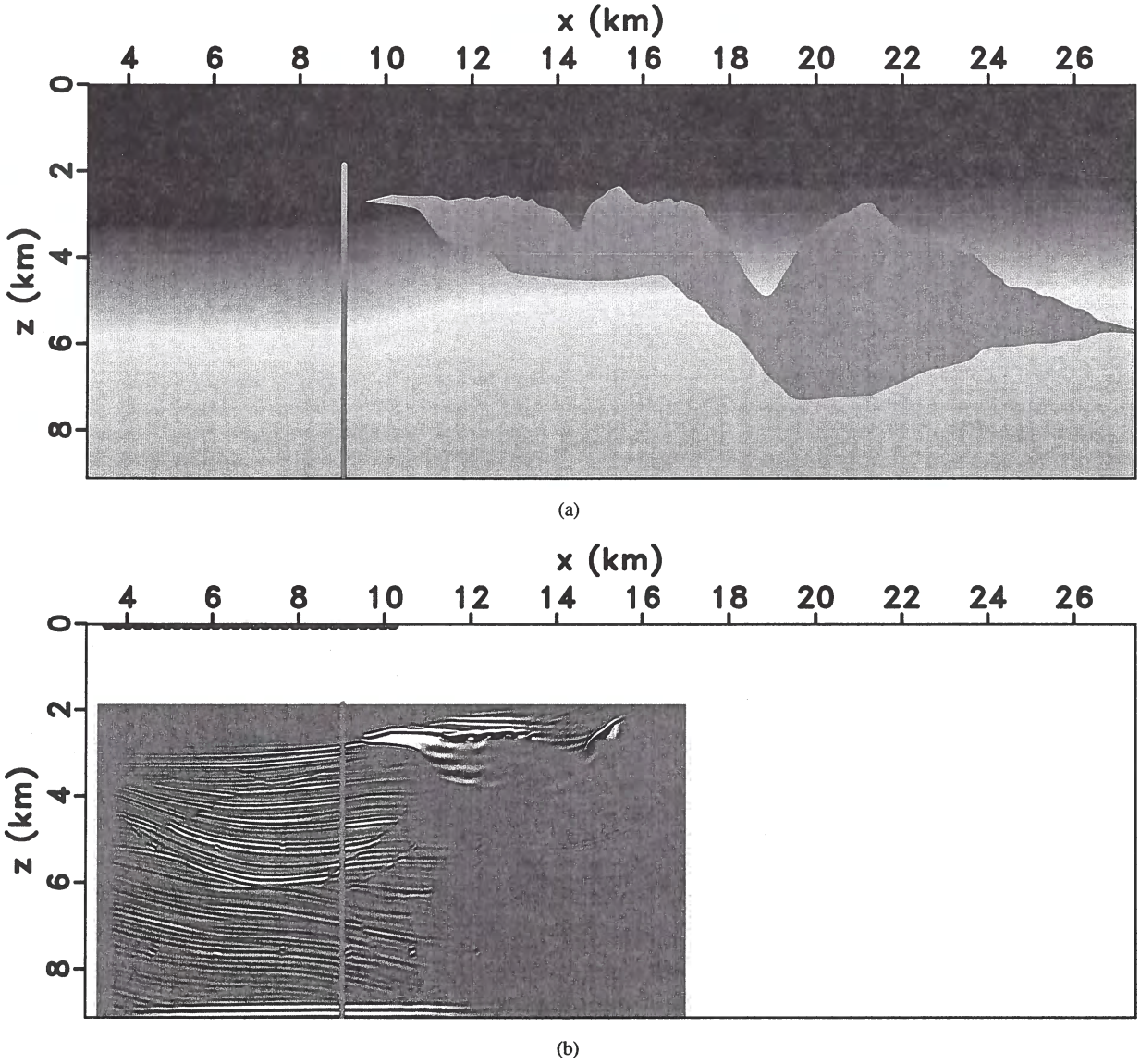

Figure 12. Sigsbee model. (a) correct velocity model and (b) corresponding image.

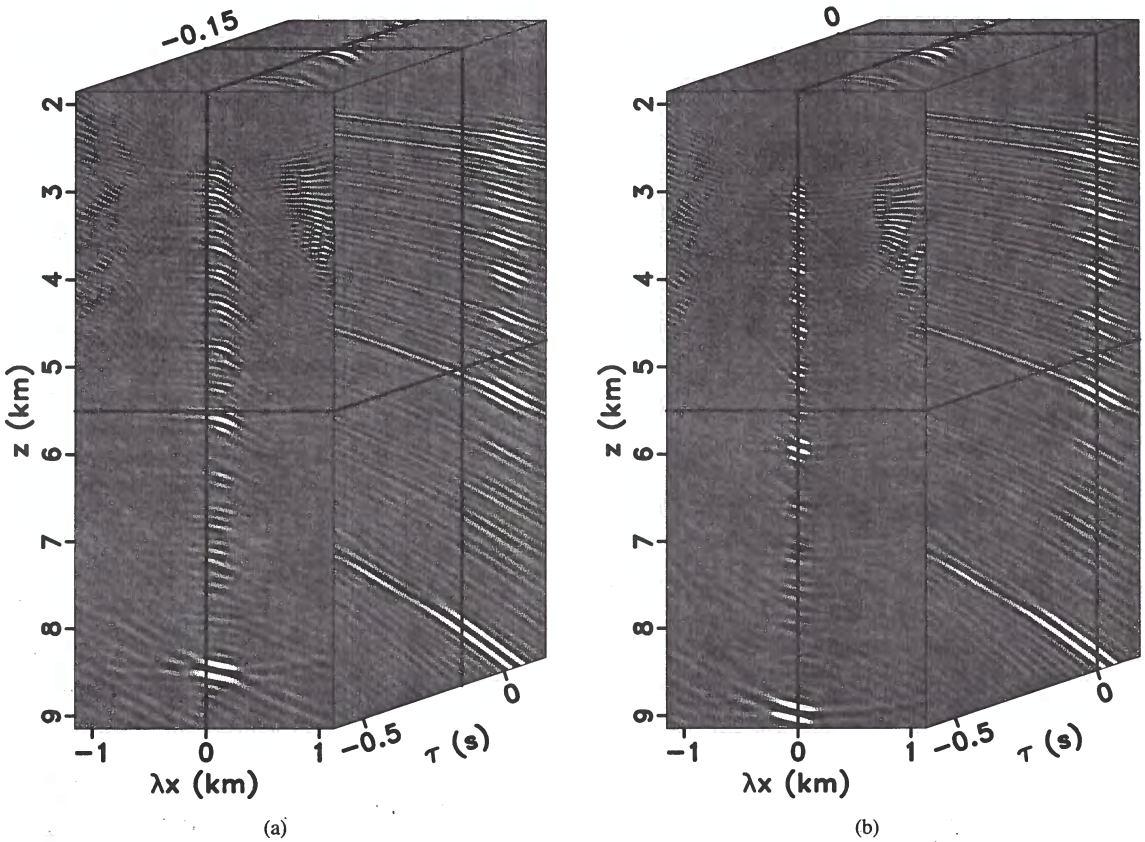

Figure 14. Moveout surface at different time-lags for correct velocity. Panels (a) and (b) correspond to slices of the light cone at $\tau = \{-0.15, 0\}$ s, respectively.

Wave-equation migration velocity analysis using extended images

Tongning Yang and Paul Sava
Center for Wave Phenomena, Colorado School of Mines

ABSTRACT
Wave-equation migration velocity analysis (WEMVA) is a velocity estimation technique designed to invert for velocity information using migrated images. Its capacity for handling multi-pathing makes it appropriate in complex subsurface regions characterized by strong velocity variation. WEMVA operates by establishing a linear relation between a velocity model perturbation and a corresponding migrated image perturbation. The linear relationship is derived from conventional extrapolation operators and it inherits the main properties of frequency-domain wavefield extrapolation. A key step in implementing WEMVA is to design an appropriate procedure for constructing image perturbations. Using time-lag extended images, one can characterize the error in migrated images by defining the focusing error as the shift of the focused reflection along the time-lag axis. Under the linear approximation, the focusing error can be transformed into an image perturbation by multiplying it with an image derivative taken relative to the time-lag parameter. The resulting image perturbation is thus a mapping of the velocity error in image space. This approach is computationally efficient and simple to implement, and no further assumptions about smoothness and homogeneity of the velocity model and reflector geometry are needed. Synthetic examples demonstrate the successful application of our method to a complex velocity model.

Key words: wave-equation, migration velocity analysis, time-lag extended imaging, focusing

1 INTRODUCTION

In regions characterized by complex subsurface structure, wave-equation depth migration is a powerful tool for accurately imaging the earth's interior. However, the quality of the final image greatly depends on the quality of the velocity model, thus constructing accurate velocity is essential for imaging.

Based on the domain in which the velocity estimation is implemented, velocity analysis techniques can be roughly divided into two categories. The first category includes techniques developed in the data domain prior to migration and usually described as tomography. The input for this type of techniques is the recorded seismic data. Velocity update is achieved by adjusting the velocity model to minimize the difference between the recorded and predicted seismograms. The second category includes techniques developed in the image domain after migration and usually described as migration velocity analysis (MVA). The input for this type of techniques is the migrated image obtained using an approximation of the velocity model. Velocity update is performed by adjusting the velocity model to optimize certain properties of the images, e.g. by using focusing or semblance analysis.

In practice, there are many possible approaches to employ the techniques in the two categories mentioned here. However, all such realizations share a common element that they need a carrier of information to connect the input data or image to the output velocity model. Thus the techniques for velocity updates can also be divided into two categories as ray-based and wave-based methods. The first category refers to techniques which use wide-band rays as the information carrier (Bishop et al., 1985; Stork & Clayton, 1991). By contrast, the second category refers to techniques which use band-limited wavefields as the information carrier (Woodward, 1992; Pratt, 1999; Sirgue & Pratt, 2004). Generally speaking, ray-based methods have the advantages of simple implementation and efficient computation over wave-based methods. On the other hand, wave-based methods are capable of handling compli-

τ is

$$\frac{\partial r\left(\mathbf{x},\tau\right)}{\partial \tau} = \sum_{\omega} \left(2i\omega\right) u_r\left(\mathbf{x},\omega\right) u_s^*\left(\mathbf{x},\omega\right) e^{2i\omega\tau}. \qquad (9)$$

Notice that the construction of the extended image derivative requires the same procedure as the one used for constructing the extended images. The additional term $2i\omega$ acts as a scaling factor applied at each frequency.

In summary, we construct the image perturbations for use in connection with WEMVA using the following procedure:

- Migrate the image and output time-lag extended images according to equation 4;
- Measure $\Delta\tau$ on time-lag panels by direct picking;
- Construct the extended image derivatives according to equation 9;
- Construct the linearized image perturbation according to equation 8.

Our methodology has the advantage over the method of Sava & Biondi (2004a,b) that we do not need to make assumptions about the slowness background as is required by the linearized Stolt procedure. Furthermore, our method does not assume horizontal reflectors, as required by conventional depth-focusing analysis technique. Our method also maintain a low computational cost, since the calculation of the linearized image perturbation, equation 8, adds just a trivial cost to that of conventional migration. Overall, our approach provides an efficient way to construct image perturbations consistent with the assumptions made about the WEMVA operator.

3 EXAMPLE

We illustrate our procedure using the Sigsbee 2A model (Paffenholz et al., 2002). For simplicity, we consider just one reflector of the model in order to highlight the behavior of our operator (Figure 1(a)-1(c)). Given the linear nature of the imaging process, more reflectors contribute independently to the velocity update. We use a scaled version of the true model as the background slowness model for migration with extended images. We refer to the difference between the true and background slowness models as the true slowness perturbation Δs. Figures 1(b) and 1(c) show the image and time-lag extended images migrated with the background slowness model. The reflector is mispositioned due to the incorrect slowness model.

Figure 2(a) and 2(b) show the time-lag CIG and the constructed $\Delta\tau$ panel obtained by picking $\Delta\tau$ on panel 2(a) and by spreading that information evenly along the corresponding reflector. Then we construct the image perturbation by the procedure introduced in the preceding section.

To verify the accuracy of the constructed image perturbation, we apply the forward WEMVA operator to the true slowness perturbation and obtain the true image perturbation. Figures 3(c) and 3(d) depict the image perturbations obtained by the forward WEMVA operator and our method, respectively. The two images are similar both kinematically and dynamically. We apply the adjoint WEMVA operator to both image perturbations to obtain slowness perturbations shown in Figures 3(a) and 3(b), which also exhibit good similarity. Therefore, we conclude that the image perturbation constructed by our method is applicable to WEMVA since it matches the corresponding perturbation.

Figures 4(a) to 4(e) depict the slowness perturbation back-projected from the constructed image perturbation for different shots, and Figure 4(f) depicts the result of slowness perturbation stacked for all shots. The images show that the illumination pattern of the various shots is different, although consistent with the illumination of the corresponding migration procedure.

This example demonstrates that our procedure is applicable to a shot-record imaging framework in complex media. This conclusion makes our technique particularly attractive for MVA using wide-azimuth data. However, there is no particular limitation of the type of carrier used to transfer the time-lag information measured on the migrated images into velocity updates. We could, in principle, use plane waves instead of shot, thus achieving even higher computational efficiency.

4 CONCLUSIONS

We develop a new method to construct image perturbations for wave-equation migration velocity analysis. The methodology relies on the focusing information extracted from time-lag extended images. The shift of the reflection focusing along the time-lag axis provides a measure of error. We use this information in conjunction with image derivatives relative to the time-lag parameter to construct image perturbations. Compared with more conventional techniques for constructing image perturbation, our approach is efficient, since it represents a relatively trivial extension of the time-lag extended imaging condition, and accurate, since it does not make use of Stolt-like procedures which incorporate strong assumptions about the smoothness of the background model. The results obtained using the complex Sigsbee 2A model demonstrate the validity of our method in complex environments.

5 ACKNOWLEDGMENTS

We acknowledge the support of the sponsors of the Center for Wave Phenomena at Colorado School of Mines. This work is also partially supported by a research grant from StatoilHydro.

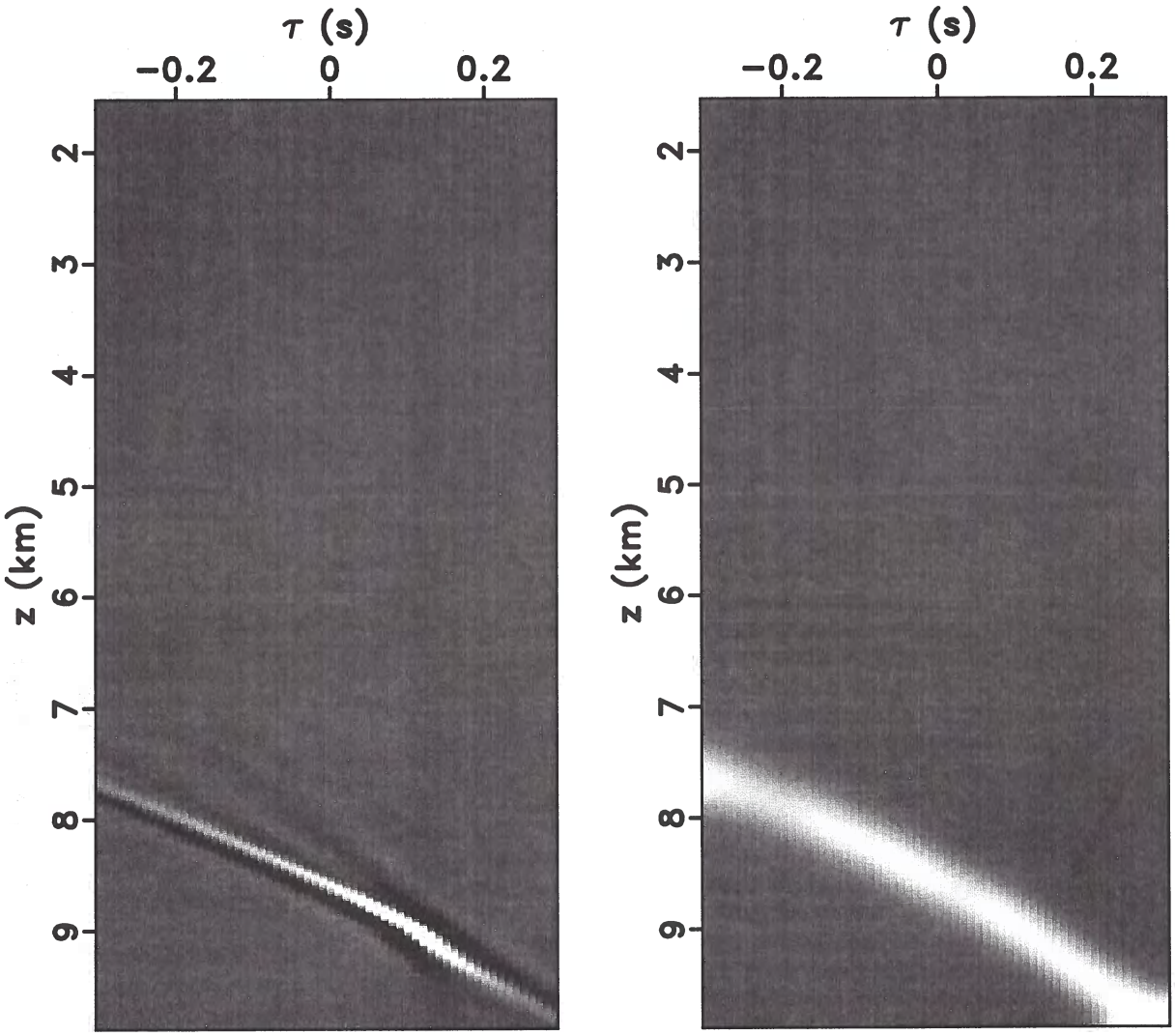

Figure 2. (a) Time-lag CIG panel at $x = 10.1$ km and (b) picked time-lag perturbation spread along the corresponding reflector.

REFERENCES

Albertin, U., Sava, P., Etgen, J., and Maharramov, M., 2006, Image differencing and focusing in wave-equation velocity analysis: 68th Mtg., Eur. Assoc. Expl. Geophys., Abstracts.

Berkhout, A. J., 1982, Imaging of acoustic energy by wave field extrapolation: , Elsevier.

Biondi, B., and Sava, P., 1999, Wave-equation migration velocity analysis: 69th Annual International Meeting, SEG, Expanded Abstracts, 1723–1726.

Bishop, T. N., Bube, K. P., Cutler, R. T., Langan, R. T., Love, P. L., Resnick, J. R., Shuey, R. T., Spindler, D. A., and Wyld, H. W., 1985, Tomographic determination of velocity and depth in laterally varying media: Geophysics, **50**, no. 06, 903–923.

Claerbout, J. F., 1985, Imaging the Earth's interior: , Blackwell Scientific Publications.

Higginbotham, J. H., and Brown, M. P., 2008, Wave equation migration velocity focusing analysis: 78th Annual International Meeting, SEG, Expanded Abstracts.

Lafond, C. F., and Levander, A. R., 1993, Migration moveout analysis and depth focusing: Geophysics, **58**, no. 01, 91–100.

MacKay, S., and Abma, R., 1992, Imaging and velocity estimation with depth-focusing analysis: Geophysics, **57**, no. 12, 1608–1622.

Paffenholz, J., McLain, B., Zaske, J., and Keliher, P., 2002, Subsalt multiple attenuation and imaging: Observations from the sigsbee 2b synthetic dataset: 72nd Annual International Meeting, SEG, Expanded Abstracts, 2122–2125.

Pratt, R. G., 1999, Seismic waveform inversion in the frequency domain, Part 1: Theory and verification in a physical scale model: Geophysics, **64**, no. 3, 888–901.

Sava, P., and Biondi, B., 2004a, Wave-equation migration velocity analysis - I: Theory: Geophysical Prospecting, **52**, 593–606.

——— 2004b, Wave-equation migration velocity analysis - II: Subsalt imaging examples: Geophysical Prospecting, **52**, 607–623.

Sava, P., and Fomel, S., 2006, Time-shift imaging condition in seismic migration: Geophysics, **71**, no. 6, S209–S217.

Sava, P., and Vlad, I., 2008, Numeric implementation of wave-equation migration velocity analysis operators: Geophysics, **73**, VE145–VE159.

Sava, P., 2003, Prestack residual migration in the frequency domain: Geophysics, **67**, no. 2, 634–640.

Sirgue, L., and Pratt, R., 2004, Efficient waveform inversion and imaging: A strategy for selecting temporal frequencies: Geophysics, **69**, no. 1, 231–248.

Stork, C., and Clayton, R. W., 1991, An implementation of tomographic velocity analysis: Geophysics, **56**, no. 04, 483–495.

Woodward, M. J., 1992, Wave-equation tomography: Geophysics, **57**, no. 01, 15–26.

Yilmaz, O., and Chambers, R. E., 1984, Migration velocity analysis by wave-field extrapolation: Geophysics, **49**, no. 10, 1664–1674.

Probabilistic micro-earthquake location for reservoir monitoring and characterization

Ran Xuan and Paul Sava
Center for Wave Phenomena, Colorado School of Mines

ABSTRACT
Micro-seismicity is used to monitor fluid migration during reservoir production and hydro-fracturing operations. This is usually done with sparse networks of seismic sensors located in boreholes. The data used for micro-earthquake monitoring are corrupted by noise which reduces the signal-to-noise ratio to values as low as 0.1. Monitoring methods based on traveltime picking of various wave modes (P or S) cannot deal with this level of noise and require extensive user interaction. An alternative class of methods uses time reversal to focus micro-earthquake information at the source position. These methods can handle noisier signals, but are also costlier to run. The technique advocated in this paper exploits time-reversal within the general framework of Bayesian inversion. Given an assumption about the possible locations of micro-earthquakes, we use recorded data to evaluate the feasibility of micro-earthquakes occurring at various locations in the Earth. The method takes into account imaging imperfections due to unknown components of the model or acquisition array aperture. We simulate wavefields corresponding to possible sources distributed in the model and evaluate their match with the wavefield reconstructed from real data recorded in the field. In this regard, the method operates like a pattern-recognition procedure and can exploit a wide variety of techniques designed for this purpose. We use simple cross-correlation to take advantage of the speed and robustness of this technique. The wavefields reconstructed at various locations are used to scan over time the wavefield constructed from field data, thus our method is able to identify not only the position of the micro-earthquakes but also their onset times. The final outcome of this automated process is a map of probabilities indicating the confidence of micro-earthquake occurrence at various positions and times.

Key words: wave equation, imaging

1 INTRODUCTION

High-pressure fluid injected into oil and gas reservoirs causes time-invariant stress and strain changes. When the stress exceeds a threshold characterizing the resistance of rock materials to stress, micro-seismicity is triggered by the release of pressure along pre-existing fractures or through the creation of new fractures (Maxwell & Urbancic, 2001; Duncan, 2005). Precisely locating micro-seismic events can be used to monitor the hydraulic fracturing and for reservoir characterization (Rentsch, 2004).

Most location methods currently used require the identification of seismic arrivals which involves accurate picking of P- and S-wave arrival times. The onset time and the coordinates of the hypocenter of micro-seismic events are given by calculations which require accurate knowledge of the velocity model and of the physical relationships describing wave propagation in the subsurface. The source is located by optimizing a misfit function between measured and calculated quantities (Pujol, 2004; Lay & Wallace, 1995; Thurber & Rabinowitz, 2000). The methods in this category assume that the arrival time of a specific event can be identified on seismic

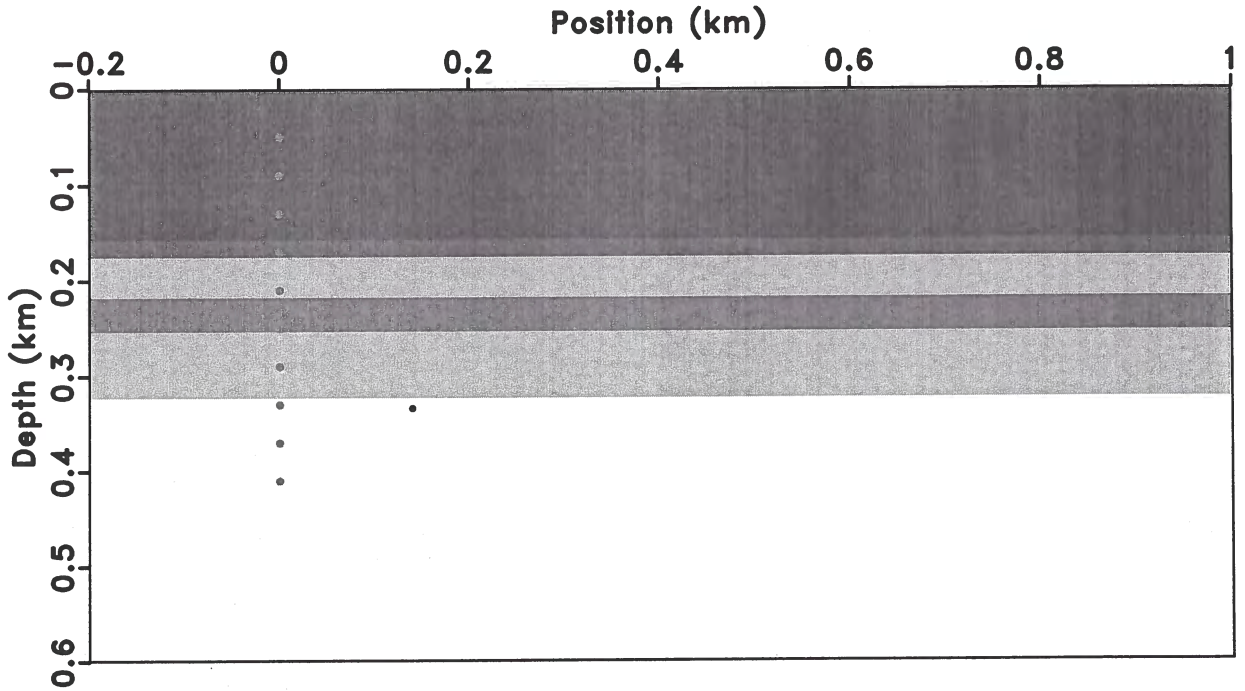

(a)

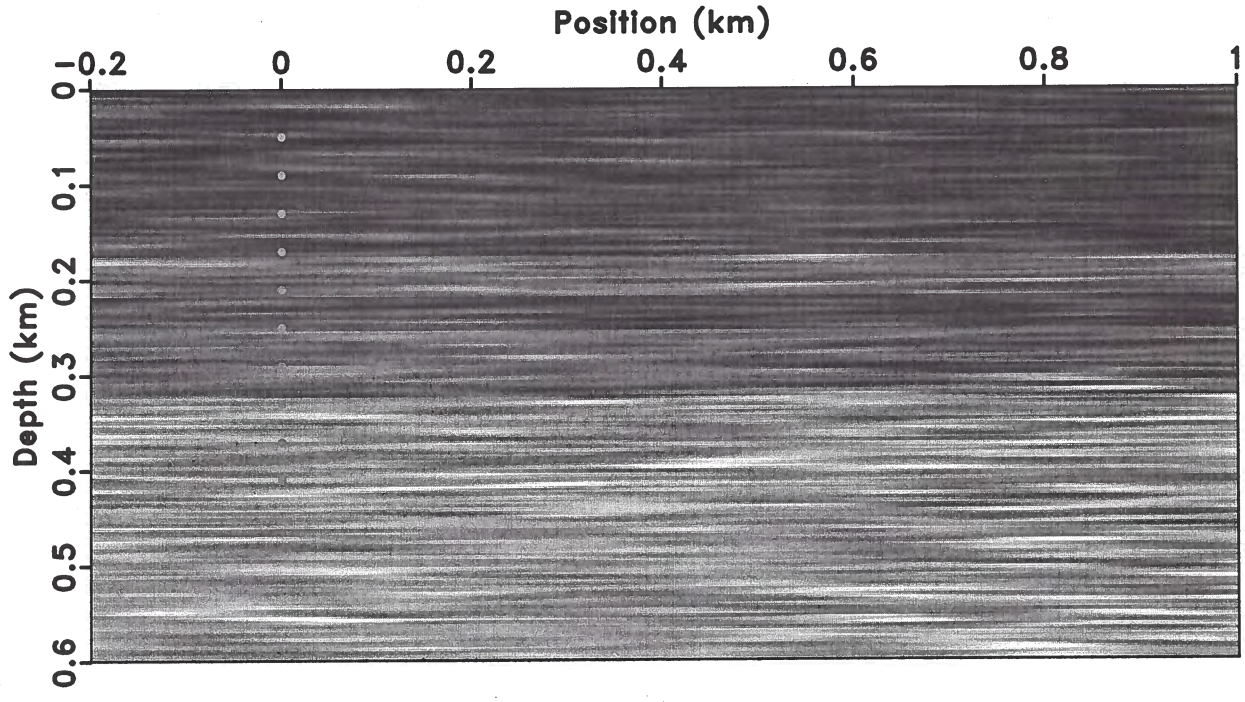

(b)

Figure 1. (a) The velocity model used for the kernel function and (b) the velocity model with random variability used to simulate data. The random velocity in panel (b) is the sum of the velocity in model (a) with correlated Gaussian noise with a magnitude of 40% of the background. The background velocity model is sampled every 2 m and ranges between 1900 and 2400 m/s. The acquisition array consists of 10 receivers placed at $x = 0$ km with a spacing of 40 m. We simulate an explosive seismic source at $x = 0.136$ km and $z = 0.333$ km.

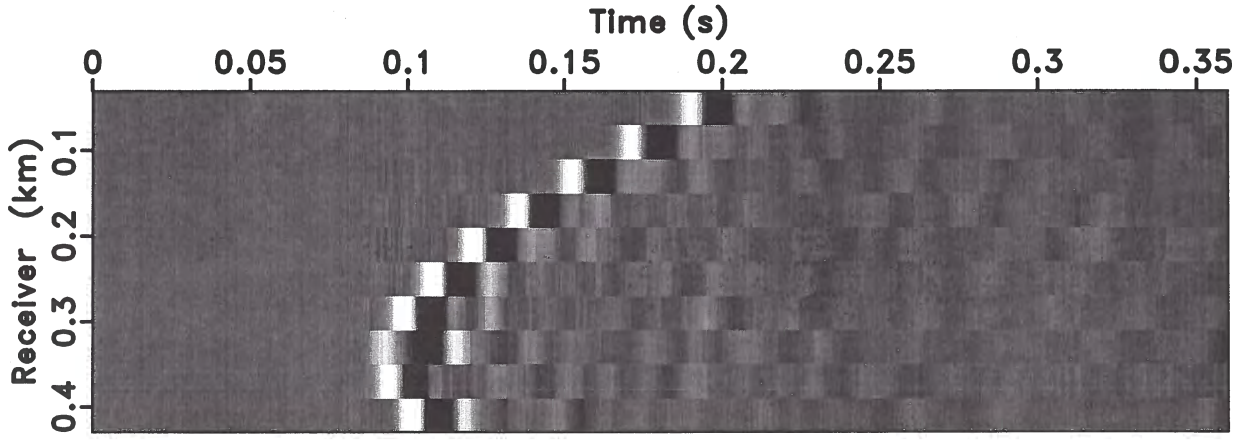

Figure 2. The synthetic seismogram simulated using the velocity model shown in Figure 1(b). We consider an absorbing surface. The source used to simulate this event is a Ricker wavelet with a dominant frequency of 50 Hz. A total of 2000 time steps with a time increment of 0.2 ms are calculated.

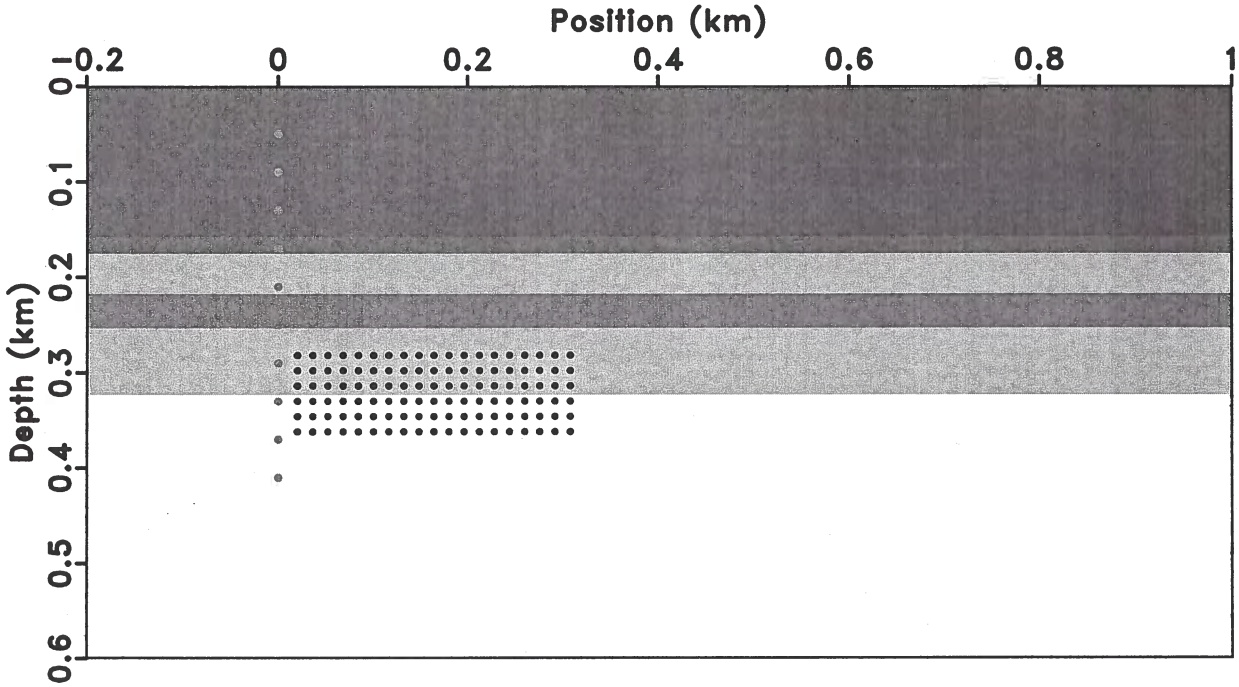

Figure 3. A schematic representation of the a priori information on the model space. We assume that the micro-earthquakes occur in the region indicated by the dense dots between $x = 0 - 0.35$ km and $z = 0.25 - 0.35$ km. A similar discrete set of possible onset times are defined along the time axis.

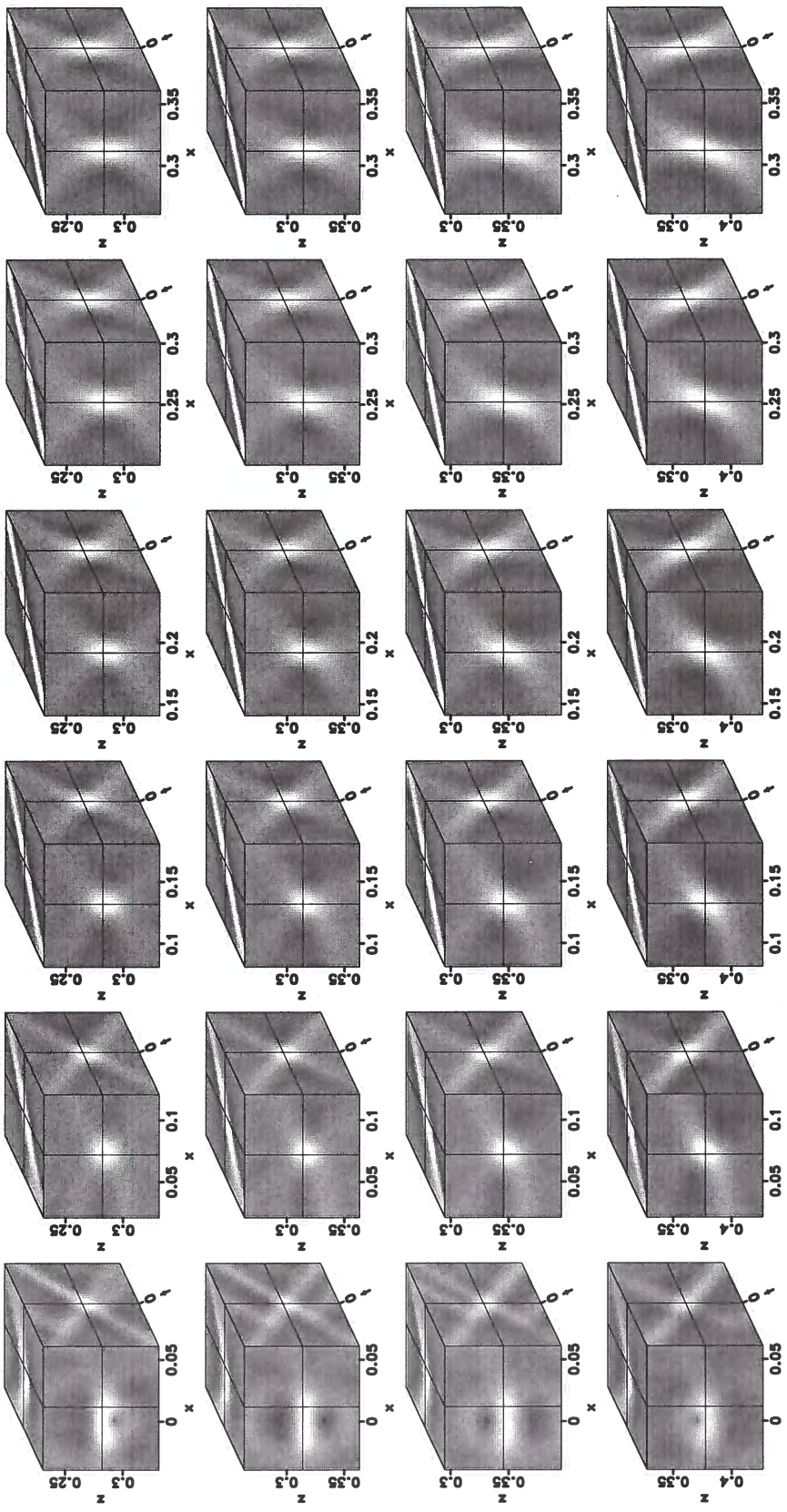

Figure 4. Seismic wavefield database. The center of each cube is the source location of the predicted data.

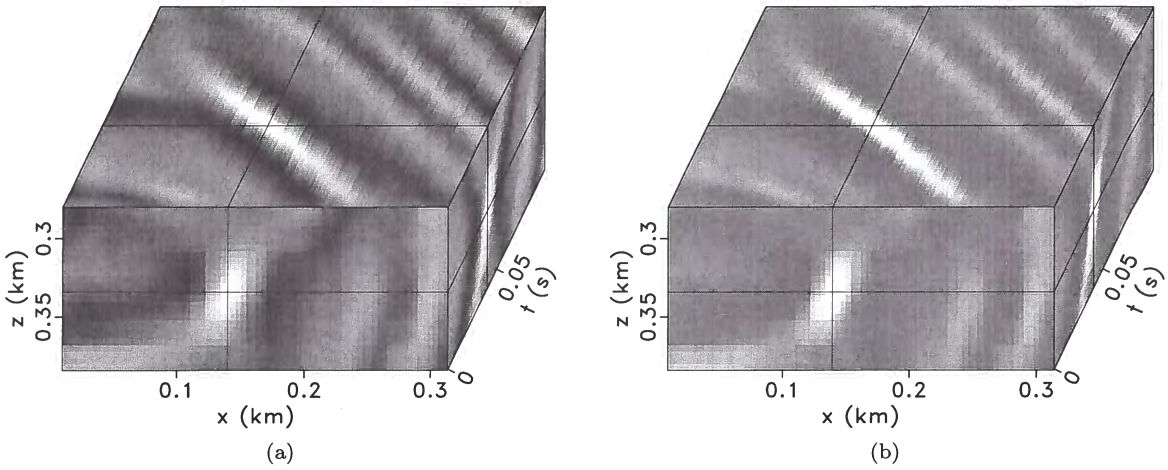

Figure 7. (a) Normalized cross-correlation. (b) Probability distribution based on the normalized cross-correlation value. The measurement uncertainty controls the width of the probability distribution around the maximum value.

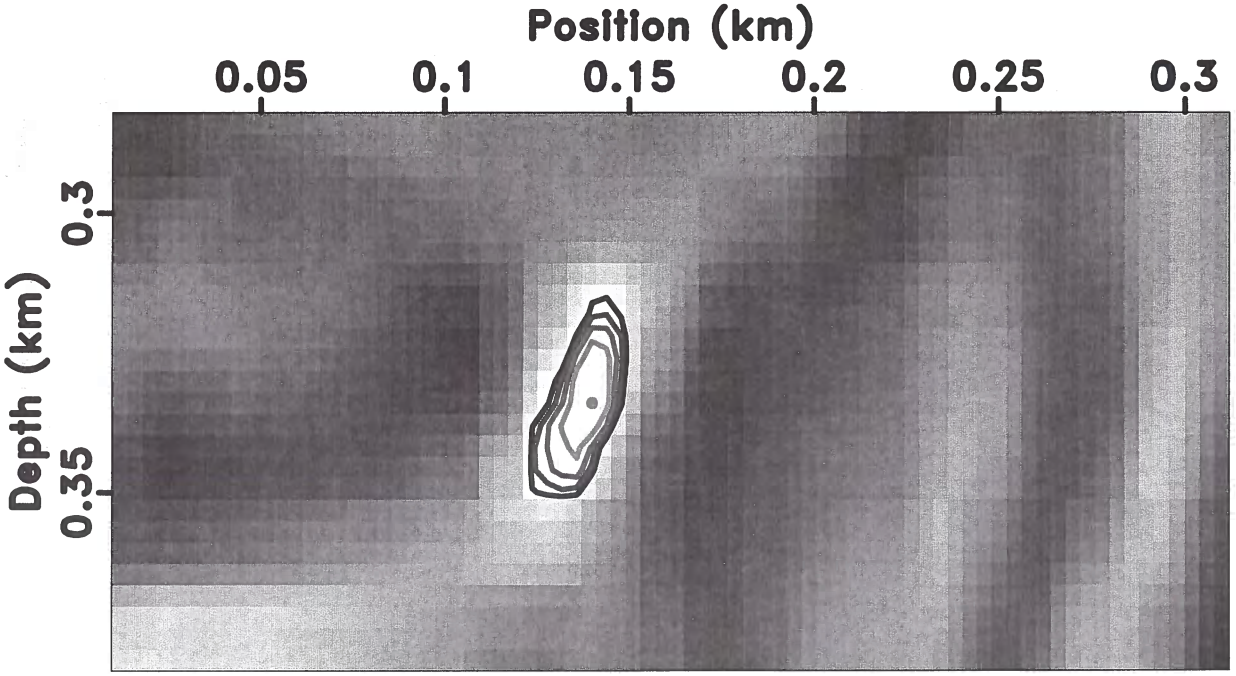

Figure 8. One snapshot of the probability density function, where the dot is the hypocenter of the micro-earthquake. The outer contour has probability of 0.8 and the contour interval is 0.05.

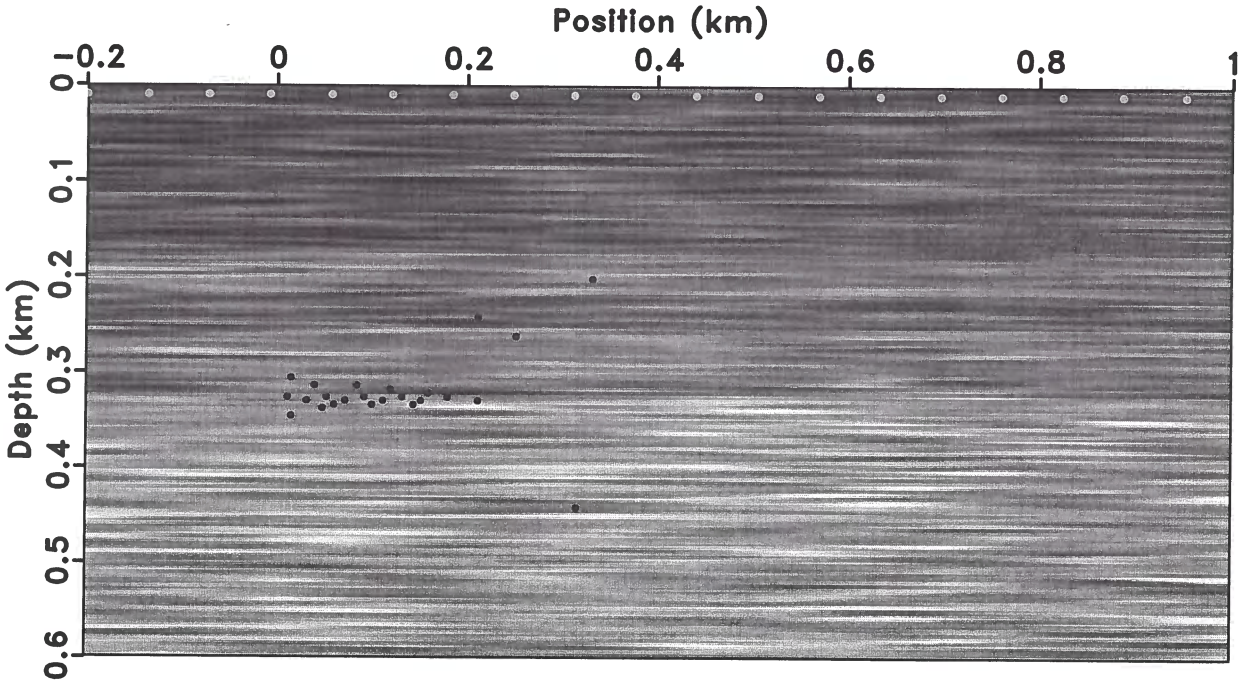

Figure 9. Synthetic model. The dots located at about $z = 0$ km represent receivers, the other dots represent the micro-seismic events.

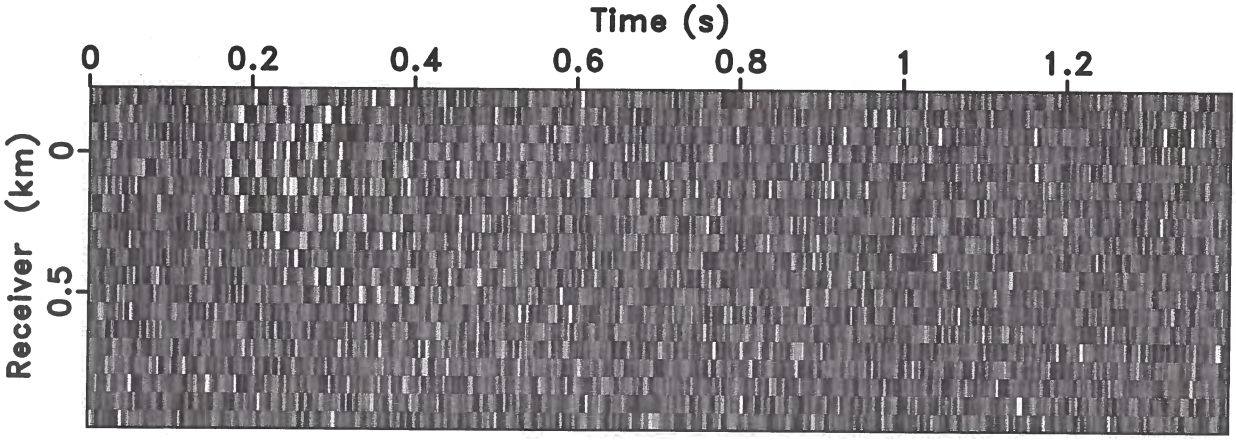

Figure 10. Synthetic seismogram. A total of 7000 time steps with an increment of 0.2 ms are calculated.

4 CONCLUSION

We present a method for automatic micro-earthquake location using Bayesian inversion theory. Our method exploits the unique shape of wavefields partially refocused at the source position. This method does not require picking of arrival times but relies on wavefield focusing obtained by time reversal. Our method not only identifies the spatial location of the source, but also specifies the onset time of the source. Furthermore, since we are using a probabilistic approach to micro-earthquake location, our method provides confidence maps of micro-earthquake locations which can be used for risk assessment.

Synthetic data examples demonstrate the robustness of the method and its applicability to situations when micro-earthquakes occur in close succession in a small region in space and are recorded in a noisy environment with a SNR as low as 0.1.

5 ACKNOWLEDGMENTS

This work was supported by ExxonMobil URC. We are grateful to Mike Payne, Jie Zhang, Rongrong Lu, Alex Martinez, and Anupama Venkataraman at ExxonMobil URC for access to data, technical discussions and financial support of this project.

REFERENCES

Born, M., and Wolf, E., 2003, Principles of optics: Electromagnetic theory of propagation, interference and diffraction of light: , Cambridge University Press.

Duncan, M., 2005, Is there a future for passive seismic?: First Break, **23**, 111–115.

Gajewski, D., 2005, Reverse modelling for seismic event characterization: Geophys.F.Int, **163**, 276–284.

Gajewski, D., 2007, Localization of seismic events by diffraction stacking: SEG Expanded Abstracts, **26**, 1287–1291.

House, L., 1987, Locating microearthquakes induced by hydraulic fracturing in crystalline rock: Geophysical Research Letters, **14**, no. 9, 919–921.

Jaynes, E., 2003, Probability theory: The logic of science: , Cambridge University Press.

Keppler, H., Pearson, C., Potter, R., and Albright, J., 1982, Microearthquakes induced during hydraulic fracturing at the Fenton Hill HDR site: the 1982 experiments: 1983 Geothermal Resources Council's annual meeting, pages 1–9.

Lay, T., and Wallace, T., 1995, Modern global seismology: , Academic Press.

Maxwell, S., and Urbancic, T., 2001, The role of passive microseismic monitoring in the instrumented oil field: The Leading Edge, pages 636–639.

Mosegaard, K., and Tarantola, A., 2002, Probabilistic approach to inverse problems: , Academic Press.

Phillipsa, W., 1998, Induced microearthquake patterns and oil-producing fracture systems in the Austin chalk: Tectonophysics, **289**, 153–169.

Pujol, J., 2004, Earthquake location tutorial: Graphical approach and approximate epicentral location techniques: Seismological Research Letters, **75**, 63–74.

Rentsch, S., 2004, Location of seismicity using gaussian beam type migration: SEG Expanded Abstracts, **23**, 354–357.

Rentsch, S., 2007, Fast location of seismicity:a migration-type approach with application to hydraulic-fracturing data: Geophysics, **72**, no. 1, S33–S40.

Rutledge, J., and Phillips, W., 2001, Hydraulic stimulation of natural fractures as revealed by induced microearthquakes, carthage cotton valley gas field, east texas: Geophysics, pages 1–37.

Shapiro, S., Dinske, C., and Rothert, E., 2006, Hydraulic-fracturing controlled dynamics of microseismic clouds: Geophysical Research Letter, **33**, no. 14, 1–5.

Tarantola, A., 2005, Inverse Problem Theory and Methods for Model Parameter Estimation: , Society for Industrial and Applied Mathematics.

Thurber, C., and Rabinowitz, N., 2000, Advances in seismic event location: , Modern Approaches in Geophysics.

Zitova, B., and Flusser, J., 2003, Image registration methods: a survey: Image and Vision Computing, **21**, 977–1000.

6 APPENDIX A

This appendix summarizes the main elements of Bayesian inversion theory. Bayesian inversion theory characterizes our state of knowledge in a probabilistic manner through the use of probability density functions (PDFs) linking model and data parameters (Jaynes, 2003). We can define two states of knowledge. The *prior* characterizes our knowledge about the model and data parameters before any measurements are taken. This information is based on our general knowledge of the phenomenon under investigation and on the distribution of model parameters and assumptions about reliability of our measurements. The *posterior* characterizes our knowledge about the model and data parameters after measurements are made and data are processed and interpreted. Both states of knowledge are characterized by PDFs linking model and data parameters. Ideally, the measurements help refine the prior into the posterior state of knowledge which provides a tighter connection between model and data parameters. In describing Bayesian inversion theory, we need to discuss the fol-

lowing elements: model ($\mathbf{m}$) and model space, data ($\mathbf{d}$) and data space, the prior state of knowledge (a priori PDF $\rho(\mathbf{m},\mathbf{d})$), the theoretical relations between model and data (theoretical PDF $\Theta(\mathbf{m},\mathbf{d})$), and the posterior state of knowledge (a posteriori PDF $\sigma(\mathbf{m},\mathbf{d})$).

6. 1 Model and data spaces

The model space ($\mathfrak{M}$) is composed of a set of individual models which can be denoted by $\mathbf{m}_i$ ($i \in \{1,2,...,N\}$). The model space represents all the models that can possibly characterize the physical phenomenon under investigation.

The data space $\mathfrak{D}$ is composed of all instrumental responses to the investigated models which can be denoted by $\mathbf{d}_i$ ($i \in \{1,2,...,M\}$). The data space represents all data that can possibly be recorded and characterize the physical phenomenon under investigation.

6. 2 A priori probability density $\rho(\mathbf{m},\mathbf{d})$

We describe $\rho(\mathbf{m},\mathbf{d})$ by a joint PDF over the model and data spaces. This prior information is independent of any measurement. Furthermore, in the special case when the prior information on the model space $\rho_{\mathfrak{M}}(\mathbf{m})$ is independent of the prior information on the data space $\rho_{\mathfrak{D}}(\mathbf{d})$, the a priori probability density function $\rho(\mathbf{m},\mathbf{d})$ is (Tarantola, 2005)

$$\rho(\mathbf{m},\mathbf{d}) = \rho_{\mathfrak{D}}(\mathbf{d})\rho_{\mathfrak{M}}(\mathbf{m}) \,, \tag{A-1}$$

where $\rho_{\mathfrak{D}}(\mathbf{d})$ describes the measurement uncertainty of the observed data, and $\rho_{\mathfrak{M}}(\mathbf{m})$ illustrates our confidence in the chosen model parameters.

Two examples of a priori probability density functions are shown in Figures 1(a) and 2(a). The vertical axis represents the value of the probability that a particular model characterizes the physical system under investigation. In Figure 1(a), $\rho(\mathbf{m},\mathbf{d}) = \rho_{\mathfrak{M}}(\mathbf{m})\delta(\mathbf{d} - D^{obs})$, where D^{obs} denote the observed data, and the a priori probability in the model space is a step function. In this case, no error is associated with the observed data. In Figure 2(a), $\rho(\mathbf{m},\mathbf{d}) = \rho_{\mathfrak{M}}(\mathbf{m})e^{-\frac{(\mathbf{d}-D^{obs})^2}{2C_d}}$, where $\rho_{\mathfrak{M}}(\mathbf{m})$ is a tapered step function, and C_d is the measurement uncertainty of the data. We assume that the data are distributed following a Gaussian distribution.

6. 3 Homogeneous probability density $\mu(\mathbf{m},\mathbf{d})$

In order to remove the effect of the discretization of the model and data parameters, we define a homogeneous PDF $\mu(\mathbf{m},\mathbf{d})$ whose role is to balance the discrete model and data spaces. By definition, the homogeneous probability distribution states that a probability assigned to each region of the space is proportional to the volume of the region (Mosegaard & Tarantola, 2002). In the special case when the homogeneous probability densities on the model and data spaces are independent, $\mu(\mathbf{m},\mathbf{d})$ is expressed as

$$\mu(\mathbf{m},\mathbf{d}) = \mu_{\mathfrak{D}}(\mathbf{d})\mu_{\mathfrak{M}}(\mathbf{m}) \,, \tag{A-2}$$

where $\mu_{\mathfrak{M}}(\mathbf{m})$ is the homogeneous probability density on the model space and $\mu_{\mathfrak{D}}(\mathbf{d})$ is the homogeneous probability density on the data space.

For example, in spherical coordinates, the volume of a standard region is $dV(r,\theta,\varphi) = r^2 \sin\theta dr d\theta d\varphi$. The homogeneous probability distribution is $\mu = kr^2 \sin\theta$, where k is an arbitrary constant. For 3-D Cartesian coordinates, $dV(x,y,z) = dxdydz$ and μ is a constant.

6. 4 Theoretical probability density $\Theta(\mathbf{m},\mathbf{d})$

The theoretical probability density $\Theta(\mathbf{m},\mathbf{d})$ describes the correlations between the model and data parameters. The defined relationship corresponds to a physical law and may incorporate uncertainties associated with theory, for example due to assumptions or simplifications of the physical law or due to imperfect knowledge of the physical parameters underlying it. The theoretical probability density $\Theta(\mathbf{m},\mathbf{d})$ can be expressed as

$$\Theta(\mathbf{m},\mathbf{d}) = \theta(\mathbf{d}|\mathbf{m})\mu_{\mathfrak{M}}(\mathbf{m}) \,, \tag{A-3}$$

where $\theta(\mathbf{d}|\mathbf{m})$ describes the probability distribution of data for the given kernel function and model, and $\mu_{\mathfrak{M}}(\mathbf{m})$ is the marginal probability defined in the preceding section. In Figure 1(b), $\theta(\mathbf{d}|\mathbf{m}) = \delta(\mathbf{d} - G(\mathbf{m}))$, where $G(\mathbf{m})$ is the kernel function which describes the physical relationship between $\mathbf{d}$ and $\mathbf{m}$. No error is associated with this kernel function. In Figure 2(b), $\theta(\mathbf{d}|\mathbf{m}) = e^{-\frac{(\mathbf{d}-G(\mathbf{m}))^2}{2C_t}}$, where C_t describes the theory uncertainty. The error associated with this kernel function follows a Gaussian distribution.

6. 5 A posteriori probability density $\sigma(\mathbf{m},\mathbf{d})$

The conjunction between the a priori state of information $\rho(\mathbf{m},\mathbf{d})$ and the theoretical probability density function $\Theta(\mathbf{m},\mathbf{d})$, which describes the theoretical relationship between model and data, provides the a posteriori state of information $\sigma(\mathbf{m},\mathbf{d})$:

$$\sigma(\mathbf{m},\mathbf{d}) = k\frac{\rho(\mathbf{m},\mathbf{d})\Theta(\mathbf{m},\mathbf{d})}{\mu(\mathbf{m},\mathbf{d})}, \tag{A-4}$$

where k is a normalization constant that serves the purpose of keeping the area under the graph of $\sigma(\mathbf{m},\mathbf{d})$ constant. The expression for k is

$$k = \frac{1}{\int_{\mathfrak{X}} d\mathfrak{X}\rho(\mathbf{m},\mathbf{d})\Theta(\mathbf{m},\mathbf{d})/\mu(\mathbf{m},\mathbf{d})}, \tag{A-5}$$

where $\mathfrak{X} = (\mathfrak{D},\mathfrak{M})$ is the joint space of the data and the model.

The posterior information $\sigma(\mathbf{m},\mathbf{d})$ is computed

based on observations. In the special case when both the model space and the data space are described in Cartesian coordinates, the posterior information is proportional to the conjunction between the prior information and the theoretical information:

$$\sigma(\mathbf{m},\mathbf{d}) \propto \rho(\mathbf{m},\mathbf{d})\Theta(\mathbf{m},\mathbf{d}). \qquad \text{(A-6)}$$

Figures 1(c) and 2(c) show the conjunction between the $\rho(\mathbf{m},\mathbf{d})$ and $\Theta(\mathbf{m},\mathbf{d})$. In Figure 1(c), $\sigma(\mathbf{m},\mathbf{d}) \propto \delta(D^{obs} - G(\mathbf{m}))$ which is shown in Figure 1(d). Figure 2(c) gives the conjunction between the PDFs shown in Figures 2(a) and 2(b). Its physical meaning is that the observed data are exactly the same as the data calculated from the kernel function. In Figure 2(c), $\sigma(\mathbf{m},\mathbf{d}) \propto e^{-\frac{(D^{obs}-G(\mathbf{m}))^2}{2C}}$, where $C = C_d + C_t$. Figure 2(d) shows $\sigma(\mathbf{m},\mathbf{d})$. The probability distribution in Figure 2(d) shows how well the data calculated from the kernel function explain the observed data.

6. 6 The marginal probability density $\sigma_{\mathfrak{M}}(\mathbf{m})$

In order to provide a solution to the inversion problem, we have to transfer the information provided by $\sigma(\mathbf{m},\mathbf{d})$ to the model space. We obtain the marginal probability density in the model space $\sigma_{\mathfrak{M}}(\mathbf{m})$ by projecting $\sigma(\mathbf{m},\mathbf{d})$ onto the model space:

$$\sigma_{\mathfrak{M}}(\mathbf{m}) = \int_{\mathfrak{D}} \sigma(\mathbf{m},\mathbf{d}) d\mathbf{d} \, . \qquad \text{(A-7)}$$

The probability density function provided by $\sigma_{\mathfrak{M}}(\mathbf{m})$ indicates what models satisfy at the same time our prior knowledge on the distribution of model parameters, the theoretical relationships between model and data and the measurement uncertainties. A comparison between $\rho_{\mathfrak{M}}(\mathbf{m})$ and $\sigma_{\mathfrak{M}}(\mathbf{m})$ is shown in Figures 1(e) and 2(e). The distribution on $\sigma_{\mathfrak{M}}(\mathbf{m})$ is narrower on the posterior relative to the prior indicating the tighter connection introduced by the recorded data.

6. 7 Negligible theoretical uncertainties

When we assume that no uncertainty is associated with the kernel function $G(\mathbf{m})$ which describes the physical relationship between the data and the model, the theoretical probability density $\Theta(\mathbf{m},\mathbf{d})$ can be expressed as

$$\Theta(\mathbf{m},\mathbf{d}) = \delta(\mathbf{d} - G(\mathbf{m}))\mu_{\mathfrak{M}}(\mathbf{m}) \, , \qquad \text{(A-8)}$$

where $\mu_{\mathfrak{M}}(\mathbf{m})$ is a constant for models parameterized in Cartesian coordinates. The theoretical probability density $\Theta(\mathbf{m},\mathbf{d}) = 1$ when the data equal the value calculated from the kernel function and zero otherwise.

In this case, the marginal probability in the model space in equation A-7 can be expressed as

$$\sigma_{\mathfrak{M}}(\mathbf{m}) = \int_{\mathfrak{D}} \sigma(\mathbf{m},\mathbf{d}) d\mathbf{d} = k \int_{\mathfrak{D}} \frac{\rho(\mathbf{m},\mathbf{d})\Theta(\mathbf{m},\mathbf{d})}{\mu(\mathbf{m},\mathbf{d})} d\mathbf{d} \, , \qquad \text{(A-9)}$$

and when $\Theta(\mathbf{m},\mathbf{d})$ is given in equation A-8, with $\rho(\mathbf{m},\mathbf{d}) = \rho_{\mathfrak{D}}(\mathbf{d})\rho_{\mathfrak{M}}(\mathbf{m})$ and $\mu(\mathbf{m},\mathbf{d}) = \mu_{\mathfrak{D}}(\mathbf{d})\mu_{\mathfrak{M}}(\mathbf{m})$, we can write

$$\sigma_{\mathfrak{M}}(\mathbf{m}) = k\rho_{\mathfrak{M}}(\mathbf{m}) \int_{\mathfrak{D}} \frac{\rho_{\mathfrak{D}}(\mathbf{d})\delta(\mathbf{d} - G(\mathbf{m}))}{\mu_{\mathfrak{D}}(\mathbf{d})} d\mathbf{d} \, , \qquad \text{(A-10)}$$

where $\rho_{\mathfrak{D}}(\mathbf{d})$ is a function of $\mathbf{d}$ and the observed data, and $\mu_{\mathfrak{D}}(\mathbf{d})$ is a constant for data discretized in Cartesian coordinates. Thus, equation A-7 for an ideal kernel function can be written as

$$\sigma_{\mathfrak{M}}(\mathbf{m}) = \nu\rho_{\mathfrak{M}}(\mathbf{m})\rho_{\mathcal{D}}(G(\mathbf{m}), D^{obs}) \, , \qquad \text{(A-11)}$$

where

$$\nu = \int_{\mathfrak{M}} \rho_{\mathfrak{M}}(\mathbf{m})\rho_{\mathcal{D}}(\mathbf{d}, D^{obs}) d\mathbf{m} \qquad \text{(A-12)}$$

is a constant. In equation A-11, $\sigma_{\mathfrak{M}}(\mathbf{m})$ is proportional to the product of the prior probabilities on the model and data spaces.

Imaging effects due to multi-scale model heterogeneity

Yong Ma & Paul Sava
Center for Wave Phenomena, Colorado School of Mines

ABSTRACT
Velocity models used for wavefield-based seismic imaging represent approximations of the velocity characterizing the area under investigation. We can conceptually decompose the real velocity model into a background component which can be inferred using conventional velocity analysis techniques, and into another unknown component encapsulating the model heterogeneities. This unknown component is responsible for mispositioning of reflection energy which usually takes the form of imaging artifacts. Model heterogeneity can be described stochastically using, for example, correlated Gaussian random distributions or fractal distributions. Data simulated for the various distributions are characterized by spectra with different shapes when analyzed in the log-log domain. For example, Gaussian distributions are characterized by exponential functions and fractal distributions are characterized by linear functions with fractional slopes. These properties hold for both data and migrated images after deconvolution of the source wavelet. On the other hand, the image heterogeneities induced by model heterogeneities can be considered as noise to be removed by an image filtering operation. Among many possibilities, filtering with the seislet transform (a wavelet transform technique) and Gabor-Wigner distribution (a time-frequency analysis technique) are effective at suppressing noise, although both techniques affect the signal corresponding to the major geologic structure. Such filtering can be applied at different stages of wave-equation imaging, for example on data, on the reconstructed wavefields, or on the migrated image. Of all possibilities, filtering of the wavefield is the most effective.

Key words: multi-scale heterogeneity, noise attenuation

1 INTRODUCTION

Wave-equation migration consists of two steps (Claerbout, 1985). The first step represents wavefield reconstruction at every location in the subsurface from data recorded at the surface using a numeric solution to a wave equation. The second step consists of extracting reflectivity information from the reconstructed wavefields using an imaging condition. The accuracy of wavefield reconstruction, which directly determines the quality of migrated images, depends on the accuracy of both the velocity model and the wave-equation used for wavefield reconstruction.

Conventionally, we decompose the Earth's velocity into two models corresponding to large-scale (low-frequency) and to small-scale (high-frequency) components. We refer to the large-scale component as the velocity model and to the small-scale component as the reflectivity model. The large-scale component of the model is used for wavefield reconstruction, and the small-scale component of the model is the object of the imaging condition. However, real geologic environments do not follow this clear separation of scales. Evidence from well logs and rock outcrops indicates that a better description of the subsurface requires heterogeneity at all scales of variation (Richter-Bernburg, 1987). We refer to this type of models as *multi-scale*. The multi-scale variability is usually ignored in imaging which usually assumes that the mid-range of variability does not exist. As a consequence, imaging with smooth models leads to inaccurate wavefield reconstruction and to corresponding distortions of migrated images.

In this paper, we study the effects of multi-scale heterogeneity on imaging. First, we analyze various types of heterogeneity, their impact on seismic data and migrated images and whether this information can be extracted from data or migrated images. Since the mid-scale heterogeneities are not accounted for in imaging, their effect on images has the character of artifacts overlapping the geologic structure which corresponds to the bi-modal decomposition of the model. Second, we evaluate techniques designed to attenuate the arti-

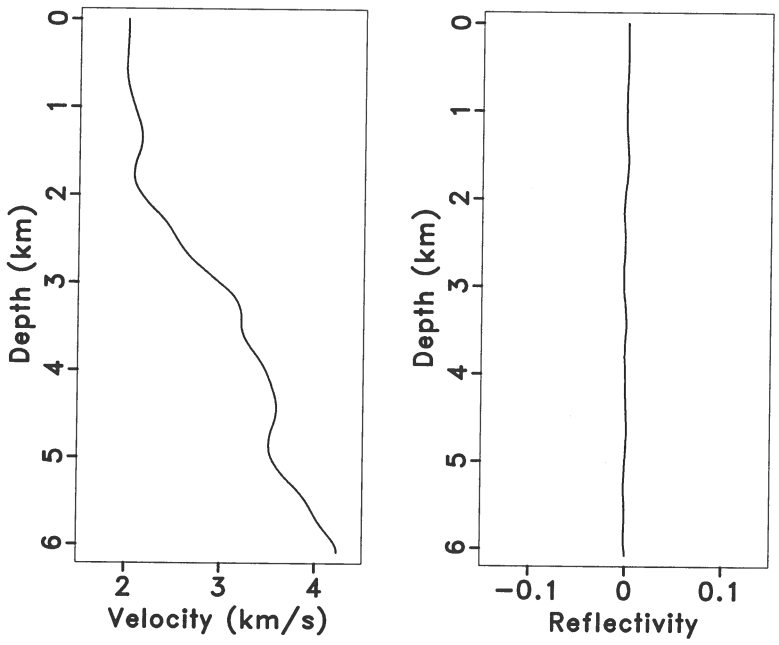

Figure 1. (a) A smooth background vertical velocity profile that has no significant local heterogeneity to generate details in the reflection coefficients, which is shown in (b).

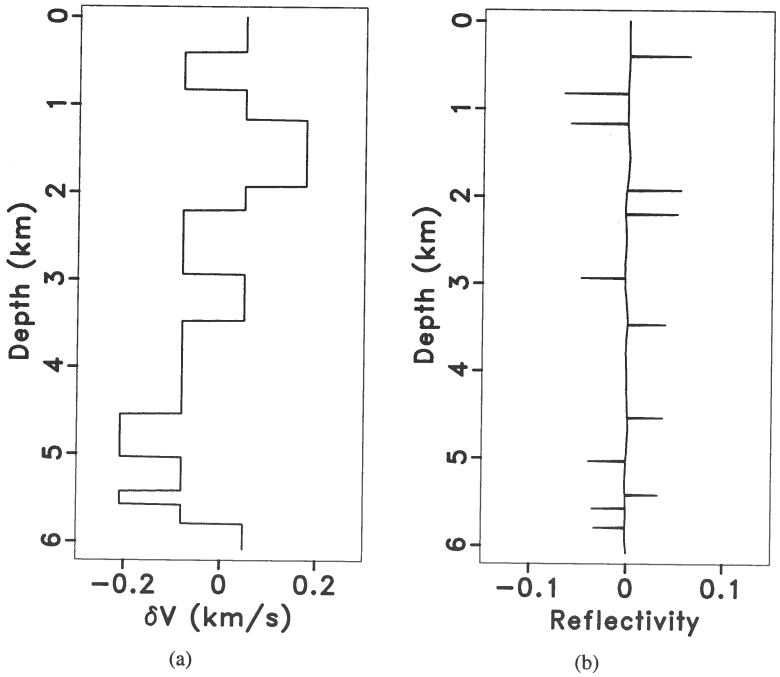

Figure 2. (a) A blocky heterogeneity and (b) its resulting reflection-coefficient series in depth.

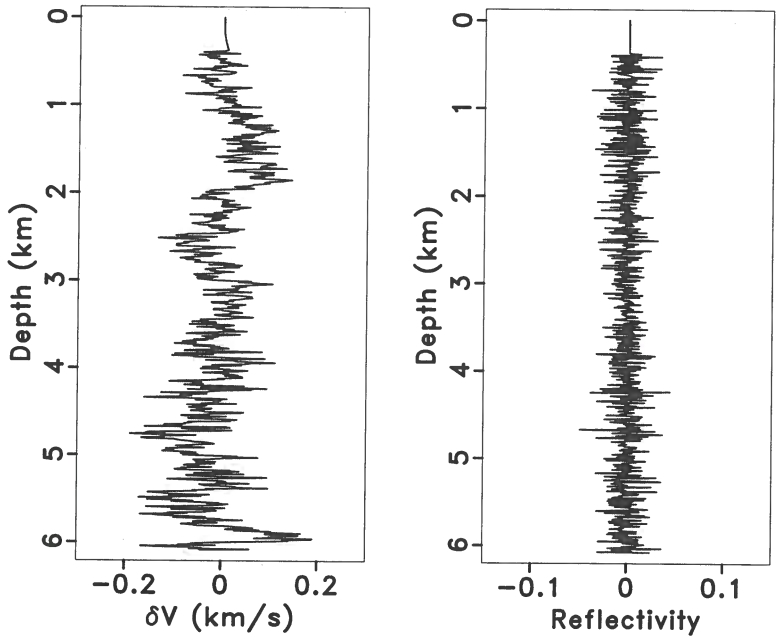

Figure 5. (a) The fractal perturbations with a order of 0.50, corresponding to the log-log spectrum in Figure 7(d). (b) The primary reflection-coefficient series governed by the fractal heterogeneity in (a).

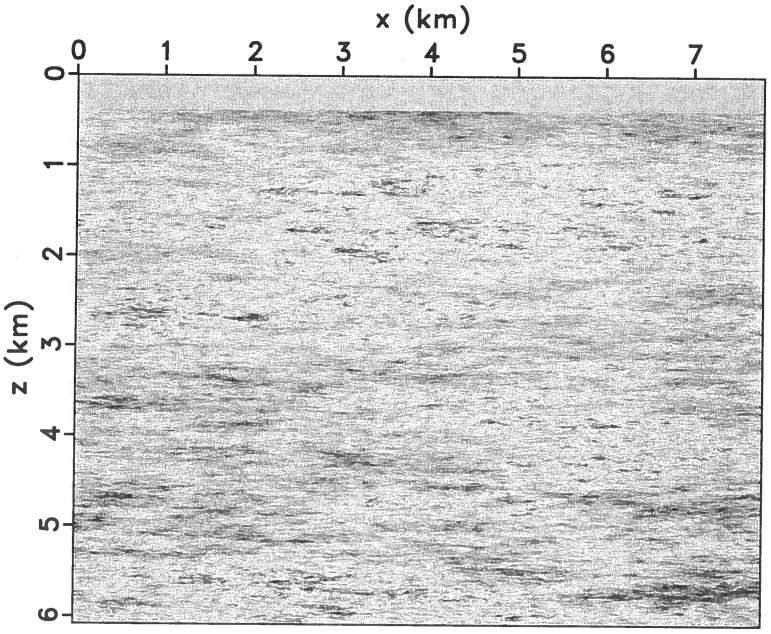

Figure 6. Fractal random perturbations in a velocity model with power law of order $\beta = 0.5$.

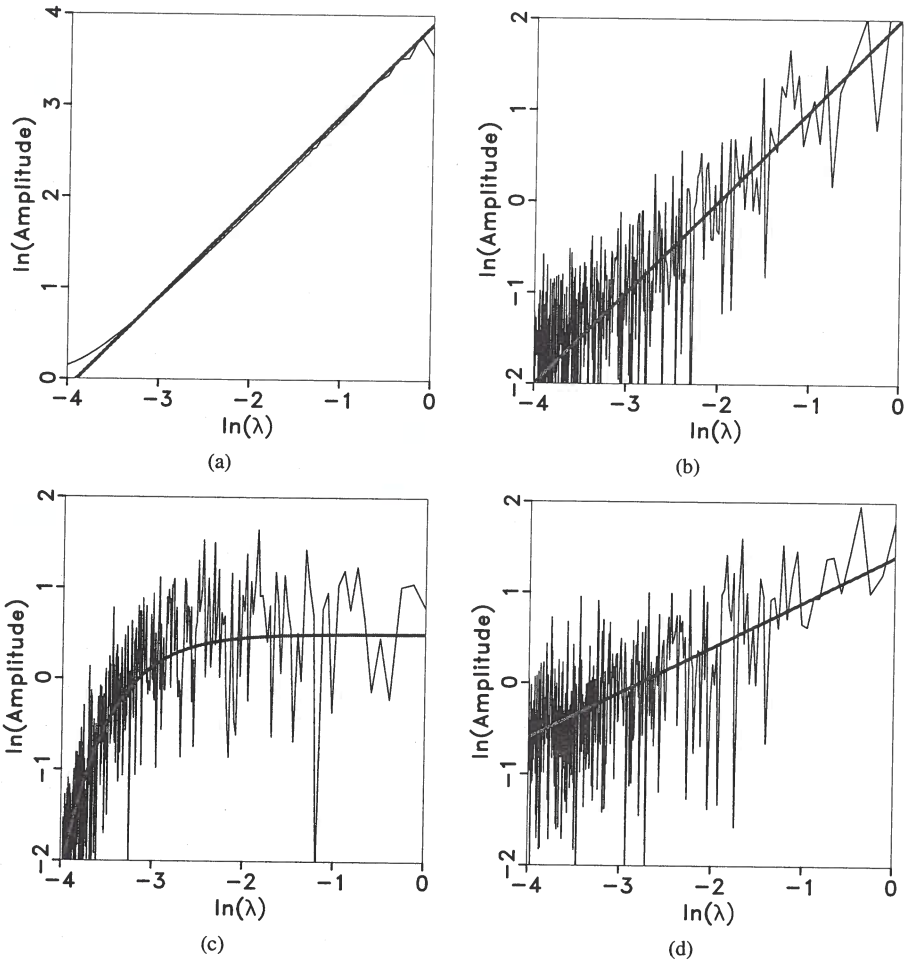

Figure 7. Log-log spectra corresponding to (a) a smooth background velocity, (b) a blocky perturbation, and (c) a depth-correlated Gaussian random perturbation in log-log spectrum analyses. Thick lines are least-squares fittings of the log-log spectra. Both the smooth background and blocky perturbations show a trending slope of about 1. The correlated random noise in (c) gives an exponential relationship in the log-log graphic. In contrast, (d) shows a fractal power-law example, which depicts a linear least-squares fit with slope $\beta = 0.5$.

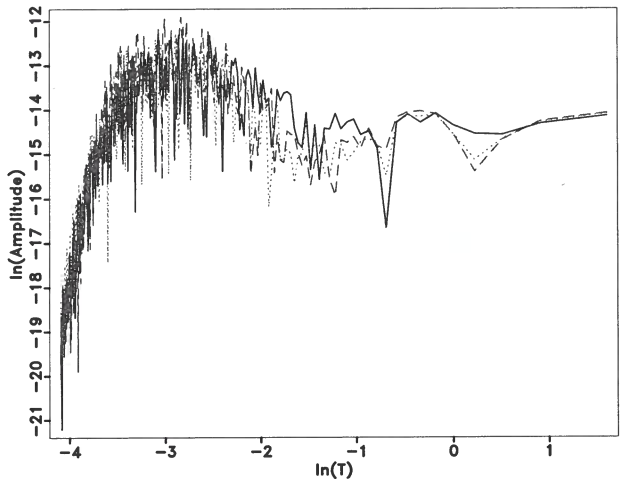

Figure 10. Spectra comparison of data shown in Figure 9(a)–9(c) in a log-log plot. Solid: blocky-model data in Figure 9(a); dashed: Gaussian-random data in Figure 9(b); dotted: fractal-random data in Figure 9(c).

4 IMAGE VARIABILITY DUE TO MODEL HETEROGENEITY

The analysis performed in the preceding section addresses the question whether we can access information about the model heterogeneity through the analysis of recorded data. In this section we address an alternative question, i.e. whether we can access the same information through analysis of migrated images. For this analysis, we use a portion from a well-log acquired in the field. In this case, we do not know a-priori the nature of the randomness. Figure 12(a) shows the P-wave velocity constructed from well measurements superimposed on a velocity model obtained as horizontal extension of the well-log.

Figure 13(a) shows the log-log spectrum of the well-log. The thick straight line represents the linear least-squares fit applied to the spectrum. The slope is equal to 1 which is consistent to the fact that the well log is dominated by a smooth non-constant background component, or put another way, the spectrum is dominated by a slope inversely proportional with the wavenumber k (Shtatland, 1991). In order to emphasize the heterogeneities presented in the model, we first remove the k^{-1} spectrum. In the k domain, according to the nonlinear least-squares fitting $y = ak^{-1}$, we estimate the intensity of the k^{-1} component which corresponds to the background velocity. Because of the linear assumption of velocity model composition, we can apply a linear operation in the k domain, i.e. we subtract the nonlinear least-squares fit from the entire spectrum. After removing the k^{-1} component, we analyze separately the remaining spectrum shown in Figure 13(b). The slope of the linear least-squares fit is equal to 0.53 which, as expected, indicates that the model randomness has a fractal character.

Figure 12(b) shows a simulated shot-record data with a source located at $x = 2.0$ km, $z = 0$ km. The zero-offset trace is superimposed on the data. Migration of the data in a smoothed background velocity produces the image shown in Figure 12(c). The zero-offset image trace is also superimposed on the image. As for the preceding example, we analyze the expression of model randomness on image using the log-log plots of the spectra, after we deconvolve the seismic wavelet from the image. Figure 14(a) displays log-log spectra of the zero-offset image trace. As before, we separate the k^{-1} component obtaining the spectrum shown in Figure 14(b). The linear least-squares fit to the image spectrum has a slope of 0.54, which is close to the slope obtained from the direct analysis of the well-log. Thus, we can conclude that the migrated image indicates the presence of a model with fractal parameter β approximately equal to 0.53. Figure 15 shows the dependence of extracted heterogeneity information from image on the horizontal position with respect to the source location. It is apparent that the extracted heterogeneity parameters in the near offset are more precise than in the far offset.

The procedure discussed here requires knowledge of the source wavelet to extract heterogeneity parameters from data or migrated images. However, only the amplitude spectrum matters, therefore we conjecture that we can still obtain satisfactory results even if small phase errors in our wavelet estimation exist.

Our analysis show that various types of heterogeneity look different when analyzed in log-log plots, as illustrated in Figures 11(a)-11(f). Assuming that the background model of the subsurface is a combination of a relatively smooth background plus a few strong interfaces with a blocky character, we can attempt to infer the statistics of model heterogeneities currently undetectable by conventional seismic methodology.

Alternatively, we can consider the effects of mid-scale heterogeneities on seismic data as noise and attempt to remove them from migrated images. Our experiments show that conventional denoising methods based on bandwidth analysis do not have a good chance of success given the overlap between various components of the model. However, we suggest that it would be helpful to understand the statistics of this noise before attempting to remove it.

5 NOISE ATTENUATION IN SEISMIC IMAGING

Despite the fact that multi-scale heterogeneities are present in the Earth, we normally describe their expression in seismic data as noise and their expression on migrated images as artifacts. This is simply because we do not have good procedures to estimate models with such variability and to image those data. In this section, we explore the applicability of two kinds of de-noising procedures: seislet transform (ST) which belongs to the wavelet transform methods, and Gabor-Wigner distribution (GWD) which belongs to the time-frequency analysis (TFA) methods.

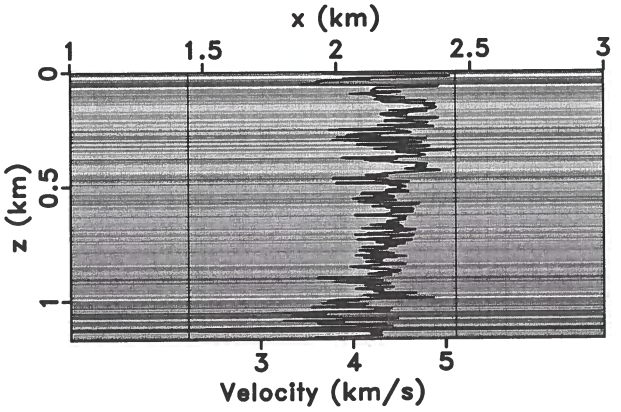

(a)

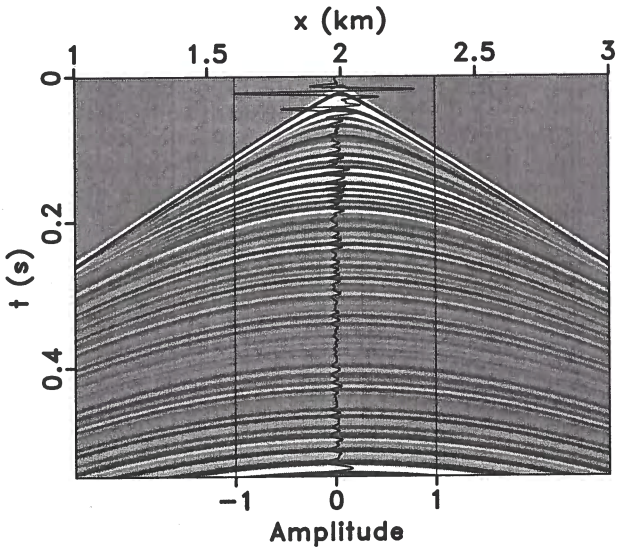

(b)

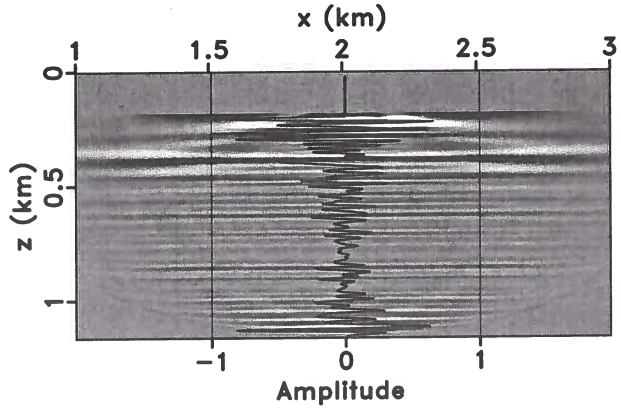

(c)

Figure 12. (a) Well log data of P-wave velocity, extended horizontally to mimic a subsurface velocity model. (b) Data recorded in a shot-record experiment, with a shot at ($x = 2.0$ km, $z = 0$ km) and receivers on the surface; the zero-offset trace is superimposed on the data. (c) Image of the data Figure 12(b) using migration with a conventional imaging condition and a smoothed background velocity; the vertical image trace at $x = 2.0$ km is superimposed on the image.

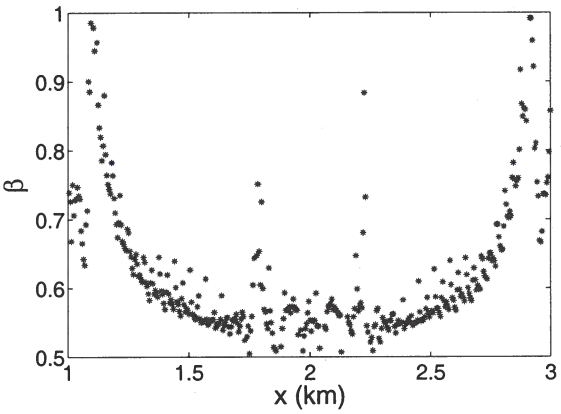

Figure 15. The heterogeneity parameter β extracted from the image at various horizontal positions.

5. 1 Seislet transform

The seislet transform belongs to the general family of wavelet transform. By definition, this transformation decomposes the signal to different scales using the dominant slope at every location (Fomel, 2006). ST can be used for de-noising by a simple soft thresholding operation in the transformed domain designed to preserve the locally dominant slopes in the data or image, thus filtering out perturbations from the dominant slope. Filtering using ST makes the assumption that the data are correctly described by locally coherent events, while noise is not.

5. 2 Gabor-Wigner distribution

TFA methods decompose non-stationary signals as functions of the local frequency at various times (Cohen, 1995). This type of transformation can be generalized to multi-dimensional signals, e.g. to seismic data or wavefields. Wigner distribution functions (WDF) (Wigner, 1932; Ville, 1948) are an example of TFA method with a quadratic character (Hlawatsch & Boudereaux-Bartels, 1992). WDFs are effective at suppressing noise from data, but suffer from the drawback that the phase of their output is ambiguous. To alleviate this problem, we use an alternative TFA transformation, called the Gabor-Wigner distribution (GWD) (Pei & Ding, 2007), which has the property that it attenuates the noise similarly to WDF, but without affecting the phase of the signal. For the multi-dimensional signal $s(\mathbf{x}, t)$, the Gabor-Wigner distribution is given by

$$s_g(\mathbf{x}, t) = s_w(\mathbf{x}, t) \int_{|t_h| \le T} dt_h \int_{|\mathbf{x}_h| \le X} d\mathbf{x}_h \; g(\mathbf{x}, t)\, s(\mathbf{x}, t) \;, \quad (10)$$

where

$$s_w(\mathbf{x}, t) = \int_{|t_h| \le T} dt_h \int_{|\mathbf{x}_h| \le X} d\mathbf{x}_h \; g(\mathbf{x}, t)\, s\left(\mathbf{x} - \frac{\mathbf{x}_h}{2}, t - \frac{t_h}{2}\right) s\left(\mathbf{x} + \frac{\mathbf{x}_h}{2}, t + \frac{t_h}{2}\right) \quad (11)$$

In equations 10 and 11, $g(\mathbf{x}, t) = e^{-\frac{(\mathbf{x}-\mathbf{x}_h)^2}{2\sigma_{\mathbf{x}}^2}} e^{-\frac{(t-t_h)^2}{2\sigma_t^2}}$ is a multi-dimensional Gaussian window with spatial and temporal standard deviations of $\sigma_{\mathbf{x}}$ and σ_t, which has the purpose of reducing cross-talk (Choi & Williams, 1989); $s_w(\mathbf{x}, t)$ is the WDF transform result of $s(\mathbf{x}, t)$ in the time-space domain; $\mathbf{x}_h$ and t_h are variables spanning space and time intervals within X and T, respectively.

5. 3 Strategies for noise attenuation

Wave-equation imaging for shot-record experiments consists of two steps: first, simulate the source and receiver wavefields using the background velocity model; second, apply an imaging condition to extract the reflectivity information from the reconstructed source and receiver wavefields. A conventional imaging condition extracts the image as the zero-lag of the cross-correlation between the reconstructed wavefields

$$R(\mathbf{y}) = \int_t dt \; u_s(\mathbf{y}, t)\, u_r(\mathbf{y}, t) \;, \quad (12)$$

where $\mathbf{y}$ denotes the image coordinates, $u_s(\mathbf{y}, t)$ and $u_r(\mathbf{y}, t)$ are the reconstructed source and receiver wavefields, and $R(\mathbf{y})$ is the extracted image.

Wavefields corresponding to propagation in models with multi-scale heterogeneity are not properly reconstructed in the subsurface if we use an approximate blocky model for wavefield reconstruction. Consequently, fluctuations corresponding to the part of the model that is not accounted for during extrapolation are present in the wavefields. The question we address here is whether we can use one of the noise attenuation techniques outlined earlier to filter out the unwanted component of data. We discuss three possible strategies corresponding to filtering before wavefield reconstruction (i.e. filter the data), filtering before the imaging condition (i.e. filter the wavefields), or filtering after the imaging condition (i.e. filter the image) as illustrated in Figure 16.

In workflow (a), the denoising process is directly applied to the recorded data before wavefield reconstruction. In this case, we attempt to remove from the data what we consider to be unwanted signal and then follow with a conventional imaging procedure. This option is advantageous because it operates on relatively small data volumes, but it has the disadvantage that data are often complicated with many conflicting dips which makes it difficult to define a predominant slope at some location and time.

In workflow (b), the denoising process is applied to the reconstructed wavefields before the application of the imaging condition. This is the strategy employed by Sava & Poliannikov (2008) in the design of the so-called interferometric

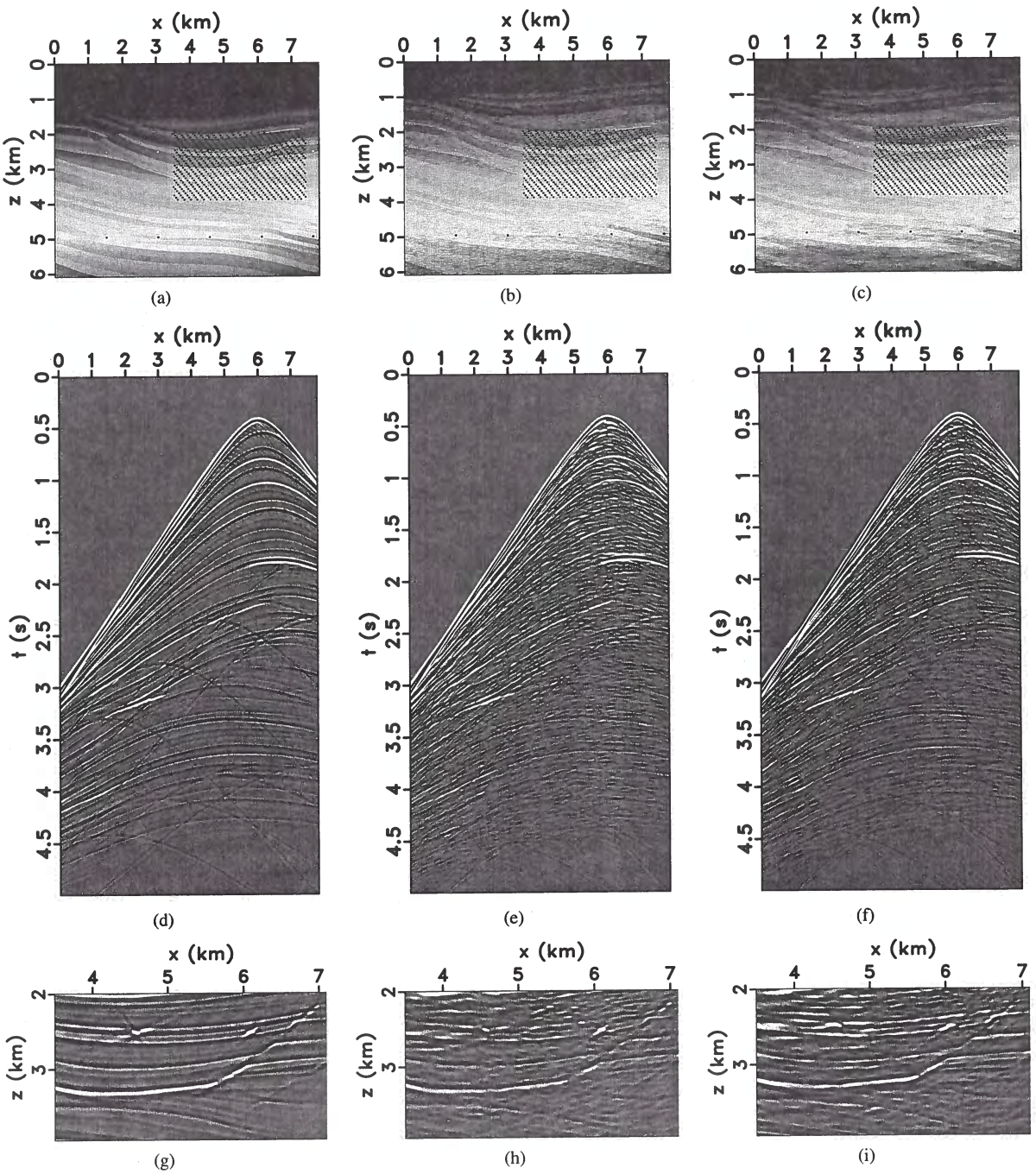

Figure 17. Sigsbee 2A models: (a) blocky velocity, (b) Gaussian random velocity and (c) fractal velocity. Finite-difference modeled data for a source located at $x = 4.0$ km and receivers distributed along the surface corresponding to (d) the blocky model, (e) the Gaussian random model and (f) the fractal random model. The zero-offset trace overlays the data in panels (d)-(f). (g) Image with the conventional imaging condition using the blocky velocity model for both modeling and migration. (h) Migrated image using the blocky velocity and the conventional imaging condition applied to data simulated in the Gaussian random velocity. (i) Migrated image using the blocky velocity and the conventional imaging condition applied to data simulated in the fractal velocity.

workflow	Figure 18		Figure 19	
	ST	GWD	ST	GWD
a	0.0100	0.0094	0.0104	0.0112
b	0.0076	0.0066	0.0103	0.0088
c	0.0093	0.0107	0.0133	0.0104

Table 2. MSEs comparisons of images in Figures 18 and 19 with the benchmark image in Figure 17(g).

the ST applied to the data, wavefield and image, respectively, and panels 19(d)-19(f) correspond to de-noising using GWD applied to the data, wavefield and image, respectively.

Both ST and GWD used in all three workflows help reduce the random fluctuations from the migrated images, although none produces images with the coherence comparable with that of the reference image, Figure 17(g). This is not surprising since both de-noising techniques attempt to filter-out information incorrectly positioned in the subsurface, rather than relocate it. However, it is apparent that better results are produced when de-noising is applied to the wavefields, rather than to the data or the image. The main reason for this is that more coherency exists in the wavefields along the space and time axes. The data and the image are subsets of the wavefields, therefore these domains are not as effective at noise suppression.

We can quantify the differences between the various de-noised images and our benchmark image using the mean squared error (MSE) (Lehmann & Casella, 2003). The MSE values characterize the dissimilarity between the de-noised images and the reference and the larger the MSE value, the more dissimilar the images. The raw images shown in Figures 17(h) and 17(i) have a mean squared error of 0.011 and 0.014, respectively, relative to the benchmark image shown in Figure 17(g). Table 2 lists the mean square errors between the images in Figures 18(a)-18(f) and Figures 19(a)-19(f) relative to the benchmark image. According to this analysis, the best denoising strategy is to apply either ST or GWD to the wavefields after wavefield reconstruction but before the imaging condition, with a slight efficiency advantage for GWD relative to ST.

7 CONCLUSIONS

We compare different types of multi-scale heterogeneities and investigate whether information about the parameters characterizing such models can be derived from the images. Assuming that we can estimate the seismic wavelet with sufficient accuracy, we can isolate reflectivity profiles from both recorded data and migrated images and extract the media properties. We can identify models with correlated Gaussian fluctuations by their exponential dependence in log-log spectra. In contrast, models with fractal fluctuations show, as predicted by the theory, a linear dependence of the log-log spectra with a fractional slope. This conclusion holds for both the data and image domains. Regardless of the type of fluctuations in the model, imaging with approximate velocity (e.g. blocky models) leaves a distinct random-looking imprint on the migrated images which may obstruct identification of geologic structures.

We refer to this kind of imprint as noise and attempt to remove it using conventional statistical procedures. We test the seislet transform (curvelet-like method) and Gabor-Wigner distributions (time/fraquency-like method) to attenuate noise at different stages of depth migration. The noise attenuation can be applied to the data before wavefield reconstruction, or to the reconstructed wavefields, or to the migrated image, after the application of the imaging condition. Of all possibilities, filtering of the wavefield seems to be the most effective method of noise attenuation, although this option is also the costliest.

ACKNOWLEDGMENT

We acknowledge the support of the sponsors of the Center for Wave Phenomena at Colorado School of Mines. We are grateful to Prajnajyoti Mazumdar from the Colorado School of Mines Reservoir Characterization Project (RCP) for supplying the well log data.

REFERENCES

Choi, H. I., and Williams, W. J., 1989, Improved time-frequency representation of multicomponent signals using exponential kernels: IEEE Transaction on Acoustics and Speech Signal Processing, **37**, no. 6, 862–871.

Claerbout, J. F., 1985, Imaging the Earth's interior: , Blackwell Scientific Publications.

Cohen, L., 1995, Time Frequency Analysis: , Prentice Hall signal processing series.

Dolan, S. S., Bean, C. J., and Riollet, B., 1998, The broadband fractal nature of heterogeneity in the upper crust from petrophysical logs: Geophysical Journal International, **132**, no. 3, 489–507.

Fomel, S., 2006, Towards the seislet transform: SEG Expanded Abstracts, **25**, no. 1, 2847–2850.

Hlawatsch, F., and Boudereaux-Bartels, G. F., 1992, Linear and quadratic time-frequency signal representation: IEEE Signal Processing, **24**, 21–67.

Hoshiba, M., 2000, Large fluctuation of wave amplitude produced by small fluctuation of velocity structure: Physics of the earth and planetary interiors, **120**, 201–217.

Lehmann, E. L., and Casella, G., 2003, Theory of point estimation: , Springer, 2nd edition.

Mandelbrot, B. B., 1982, The Fractal Geometry of Nature: , Freeman, San Francisco.

Paffenholz, J., McLain, B., Zaske, J., and Keliher, P., 2002, Subsalt multiple attenuation and imaging: Observations from the sigsbee2b synthetic dataset: 72nd Annual International Meeting, SEG, Expanded Abstracts, pages 2122–2125.

Freeform modeling of faulted surfaces in seismic images

Derek Parks
Center for Wave Phenomena, Colorado School of Mines, Golden CO 80401, USA

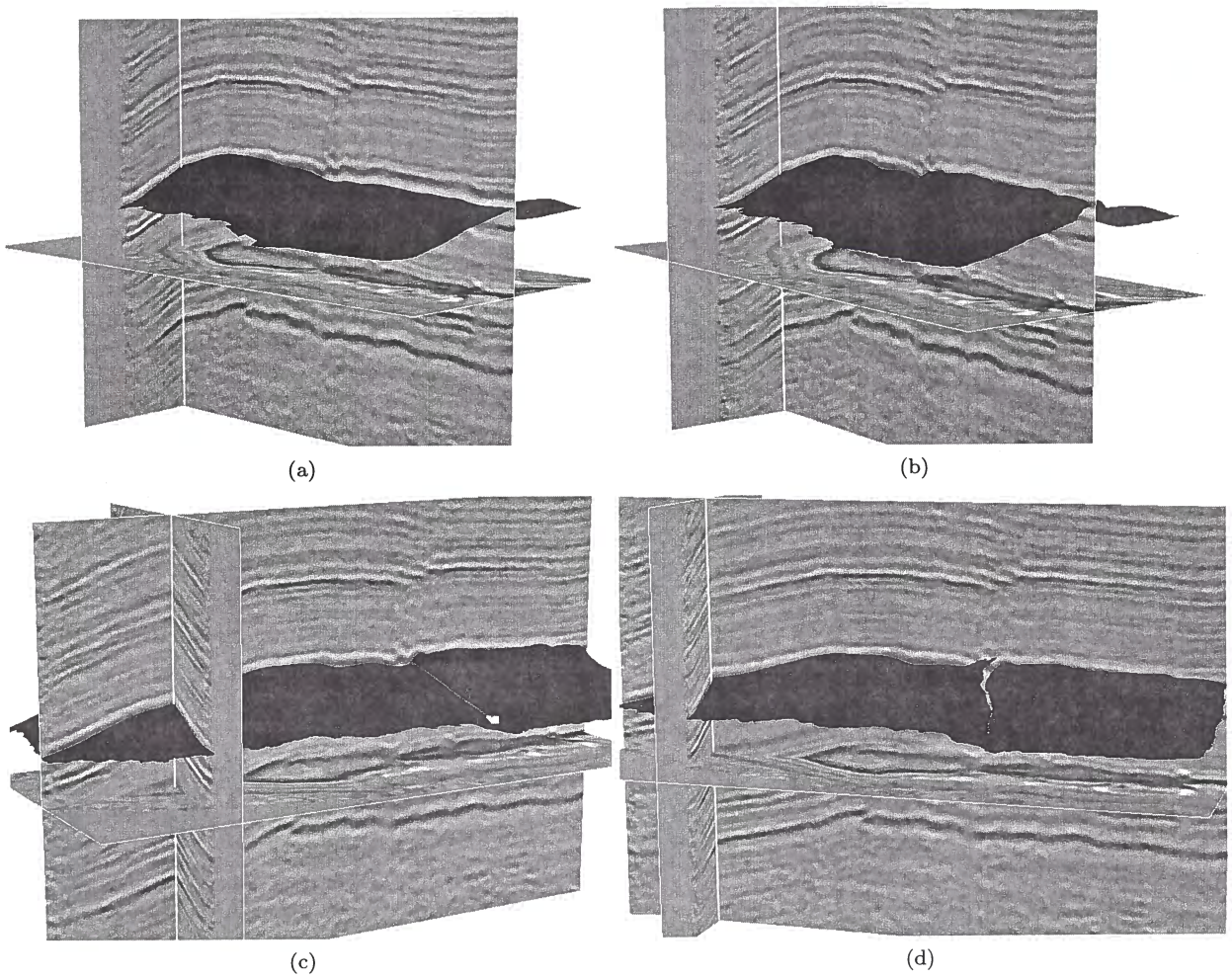

Figure 1. (a) The blue surface which was estimated using an image processing technique attempts to track a geologic horizon in the 3D seismic image, but the automatic tracking has gone off course. (b) The surface after interactive deformation to improve tracking of the structure seen in the seismic image. (c) A cut created in the surface to model a fault. (d) After cutting and further deformations the surface conforms to discontinuities apparent in the seismic image.

ABSTRACT
An interactive surface editing framework that is well suited to the needs of geophysical modelers and interpreters is described. This surface editing framework allows a non-expert user to quickly create complicated surfaces by combining two simple concepts: deformation and cutting. Deformations change the geometry of a surface and allow a user to model continuous geologic horizons. Cutting changes the topology of the surface to model geologic faults.

Key words: surface modeling freeform deformation cutting

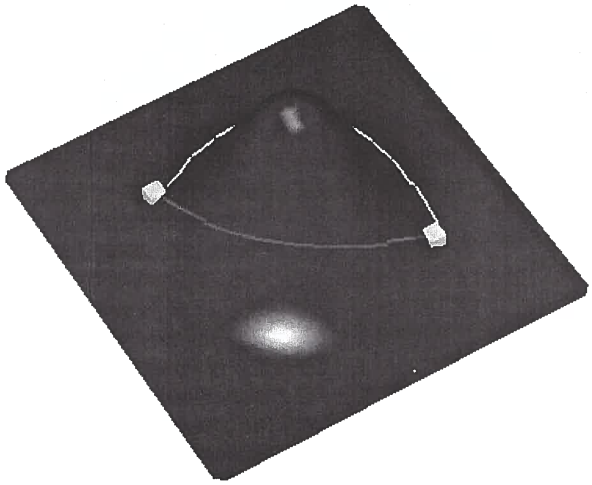

Figure 3. Two possible paths between seed points (yellow boxes). The geodesic shortest path (cyan) runs behind the bump in the surface. The user probably did not have this path in mind. A path that takes into account the user's current view of the surface is shown in red.

rithm. The method has a worst case computational cost of $O(n^2 \log n)$, where n is the number of edges in a mesh.

Unfortunately, using the geodesic shortest path to connect seed points has a drawback which is illustrated in Figure 3. As we can see, the geodesic shortest path between points is not easily predictable. This path may not look like the shortest possible path when the surface is projected into a 3D perspective view, and may be an undesirably convoluted path that runs behind parts of the surface.

Here, I present a method for finding a path along a surface between seed points that is more intuitive, more efficient, and easier to implement than the geodesic shortest distance path. The new method takes into account the user's current view of the surface, and ensures that the path between seed points can be seen. This leads to less ambiguity in the user interface. The new path can be found by performing simple object intersection tests and can be computed in time proportional to the number of edges intersected by the cut path.

After a cut path has been created, the area around the path must be remeshed to open a cut in the surface. As stated above, care must be taken to ensure that a resulting mesh is valid. Many methods for performing cut remeshing have been presented in the surgical simulation literature (Bielser and Gross, 2000; Bruyns and Senger, 2001; Nienhuys and van der Stappen, 2001; Choi, 2006) however, these interfaces interactively remesh a cut as a tool is moved along a surface. I describe a method that is similar to many of the surgical simulator remeshing algorithms but is better suited for use with a seed point based cut path.

2 BOUNDARY CONSTRAINT MODELING

BCM uses a simple modeling metaphor that allows a user to quickly make changes to a surface. In order to perform a deformation, a user must first select an area of the surface to be modified. I call this area the deformable region. An example of a user selected deformable region is shown in Figure 4a (the green area). The remaining surface, the part outside of the deformable region, is defined to be fixed; thus a user knows that a deformation will only make local changes to a surface.

It should be noted that, by selecting a deformable region, a user is actually specifying the boundary conditions of a cost function that will be minimized to find the new deformed surface. The cost function is made to favor smooth surfaces. The deformed surface is then defined to be the surface that meets the boundary constraints and minimizes the cost.

There are several possible user interfaces for interactively selecting a deformable region. The deformable region in Figure 4a was selected by interactively painting the surface. As a user clicks and drags on the surface, the vertex nearest to the user's clicked point is found and added to the deformable region. The paint brush size can be enlarged by adding the neighboring vertices to the deformable region, and an arbitrarily-sized paint brush can be created by recursively adding the neighbors of already selected vertices to the deformable region.

Alternatively, a deformable region can be selected by placing a loop on the surface, and then adding all of the vertices inside of the loop to the deformable region. A loop path can be thought of as a cut path that starts and ends at the same point.

After selecting a deformable region, a user can drag any point in the region to a desired location. The remaining deformable region is smoothly pulled along as the point is moved (Figure 4b). The deformed surface is displayed in real time as the point is moved. Normally, this real-time update would not be possible as the cost function minimization must be performed many times per second in order to achieve a sufficient frame rate. However, Botsch and Kobbelt (2004a) perform a pre-computation step that allows the minimization to be performed only once for an entire deformation. This speedup means that BCM is capable of performing freeform deformations on a large number of triangles (250k) interactively. By repeating this procedure of defining a deformable region and pulling on the surface, a user can quickly create a complicated shape.

3 FINDING THE CUT PATH

Before a cut can be created in a surface, the cut must be defined. As stated above, the cut path is created by placing seed points on the surface, and then the soft-

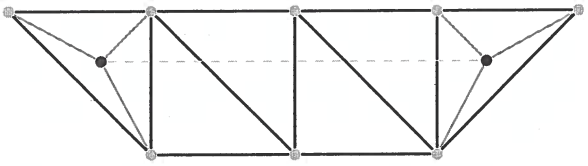

Figure 8. The triangle strip from Figure 6 after subdividing the triangles that begin and end the cut path. Newly added edges are shown in red.

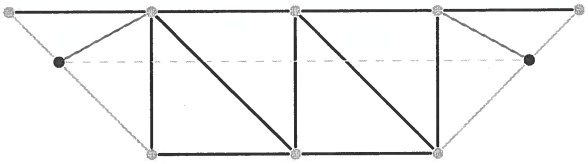

Figure 9. If the cut path seed points are near a boundary, then the end points are snapped to the boundary and an edge break operation is performed on the boundary edges. The broken edges are shown in green and the newly created edges are shown in red.

break adds a new vertex in the middle of an edge. The original edge is divided into two edges and two new edges are added in the neighboring triangles.

Triangle subdivision (Figure 8) creates new vertices at cut path seed points. The new vertices form the ends of the cut. A special case arises if the cut path begins or ends on a boundary. In this case, the cut actually does not create a new hole the mesh. The cut extends a preexisting boundary of the mesh, and the normal subdivide operation is replaced with an edge break operation (Figure 9). Note that, a cut of this type may break the mesh into two pieces.

The next operations, edge cloning (Figure 11) and vertex cloning (Figure 12), are always performed in tandem and complete the hole in the mesh. In this sense,

Algorithm 1 REMESHCUT(*edges*, *points*)

n = LENGTH(*points*)
{get an empty array of vertices}
verts = GETVERTSARRAY(n)

{subdivide end triangles (Figure 8)
or break end edges (Figure 9)}
verts[0] = SUBORBREAK(*verts*[0], *edges*[0])
verts[$n-1$] =
    SUBORBREAK(*verts*[$n-1$], *edges*[$n-3$])

for $i = 1$ to n-2 **do** {Figure 10}
  verts[i] = BREAKEDGE(*edges*[$i-1$], *points*[i]))
end for

for $i = 0$ to n-2 **do** {Figure 11}
  CLONEEDGEBETWEEN(*verts*[i], *verts*[$i+1$])
end for

for $i = 1$ to n-2 **do** {Figure 12}
  CLONEVERTEX(*verts*[i])
end for

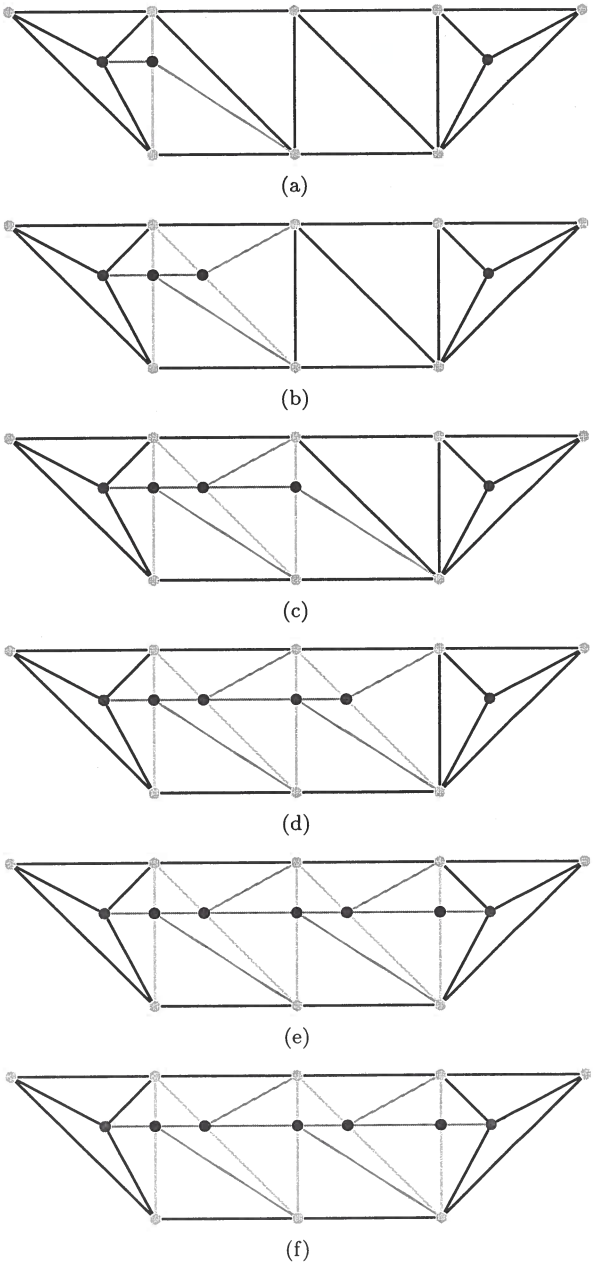

Figure 10. The triangle strip from Figure 8 during and after edge break operation. Each edge that is intersected by the cut path has been broken. Broken edges are shown in green. Edges that will be part of the cut are shown in blue and newly added edges that are not part of the cut are shown in red.

ACKNOWLEDGEMENTS

I would like to thank Landmark Graphics for their financial support, and Dave Hale, Luming Liang, and Andrzej Szymczak for their insightful suggestions and feedback. The U.S. Department of Energy provided the seismic image shown in Figure 1.

References

Bielser, D. and M. H. Gross, 2000, Interactive simulation of surgical cuts: Pacific Conference on Computer Graphics and Applications, 116, Institute of Electrical and Electronics Engineers Computer Society.

Botsch, M. and L. Kobbelt, 2004a, An intuitive framework for real-time freeform modeling: Association for Computing Machinery Transactions on Graphics, **23**, 630–634.

———, 2004b, A remeshing approach to multiresolution modeling: Proceedings of the 2004 Eurographics, 185–192.

Botsch, M., M. Pauly, C. Rössl, S. Bischoff, and L. Kobbelt, 2006, Geometric modeling based on triangle meshes: Presented at the Eurographics.

Bruyns, C. D. and S. Senger, 2001, Interactive cutting of 3d surface meshes: Computers & Graphics, **25**, 635–642.

Bruyns, C. D., S. Senger, A. Menon, K. Montgomery, S. Wildermuth, and R. Boyle, 2002, A survey of interactive mesh-cutting techniques and a new method for implementing generalized interactive mesh cutting using virtual tools: The Journal of Visualization and Computer Animation, **13**, 21–42.

Choi, K.-S., 2006, Interactive cutting of deformable objects using force propagation approach and digital design analogy: Computers & Graphics, **30**, 233 – 243.

Dijkstra, E. W., 1959, A note on two problems in connexion with graphs: Numerische Mathematik, **1**, 269–271.

Kimmel, R. and J. A. Sethian, 1998, Computing geodesic paths on manifolds: Proceedings of the National Academy of Sciences, 8431–8435.

Mitchell, J. S. B., D. M. Mount, and C. H. Papadimitriou, 1987, The discrete geodesic problem: Society for Industrial and Applied Mathematics Journal on Computing, **16**, 647–668.

Nienhuys, H.-W. and A. F. van der Stappen, 2001, A surgery simulation supporting cuts and finite element deformation: Springer-Verlag.

Welch, W. and A. Witkin, 1994, Free-form shape design using triangulated surfaces: Computer Graphics, **28**, 247–256.

Image-guided blended neighbor interpolation

Dave Hale
Center for Wave Phenomena, Colorado School of Mines, Golden CO 80401, USA

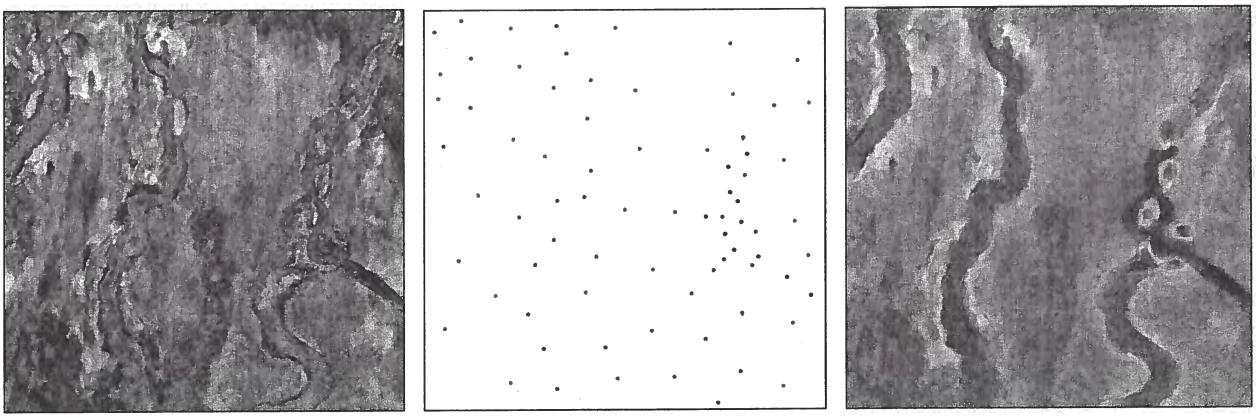

(a) (b) (c)

Figure 1. A seismic image (a) and scattered data (b) used in image-guided blended neighbor interpolation (c).

ABSTRACT
Uniformly sampled images are often used to interpolate other data acquired more sparsely with an entirely different mode of measurement. For example, downhole tools enable geophysical properties to be measured with high precision near boreholes that are scattered spatially, and less precise seismic images acquired at the earth's surface are used to interpolate those properties at locations far away from the boreholes. *Image-guided interpolation* is designed specifically to enhance this process.
Most existing methods for interpolation require distances from points where data will be interpolated to nearby points where data are known. Image-guided interpolation requires non-Euclidean distances in metric tensor fields that represent the coherence, orientations and shapes of features in images. This requirement leads to a new method for interpolating scattered data that I call *blended neighbor interpolation*. For simple Euclidean distances, blended neighbor interpolation resembles the classic natural neighbor interpolation.

Key words: seismic image interpolation interpretation

1 INTRODUCTION

Interpolation of spatially scattered data is a classic problem. In the example shown in Figure 1, I guided this interpolation to conform to buried channels in a uniformly-sampled seismic image of the earth's subsurface. The 76 scattered sample values are represented by just three colors cyan, red and blue. Image-guided blended neighbor interpolation honors these values while computing a second transparent image overlay with a continuous spectrum of colors. The color yellow, not represented in the scattered data, corresponds to a value between the values for red and cyan; features painted yellow therefore lie between those painted red and cyan. In this example, I painted the scattered data values interactively.

More generally, the scattered data that we seek to

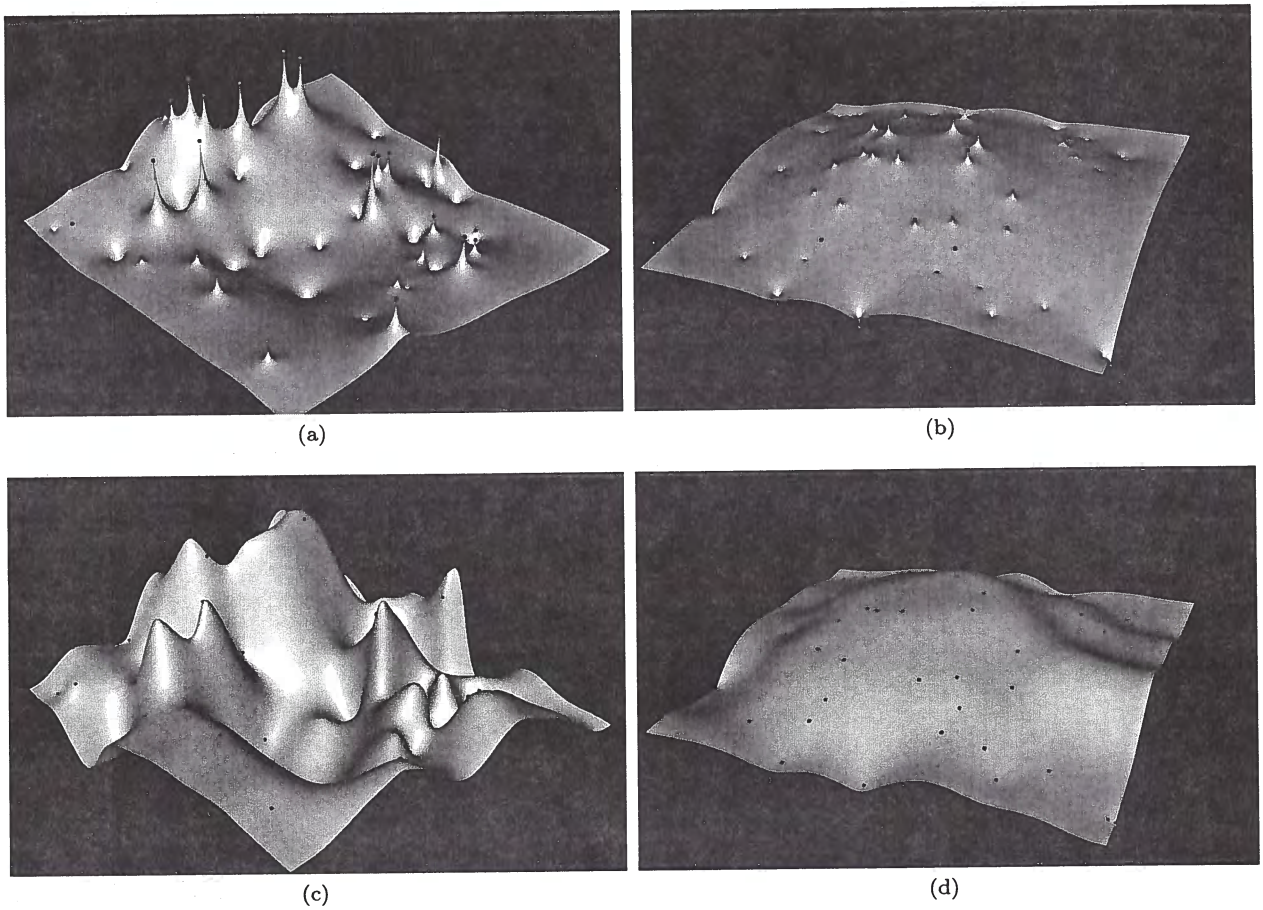

Figure 2. Harmonic (a and b) and biharmonic (c and d) interpolation of scattered samples of rough and smooth functions.

the biharmonic equations 5. In this respect, biharmonic interpolation is less robust than harmonic interpolation.

To reduce the amount of overshoot, we may construct a weighted combination of the harmonic equations 4 and the biharmonic equations 5. The weight in this combination is sometimes called *tension* (Mitášová and Luboš, 1993), and for any given set $\mathcal{K}$ of scattered data it is difficult to know what tension is appropriate before solving the equations.

1.2 RBF methods for interpolation

The harmonic and biharmonic interpolants are closely related to another family of interpolants of the form

$$q(\mathbf{x}) = \sum_{k=1}^{K} w_k \phi(\|\mathbf{x} - \mathbf{x}_k\|), \tag{7}$$

where $\phi(r) : \mathbb{R} \to \mathbb{R}$ is a *radial basis function* (RBF) of distance r (Dyn, 1987; Carr et al., 1997). For example, in two dimensions, the thin-plate spline (Duchon, 1977) corresponds to the RBF $\Phi(\mathbf{x}) \equiv \phi(\|\mathbf{x}\|) = \|\mathbf{x}\|^2 \log\|\mathbf{x}\|$, which is a fundamental solution of the biharmonic equation $(\nabla^2)^2\Phi(\mathbf{x}) = 0$.

To determine the weights w_k in equation 7, we use the interpolation conditions $q(\mathbf{x}_k) = f_k$ to obtain a system of K linear equations for the K unknown weights. For an RBF without compact support this system of equations is dense, not sparse, and the computational cost of solving them is $O(K^3)$.

In other words, the cost of RBF interpolation grows quickly with the number K of known samples, in part because each interpolated sample depends through equation 7 on every known sample. Like the PDE methods described above, RBF methods for interpolation are *global*. If a known sample $(f_k, \mathbf{x}_k)$ in the set $\mathcal{K}$ is added, removed, or modified, all interpolated values $q(\mathbf{x})$ must be recomputed, no matter how great the distance $\|\mathbf{x} - \mathbf{x}_k\|$.

To reduce this cost we might use an RBF with compact support (Franke, 1982; Schaback, 2005) to obtain a sparse system of equations. But the resulting interpolation methods raise a new question. For what distance $\|\mathbf{x} - \mathbf{x}_k\|$ should the RBF $\Phi(\mathbf{x} - \mathbf{x}_k)$ go to zero? That

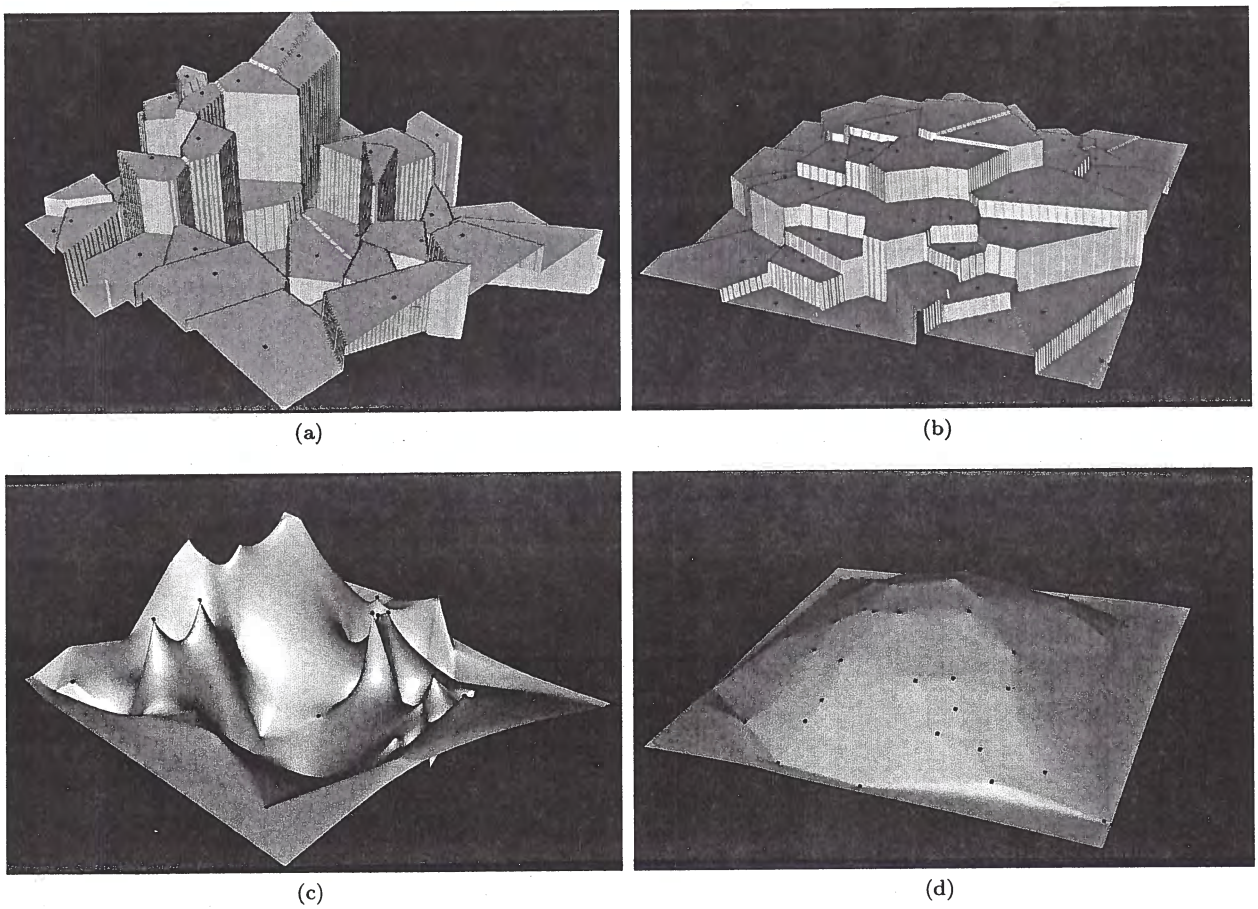

Figure 4. Nearest neighbor (a and b) and natural neighbor (c and d) interpolation of scattered samples.

$d(\mathbf{x}) : \mathbb{R}^n \rightarrow \mathbb{R}$ is the distance $\|\mathbf{x} - \mathbf{x}_k\|$ from $\mathbf{x}$ to the nearest known sample point $\mathbf{x}_k$, and

$p(\mathbf{x}) : \mathbb{R}^n \rightarrow \mathbb{R}$ is the value f_k corresponding to the sample point $\mathbf{x}_k$ nearest to the point $\mathbf{x}$.

In other words, $d(\mathbf{x})$ is the *distance map* and $p(\mathbf{x})$ is the *nearest neighbor interpolant* for the scattered data $\mathcal{K}$.

With these two functions, the natural neighbor interpolant is defined by

$$q(\mathbf{x}) = \frac{\int h(\mathbf{x},\mathbf{y})\, p(\mathbf{y})\, \mathrm{d}^n\mathbf{y}}{\int h(\mathbf{x},\mathbf{y})\, \mathrm{d}^n\mathbf{y}}, \tag{10}$$

where

$$h(\mathbf{x},\mathbf{y}) \equiv \begin{cases} 1, & \text{if } \|\mathbf{x}-\mathbf{y}\| \leq d(\mathbf{y}); \\ 0, & \text{otherwise.} \end{cases} \tag{11}$$

This definition of natural neighbor interpolation is equivalent to Sibson's (1981) definition in equation 9. For any interpolated point $\mathbf{x}$, the function $h(\mathbf{x},\mathbf{y})$ defined in equation 11 restricts the integrals in equation 10 to precisely the shaded polygon illustrated in Figure 3b.

We may interpret equation 10 in two different ways. The first and perhaps most obvious interpretation is that numerous $p(\mathbf{y})$-weighted infinitesimal elements $\mathrm{d}^n\mathbf{y}$ are gathered into a single interpolated value $q(\mathbf{x})$. The second interpretation is that a single $p(\mathbf{y})$-weighted infinitesimal element $\mathrm{d}^n\mathbf{y}$ is scattered into numerous interpolated values $q(\mathbf{x})$. These two interprations are illustrated in Figure 5.

Both the gather and scatter interpretations of equation 10 imply that the natural neighbor interpolant $q(\mathbf{x})$ is obtained by smoothing the nearest neighbor interpolant $p(\mathbf{x})$. And in both interpretations the smoothing filter $h(\mathbf{x},\mathbf{y})$ varies spatially according to equation 11. However, the circular region of support for $h(\mathbf{x},\mathbf{y})$ used in scattering is simpler than the polygonal region used in gathering.

In a discrete approximation of natural neighbor interpolation (Park et al., 2006), scattering may be more efficient than gathering. In this approximation, the functions in equations 10 and 11 are sampled uniformly and the integrals become sums. Gathering then implies an outer loop over sampled $\mathbf{x}$ and an inner loop over sam-

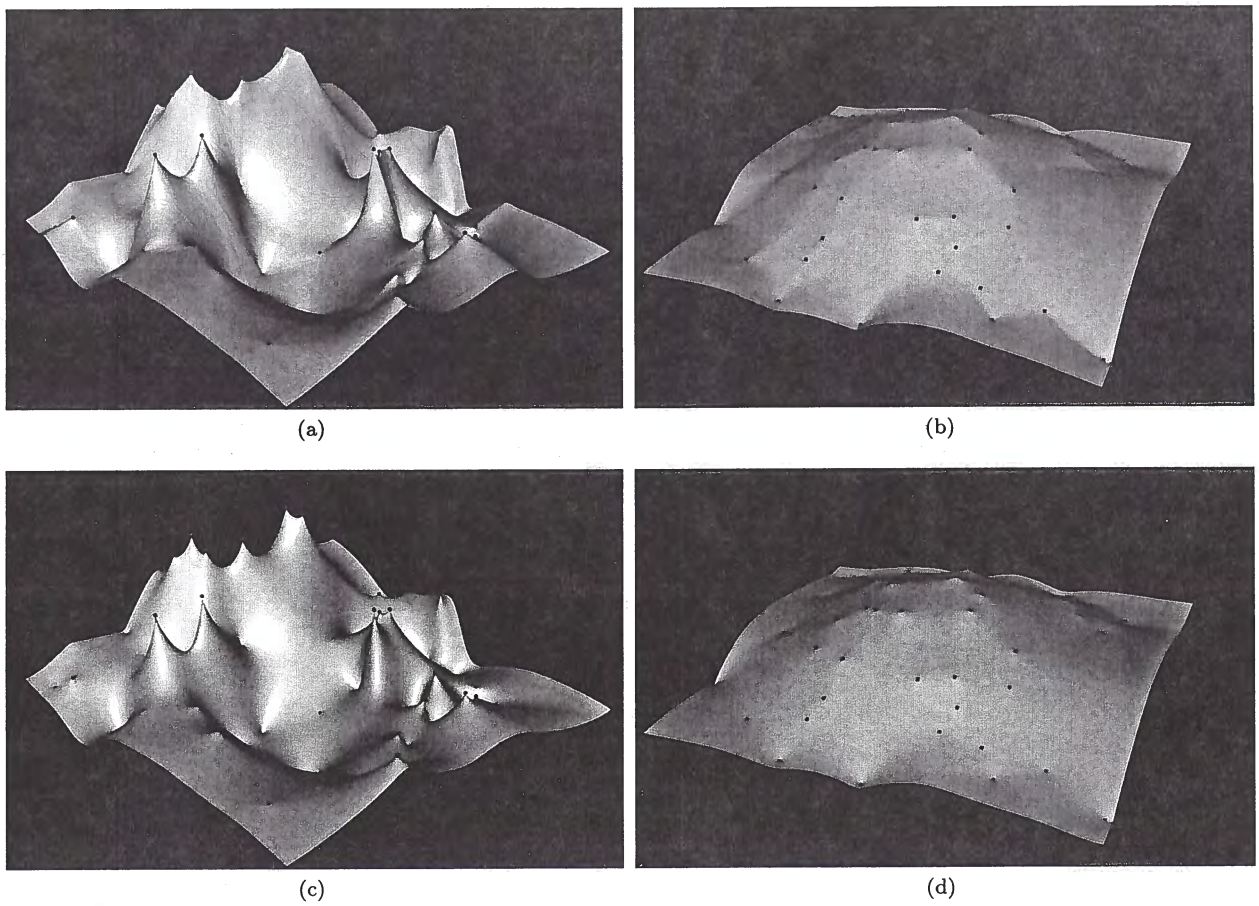

Figure 6. Discrete natural neighbor (a and b) and blended neighbor (c and d) interpolation of scattered samples.

2.2 Alternative blending PDEs

We may obtain alternatives to the blending equation 12 by simply modifying its coefficients. For example, we might restrict the variable coefficient $d(\mathbf{x})$ in equation 12 to not exceed some specified maximum distance. This maximum would limit the extent of smoothing and thereby also limit the number of iterations required to converge to a solution $q(\mathbf{x})$. Linear precision of the blended neighbor interpolant would be lost for large distances but maintained where perhaps most desirable, at locations $\mathbf{x}$ where the density of known samples is high and distances $d(\mathbf{x})$ are relatively small.

A related alternative is to replace the constant coefficient $\frac{1}{2}$ in equation 12 with a smaller value. In doing so, we lose linear precision for all $\mathbf{x}$, but gain smoothness at the known sample points $\mathbf{x}_k$, where $\nabla q(\mathbf{x}_k) = 0$. In effect, decreasing this coefficient reduces the amount of smoothing performed by the blending equation 12. Indeed, in the limit as this coefficient goes to zero, no smoothing is performed and the blended neighbor interpolant $q(\mathbf{x})$ equals the nearest neighbor interpolant $p(\mathbf{x})$.

More generally, we may solve

$$q(\mathbf{x}) - \frac{1}{e} \nabla \cdot d^2(\mathbf{x}) \nabla q(\mathbf{x}) = p(\mathbf{x}), \tag{15}$$

for some constant $e \geq 2$. Figures 6c and 6d correspond to the choice $e = 2$, for interpolants with linear precision.

Figure 7 displays blended neighbor interpolants for $e = 4$ and $e = 8$. While smoother at the known sample points $\mathbf{x}_k$, these interpolants have flat spots, small plateaus at those points, and cannot precisely interpolate data sampled from linear functions.

The choice $e = 3$ is interesting because, inside the Voronoi neighborhood of any known sample point $\mathbf{x}_k$, equation 15 then has the solution

$$q_k(\mathbf{x}) = f_k + h_k \|\mathbf{x} - \mathbf{x}_k\|, \tag{16}$$

for some constant h_k. Although the solution $q_k(\mathbf{x})$ lacks linear precision, its dependence on the radial distance $\|\mathbf{x} - \mathbf{x}_k\|$ reminds us of RBF methods for interpolation. In particular, the RBF $\phi(\|\mathbf{x} - \mathbf{x}_k\|) = \|\mathbf{x} - \mathbf{x}_k\|$ corresponds to the 3D biharmonic interpolant (Sandwell, 1987).

2.3 Summary

Blended neighbor interpolation is a two-step process.

Blended neighbor interpolation

Step 1: solve

$$\nabla d(\mathbf{x}) \cdot \nabla d(\mathbf{x}) = 1, \quad \mathbf{x} \notin \mathcal{X};$$
$$d(\mathbf{x}) = 0, \quad \mathbf{x} \in \mathcal{X} \tag{20}$$

for

$d(\mathbf{x})$: the distance $\|\mathbf{x} - \mathbf{x}_k\|$ from $\mathbf{x}$ to the nearest known sample point $\mathbf{x}_k$, and
$p(\mathbf{x})$: the known value f_k corresponding to the sample point $\mathbf{x}_k$ nearest to the point $\mathbf{x}$.

Step 2: for a specified constant $e \geq 2$, solve

$$q(\mathbf{x}) - \frac{1}{e} \nabla \cdot d^2(\mathbf{x}) \nabla q(\mathbf{x}) = p(\mathbf{x}), \tag{21}$$

for the blended neighbor interpolant $q(\mathbf{x})$.

When computing $d(\mathbf{x})$ in step 1, it is straightforward to simultaneously compute the nearest neighbor interpolant $p(\mathbf{x})$. Finite-difference approximation of the eikonal equation 20 is unnecessary, because efficient exact solutions are possible. Park et al. (2006), suggest using a kD tree for this purpose.

After computing $d(\mathbf{x})$ and $p(\mathbf{x})$ on a uniformly sampled grid, I use an iterative conjugate-gradient method to solve a finite-difference approximation of equation 21 for the blended neighbor interpolant $q(\mathbf{x})$.

3 BLENDING IN TENSOR FIELDS

In image-guided interpolation I replace Euclidean distance with time, so that "nearest" corresponds to paths of minimum time between points $\mathbf{x}$ and $\mathbf{x}_k$, not minimum distance $\|\mathbf{x} - \mathbf{x}_k\|$. The result is again a two-step process.

Image-guided blended neighbor interpolation

Step 1: solve

$$\nabla t(\mathbf{x}) \cdot \mathbf{D}(\mathbf{x}) \nabla t(\mathbf{x}) = 1, \quad \mathbf{x} \notin \mathcal{X};$$
$$t(\mathbf{x}) = 0, \quad \mathbf{x} \in \mathcal{X} \tag{22}$$

for

$t(\mathbf{x})$: the minimum traveltime from $\mathbf{x}$ to the nearest known sample point $\mathbf{x}_k$, and
$p(\mathbf{x})$: the value f_k corresponding to the sample point $\mathbf{x}_k$ nearest to the point $\mathbf{x}$.

Step 2: for a specified constant $e \geq 2$, solve

$$q(\mathbf{x}) - \frac{1}{e} \nabla \cdot t^2(\mathbf{x}) \mathbf{D}(\mathbf{x}) \nabla q(\mathbf{x}) = p(\mathbf{x}), \tag{23}$$

for the blended neighbor interpolant $q(\mathbf{x})$.

3.1 Computing the tensor field

The metric tensor field $\mathbf{D}(\mathbf{x})$ in equations 22 and 23 is the link between distance and time. It represents the coherence, orientation, and dimensionality of features in the image that will guide interpolation. Intuitively, this tensor field alters interpolation so that known sample values within spatially coherent image features are given more weight than values on opposite sides of such features or where the image is less coherent.

In some applications, a suitable $\mathbf{D}(\mathbf{x})$ is readily available. For example, to track white matter in diffusion-tensor magnetic-resonance images (DT-MRI), Jbabdi et al. (2008) choose $\mathbf{D}(\mathbf{x})$ to be simply the inverse of acquired tensor-valued images. For scalar-valued images, including most seismic images, $\mathbf{D}(\mathbf{x})$ may be computed from structure tensors $\mathbf{S}(\mathbf{x})$, which are smoothed outer products of gradient vectors (van Vliet and Verbeek, 1995).

In two dimensions, each tensor in the field $\mathbf{D}(\mathbf{x})$ is a 2×2 symmetric positive-definite matrix

$$\mathbf{D} = \begin{bmatrix} d_{11} & d_{12} \\ d_{12} & d_{22} \end{bmatrix}. \tag{24}$$

Equations 22 and 23 imply that the tensor elements d_{11}, d_{12}, and d_{22} have units of velocity squared.

Because the units of time t are arbitrary in equations 22 and 23, I scale the tensor field $\mathbf{D}(\mathbf{x})$ so that the maximum eigenvalue (maximum velocity squared) in any of these matrices is one. Eigenvalues less than one therefore imply slower velocities in directions of the corresponding eigenvectors.

In directions in which velocities are slow, two points that are nearby in the Euclidean distance map $d(\mathbf{x})$ may be far apart in the time map $t(\mathbf{x})$, the solution to equation 22 computed in step 1. Time, not distance, now determines which neighboring known sample points $\mathbf{x}_k$ are nearest in step 1, and the amount of blending of nearest neighbors performed in step 2.

Figure 8 shows examples of tensor fields $\mathbf{D}(\mathbf{x})$ computed from two different 2D scalar-valued seismic images to guide interpolation of scattered data. Each ellipse represents one of the symmetric positive-definite 2×2 tensors that I computed for every sample in these images.

For both images, I computed the displayed tensor fields $\mathbf{D}(\mathbf{x})$ from a structure tensor field $\mathbf{S}(\mathbf{x})$ by

$$\mathbf{D}(\mathbf{x}) = s \frac{\mathbf{S}^{-1}(\mathbf{x})}{1 - c(\mathbf{x})}, \tag{25}$$

where the constant scale factor s ensures that the maximum eigenvalue in $\mathbf{D}(\mathbf{x})$ is one. The function $c(\mathbf{x})$ is a measure of coherence computed from structure tensors $\mathbf{S}(\mathbf{x})$ using the method suggested by Fehmers and Höcker(2003).

Alternative measures of coherence (e.g., Bahorich and Farmer, 1995) in the range $0 \leq c(\mathbf{x}) < 1$ could be used instead. The significance of the divisor $1 - c(\mathbf{x})$ is

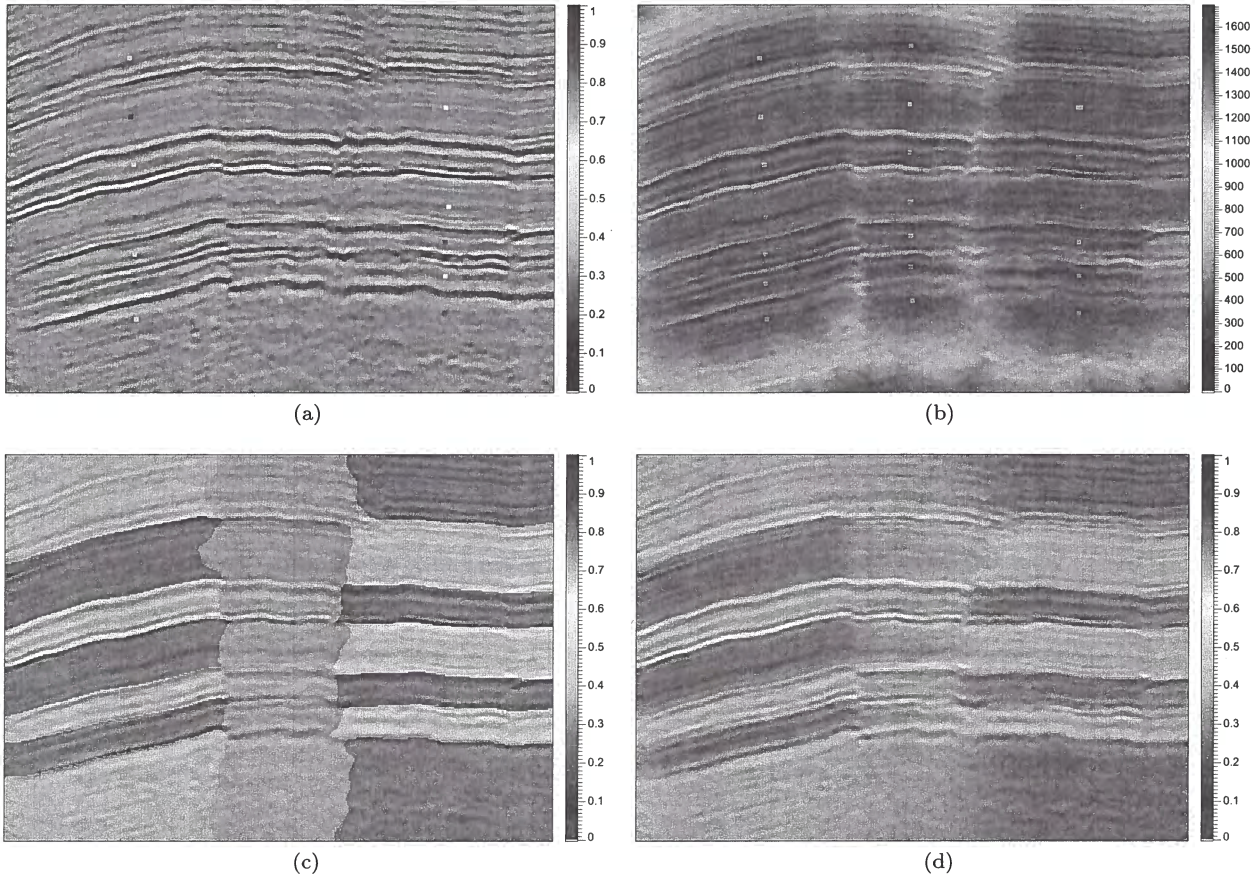

Figure 9. Image-guided blended neighbor interpolation. For a set $\mathcal{K}$ of known samples (a), we first use equation 22 to compute the time map (b) and nearest neighbor interpolant (c), and then solve equation 23 for the blended neighbor interpolant (d).

ity for my implementation of step 1 is $O(NK)$, but the average-case complexity is only $O(N \log K)$.

In step 2 I solved a finite-difference approximation to the blending equation 23 with $e = 4$ using an iterative conjugate-gradient solver. With $K = 21$ scattered samples and $N = 251 \times 357$ image samples, I performed 709 iterations to converge to the blended neighbor interpolant $q(\mathbf{x})$ displayed in Figure 9d. As expected, this blended neighbor interpolant conforms to features in the seismic image. Contours of constant color are aligned with both near-horizontal features (geologic layers) and near-vertical discontinuities (geologic faults).

To compare the image-guided process to one similar to a discrete natural neighbor interpolant (Park et al., 2006), I solved equations 20 and 21 with $e = 4$ for the same set of scattered data. In this isotropic and homogeneous case, 243 conjugate-gradient iterations were required to converge to the blended neighbor interpolant displayed in Figure 10.

As expected, without the tensor field $\mathbf{D}(\mathbf{x})$ to guide the interpolation, the blended neighbor interpolant is smooth between sample points but does not conform to image features. Both image-guided and image-ignorant interpolants honor the scattered data values, but the image-guided interpolant is more accurate where the values to be interpolated are correlated with image features.

4 DISCUSSION

Assuming that an image is available, the accuracy of image-guided interpolation depends on the extent to which the property being interpolated is correlated with image features. If no such correlation exists, then a simpler and faster image-ignorant interpolation may be more accurate than image-guided interpolation with an irrelevant image. In this case, blended neighbor interpolation is an efficient alternative to discrete natural neighbor interpolation.

In many contexts, however, an isotropic and constant tensor field is inappropriate. Even when a useful image is unavailable, it may still be possible to construct an anisotropic and inhomogeneous tensor field $\mathbf{D}(\mathbf{x})$ to guide interpolation. The proposed two-step process

must be computed numerically by solving an eikonal equation 22 for every image sample. And even supposing that this region could be computed quickly for every sample, the computational cost of scattering remains proportional to the areas (or volumes) of such regions in 2D (or 3D).

In contrast, the cost of solving the blending equations with the simplest conjugate-gradient method grows only linearly with distances or times to nearest known samples. The number of iterations required for such an iterative solver to converge depends in part on the accuracy required in the blended neighbor interpolant. The number of iterations might be reduced by the use of preconditioners, including multigrid methods, but in my experience these techniques have yielded only moderate improvements in efficiency when tensor fields are as inhomogeneous and anisotropic as those displayed in Figure 8.

Closely related to the problem of image-guided interpolation are the problems of computing geodesic distances and interpolation on surfaces embedded in a 3D space (Kimmel and Sethian, 1998; Boissonnat and Flötotto, 2004; Surazhasky et al., 2005) or manifolds in higher dimensions (Bronstein et al., 2007). For example, when interpolating scattered geophysical data acquired on a global scale, one might use non-Euclidean distances measured on the earth's surface. Surfaces on which geodesic distances are computed correspond to metric tensor fields, but tensor fields computed as in equation **??** need not correspond to any surface. Nevertheless, improved algorithms for computing geodesic distances may lead to better algorithms for image-guided interpolation.

5 CONCLUSION

Blended neighbor interpolation of scattered data is similar to the classic method of natural neighbor interpolation, in that both methods smooth a nearest neighbor interpolant, and the extent of smoothing grows with distance to the nearest known sample point.

The interpolants are similar but not identical, and the difference between the two methods lies in their smoothing filters. In blended neighbor interpolation a smoothing filter is implied by the solution of a partial differential equation. In natural neighbor interpolation the smoothing filter explicitly computes weighted sums of nearest neighbor sample values.

When Euclidean distances are used, the weights in natural neighbor interpolation are simply the areas of polygons, and can be computed efficiently with suitable data structures. However, in non-Euclidean metric tensor fields, these areas must be computed numerically, and for this case blended neighbor interpolation is an efficient alternative to natural neighbor interpolation.

In image-guided interpolation we derive metric tensor fields from images, so that the blended neighbor interpolant conforms to image features, while retaining many of the attractive features of the natural neighbor interpolant.

ACKNOWLEDGMENTS

Thanks to Luming Liang for many thoughtful discussions of the ideas presented in this paper, and to Myoung Jae Kwon, Ken Larner, and Derek Parks for helpful reviews. WesternGeco provided the seismic data displayed in Figures 1 and 8a. The U.S. Department of Energy provided the seismic data displayed in Figures 8b, 9 and 10.

REFERENCES

Bahorich, M.S., and S.L. Farmer, 1995, 3-D seismic coherency for faults and stratigraphic features: The coherence cube: The Leading Edge, **14** 1053–1058.

Bobach, T., G. Farin, D. Hansford and G. Umlauf, 2008, Natural neighbor extrapolation using ghost points: Computer-Aided Design, in press.

Boissonnat, J.-D., and J. Flötotto, 2004, A coordinate system associated with points scattered on a surface: Computer-Aided Design, **36**, 161–174.

Bronstein, A.M., M.M. Bronstein and R. Kimmel, 2007, Weighted distance maps computation on parametric three-dimensional manifolds: Journal of Computational Physics, **225**, 771–784.

Carr, J.C., W.R. Fright and R.K. Beatson, 1997, Surface interpolation with radial basis functions for medical imaging: IEEE Transactions on Medical Imaging, **16**, 96–107.

Cormen, T.H., C.E. Leiserson and R.L. Rivest, 2001, Introduction to algorithms, second edition: MIT Press.

Duchon, J., 1977, Splines minimizing rotation-invariant seminorms in Sobolev spaces, *in* W. Schempp and K. Zeller, eds., Constructive Theory of Functions of Several Variables, Lecture Notes in Mathematics 571, Springer-Verlag, 85–100.

Dyn, N., 1987, Interpolation of scattered data by radial functions, *in* C.K. Chui and L.L. Schumaker and F. Utreras, eds., Topics in Multivariate Approximation: Academic Press, 47–61.

Farin, G., 1990, Surfaces over Direchlet tesselations: Computer Aided Geometric Design, **7**, 281–292.

Fehmers, G.C., C.F.W. Höcker, 2003, Fast structural interpretations with structure-oriented filtering: Geophysics, **68**, 1286–1293.

Foster, M.P., and A.N. Evans, 2008, An evaluation of interpolation techniques for reconstructing ionospheric TEC maps: IEEE Transactions on Geoscience and Remote Sensing, **46**, 2153–2164.

Franke, R., 1982, Smooth interpolation of scattered data by local thin plate splines: Computers & Mathematics with Applications, **8**, 237-281.

Gáspár, C., 1999, Multigrid technique for biharmonic interpolation with application to dual and multiple reciprocity method: Numerical Algorithms, **21**, 165–183.

Goovaerts, P., 1997, Geostatistics for natural resources evaluation: Oxford University Press.

Structure-oriented smoothing and semblance

Dave Hale
Center for Wave Phenomena, Colorado School of Mines, Golden CO 80401, USA

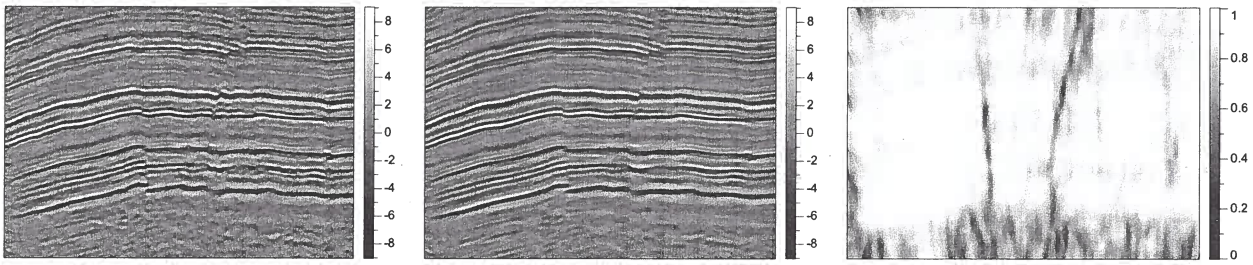

(a) (b) (c)

Figure 1. A seismic image (a) after applying structure-oriented smoothing (b) and semblance (c) filters.

ABSTRACT
Smoothing along structures apparent in seismic images can enhance these structural features while preserving important discontinuities such as faults or channels. Filters appropriate for such smoothing must seamlessly adapt to variations in the orientation and coherence of image features. I describe an implementation of smoothing filters that does this and is both computationally efficient and simple to implement.
Structure-oriented filters lead naturally to the computation of structure-oriented semblance, an attribute commonly used to highlight discontinuities in seismic images. Semblance is defined in this paper as simply the ratio of a squared smoothed-image to a smoothed squared-image. This definition of semblance generalizes that commonly used today, because an unlimited variety of smoothing filters can be used to compute the numerator and denominator images in the semblance ratio. The smoothing filters described in this paper yield an especially flexible method for computing structure-oriented semblance.

Key words: seismic image smoothing semblance

1 INTRODUCTION

Images like those displayed in Figure 1 are familiar in the context of exploration seismology, where spatial sampling is sufficiently uniform to enable the application of a variety of generic image-processing techniques. For example, coherency-enhancing anisotropic diffusion filters, as described by Weickert (1997, 1999), have been adapted by Fehmers and Höcker (2003) for structure-oriented filtering of seismic images to enhance their interpretation. Figure 1b illustrates a similar *structure-oriented smoothing* process that smooths along coherent reflections while preserving faults.

Faults apparent in Figure 1a are highlighted in Figure 1c using a process that (in the sense of Fehmers and Höcker, 2003) I call *structure-oriented semblance*. As shown here, semblance is a normalized measure of coherence with values between zero and one, where zero corresponds to no coherence. I used the semblance image in structure-oriented filtering to inhibit smoothing across the faults in Figure 1b. However, semblance images like that in Figure 1c are often used directly in seismic interpretation to construct geologic models of faults and stratigrathic features such as channels (e.g., Bahorich and Farmer, 1995; Marfurt et al., 1998).

The purpose of this paper is to describe new methods for computing smoothed and semblance images like

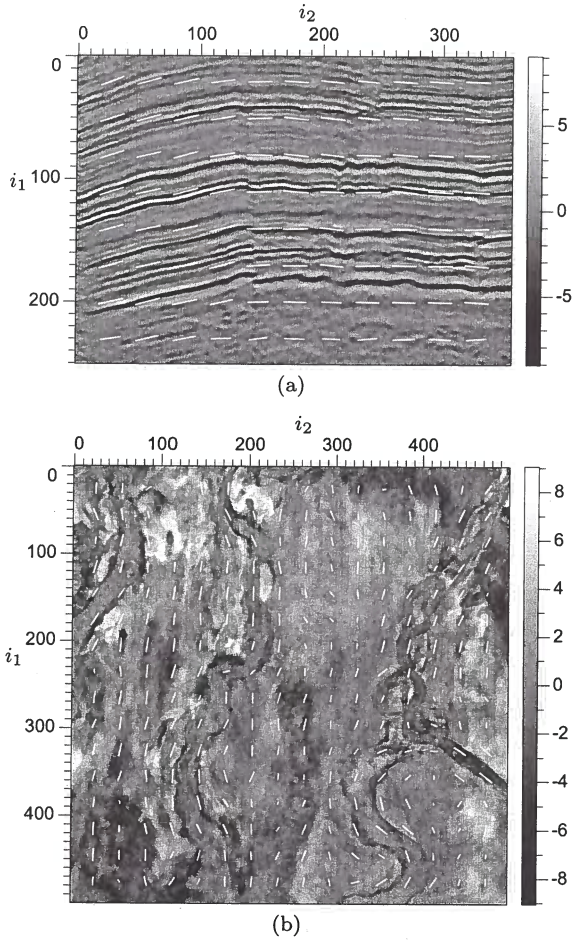

Figure 2. Eigenvectors $\mathbf{v}$ for 2D slices of two different 3D seismic images of faulted geologic layers (a) and buried channels (b).

by reflection slope cannot be used to smooth along the features apparent in Figure 2b.

2.2 Smoothing with anisotropic diffusion

A more generally useful alternative proposed by Weickert (1997,1999) and Fehmers and Höcker (2003) (and others) is to parameterize a structure-oriented smoothing filter by a tensor field. For an input image $f(\mathbf{x})$ and a corresponding structure-tensor field $\mathbf{T}(\mathbf{x})$, these authors propose the solution of an anisotropic diffusion equation

$$\frac{\partial g(\mathbf{x};\tau)}{\partial \tau} = \nabla \cdot \mathbf{D}(\mathbf{x}) \nabla g(\mathbf{x};\tau) \qquad (4)$$

with initial condition $g(\mathbf{x};\tau = 0) = f(\mathbf{x})$. For any time $\tau > 0$, the solution $g(\mathbf{x};\tau)$ is a smoothed version of the input image $f(\mathbf{x})$.

This anisotropic diffusion equation is parameterized by a diffusion-tensor field $\mathbf{D}(\mathbf{x})$ that shares the eigenvectors of the structure-tensor field $\mathbf{T}(\mathbf{x})$. To smooth along the eigenvectors $\mathbf{v}(\mathbf{x})$ illustrated in Figure 2, we might set $\lambda_u(\mathbf{x}) = 0$ and $\lambda_v(\mathbf{x}) = 1$ for all tensors in the field $\mathbf{D}(\mathbf{x})$. More generally, we might let the eigenvalues of $\mathbf{D}(\mathbf{x})$ depend on the measures of isotropy and linearity computed from $\mathbf{T}(\mathbf{x})$ according to equations 3.

Unfortunately, as noted by Fehmers and Höcker (2003), straightforward explicit and stable numerical solutions to the anisotropic diffusion equation 4 may require a prohibitively large number of time steps. So they instead use an unspecified solution method that they liken to a "rudimentary multigrid implementation".

2.3 An anisotropic smoothing filter

When considering the efficiency of structure-oriented smoothing with anistropic diffusion, Fehmers and Höcker (2003) suggest that it is unnecessary to model the diffusion process exactly. Consistent with their suggestion, I propose here the numerical solution of a different partial differential equation

$$g(\mathbf{x}) - \alpha \nabla \cdot \mathbf{D}(\mathbf{x}) \nabla g(\mathbf{x}) = f(\mathbf{x}). \qquad (5)$$

Here, $f(\mathbf{x})$ represents the input image and $g(\mathbf{x})$ represents the output smoothed image. The constant filter parameter α could be absorbed into the smoothing-tensor field $\mathbf{D}(\mathbf{x})$, but is kept separate to provide a convenient control for the extent of smoothing. For $\alpha = 0$, we have $g(\mathbf{x}) = f(\mathbf{x})$, and no smoothing is performed.

Unlike the solution of the diffusion equation 4, the solution to the smoothing equation 5 does not depend on time τ. However, smoothing with equation 5 does require the numerical solution of a large sparse system of equations. (Numerical solution of equation 5 is equivalent to a single but possibly large time step in an unconditionally stable implicit numerical solution of the diffusion equation 4.) Fortunately, simple finite-difference approximations suffice to obtain a sparse symmetric positive-semidefinite system of equations that we may solve efficiently using conjugate-gradient iterations.

I use the bilinear transform (e.g., Oppenheim et al., 1999) to approximate the partial derivatives in equation 5. As a simple example, consider the 1D version of equation 5 with constant coefficients

$$g(x) - \alpha g''(x) = f(x). \qquad (6)$$

Using z-transform notation, the bilinear transform of a derivative is the substitution

$$g'(x) \Rightarrow 2\frac{1 - z^{-1}}{1 + z^{-1}} G(z) \qquad (7)$$

or, equivalently,

$$-g'(x) \Rightarrow 2\frac{1 - z}{1 + z} G(z). \qquad (8)$$

With this approximation, the z-transform of equation 6

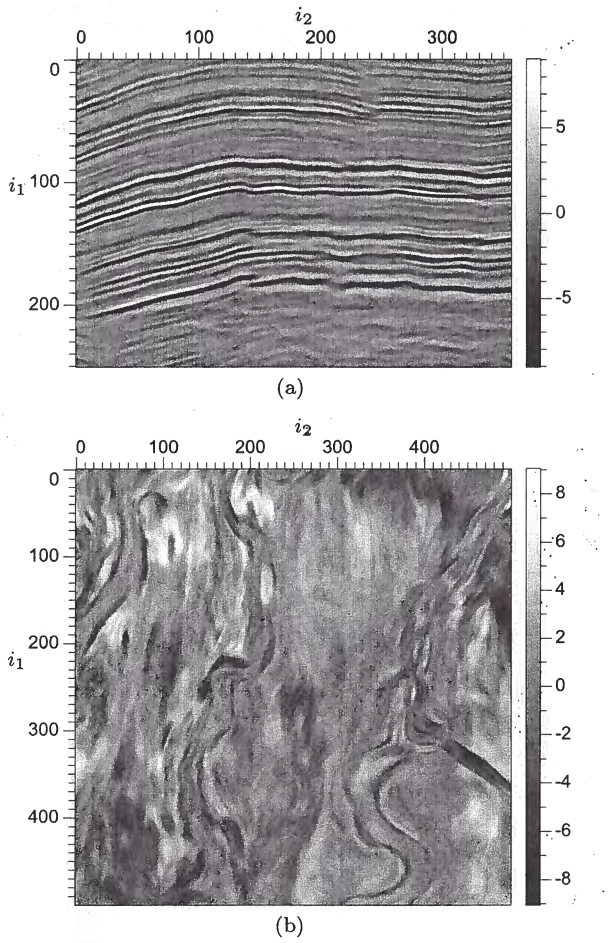

Figure 3. Anisotropic smoothing (for $\alpha = 18$) along the eigenvectors $\mathbf{v}$ of Figure 2 for two seismic images.

step is to recognize that sums in conventional definitions of semblance perform a sort of smoothing. We can then replace those sums with the weighted sums of smoothing filters.

3.1 Conventional semblance

Semblance was first defined by Taner and Koehler (1969) and developed further by Neidell and Taner (1971) in the context of velocity spectra, where they computed semblance as a function of time for CMP gathers after normal moveout correction. An equivalent definition that is consistent with the notation used elsewhere in this paper is

$$s[i_1] = \frac{\sum_{j_1=i_1-M_1}^{i_1+M_1} \left(\sum_{j_2=0}^{N_2-1} f[j_1,j_2] \right)^2}{N_2 \sum_{j_1=i_1-M_1}^{i_1+M_1} \sum_{j_2=0}^{N_2-1} (f[j_1,j_2])^2}. \qquad (12)$$

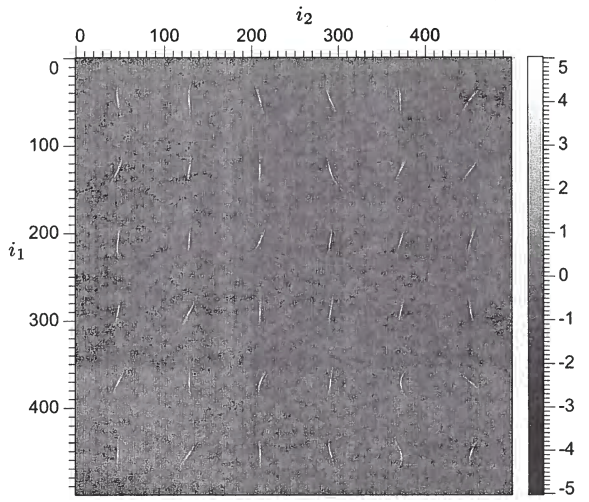

Figure 4. Anisotropic smoothing-filter weights for $\alpha = 70$. These weights conform to the eigenvector field $\mathbf{v}$ of Figure 2b, and imply curvilinear smoothing paths. Weights shown here are scaled by a factor of 100 for display.

For all indices i_1, semblance $s[i_1]$ is maximized and equals one when the values $f[j_1,j_2]$ do not vary with the index j_2. For Taner and Koehler's velocity spectra, the index j_2 corresponds to a trace number and the index j_1 corresponds to a time sample. The inner sums over j_2 correspond to N_2 NMO-corrected traces in a CMP gather. The outer sums over j_1 correspond to a window of $2M_1+1$ time samples centered at the sample i_1 for which semblance $s[i_1]$ is to be computed.

Marfurt et al. (1998) used a similar definition of semblance as the ratio of sums like these to compute local measures of coherence. Instead of scanning over different NMO velocities to maximize semblance, they instead scanned over different planar reflection slopes in local windows of seismic traces. A simplified version (omitting Hilbert tranforms) of their semblance measure for 2D images would be

$$s[i_1,i_2] = \frac{\sum_{j_1=i_1-M_1}^{i_1+M_1} \left(\sum_{j_2=i_2-M_2}^{i_2+M_2} f[j_1,j_2] \right)^2}{(2M_2+1) \sum_{j_1=i_1-M_1}^{i_1+M_1} \sum_{j_2=i_2-M_2}^{i_2+M_2} (f[j_1,j_2])^2}. \qquad (13)$$

In this definition, $f[j_1,j_2]$ corresponds to a window of $(2M_1+1) \times (2M_2+1)$ image samples after shifting in time to flatten planar reflections for a specified slope. Semblance is maximized if that specified slope matches the slope of a planar reflection in the image.

Semblance computed by equation 13 is stored at indices i_1 and i_2 that correspond to the centers of the summation windows. Therefore, the sums in the numerator and denominator of this equation work much like symmetric local smoothing filters. However, these smoothing filters have constant weights, implying that

are non-negative. The leftmost term in the denominator is unity because it equals the sum of those weights. Then, by the Cauchy-Schwarz inequality, we have $s \leq 1$.

Equation 16 is written carefully to show that weighted semblance is equivalent to a normalized correlation coefficient for two sequences $\sqrt{h[j]}$ and $\sqrt{h[j]}f[j]$. This coefficient is unity if the sequence $f[j]$ is constant. When this sequence is not constant, more weight is given to the values $f[j]$ for which the weights $h[j]$ are largest.

To compute weighted semblance in sliding and seamlessly overlapping windows of the sequence $f[j]$, we simply write

$$s[i] = \frac{\left(\sum_j h[i-j]f[j]\right)^2}{\sum_j h[i-j]\left(f[j]\right)^2}. \tag{17}$$

Both numerator and denominator in this ratio include convolution with a smoothing filter like those shown in Figure 5a. In this sense, *semblance is the ratio of a squared smoothed-sequence to a smoothed squared-sequence.*

However, the smoothing filter need not be shift invariant. An even more general form of equation 17 is

$$s[i] = \frac{\left(\sum_j h[i;j]f[j]\right)^2}{\sum_j h[i;j]\left(f[j]\right)^2}. \tag{18}$$

In other words, smoothing-filter coefficients $h[i;j]$ may vary with index i, provided that the properties in equations 15 are satisfied for all i.

Before extending the notion of weighted semblance to 2D and 3D images, it will help to simplify notation further by letting $\langle\cdot\rangle$ denote smoothing of whatever is inside the angle brackets, so that semblance becomes simply

$$s = \frac{\langle f\rangle^2}{\langle f^2\rangle}. \tag{19}$$

3.4 2D structure-oriented semblance

For 2D images, we have the opportunity to include a second smoothing, as in the conventional definition of semblance in equation 13. Using the concise notation described above, we may rewrite this equation as

$$s_{2,1} = \frac{\langle\, \langle f\rangle_2^2\,\rangle_1}{\langle\, \langle f^2\rangle_2\,\rangle_1}, \tag{20}$$

where $\langle\cdot\rangle_1$ denotes smoothing along the 1st image axis, and $\langle\cdot\rangle_2$ denotes smoothing along the 2nd axis. The outer smoothing $\langle\cdot\rangle_1$ helps to stabilize semblance values where the inner smoothing $\langle\cdot\rangle_2$ accumulates only very small and perhaps noisy values. Depending on expected orientations of image features, we might switch the 1st and 2nd smoothing directions.

For structure-oriented semblance, I simply replace axis-aligned smoothing with structure-oriented smoothing. When computing semblance for 2D images, we may define the smoothing filters using eigenvectors $\mathbf{u}$ and $\mathbf{v}$ computed from structure tensors. Structure-oriented semblance is then

$$s_{v,u} = \frac{\langle\, \langle f\rangle_v^2\,\rangle_u}{\langle\, \langle f^2\rangle_v\,\rangle_u}. \tag{21}$$

The inner smoothing $\langle\cdot\rangle_v$ is along image features, and the outer smoothing $\langle\cdot\rangle_u$ is across those features.

I computed the structure-oriented semblance shown in Figure 1c using structure-oriented smoothing filters with $M = 4$ ($\alpha = M(M+1)/6$) for inner smoothing $\langle\cdot\rangle_v$ along image features and $M = 16$ for outer smoothing $\langle\cdot\rangle_u$ across those features. As expected, semblance is low near faults and near the bottom where the image f is less coherent.

The structure-oriented smoothing filters used to compute semblance in this and other examples shown in this paper do not strictly satisfy the second requirement of equation 15 that all weights be non-negative. Recall the smoothing-filter weights shown in Figure 4, which are mostly positive, but on close inspection exhibit negative values. Non-negative weights are easy to obtain for 1D smoothing; e.g., the smoothed exponential sequence in Figure 5a. However, I have been unable to guarantee non-negative weights in useful finite-difference approximations of the more general anisotropic smoothing equation 5.

Nevertheless, these smoothing filters yield a useful semblance measure. I simply clip the values of $s_{v,u}$ so that values less than zero are replaced with zero and values greater than one are replaced with one. In my experience, computing structure-oriented semblance for both 2D and 3D images, this clipping occurs rarely. In the example shown in Figure 1c, no such clipping was necessary.

Figure 6 shows the same semblance image again for comparison with a more conventional slope-based semblance image. I computed this slope-based semblance for a sliding window of nine traces ($M = 4$). Within each such window, I used sinc interpolation of each trace to flatten the nine-trace image before computing the inner horizontal sums with constant (boxcar) weights. I then computed the outer vertical sums by applying vertical Gaussian smoothing for $M = 16$ ($\sigma = \sqrt{M(M+1)/3}$), before finally computing the semblance ratios. Although smoothing filters varied, this example of slope-based semblance is comparable to that of structure-oriented semblance because I chose consistent half-widths $M = 4$ and $M = 16$ in both examples.

A notable difference between the two semblance images in Figure 6 is the appearance of faults as piecewise vertical features in the slope-based semblance image. This vertical bias is caused by the outer Gaussian filtering that in the conventional slope-based method smooths semblance numerators and denominators only

orthogonal to linear or planar features. The eigenvectors $\mathbf{w}$, which correspond to the smallest eigenvalues λ_w, will be aligned with linear features, such as the channels in Figure 7a. Both eigenvectors $\mathbf{v}$ and $\mathbf{w}$ will lie within the planes of any planar features.

Structure-oriented semblance measured within local planes defined by eigenvectors $\mathbf{v}$ and $\mathbf{w}$ is then simply

$$s_{vw,u} = \frac{\langle\, \langle f \rangle_{vw}^2 \,\rangle_u}{\langle\, \langle f^2 \rangle_{vw} \,\rangle_u}. \tag{23}$$

This equation defines a *planar semblance*. For the inner curviplanar smoothing, we use smoothing tensors $\mathbf{D} = \mathbf{v}\mathbf{v}^T + \mathbf{w}\mathbf{w}^T$. For the outer orthogonal curvilinear smoothing, we use $\mathbf{D} = \mathbf{u}\mathbf{u}^T$. Unlike slope-based semblance, planar semblance remains well defined for steeply dipping, even vertical, features in 3D seismic images.

Choosing the eigenvalues of smoothing tensors $\mathbf{D}$ in a different way, we can likewise define a *linear semblance*

$$s_{w,uv} = \frac{\langle\, \langle f \rangle_w^2 \,\rangle_{uv}}{\langle\, \langle f^2 \rangle_w \,\rangle_{uv}}. \tag{24}$$

As its name implies, this linear semblance measures coherence along curvilinear paths within an image.

Planar and linear semblance are two extremes in a continuum of semblance measures we may define by choosing the eigenvalues of smoothing tensors $\mathbf{D}$ in different ways. We may, for example, choose the eigenvalues of $\mathbf{D}$ to be functions of the eigenvalues of the corresponding structure tensors $\mathbf{T}$, perhaps using the following measures of isotropy, linearity and planarity:

$$\begin{aligned} \textit{isotropy:} \quad & \lambda_0 = \lambda_w/\lambda_u \\ \textit{linearity:} \quad & \lambda_1 = (\lambda_v - \lambda_w)/\lambda_u \\ \textit{planarity:} \quad & \lambda_2 = (\lambda_u - \lambda_v)/\lambda_u, \end{aligned} \tag{25}$$

defined here such that $\lambda_0 + \lambda_1 + \lambda_2 = 1$. In any case, the outer smoothing we perform in the semblance calculation is an orthogonal complement to the inner smoothing.

Figure 8 shows examples of both planar and linear semblance. All smoothing filters in these examples have half-width $M = 2$ samples. (Shorter filters are more suitable for 3D images than for 2D images because of the extra dimension in which smoothing can be performed.) Planar semblance highlights (with low values) all features that are not planar, such as the channels, which are linear. Linear semblance highlights variations within those channels, features that are neither linear nor planar, but may be significant.

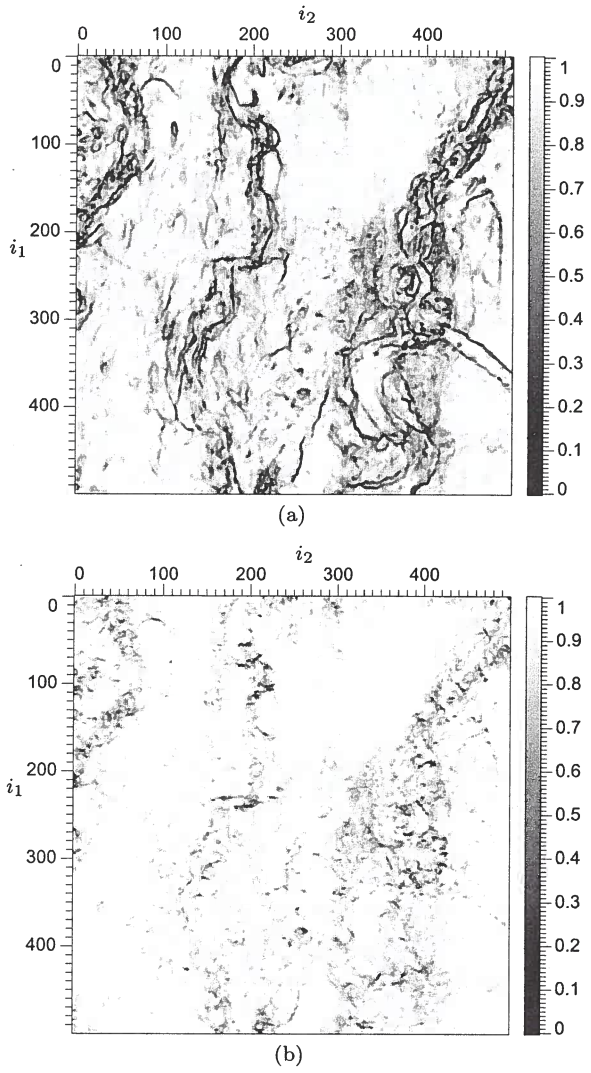

Figure 8. 3D structure-oriented planar semblance $s_{vw,u}$ (a) and linear semblance $s_{w,uv}$ (b) computed for a 3D seismic image of buried channels. Shown here are horizontal 2D slices (coincident with the 2D slices shown in Figure 7) extracted from 3D semblance images.

4 CONCLUSION

Structure-oriented smoothing filters as described in this paper are quite general, with parameters derived mostly from structure-tensor fields. In contrast to smoothing filters parameterized by slopes of image features, this generality enables smoothing of 2D and 3D images with arbitrary orientations and dimensionalities.

Structure-oriented smoothing filters are also simple to implement with small computer programs. The most significant part of the implementation for 2D filters (not including a necessary but readily available conjugate-gradient solver) is a computer program with only 23 lines. A similar program for 3D structure-oriented smoothing consists of only 42 lines.

From structure-oriented smoothing we may define structure-oriented semblance as the ratio of a squared smoothed-image to a smoothed squared-image.